

**LEVEL II**

**2**  
B.S.

AFFDL-TR-79-3066

**AD A 071573**

**AERODYNAMIC HEATING IN THE FIN INTERACTION REGION OF  
GENERALIZED MISSILE SHAPES AT MACH 6  
(MODULAR MISSILE TEST PROGRAM)**

**High Speed Aero-Performance Branch  
Aeromechanics Division**

**Richard D. Neumann**

**James R. Hayes**

**May 1979**

**TECHNICAL REPORT AFFDL-TR-79-3066**

**Final Report for the Period July 1975 Through June 1978**

**DDC FILE COPY.**

**DDC  
RECEIVED  
JUL 23 1979  
REGISTRY  
D**

**Approved for public release; distribution unlimited**

**AIR FORCE FLIGHT DYNAMICS LABORATORY  
AIR FORCE WRIGHT AERONAUTICAL LABORATORIES  
AIR FORCE SYSTEMS COMMAND  
WRIGHT-PATTERSON AIR FORCE BASE, OHIO 45433**

**79 07 19 006**

NOTICE

When Government drawings, specifications, or other data are used for any purpose other than in connection with a definitely related Government procurement operation, the United States Government thereby incurs no responsibility nor any obligation whatsoever; and the fact that the government may have formulated, furnished, or in any way supplied the said drawings, specifications, or other data, is not to be regarded by implication or otherwise as in any manner licensing the holder or any other person or corporation, or conveying any rights or permission to manufacture, use, or sell any patented invention that may in any way be related thereto.

This report has been reviewed by the Information Office (OI) and is releasable to the National Technical Information Service (NTIS). At NTIS, it will be available to the general public, including foreign nations.

This report has been reviewed and is approved for publication.




RICHARD D. NEUMANN



JAMES R. HAYES

Project Engineers

FOR THE COMMANDER



H. MAX DAVIS  
Asst. for Research and Technology  
Flight Mechanics Division

Copies of this report should not be returned unless return is required by security considerations, contractual obligations, or notice on a specific document.

Unclassified

SECURITY CLASSIFICATION OF THIS PAGE (When Data Entered)

REPORT DOCUMENTATION PAGE

READ INSTRUCTIONS BEFORE COMPLETING FORM

14. REPORT NUMBER AFFDL-TR-79-3066	2. GOVT ACCESSION NO.	3. RECIPIENT'S CATALOG NUMBER 9
6. TITLE (and Subtitle) Aerodynamic Heating in the Fin Interaction Region of Generalized Missile Shapes at Mach 6 (Modular Missile Test Program)	5. TYPE OF REPORT & PERIOD COVERED Final Report July 1974 - April 1979	
10. AUTHOR(S) Richard D. Neumann James R. Hayes	8. CONTRACT OR GRANT NUMBER(s)	
9. PERFORMING ORGANIZATION NAME AND ADDRESS Air Force Flight Dynamics Laboratory High Speed Aero Performance Branch Wright-Patterson Air Force Base, Ohio 45433	10. PROGRAM ELEMENT, PROJECT, TASK AREA & WORK UNIT NUMBERS Project 2404 Task 240407 Work Unit 24040713	
11. CONTROLLING OFFICE NAME AND ADDRESS Air Force Flight Dynamics Laboratory Aeromechanics Division (FX) Wright-Patterson Air Force Base Ohio 45433	12. REPORT DATE May 1979	
14. MONITORING AGENCY NAME & ADDRESS (if different from Controlling Office) <i>12-171p.</i>	15. SECURITY CLASS. (of this report) Unclassified	
16. DISTRIBUTION STATEMENT (of this Report) Approved for Public Release, Distribution Unlimited		
17. DISTRIBUTION STATEMENT (of the abstract entered in Block 20, if different from Report)		
18. SUPPLEMENTARY NOTES		
19. KEY WORDS (Continue on reverse side if necessary and identify by block number) Three-Dimensional Interaction Turbulent Boundary Layer Boundary Layer Separation Peak Heating Ogive-Cylinder		
20. ABSTRACT (Continue on reverse side if necessary and identify by block number) The characteristics of three-dimensional shock wave turbulent boundary layer interactions are investigated for a finned ogive-cylinder configuration. An extensive experimental program was conducted in the AEDC/VKF Tunnel "B" at Mach 6 and a unit Reynolds number of <u>4.9 x 10<sup>6</sup></u> per foot. The model was an ogive-cylinder 50 inches long and 8.5 inches in diameter with fins mounted at model station 42. <i>4.9 million</i>		

79 07 19 006

Unclassified

SECURITY CLASSIFICATION OF THIS PAGE(When Data Entered)

Heat transfer data were taken on the cylinder and on the fin surface in the interaction region of swept and unswept fins sealed to the cylinder and for a swept fin mounted on a torque tube. The fin-cylinder gap produced by the torque tube was varied from 0.00 to 0.50 inches. Recovery factors produced in the interaction region of the unswept fin sealed to the cylinder were also evaluated from thin skin heat transfer data. All fin configurations were tested at ogive-cylinder angles of attack of 0°, 4°, 8°, and 12° and with the fins rolled 0°, 30°, 60°, 90°, and 120° off the cylinder's windward centerline.

The objective of this effort was to correlate the peak interaction heating produced by missile control surfaces through extension of more geometrically simple concepts. Previous work reported for these more simple geometries is extended through this report to more practical configurations. The principle correlating parameter must be based on local flow properties which may be obtained from inviscid flow field computer program solutions. Extensive flow field probing of the shock layer on the ogive-cylinder alone was conducted and the results are shown to agree well with inviscid solutions.

Unclassified

SECURITY CLASSIFICATION OF THIS PAGE(When Data Entered)

FOREWORD

This document presents the results of an experimental and analytical investigation into the characteristics of three dimensional shock wave turbulent boundary layer interactions produced by missile control surfaces. The study was conducted by the High Speed Aero Performance Branch (FXG), Aeromechanics Division, Air Force Flight Dynamics Laboratory, Wright-Patterson Air Force Base, Ohio. The work concludes an in-house research program and was performed under Project 2404 "Aeromechanics", Task 240407 "Aeroperformance and Aeroheating Technology". This report covers analytical & experimental work conducted from July 1975 to June 1978 and concludes work unit 24040713 "Interference Heating to Modular Missile Configurations".

Accession For	
PERM GR&I	<input checked="" type="checkbox"/>
DOC TAB	<input type="checkbox"/>
Unannounced	<input type="checkbox"/>
Classification	
Distribution/	
Availability Codes	
	Avail and/or special
A	

DDC  
 RECEIVED  
 JUL 23 1979  
 D

## TABLE OF CONTENTS

<u>Section</u>		<u>Page</u>
1.0	INTRODUCTION	1
2.0	MODEL AND TEST CONDITIONS	2
	2.1 Modular Missile Model	2
	2.2 Test Conditions and Procedures	4
3.0	PROGRAM OUTLINE	20
	3.1 Sealed Fin Body Interactions	20
	3.2 Total Pressure Surveys and Surface Pressures	21
	3.3 Heating to Surface of Fins	21
	3.4 Interaction Effects of a Torque Tube Fin Mount	22
	3.5 Recovery Factors on a Sealed Fin Interaction	23
4.0	UNDISTURBED DATA	24
	4.1 Heat Transfer Data	24
	4.2 Surface Pressure Data	28
	4.3 Pitot Pressure Surveys	29
	4.4 Inviscid Flow Fields Computer Program	31
5.0	SEALED FIN INTERACTIONS	74
	5.1 Peak Heating at Zero Angle of Attack	74
	5.2 Peak Heating at Angle of Attack, Zero Roll	76
	5.3 Peak Heating at Angle of Attack, Arbitrary Roll	77
	5.4 Location of Peak Aerodynamic Heating	78
	5.5 Effects of Fin Sweep and Bluntness	79
	5.6 Heating to Surface of Fins	81
6.0	FIN-TORQUE TUBE INTERACTIONS	102
	6.1 Heat Transfer Downstream of the Torque Tube	103
	6.2 Heat Transfer Upstream of the Torque Tube	104
7.0	INTERACTION RECOVERY TEMPERATURES	118
8.0	CONCLUSIONS	131
	REFERENCES	134
	Appendix A	135
	Appendix B	143

## LIST OF ILLUSTRATIONS

<u>Figure</u>		<u>Page</u>
2.1	Model Photograph	10
2.2	Ogive-Cylinder Model Dimensions	11
2.3	Instrumentation Locations	12
2.4	Thin Skin Insert Details	13
2.5	Thermocouple Installation Details	14
2.6	Body Contoured (Sealed) Fins	15
2.7	Fin Surface Heating Model	16
2.8	Fin-Torque Tube Model	17
2.9	Shock Layer Pitot Rake Dimensions	18
2.10	Boundary Layer Pitot Rake Dimensions	19
4.1	Untripped, Clean Body Heating, $\alpha=0^\circ$	34
4.2	Untripped, Clean Body Heating, $\alpha=4^\circ$	35
4.3	Untripped, Clean Body Heating, $\alpha=8^\circ$	36
4.4	Untripped, Clean Body Heating, $\alpha=12^\circ$	37
4.5	Transition on the Clean Body at $\alpha=0^\circ$	38
4.6	Transition on the Windward Centerline at $\alpha=12^\circ$	39
4.7	Tripped, Clean Body Heating, $\alpha=0^\circ$	40
4.8	Tripped, Clean Body Heating, $\alpha=4^\circ$	41
4.9	Tripped, Clean Body Heating, $\alpha=8^\circ$	42
4.10	Tripped, Clean Body Heating, $\alpha=12^\circ$	43
4.11	Tripped Heat Transfer Coefficients for Data Normalization, $\alpha=0^\circ$	44
4.12	Tripped Heat Transfer Coefficients for Data Normalization, $\alpha=4^\circ$	45
4.13	Tripped Heat Transfer Coefficients for Data Normalization, $\alpha=8^\circ$	46
4.14	Tripped Heat Transfer Coefficients for Data Normalization, $\alpha=12^\circ$	47
4.15	Longitudinal Heating Distribution for $\alpha=0^\circ$	48
4.16	Surface Pressure Data	49
4.17	Undisturbed Pressure-Heating Correlation	50
4.18	Leeward Centerline Oilflow, $\alpha=8^\circ$	51
4.19	Leeward Centerline Oilflow, $\alpha=10^\circ$	52
4.20	Leeward Centerline Oilflow, $\alpha=12^\circ$	53
4.21	Leeward Separation Induced Heating Minimum, $\alpha=12^\circ$	54
4.22	Extent of Minimum Heating Region at $\alpha=12^\circ$	55
4.23	Shock Layer Pitot Pressure Profiles, $\alpha=4^\circ$	56
4.24	Shock Layer Pitot Pressure Profiles, $\alpha=6^\circ$	57
4.25	Shock Layer Pitot Pressure Profiles, $\alpha=8^\circ$	58
4.26	Shock Layer Pitot Pressure Profiles, $\alpha=10^\circ$	59
4.27	Boundary Layer Pitot Pressure Profiles, $\alpha=0^\circ$	60
4.28	Boundary Layer Pitot Pressure Profiles, $\alpha=4^\circ$	61
4.29	Boundary Layer Pitot Pressure Profiles, $\alpha=8^\circ$	62
4.30	Boundary Layer Pitot Pressure Profiles, $\alpha=12^\circ$	63
4.31	Boundary Layer Thickness	64
4.32	Constant Pitot Pressure Contours at $\alpha=10^\circ$	65
4.33	Comparison of NSWC and Experimental Mach Numbers	66
4.34	Comparison of NSWC and Experimental Pitot Pressures	67

LIST OF ILLUSTRATIONS (Con't)

<u>Figure</u>	<u>Page</u>	<u>Page</u>
4.35	NSWC Static Pressure Profile, $\alpha=8^\circ$ , $\phi=90^\circ$	68
4.36	Experimental Mach Numbers Using NSWC Static Pressures	69
4.37	NSWC Static Pressure Profiles	70
4.38	Maximum Z for Valid Assumption of $P_s = P_w$	71
4.39	Mach Number and Flow Angularity at Boundary Layer Edge	72
4.40	Local Static Temperature Ratio, NSWC Program	73
5.1	Interaction Heat Transfer Distributions, $\alpha=0^\circ$	83
5.2	Fin-Flat Plate Correlation and Ogive-Cylinder Peak Heating	84
5.3	Tripped Fin-Flat Plate Peak Heating Data	85
5.4	Ogive-Cylinder Peak Heating Correlation at Zero Angle of Attack	86
5.5	Comparison of Tripped and Untripped Fin-Flat Plate Data	87
5.6	Ogive-Cylinder Peak Heating Correlation at Angle of Attack, Zero Roll	88
5.7	Ogive-Cylinder Peak Heating Correlation at Angle of Attack and Roll	89
5.8	Ogive-Cylinder Peak Heating Correlation for Leeside of Fin	90
5.9	Peak Heating Location and Token's Prediction	91
5.10	Comparison of Fin-Flat Plate and Ogive-Cylinder Peak Locations	92
5.11	Swept Fin Peak Heating at Zero Angle of Attack	93
5.12	Blunt and Sharp Fin Peak Heating Data Comparison	94
5.13	Token's Blunt Fin Peak Heating Data at Mach 3.71	95
5.14	Fin Bluntness Effects at Mach 6	96
5.15	Vortical Flow Field at Blunt Fin Leading Edge	97
5.16	Instrumented Fin, Zero Sweep	98
5.17	Instrumented Fin, $60^\circ$ Sweep	99
5.18	Fin Surface Heating, Zero Swept Fin	100
5.19	Fin Surface Heating, $60^\circ$ Swept Fin	101
6.1	Fin-Torque Tube Model	106
6.2	Thermocouple Locations for Fin-Torque Tube Insert	107
6.3	Fin-Torque Tube Oil Flow, $\alpha=8^\circ$ , $\phi=0^\circ$ , Gap=0.1	108
6.4	Fin-Torque Tube Oil Flow, $\alpha=8^\circ$ , $\phi=0^\circ$ , Gap=0.3	109
6.5	Fin-Torque Tube Oil Flow, $\alpha=8^\circ$ , $\phi=0^\circ$ , Gap=0.5	110
6.6	Separation Upstream of the Torque Tube	111
6.7	Fin-Torque Tube Oil Flow, $\alpha=8^\circ$ , $\phi=60^\circ$ , Gap=0.1	112
6.8	Downstream Heat Transfer Distributions	113
6.9	Peak Heating Downstream of the Torque Tube	114
6.10	Upstream Heat Transfer Distributions	115
6.11	Peak Heating Upstream of the Torque Tube	116
6.12	Comparison of Upstream Peak Heating to Nestler's Correlation for Unswept Cylinders	117
7.1	Recovery Temperature Extrapolation	122
7.2	Scatter Band for Recovery Temperature Ratio	123
7.3	$T_r/T_o$ Extrapolation From Minimum Scatter of $H_{T_r}$ With $T_w$	124
7.4	Effect on $H$ of Error in the Choice of the Recovery Factor	125
7.5	Recovery Factors	126
7.6	Recovery Factors at the Trough and Separation Peak	127
7.7	Heat Transfer Coefficient Corrections for Recovery Temperature	128
7.8	Recovery Factors at Peak Heating Location & Undisturbed Region	129
7.9	Recovery Temperature Effect on Peak Heating Correlation for Sealed Fins	130



LIST OF ILLUSTRATIONS (Con't)

<u>Figure</u>		<u>Page</u>
APPENDIX A		
A-1a	Shadowgraph , $\alpha=0^\circ$ , Untripped	137
A-1b	Shadowgraph , $\alpha=0^\circ$ , Tripped	138
A-2a	Shadowgraph , $\alpha=12^\circ$ , Untripped	139
A-2b	Shadowgraph , $\alpha=12^\circ$ , Tripped	140
A-3	1/4 Scale Missile Model	141
A-4	Undisturbed Data Correlation	142
APPENDIX B		
B-1	Recovery Factors ; $\alpha=0^\circ$ , Roll= $0^\circ$	144
B-2	Recovery Factors ; $\alpha=4^\circ$ , Roll= $0^\circ$	145
B-3	Recovery Factors ; $\alpha=4^\circ$ , Roll= $30^\circ$	146
B-4	Recovery Factors ; $\alpha=4^\circ$ , Roll= $60^\circ$	147
B-5	Recovery Factors ; $\alpha=4^\circ$ , Roll= $90^\circ$	148
B-6	Recovery Factors ; $\alpha=8^\circ$ , Roll= $0^\circ$	149
B-7	Recovery Factors ; $\alpha=8^\circ$ , Roll= $30^\circ$	150
B-8	Recovery Factors ; $\alpha=8^\circ$ , Roll= $60^\circ$	151
B-9	Recovery Factors ; $\alpha=8^\circ$ , Roll= $90^\circ$	152
B-10	Recovery Factors ; $\alpha=12^\circ$ , Roll= $0^\circ$	153
B-11	Recovery Factors ; $\alpha=12^\circ$ , Roll= $30^\circ$	154
B-12	Recovery Factors ; $\alpha=12^\circ$ , Roll= $60^\circ$	155
B-13	Recovery Factors ; $\alpha=12^\circ$ , Roll= $90^\circ$	156
B-14	Recovery Factors , Undisturbed Flow , $\alpha=0^\circ$	157
B-15	Recovery Factors , Undisturbed Flow , $\alpha=4^\circ$	158
B-16	Recovery Factors , Undisturbed Flow , $\alpha=8^\circ$	159
B-17	Recovery Factors , Undisturbed Flow , $\alpha=12^\circ$	160

## LIST OF SYMBOLS

<u>Symbol</u>		<u>Units</u>
b	Thin Skin Insert Thickness	Ft
$c_p$	Specific Heat	BTU/lb-°R
H	Heat Transfer Coefficient	BTU/ft <sup>2</sup> -sec-°R
K	Constant in Eq. 5.3.1	
M	Mach Number	
P	Pressure	psia
$q$	Dynamic Pressure	psia
$\dot{Q}$	Heating Rate	BTU/ft <sup>2</sup> -sec
$Re$	Reynolds Number	
$St$	Stanton Number	
t	Time	sec
T	Temperature	°R
V	Velocity	ft/sec
w	Model Material Density	lb <sub>m</sub> /ft <sup>3</sup>
X	Axial Distance From Ogive Nose Tip	in
Z	Radial Distance From Cylinder Surface	in
$\alpha$	Missile Angle of Attack	deg
$\Delta x$	Distance from Fin Leading Edge	in
$\delta$	Boundary Layer Thickness	in
$\delta_F$	Fin Deflection Angle	deg
$\theta$	Shock Wave Angle	deg
$\Lambda$	Fin Leading Edge Sweep Angle	
$\phi$	Model Roll Angle or Peripheral Model Station Referenced from Windward Centerline	deg
$\psi$	Angle to Peak Heating Location	

### Subscripts

BL	Blunt Fin Value
i	Initial Value
L	Local Value
PK	Peak Value
r	Recovery Value
S	Static Value

LIST OF SYMBOLS (Con't)

Subscripts

SH	Sharp Fin Value
T	Total (Pitot Probe) Value
U	Undisturbed Value
W	Wall Value
o	Stagnation Value
1	Local Value Upstream of Normal Shock
2	Local Value Downstream of Normal Shock
$\infty$	Free Stream Value

## 1.0 INTRODUCTION

The investigation of shock wave/boundary layer interaction phenomena has been an area of continuing interest for the High Speed Aero Performance Branch for the past decade. Although both two and three dimensional interactions have been investigated, the area of 3-D interactions is more practical with respect to design applications. It is also more challenging for research. This is due primarily to the introduction of vorticity as a heating mechanism in the three dimensional interaction processes. Several reports have been prepared by Branch personnel on this subject, References 3, 4, 5 and 7.

The extension of this work from a flat plate receiver to an ogive-cylinder, which is considered in this report, is an attempt to make the results of an exploratory development effort more practical to the systems designer. The ogive-cylinder, while not a missile design per se, embodies many of the problems found in the evaluation of practical missile designs.

The "Modular Missile" test program spanned a three year period and generated an extensive data base in heat transfer, pressure, and oil flow photographs in the fin interaction region and flow field data about the clean (no fins) ogive-cylinder. An attempt to discuss all aspects of the data obtained could fill several volumes; therefore, the scope of this report was limited to the presentation of basic flow field data about the ogive-cylinder and its use in the correlation of peak heating in the interaction region. The complete data reports are referenced in Section 3.0, Program Outline.

## 2.0 MODEL AND TEST CONDITIONS

### 2.1 Modular Missile Model

The model is basically composed of a stainless steel ogive-cylinder, instrumented with 200 iron-constantan 30 gage thermocouples. The thermocouples are arranged in six thin skin inserts having a nominal skin thickness of 0.030 inches. The general dimensions of the model and a photograph are shown in Figures 2.1 and 2.2. During the course of the test program several types of control surfaces were fabricated and mated to this basic model. The objectives of the program were to first define the flow field properties about the clean ogive-cylinder and then study the interaction heating produced by various control surfaces mated to it.

#### 2.1.1 Thin Skin Inserts

The locations of the thermocouple inserts are shown in Figure 2.3 and details of a typical insert are shown in Figure 2.4. Minimum spacing between adjacent thermocouples was 0.25 inches, and a minimum of 0.50 inches was maintained between thermocouples and any supporting structure around the thin skin section. By installing two or three rows of thermocouples in a skewed pattern as shown in Figure 2.4 the effective spacing between measurements was 0.080 inches or about 1.2 degrees of peripheral arc.

Figure 2.5 presents details on the method of thermocouple installation. Two 0.010 inch diameter holes were drilled at each thermocouple location with a spacing equal to the skin thickness, 0.030 inches. The wires were then fed through the holes, spot welded at the

aerodynamic surface, and flushed off. With this method care must be taken that the weld completely seals the hole or transpiration cooling will occur. However, this method also allows very accurate placement of the thermocouples required for detailed measurements in the fin interaction region.

#### 2.1.2 Control Surfaces

Several types of control fins were constructed for the model. The first set is shown in Figure 2.6 and the pertinent dimensions are given in Table 2.1. All were constructed of stainless steel and were attached to the model with their leading edge at Model Station 42. The fins were all contoured on the lower surface so that they would seal to the cylinder. One of the  $20^{\circ}$  unswept fins was constructed in segments so that effects of varying the fin height could be investigated. All of the fins shown in Figure 2.6 were constructed without instrumentation; however, two fins were later modified for instrumentation along their trailing edge as shown in Figure 2.7.

When testing of this set of fins had been completed, a swept fin with a torque tube mount was designed as shown in Figure 2.8. The ogive-cylinder was modified to house an internal drive system for varying the length of the torque tube protruding from the model. With this configuration the effects of the torque tube and the fin-body gap on the interaction region were investigated.

#### 2.1.3 Pitot Pressure Probes and Surface Pressure Taps

Two pitot pressure rakes were constructed for probing the shock and boundary layers on the clean ogive-cylinder. A large rake shown in Figure 2.9 contained 11 tubes spaced 1.0 inches apart. The rake could be

moved in the radial direction in 0.25 inch increments so that pitot profiles were obtained from the wall to the shock with a resolution of 0.25 inches. Two surface pressure taps also shown in Figure 2.9 were monitored while the pitot data were being taken. Data were taken for every 10° of roll thereby generating peripheral surface pressure distributions with only two taps.

A second smaller rake was also tested which contained 10 tubes spaced 0.10 inches apart. This rake, shown in Figure 2.10, provided the necessary resolution to determine boundary layer thickness on the cylinder at various pitch and roll attitudes.

## 2.2 Test Conditions and Procedures

### 2.2.1 Wind Tunnel

All testing of the Modular Missile Model was done at the Arnold Engineering Development Center (AEDC) in Tunnel B. A detailed description of the tunnel may be found in the AEDC Test Facilities Handbook<sup>(1)</sup>. The tunnel was always operating at its maximum Reynolds number in an attempt to maintain a fully developed turbulent boundary layer at the fin station for all model attitudes. The nominal tests conditions are given below

<u>Mach No.</u>	<u>P<sub>0</sub> psia</u>	<u>T<sub>0</sub> °R</u>	<u>P<sub>∞</sub> psia</u>	<u>q<sub>∞</sub> psia</u>	<u>Re/ftx10<sup>-6</sup></u>
5.95	250	830	0.167	4.13	4.9

### 2.2.2 Heat Transfer Test Procedures

The output of the thermocouples were monitored continuously so that prior to each test run, T<sub>w</sub> and the variation of T<sub>w</sub> between thermocouples were checked to ascertain that they were less than 85°F and ±10°F, respectively. The model was then injected at the desired test attitude,

remained on the tunnel centerline about four seconds, and then retracted. From the beginning of injection until the initiation of retract, the thermocouple outputs were recorded using the VKF digital data scanner in conjunction with a Beckman 210 analog-to-digital conversion system. Each thermocouple output was scanned every 0.06 seconds. After each test run, the model was cooled to an isothermal state using high-pressure air.

The reduction of thin-skin thermocouple data normally involves only the calorimetric heat balance which in coefficient form is:

$$H(T_o) = wbc_p \frac{dT_w/dt}{T_o - T_w} \quad (1)$$

Radiation and conduction losses are neglected in this heat balance and data reduction simply requires evaluation of  $dT_w/dt$  from the temperature-time data and determination of model material properties. For the present tests, radiation effects were negligible; however, conduction effects can be significant in several regions of the models. To permit identification of these regions and to improve evaluation of the data, the following procedure was used.

Separation of variables and integration of Eq. (1) assuming constant  $w$ ,  $b$ ,  $c_p$ , and  $T_o$  yields:

$$\frac{H(T_o)}{wbc_p} (t - t_1) = \ln \frac{T_o - T_{w1}}{T_o - T_w} \quad (2)$$

Differentiation of Eq. (2) with respect to time gives

$$\frac{H(T_o)}{wbc_p} = \frac{d}{dt} \ln \frac{T_o - T_{w1}}{T_o - T_w} \quad (3)$$

Since the left side of Eq. (3) is constant, plotting  $\ln \frac{T_o - T_{w1}}{T_o - T_w}$

versus time will give a straight line if conduction is negligible. Thus,



deviation from a straight line can be interpreted as conduction effects.

The data were evaluated in this manner, and generally a linear portion of the curve was used for all thermocouples. A linear least-square curve fit of  $\ln(T_0 - T_{w_i}) / (T_0 - T_w)$  versus time was applied to the data. The interval of the curve fit began when the model reached the tunnel centerline and its duration was a function of the heating rate as follows:

<u>Range</u>	<u>Time Interval</u>	<u>No. of Points</u>
$\frac{dT_w}{dt} > 32 \text{ } ^\circ\text{R/sec}$	0.3 sec	5
$16 < \frac{dT_w}{dt} \leq 32$	0.4	7
$8 < \frac{dT_w}{dt} \leq 16$	0.5	9
$4 < \frac{dT_w}{dt} \leq 8$	0.7	13
$2 < \frac{dT_w}{dt} \leq 4$	1.0	17
$1 < \frac{dT_w}{dt} \leq 2$	1.5	25
$\frac{dT_w}{dt} < 1$	2.5	41

The time intervals listed above were adequate to keep the right-hand side of Eq. (2) within the linear region. In the strictest sense, the value of  $c_p$  is not constant with temperature as assumed in the integration of Eq. (1). The following expression was evaluated at the midpoint of the time interval used for each thermocouple

$$c_p = (3.15789 \times 10^{-5}) (T_w) + 0.098947, \frac{\text{BTU}}{\text{lbm-}^\circ\text{R}}$$

and the maximum observed variation of  $c_p$  was less than one percent. Thus, the assumption of constant  $c_p$  was reasonable. The value of density used for the type #304 stainless steel skin was 501.3 lbm/ft<sup>3</sup>.

### 2.2.3 Pressure Test Procedures

Pitot pressures and model surface pressures were measured with the Tunnel B standard pressure system, which uses 1- and 15-psid transducers. This system automatically selects the 1-psid transducers to measure pressures less than 1 psia and the 15-psid transducers for pressures greater than 1 psia. All measurements are referenced to a near vacuum. Based on periodic comparisons with secondary standards, the precision of these transducers (bands which include 95 percent of the residuals) is estimated to be  $\pm 0.2$  percent of reading or  $\pm 0.0003$  psi, whichever is greater, for the 0- to 1-psia measurements and  $\pm 0.2$  percent of reading or  $\pm 0.01$  psi, whichever is greater, for the 1- to 15- psia measurements.

After each rake vertical position change the model was injected into the test section flow at zero angle of attack, the pressures were allowed to stabilize, and the measurements were recorded. After measurements were obtained at the desired roll angles, the model was pitched to another angle and the procedure was repeated until the desired angle of attack range was completed. This procedure of obtaining data at several roll angles for each angle of attack was done to map the flow field circumferentially.

### 2.2.4 Oil Flow Test Procedures

After completion of the heat-transfer data, flow field photographs were taken to obtain surface flow patterns on the model. The model was

painted black. White oil was applied to the model and photographs were recorded with one or more cameras located on the tunnel viewing ports. The model was injected after applying the oil and photographs were taken at the rate of one per second until the model was retracted.

TABLE 2.1 FIN DIMENSIONS

<u>Number of Pins</u>	<u>Sweep Angle</u>	<u>Wedge Half Angle</u>	<u>Length</u>	<u>Height</u>
2	0	6	6	5.5
2	0	7.5	6	5.5
2	0	9	6	5.5
1	0	10	6	5.5
1	0	10	6	1.0,2.0,2.5 inch segments
2	45	10	6	6
2	60	10	6	3.3

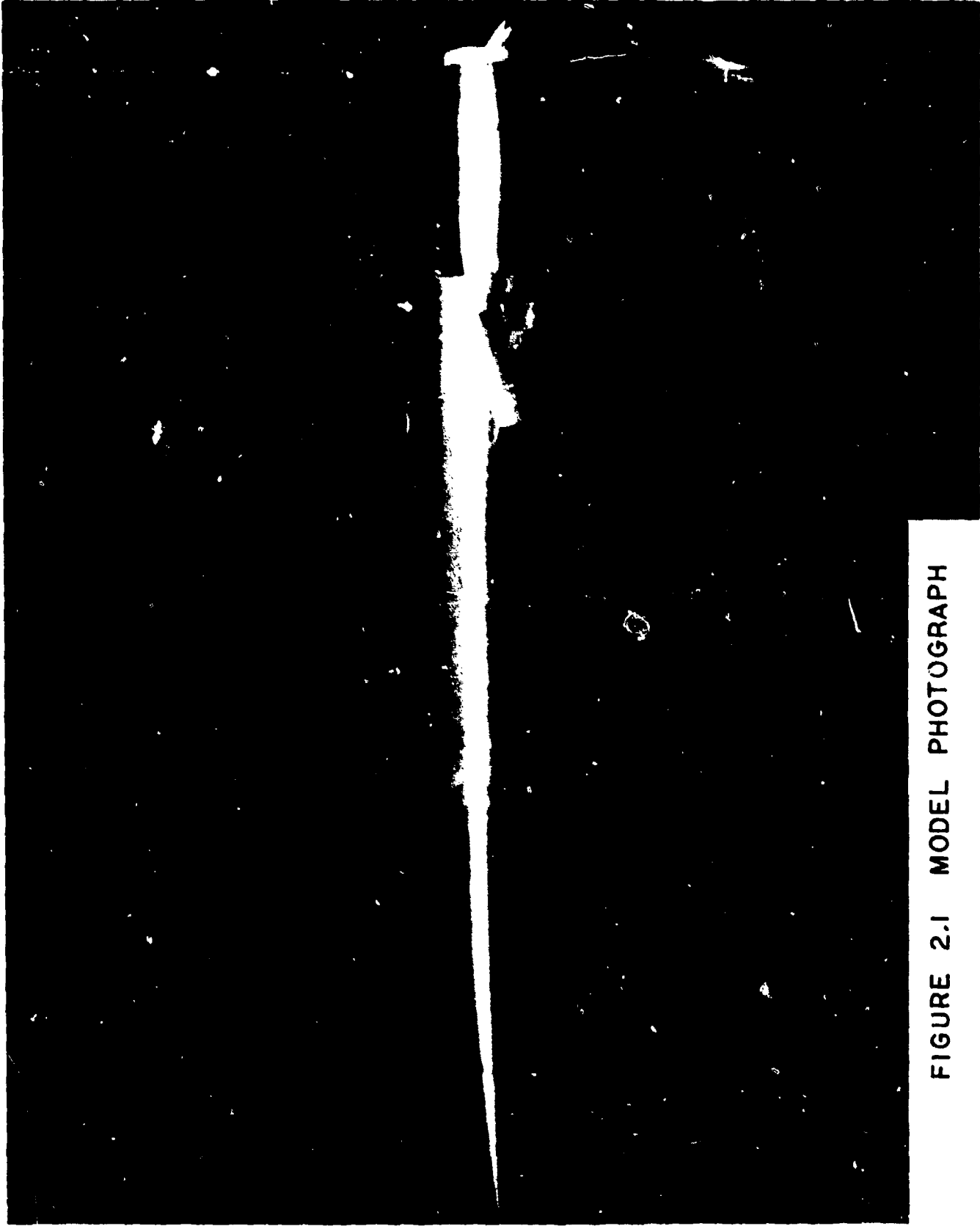


FIGURE 2.1 MODEL PHOTOGRAPH

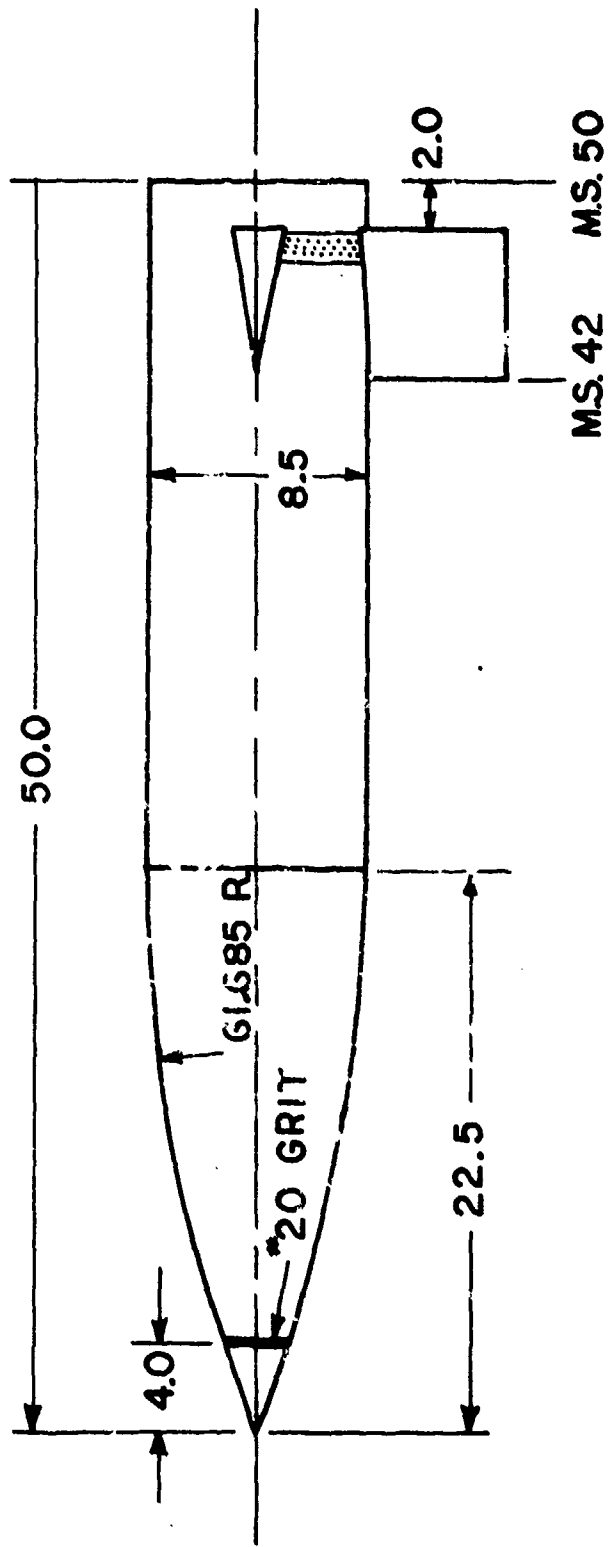


FIGURE 22 MODEL DIMENSIONS

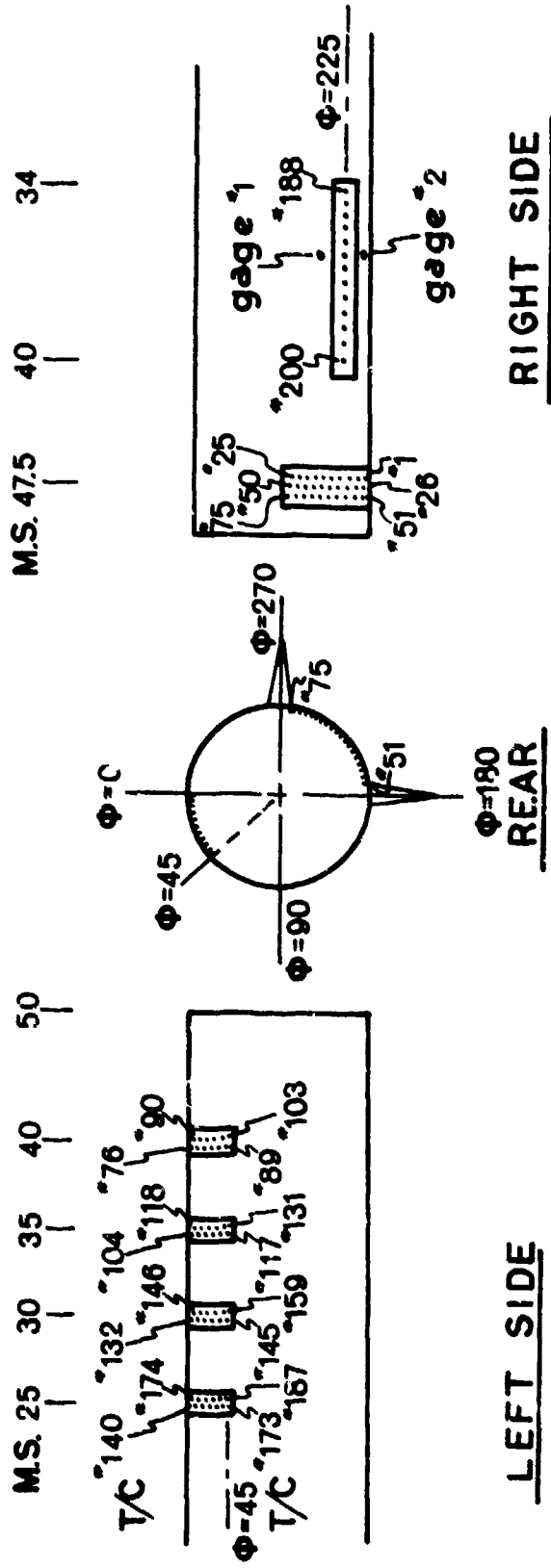


FIGURE 2.3 INSTRUMENTATION LOCATIONS

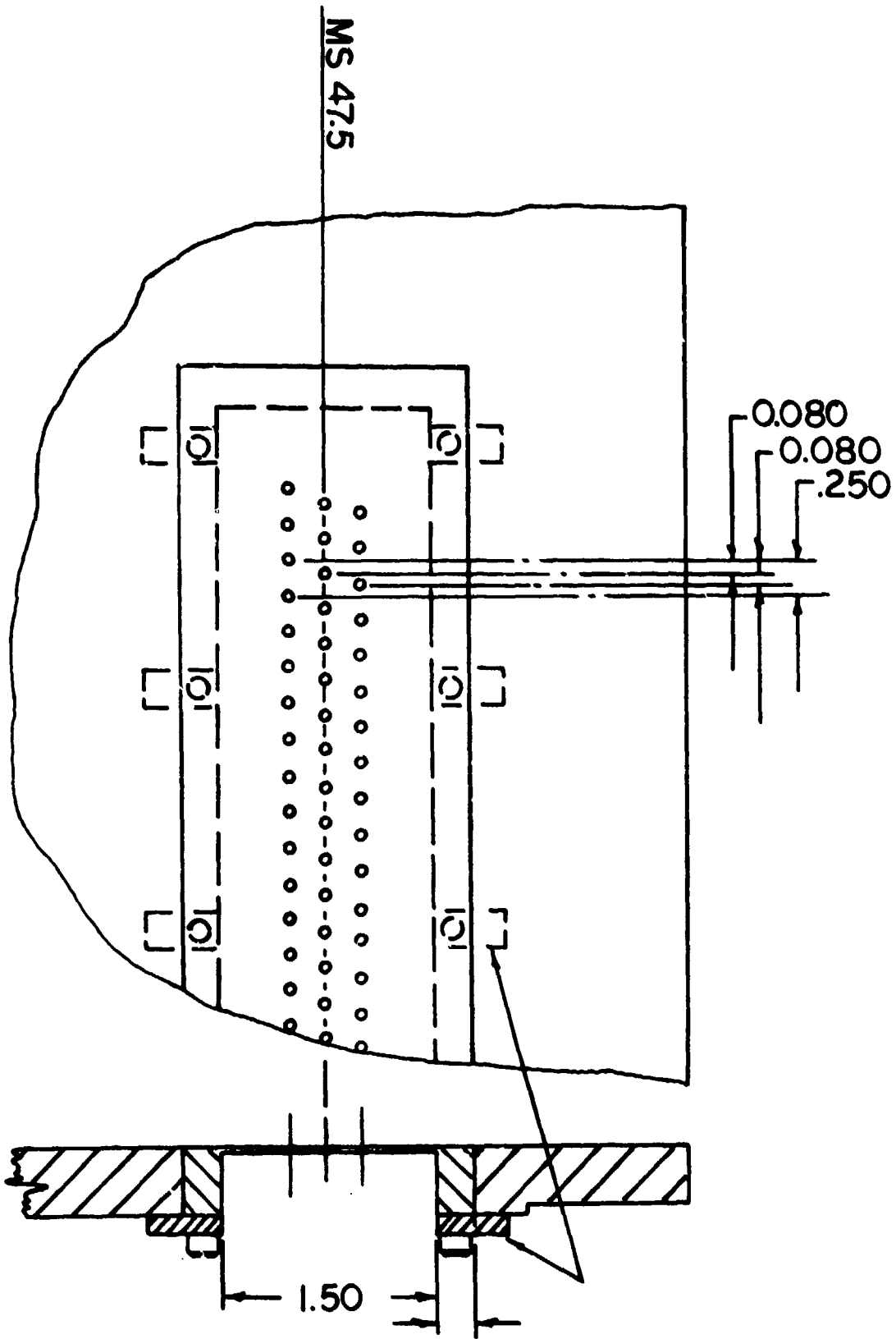


FIGURE 2.4 THIN SKIN INSERT DETAILS



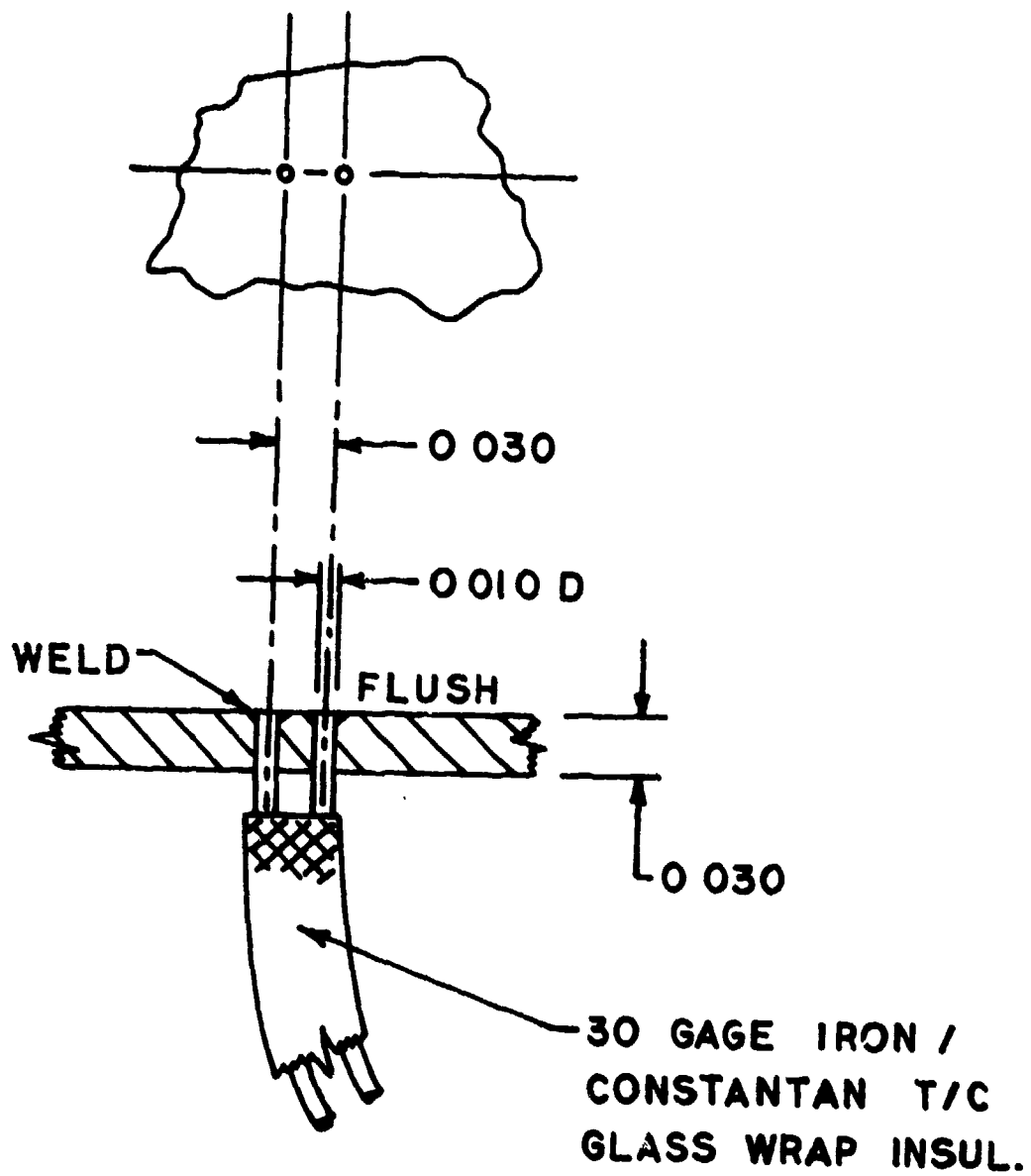


FIGURE 2.5 THERMOCOUPLE INSTALLATION DETAILS

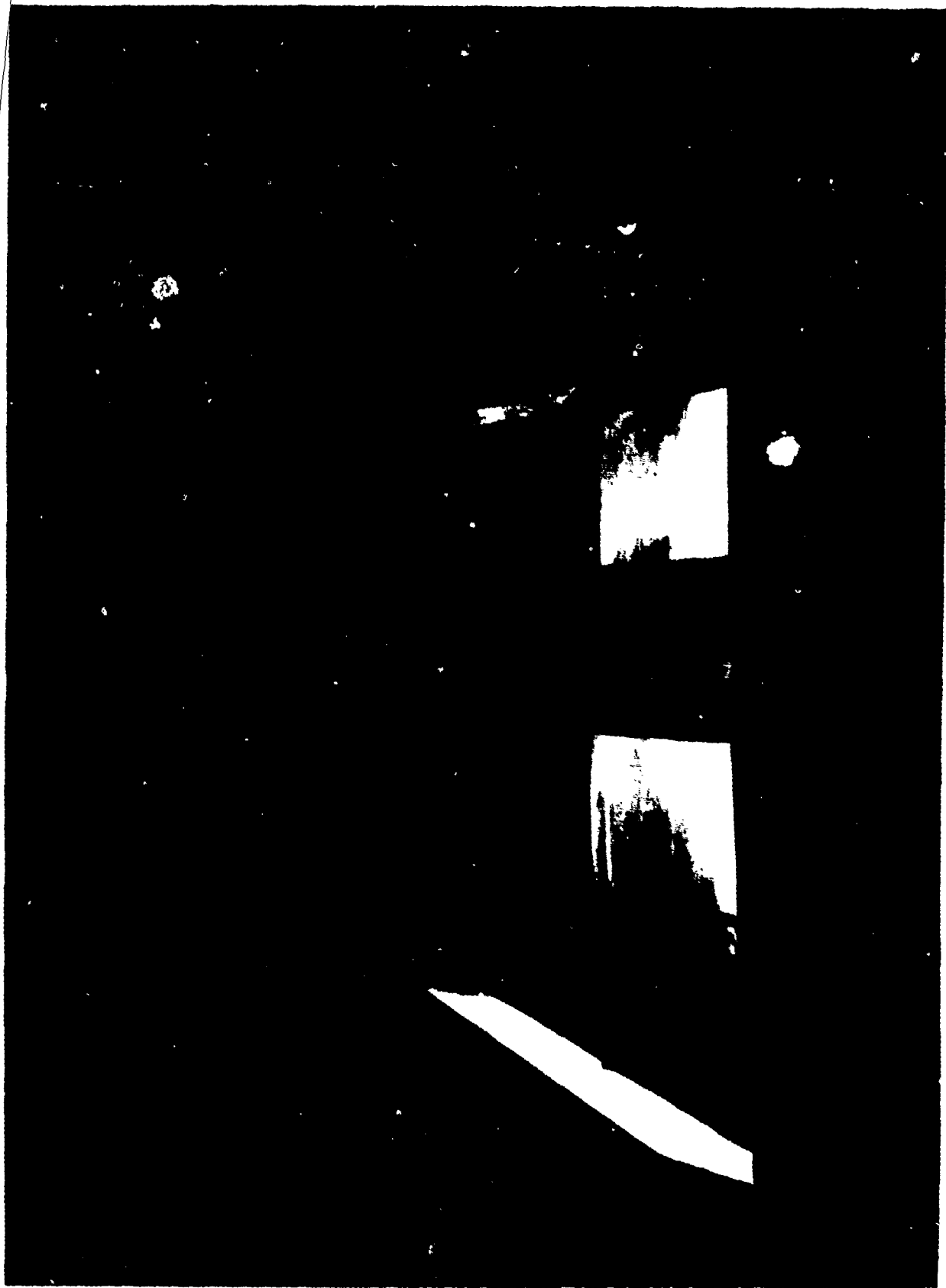


FIGURE 2.6 BODY CONTOURED (SEALED) FINS

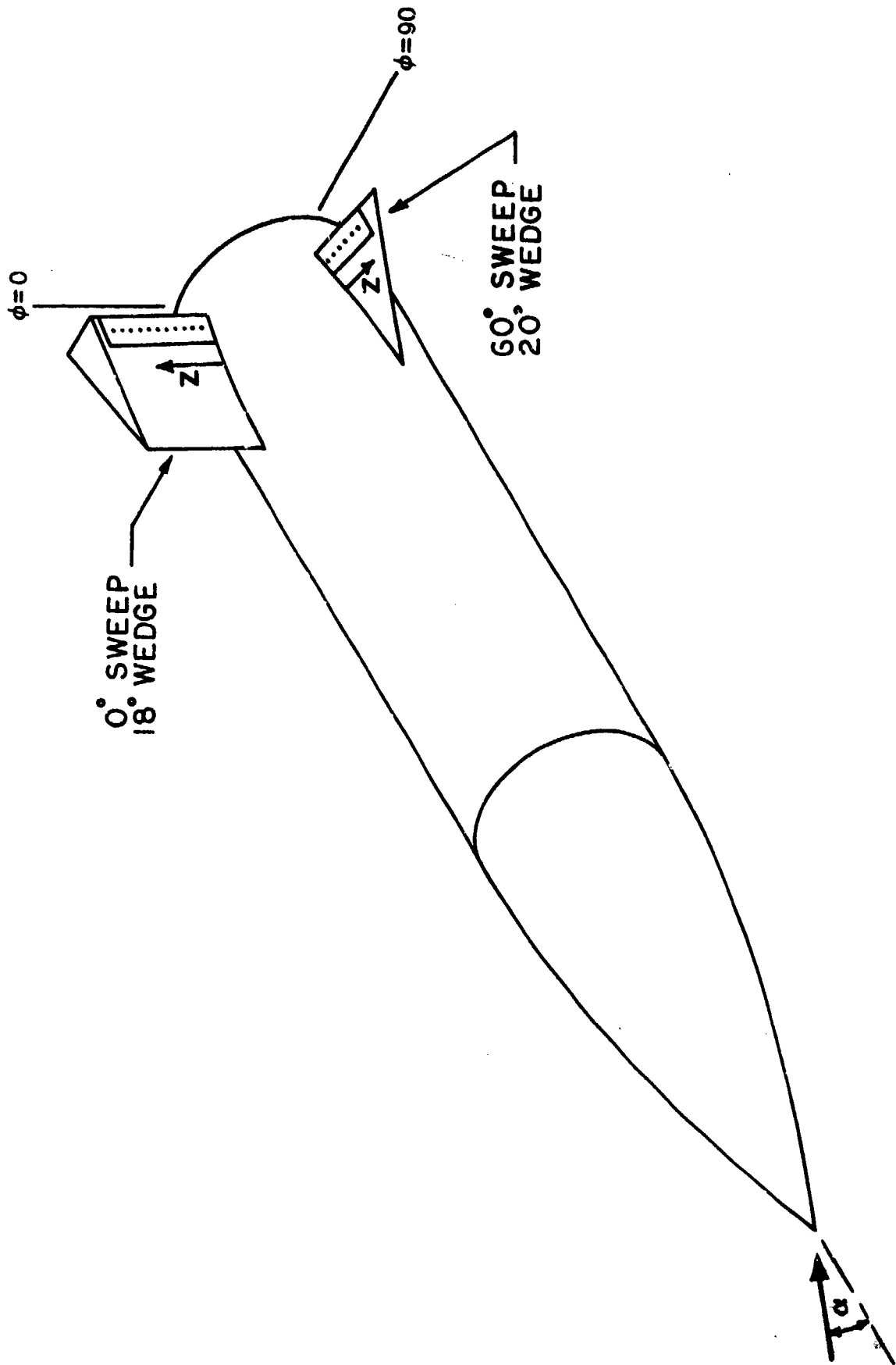


FIGURE 2.7 FIN SURFACE HEATING MODEL

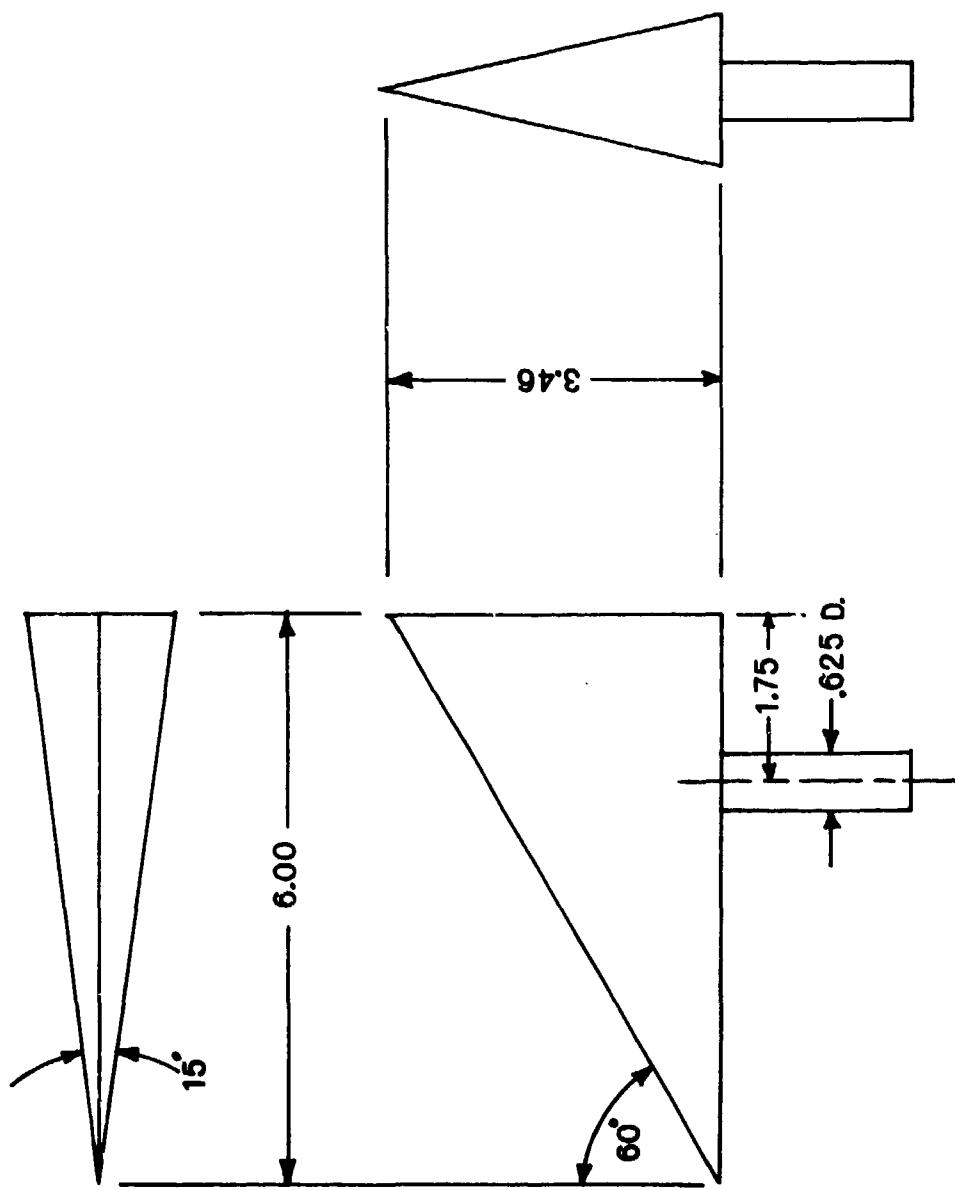


FIGURE 2.8 FIN TORQUE TUBE MODEL

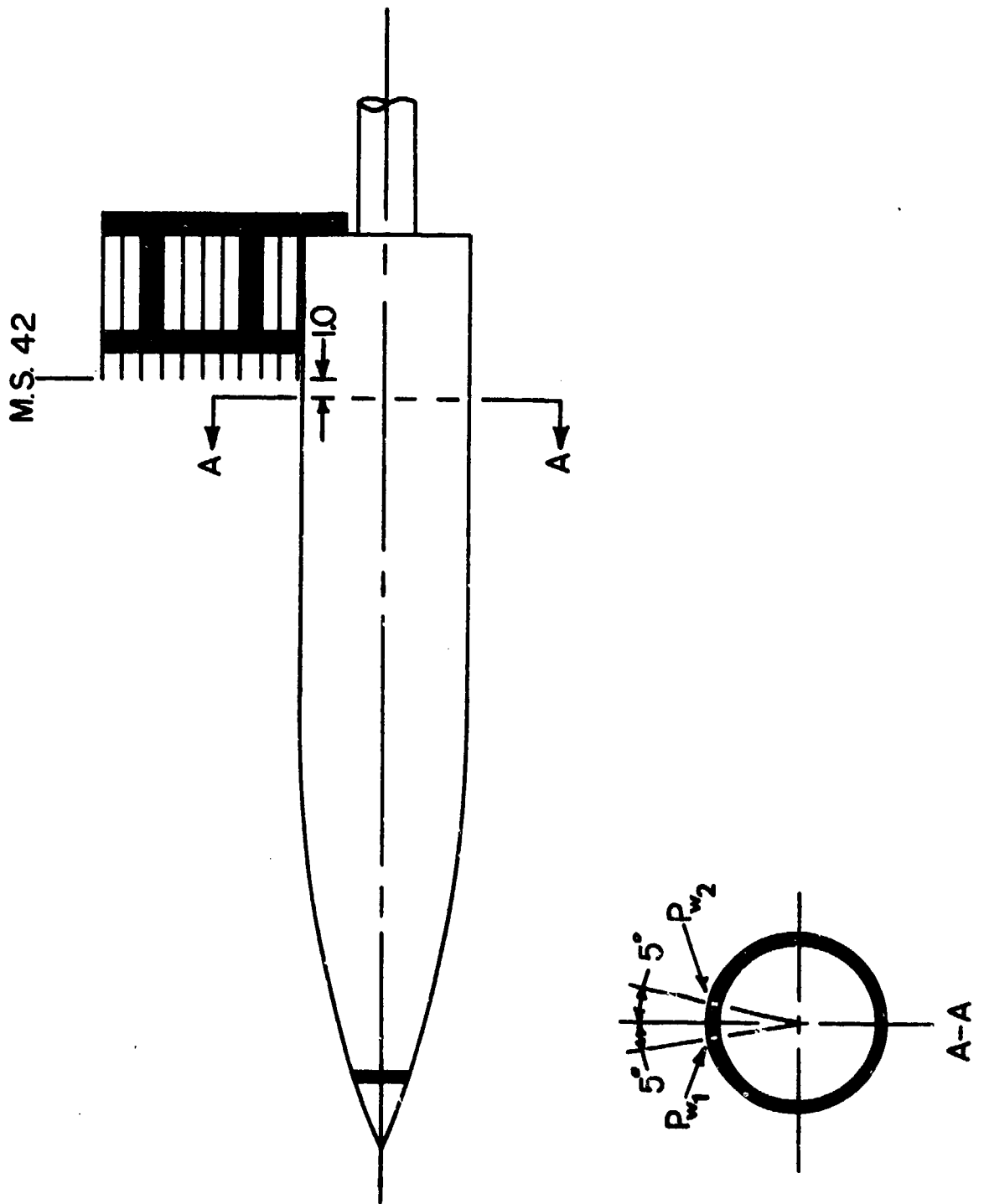


FIGURE 2.9 SHOCK LAYER PITOT RAKE DIMENSIONS

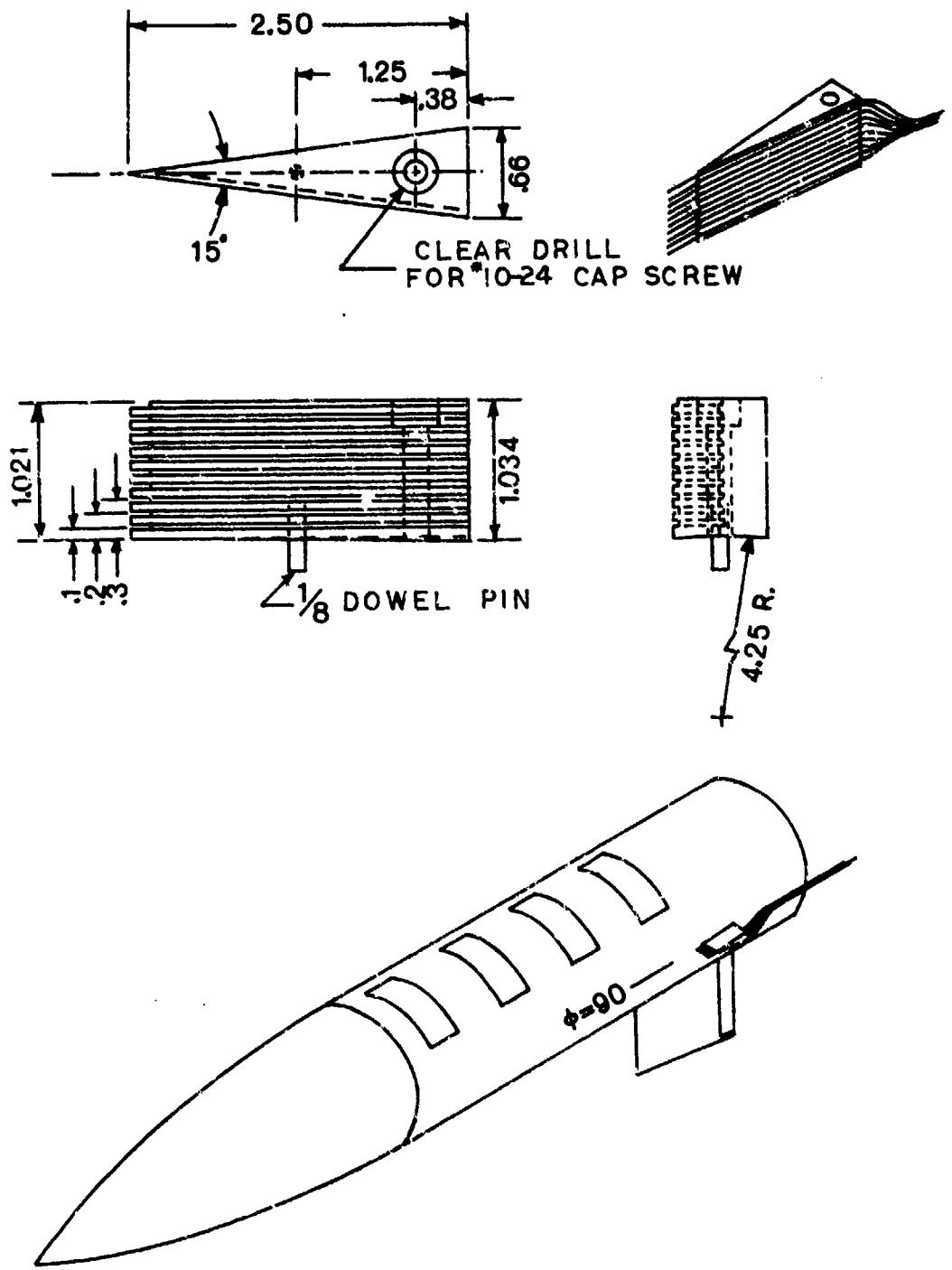


FIGURE 2.10 BOUNDARY LAYER PITOT RAKE

### 3.0 TEST PROGRAM OUTLINE

#### 3.1 Sealed Fin-Body Interactions

The Modular Missile was originally constructed with the set of fins shown in Figure 2.6. These fins were fabricated from stainless steel, were uninstrumented, nondeflectable, and were sealed to the surface of the missile body. During testing the undisturbed surface heating rates were measured on the ogive-cylinder and compared to theoretical predictions. It was found that the addition of a boundary layer trip strip was necessary to obtain fully developed turbulent flow at the fin locations. A band of #20 carborundum grit 0.75 inches wide was placed 4 inches back from the ogive nose tip. Testing then proceeded with the addition of the fin in Figure 2.6. Surface heat transfer and oil flow data were taken in the vicinity of the fins. Interest was centered on the data obtained from thermocouples 1 to 75 shown in Figure 2.3. These thermocouples measured the shockwave boundary layer interaction heating produced by the fins.

In general each fin was tested at missile angles of attack of plus and minus  $0^{\circ}$ ,  $4^{\circ}$ ,  $8^{\circ}$  and  $12^{\circ}$  and with the fin rolled  $0^{\circ}$ ,  $30^{\circ}$  and  $60^{\circ}$  off the leeward centerline as defined when the missile is at a negative angle of attack. 436 runs were made and the test data was published as a three volume data report by AEDC. The report number is AEDC-DR-75-91 and the ARO Project number was V41B-C8A.

A second test entry was made which was a direct continuation of the first employing the same fins, but providing additional roll angles. The fins were tested at missile angles of attack of plus and minus  $0^{\circ}$ ,

4°, 8° and 12° and rolled 0°, 30°, 60° and 90° off the windward centerline as defined when the missile is at a positive angle of attack. Surface heat transfer and oil flow data were taken in 341 runs. Testing was done under ARO Project number V41B-F6A and the data published as a three volume data report, AEDC-DR-75-112.

### 3.2 Total Pressure Surveys and Surface Pressure

This test entry concerned flow field measurements about the clean ogive-cylinder. A total pressure rake was constructed which was large enough to measure pressures throughout the shock layer with a resolution of 0.25 inches. Total pressure profiles were taken at angles of attack from 0° to 10° in 2° steps and at roll angles from 0° to 180° in 10° steps.

In addition to the rake, two surface pressure taps were installed at Model Station 41 as shown in Figure 2.9. Surface pressure data were taken at each roll position for which total pressure data were taken. Distributions were thereby generated around the cylinder with only two taps. 100 data sets were obtained and published in a four volume data report, AEDC-DR-76-68. The ARO Project number was V41B-HOA.

The data of this test entry was used in conjunction with an inviscid flow fields computer program to obtain boundary layer thickness, local Mach number, and flow turning angles at the fin leading edge for each model attitude. With this information the peak heating in the interaction region could be correlated.

### 3.3 Heating to the Surface of the Fins

The next test entry examined the heating rates on the fin surface. Two fins were selected from the set in Figure 2.6 to have thermocouples



installed as shown in Figure 2.7. The instrumentation was installed from root to tip along the fin trailing edge. 68 heat transfer runs and 24 oil flow runs were made.

A small pitot rake was also installed as shown in Figure 2.10 to obtain more detailed boundary layer profiles on the ogive-cylinder. 28 runs were made with the rake for various model attitudes and the data were published in a two volume data report. The ARO Project number was V41B-S3A.

#### 3.4 Interaction Effects of a Torque Tube Fin Mount

The first test entries investigated the shock wave boundary layer interaction produced by fins which were sealed to the missile body. The added problems of accounting for the effects of cross flow under the fin were therefore avoided and data could be compared to existing fin-flat plate interaction data. However, the fins on practical missile designs are usually mounted on torque tubes so that they may be deflected. A small gap is then produced under the fin. This test entry investigated the heating in the vicinity of such a fin. A  $60^\circ$  swept fin with an  $18^\circ$  included wedge angle was constructed and mounted on a shaft in the missile body so that the gap height could be adjusted. A new thin skin insert containing 85 thermocouples was also installed on the ogive-cylinder just upstream of the torque tube and under the fin.

154 heat transfer runs and 17 oil flow runs were made. The new insert provided data in the separated region under the fin and upstream of the torque tube. Data were also taken with the original fin insert (thermocouples 1 to 75) to investigate the effect on the shock wave

interaction of cross flow under the fin. The gap height was varied from 0.0 to 0.5 inches. At each gap setting the missile was pitched to  $0^\circ$ ,  $4^\circ$ ,  $8^\circ$  and  $12^\circ$  and the fin rolled  $0^\circ$ ,  $30^\circ$ ,  $60^\circ$  and  $90^\circ$  off the windward centerline. A complete set of the data was published in a three volume AEDC data report under ARO Project number V41B-S3A.

### 3.5 Recovery Factors in a Sealed Fin Interaction

The last test entry of this program concerned the acquisition of recovery factors in the interaction region of an unswept  $20^\circ$  wedge fin sealed to the missile body. Since long run times required to reach the adiabatic wall temperature would also damage the thin skin inserts, the following method was used to deduce the recovery temperature from transient heat transfer data. At each model attitude several repeat runs were made, each with the model at a different uniform initial wall temperature. The heat transfer rates for each thermocouple were then plotted as a function of the wall to stagnation temperature ratio. A linear least squares curve fit was driven through the data and extrapolated to zero heating rate. At this point the temperature ratio is the recovery temperature ratio.

The recovery factors were then used to correct the heat transfer coefficients which, until now, had been based on a constant recovery temperature equal to 1.0 times the stagnation temperature. Errors induced by the assumption of a constant recovery factor were investigated as well as its impact on the peak heating correlations derived from earlier test data.

#### 4.0 UNDISTURBED DATA

Initial testing of the model was carried out without fins attached. Heat transfer, wall pressure, and total pressure measurements were made at various model pitch and roll attitudes. This test sequence was to provide the reference data base with which to normalize all fin interaction data and to infer the state of the boundary layer on the ogive-cylinder. It was also used to determine the boundary layer thickness and to validate the computations of a numerical inviscid flow fields program which will be described later in this section.

#### 4.1 Heat Transfer

As was shown in Figure 2.3 there were five model stations at which thermocouples were installed in a peripheral direction on the cylinder. At each angle of attack a series of runs were made at various roll angles, thereby generating heat transfer distributions around the model from the windward to the leeward centerlines. These data were first used to determine the location of transition on the cylinder in the axial and peripheral directions for each angle of attack.

The heat transfer distributions are shown in Figures 4.1 through 4.4 and were measured with the tunnel operating at its maximum Reynolds number of  $4.9 \times 10^6$  per foot. For clarity only data fairings are shown in these multiple station plots. In Figures 4.5 and 4.6 the windward centerline data ( $\phi=0^\circ$ ) are cross plotted as a function of model station for  $0^\circ$  and  $12^\circ$  angle of attack. Also shown in these figures are laminar and turbulent flat plate calculations based on local flow properties about the ogive-cylinder. For zero angle of attack the boundary layer

is transitional between model stations 25 and 40. As the end of transition is approached the data overshoot the turbulent theory but relax back to the theory as X increases. Also the fact that the heating distributions in figure 4.1 are not constant with  $\phi$  indicates that transition does not occur symmetrically on the cylinder. A fully developed turbulent boundary layer probably does not exist until model station 50 is reached. For  $12^\circ$  angle of attack the windward centerline data in figure 4.6 show that most of the cylinder length is in laminar flow. Transition occurs approximately between 40 and 50 inches.

Returning to figures 4.1 through 4.4 it is observed that for all angles of attack the windward centerline is laminar or transitional over most of the cylinder length and that transitional flow extends as far as  $30^\circ$  to  $40^\circ$  from the centerline. It was apparent that in spite of our desires natural transition upstream of the fin stations would be difficult or impossible to achieve for fin locations less than  $30^\circ$  from the windward centerline.

A band of #20 carborundum grit was then applied to the ogive four inches from the nose tip in an attempt to trip the boundary layer. Undisturbed heat transfer runs were then repeated and the data are shown in figures 4.7 through 4.10. It can be seen that the entire cylinder is now in turbulent flow at all angles of attack.

Appendix A presents supplementary data on tripping of the ogive-cylinder boundary layer. Shadowgraphs are shown for the 50 inch long ogive-cylinder with and without the trip strip. Data are also presented from a similar test in the AFDL Mach 6 High Reynolds Number Facility. An ogive-cylinder 15 inches long was tested at various Reynolds numbers and

produced a naturally turbulent boundary layer. Undisturbed heating data are correlated with that of the present test and shown to agree with turbulent theory.

With these data in mind the entire test program was carried out with the trip strip applied to the ogive nose tip. Substantial tripped data were taken for the clean body configuration. The combination of dense peripheral instrumentation (one gage every 1.2 degrees) and model roll capability generated data as shown in figures 4.11 through 4.14. These figures each contain over 500 points of data. These data will be used to normalize all interaction data within this report.

Owing to the large numbers of data points at zero angle of attack, these data were evaluated statistically in order to evaluate error bands. AEDC, in their data reports, evaluate the uncertainty in data through a Taylor series method which considers the contributing uncertainties of material density, thickness and specific heats. In terms of the heat transfer coefficient, the resultant uncertainty is:

$H(T_0)$	Uncertainty (+)
$10^{-3}$	6%
$10^{-4}$	7%

Our statistical evaluation of the data considered data from various runs and each of two test entries which were spaced some months apart. Figure 4.15 indicates data for various model stations and Table 4.1 indicates the mean values and one, two and three sigma errors at each station. The fact that the heat transfer data in figure 4.15 increases from model station 25 to 40 was originally attributed to a substantial transitional region. However, observation of the calculated pressure data which will

be discussed later indicates that a part of the trend is due to a recompression of the flow aft of the ogive nose section.

TABLE 4.1

<u>Model Station</u>	<u>Stx10<sup>4</sup>(mean)</u>	<u>1σ</u>	<u>2σ</u>	<u>3σ</u>
25.0	2.965	2.97%	10.96	17.90
30.0	3.002	3.90	13.56	22.20
35.0	3.119	2.44	8.66	14.14
40.0	3.174	3.02	10.27	16.80
47.5	3.073	1.92	6.77	11.19

#### 4.2 Surface Pressure Data

Surface pressure distributions were taken on the cylinder at Model Station 42. Model angles of attack between  $0^\circ$  and  $10^\circ$  were tested in  $1^\circ$  increments and data for  $0^\circ$ ,  $4^\circ$ ,  $8^\circ$  and  $10^\circ$  are shown in Figure 4.16. The inviscid theory also shown in this figure will be discussed in Section 4.4. The pressure distributions were cross plotted with the tripped heat transfer data at various stations and the correlation shown in Figure 4.17 was observed. A least squares curve fit through the data was made yielding

$$\log St_{T_0} = \frac{\log P/P_\infty + 4.248}{.925}$$

This correspondance between pressure and heating is valid for the windward surface,  $0^\circ < \phi < 120^\circ$ , but over-predicts data on the leeward surface of the cylinder.

With increasing angle of attack, flow on the leeward surface of the cylinder becomes increasingly complex because of flow separation and reattachment. Figures 4.18 through 4.20 indicate surface flow streamlines on the leeward surface of the cylinder at angles of attack of  $8^\circ$ ,  $10^\circ$  and  $12^\circ$ . Divergence of the leeward centerline streamlines is apparent for all angles of attack. At  $10^\circ$  and  $12^\circ$  angle of attack oil accumulation lines are noted at about  $20^\circ$  and  $30^\circ$  off the leeward centerline. Oil accumulation lines indicate regions of flow separation and low heating. The thermocouple data confirm this to be a region of low heating and its extent can be traced through the heat transfer data at stations 25 to 47.5.

The minimum heating data for  $12^\circ$  angle of attack is shown in Figure 4.21 and the extent of the region is mapped in Figure 4.22. It can be seen that the region begins at or about the location of the juncture of the ogive and the cylinder and that it grows in extent from that point to the end of the body.

In Figures 4.19 and 4.20 a convergence toward the leeward centerline is noted in the oil accumulation lines at the model base. This convergence is the result of a model-tunnel interaction. For the oil flow runs it was necessary to pitch the model nose up causing the aft end of the cylinder to move downward toward the open injection tank. The base of the model then intersected a flow disturbance from the edge of this tank. This disturbance did not affect the heat transfer or pressure data because the model was then pitched nose down thereby keeping the base of the model well clear of the disturbance.

#### 4.3 Pitot Pressure Surveys

Pitot pressure surveys were conducted through the shock layer of the ogive-cylinder using the rakes shown in Section 2.1.3. The large pressure rake contained 11 tubes spaced at 1.0 inch intervals. The rake could be displaced in the radial direction in 0.25 inch increments so that pitot profiles were obtained from the wall to the shock with a 0.25 inch resolution. The small rake contained 10 tubes spaced at 0.1 inch intervals and was used to provide the resolution necessary to establish boundary layer thickness at various model pitch and roll attitudes. All measurements were taken at Model Station 42 which is the fin leading edge station.



Data were taken with the large rake for angles of attack between  $0^\circ$  and  $10^\circ$  in  $2^\circ$  increments and at roll positions between  $0^\circ$  and  $180^\circ$  in  $10^\circ$  increments. Selected profiles from this data set are shown in Figures 4.23 through 4.26. The inviscid theory also shown in these figures will be discussed in Section 4.4.

A similar set of profiles are shown for the small boundary layer rake in Figures 4.27 through 4.30. Data were taken with this rake for angles of attack of  $0^\circ$ ,  $4^\circ$ ,  $8^\circ$  and  $12^\circ$  and roll positions between  $0^\circ$  and  $180^\circ$  in  $30^\circ$  increments. The boundary layer thickness was defined as that point on the profile where a knee occurs as shown in Figure 4.27. The variations of boundary layer thickness with angle of attack and roll position are shown in Figure 4.31.

Figure 4.32 indicates the pitot pressure in the shock layer about the ogive-cylinder at station 42 for the model at  $10^\circ$  angle of attack. This figure is a cross plot of data taken at  $10^\circ$  spacings about the model and at 0.25 inch increments in the radial direction. This figure indicates a vortex centered at  $162^\circ$  ( $18^\circ$  off the leeward centerline) and possible vortices at regions marked A, B and C. In these latter three regions there is not sufficient data to plot a closed low pressure region but evidence of such a region is noted. The vortex at  $162^\circ$  is predictable through observations of oil flow data such as Figure 4.19. In Figure 4.19, strong out flow exists about the leeward centerline terminating at about  $16^\circ$  from that centerline. The second clearly defined line occurs at  $30^\circ$  from the centerline. These angular dimensions bound the low pressure region. The inviscid limit line will be discussed in Section 4.4.

#### 4.4 Inviscid Flow Fields Computer Program

The preceding sections have demonstrated the complexity of the flow field about the ogive-cylinder at angle of attack. To understand the greater complexity of a fin induced shock interaction within this flow field two additional local flow properties are required. These are the local flow turning angle with respect to the model axis and the local Mach number at the edge of the boundary layer. These two properties determine the fin shock strength which will be shown to be the correlating parameter for all interaction data. Neither of these properties can be determined from the data presented so far. An inviscid flow fields computer program<sup>(2)</sup> written by the Naval Surface Weapons Center (NSWC) was capable of computing these parameters and became the key to our understanding of the interaction data. The credibility of the NSWC calculations was tested by comparing our experimental flow field data to the NSWC computations. These comparisons will be discussed in this section.

Figure 4.16 presented the surface pressure data taken at Model Station 41 and also the inviscid computations of the NSWC program. Agreement is excellent for all angles of attack and peripheral angles,  $\phi$ , from  $0^\circ$  to  $100^\circ$ . From  $100^\circ$  to  $180^\circ$  the program underestimates the data where separation and vortical flow have been documented.

Corresponding representative pitot data were presented in Figures 4.23 through 4.26 along with the NSWC computations. Again, agreement is excellent for  $\phi=0^\circ$  and  $\phi=90^\circ$  but unacceptable at  $\phi=180^\circ$  close to the cylinder surface. The cause of this leeside divergence was shown in

Figure 4.32 for  $10^\circ$  angle of attack by plotting contours of constant pitot pressure through the flow field cross section. The solid line in this figure indicating the limit of inviscid agreement bounds the vortical portion of the flow field.

Local Mach numbers through the shock layer were computed when the pitot surveys were made by assuming a constant static pressure through the shock layer equal to the wall pressure and using the Rayleigh pitot formula. These Mach number profiles were compared to the NSWC calculations and an example is shown in Figure 4.33. Although better agreement was found at other model attitudes a complete lack of agreement is noted here. Figure 4.34 presents the pitot data for the same attitude and reestablishes the validity of the NSWC pitot predictions. Figure 4.35, however, indicated the probable error in assuming a constant static pressure equal to the wall pressure. The NSWC static pressure prediction is far from constant. The Mach number profile was recomputed using the Rayleigh pitot formula and the NSWC static pressure profile and again compared to the NSWC Mach numbers. As shown in Figure 4.36 the agreement is now excellent. Further examples of the NSWC static pressure profiles are shown in Figure 4.37. The maximum height to which one can assume a constant static pressure equal to the wall pressure is shown in Figure 4.38 as a function of angle of attack and peripheral angle  $\phi$  about the cylinder.

The NSWC program was therefore considered to provide valid flow field properties for the ogive-cylinder as long as you remained clear of the boundary layer and any vortical regions in the shock layer. The experimental pitot data was used to determine the local boundary layer thickness and the NSWC program was then used to obtain Mach number and flow

turning angle as well as local static temperature. These flow properties are shown in Figures 4.39 through 4.40 and will be used in all data correlations within this report.

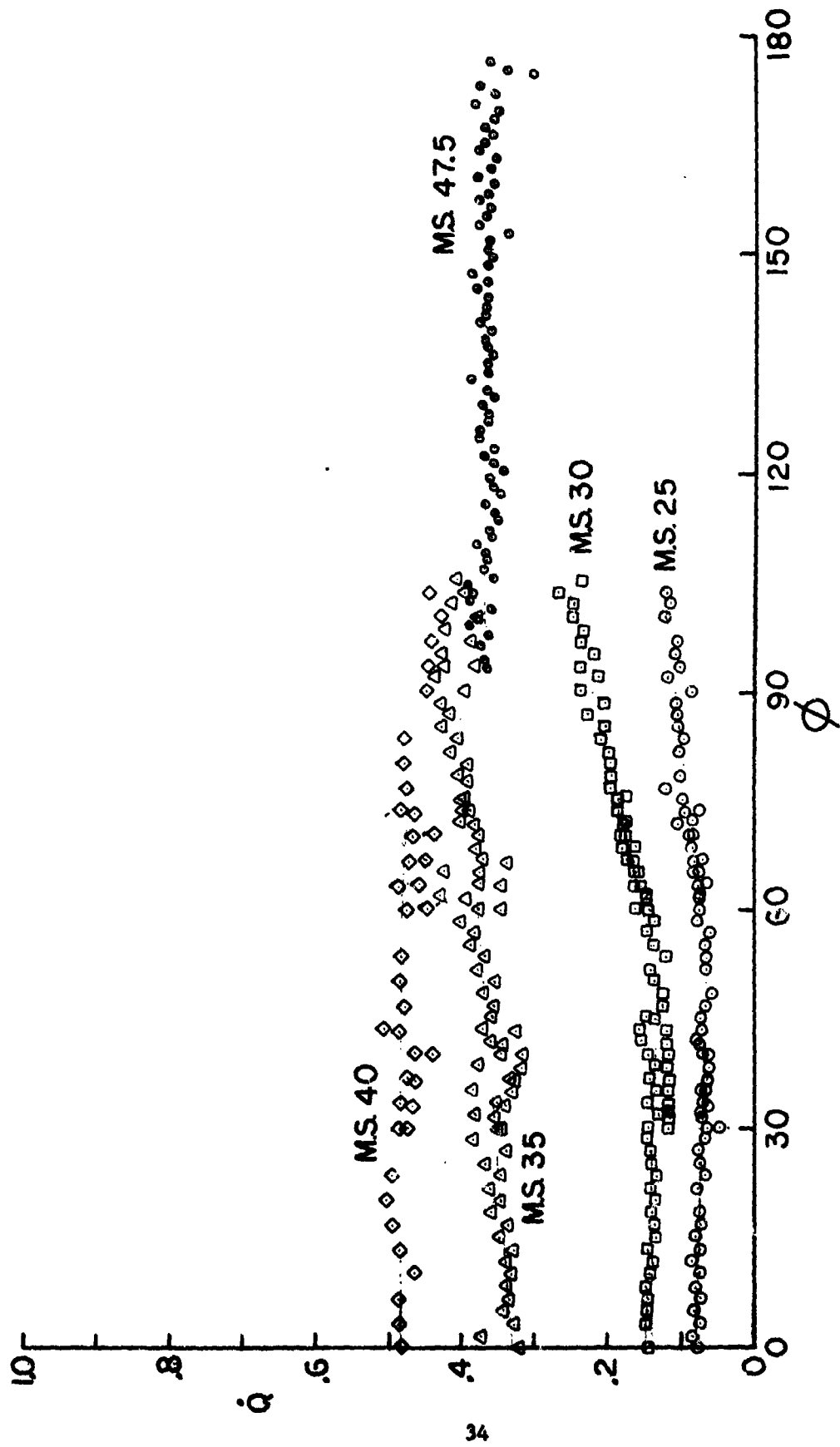


FIGURE 4.1 UNTRIPPED CLEAN BODY HEATING,  $\alpha=0^\circ$

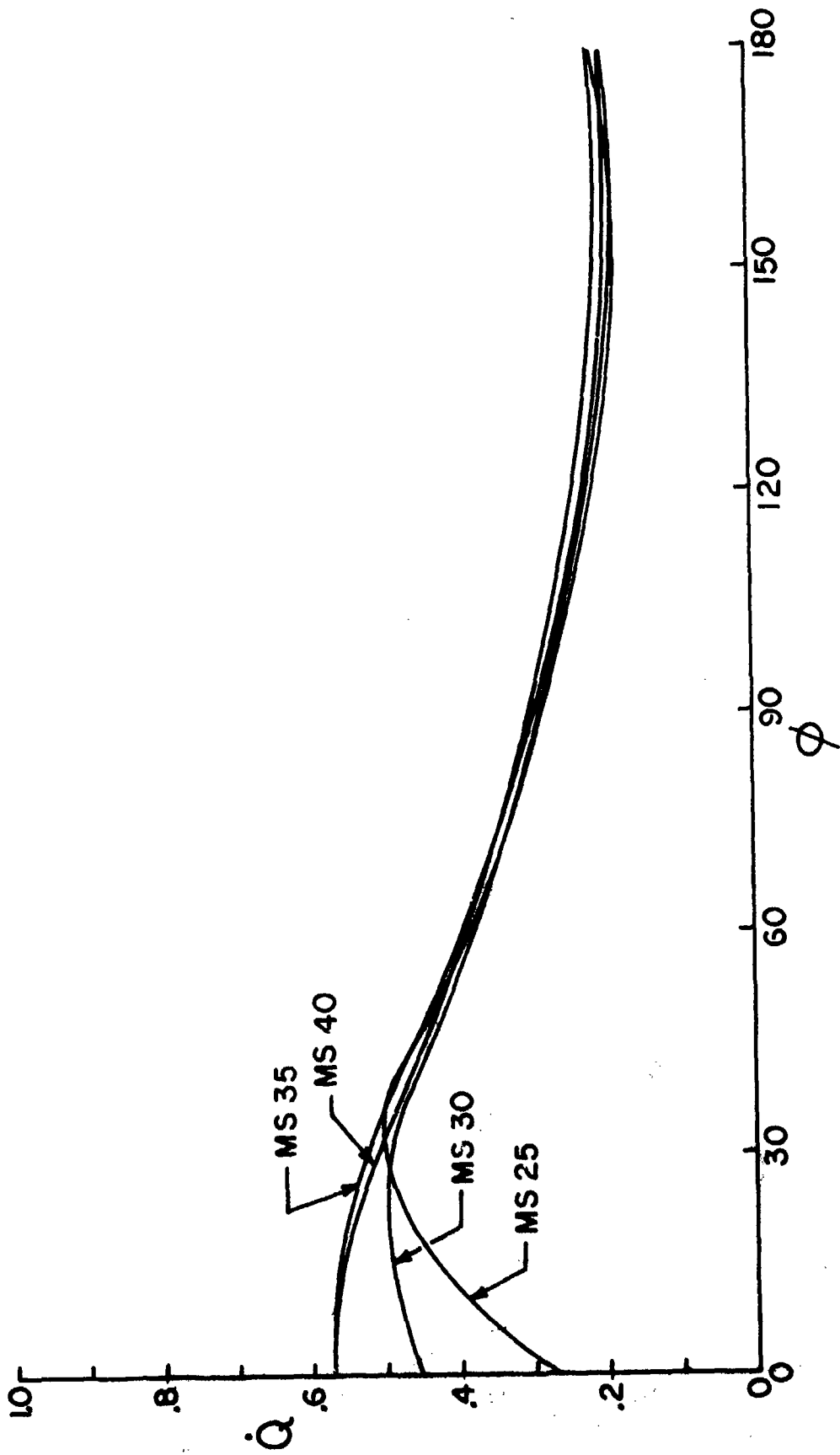


FIGURE 4.2 UNTRIPPED CLEAN BODY HEATING,  $\alpha=4^\circ$

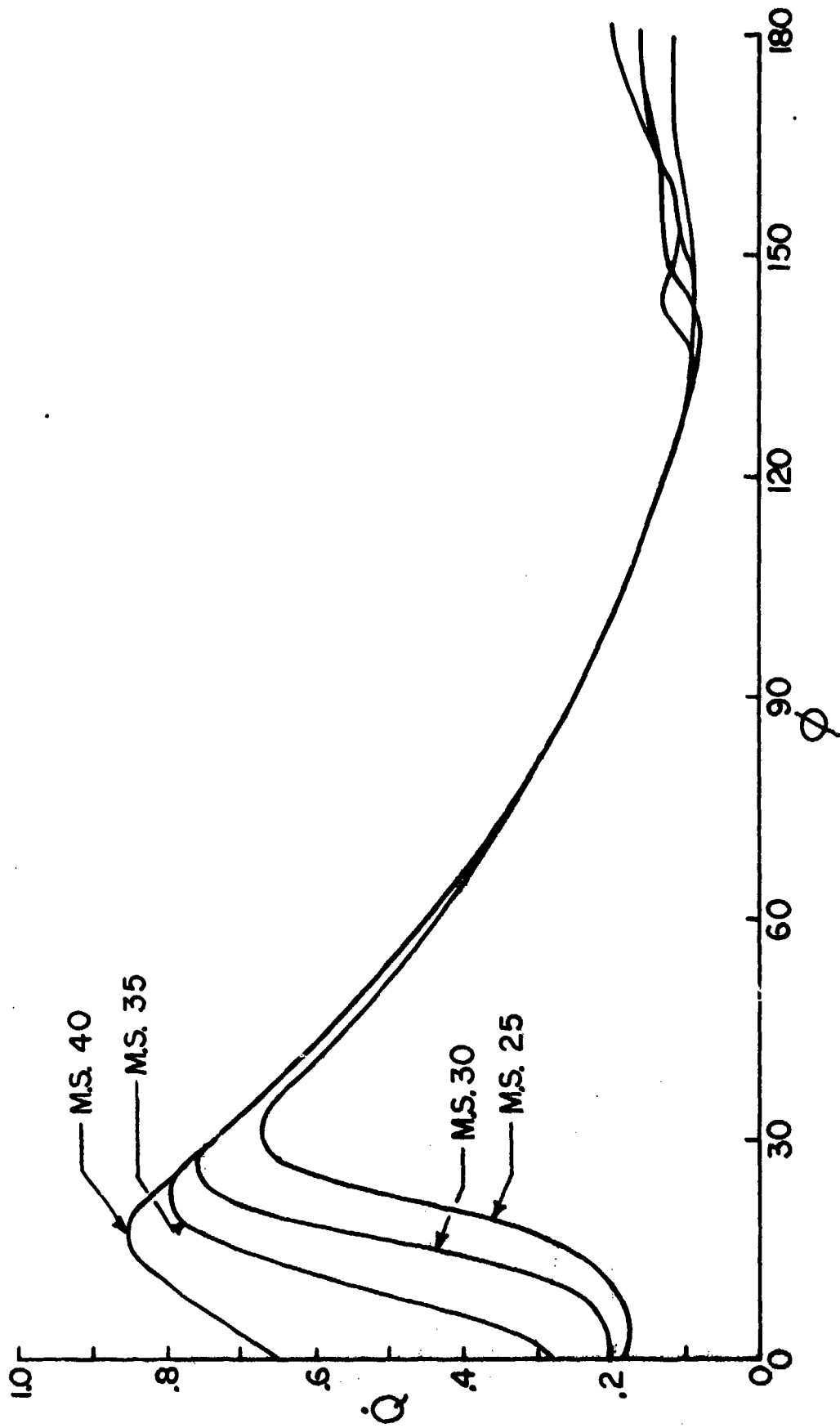


FIGURE 4.3 UNTRIPPED CLEAN BODY HEATING,  $\alpha=8^\circ$

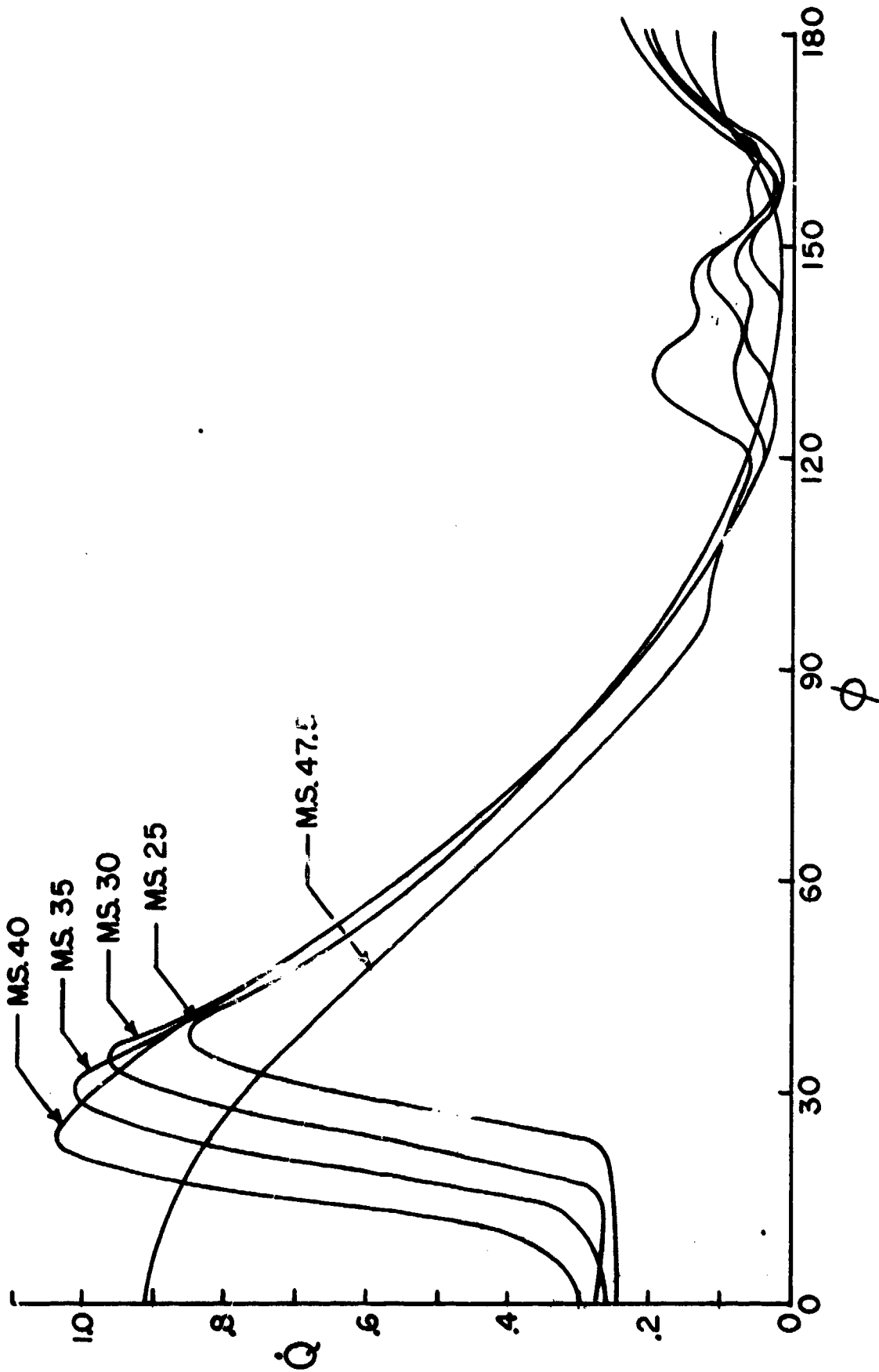


FIGURE 4.4 UNTRIPPED CLEAN BODY HEATING,  $\alpha=12^\circ$



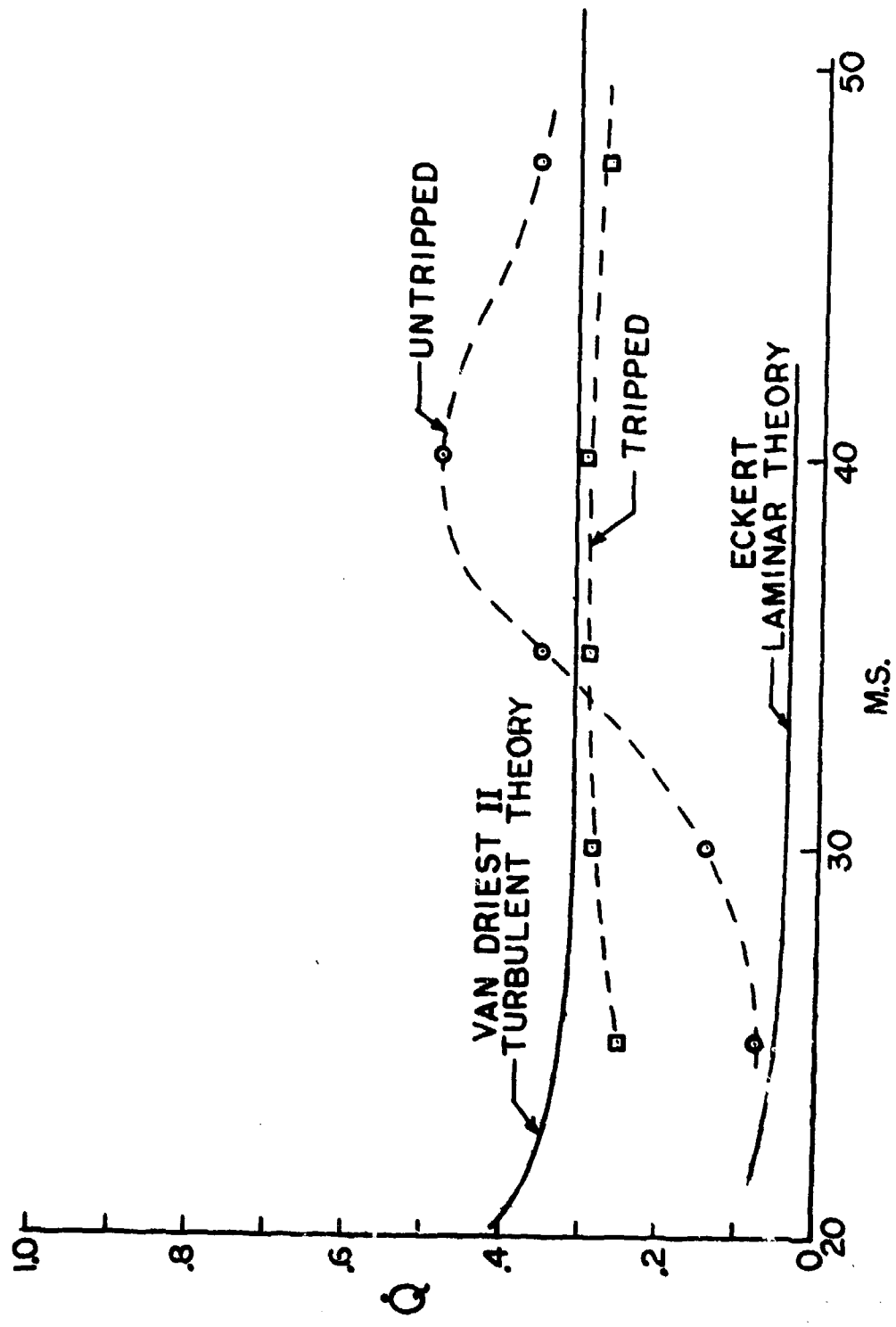


FIGURE 4.5 TRANSITION ON CLEAN BODY,  $\alpha=0^\circ$

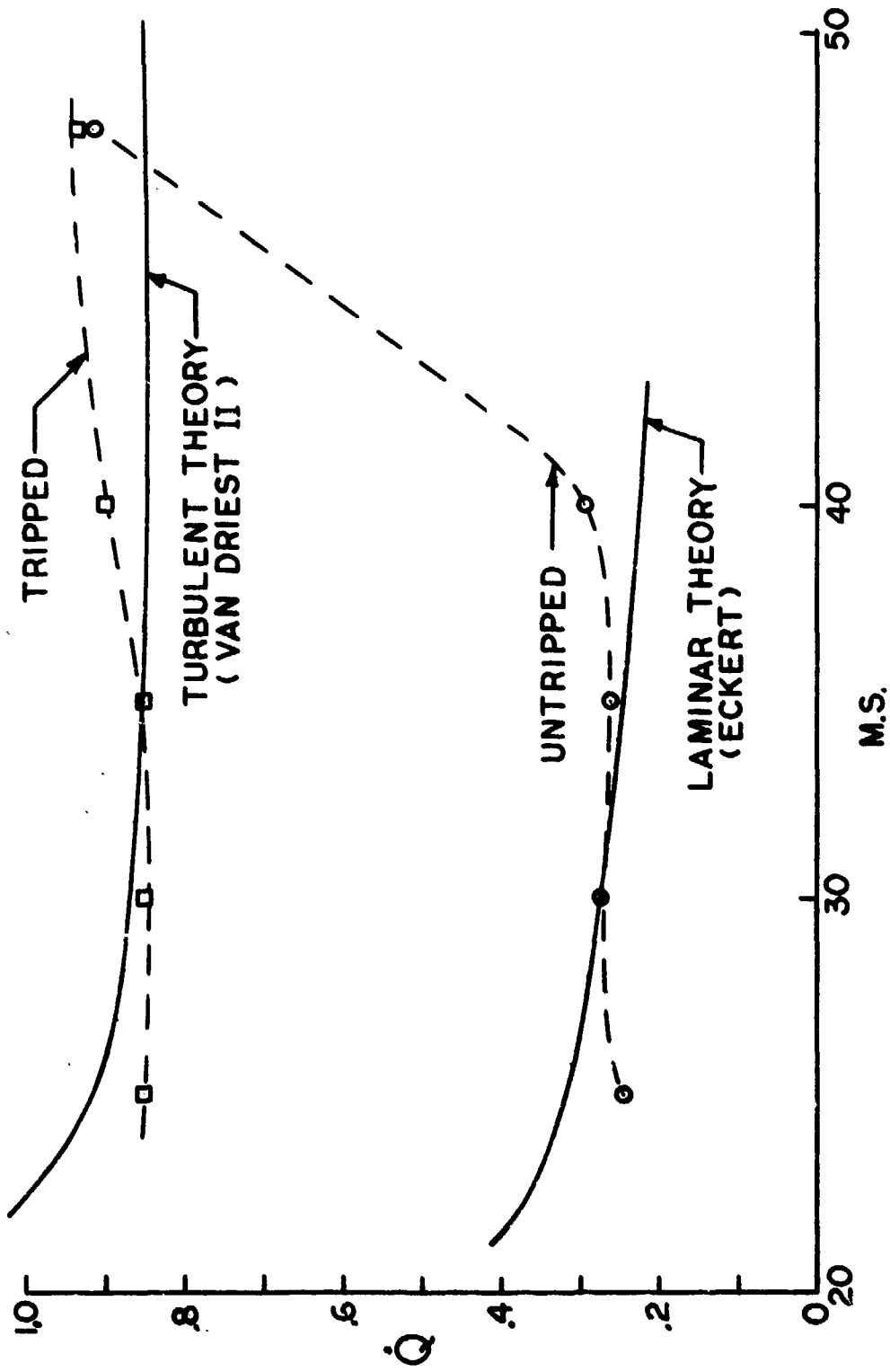


FIGURE 4.6 TRANSITION ON WINDWARD CENTERLINE ,  $\alpha=12^\circ$

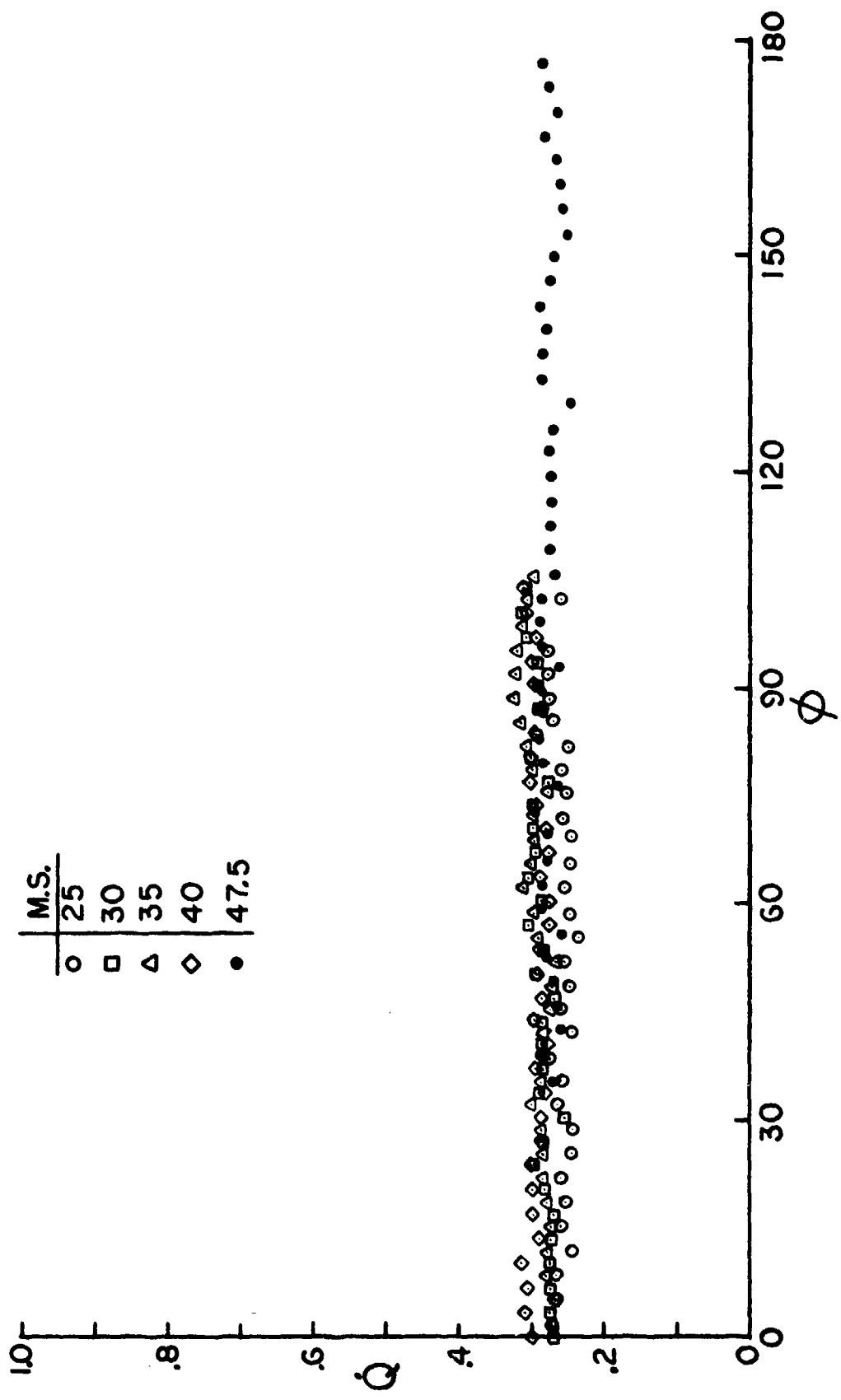


FIGURE 4.7 TRIPPED CLEAN BODY HEATING,  $\alpha=0^\circ$

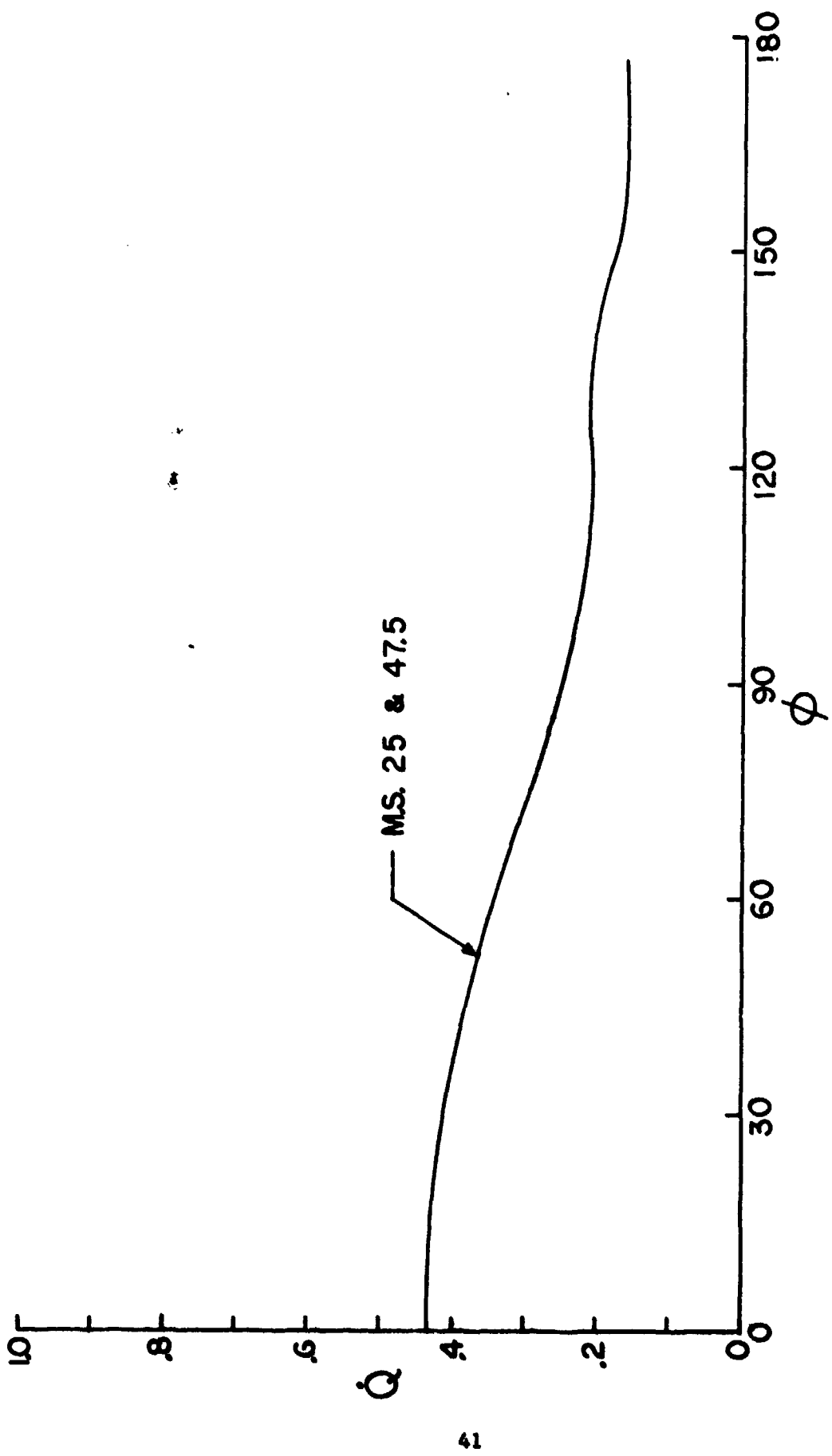


FIGURE 4.8 TRIPPED CLEAN BODY HEATING ,  $\alpha=4^\circ$

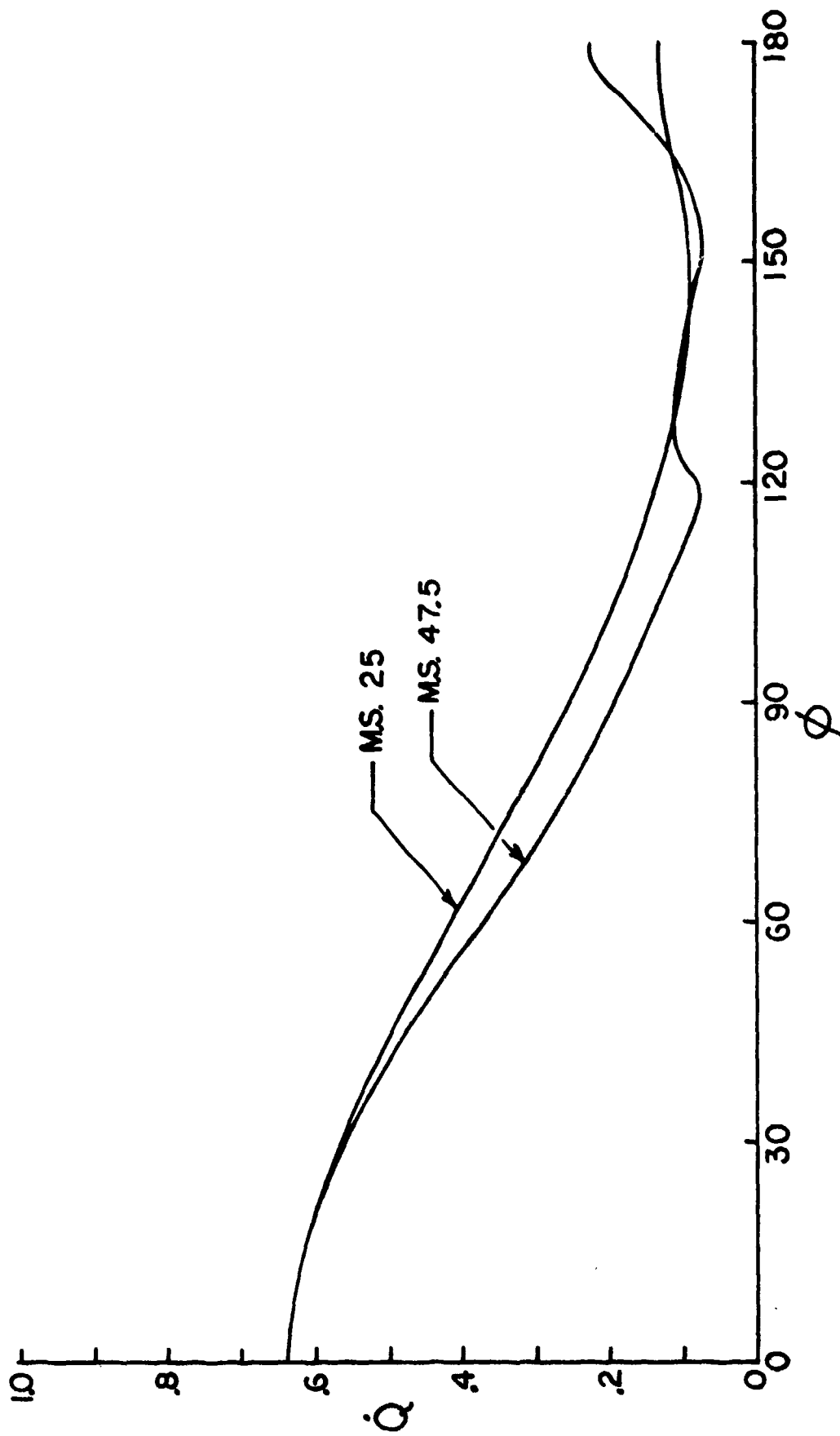


FIGURE 4.9 TRIPPED CLEAN BODY HEATING ,  $\alpha=8^\circ$

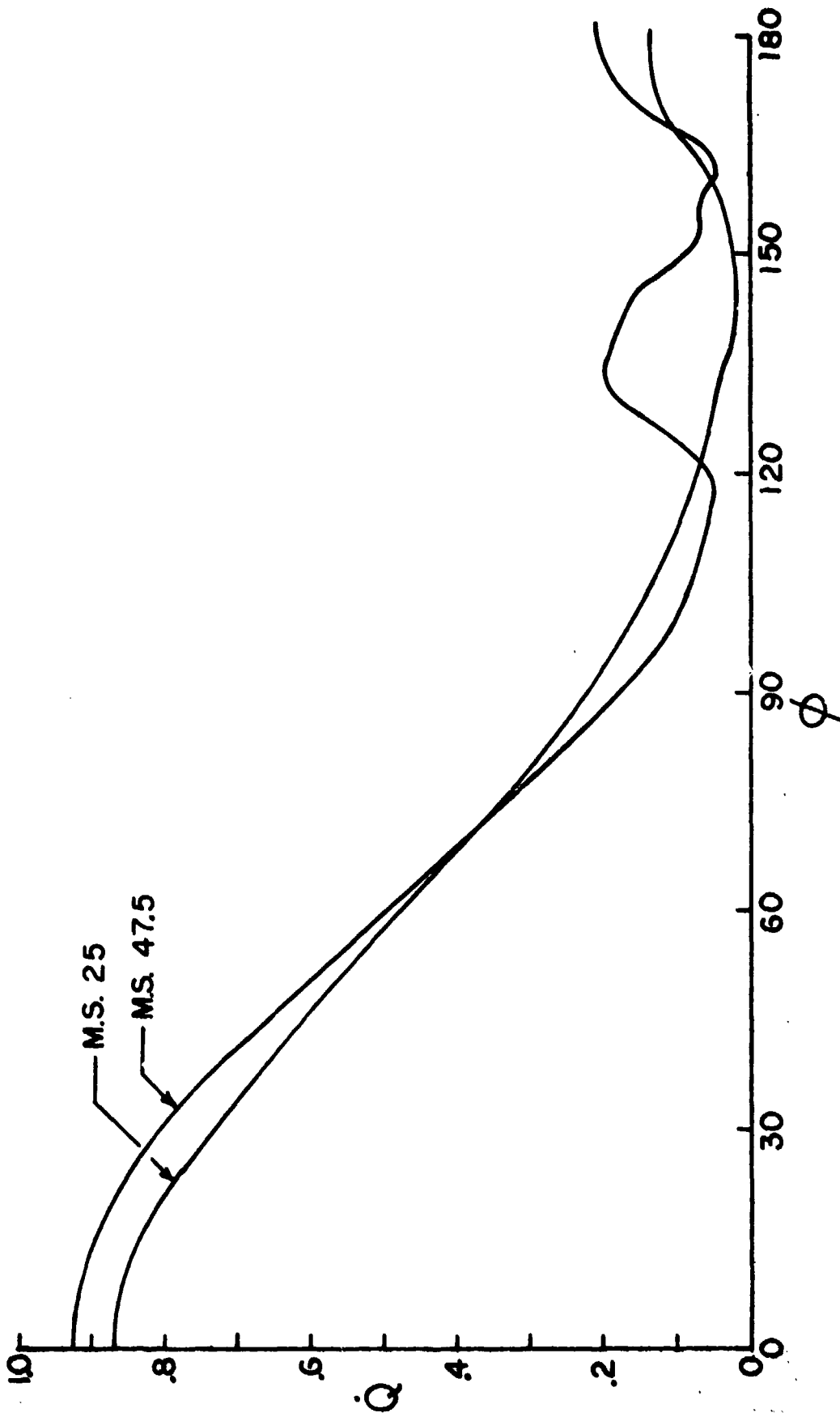


FIGURE 4.10 TRIPPED CLEAN BODY HEATING,  $\alpha=12^\circ$

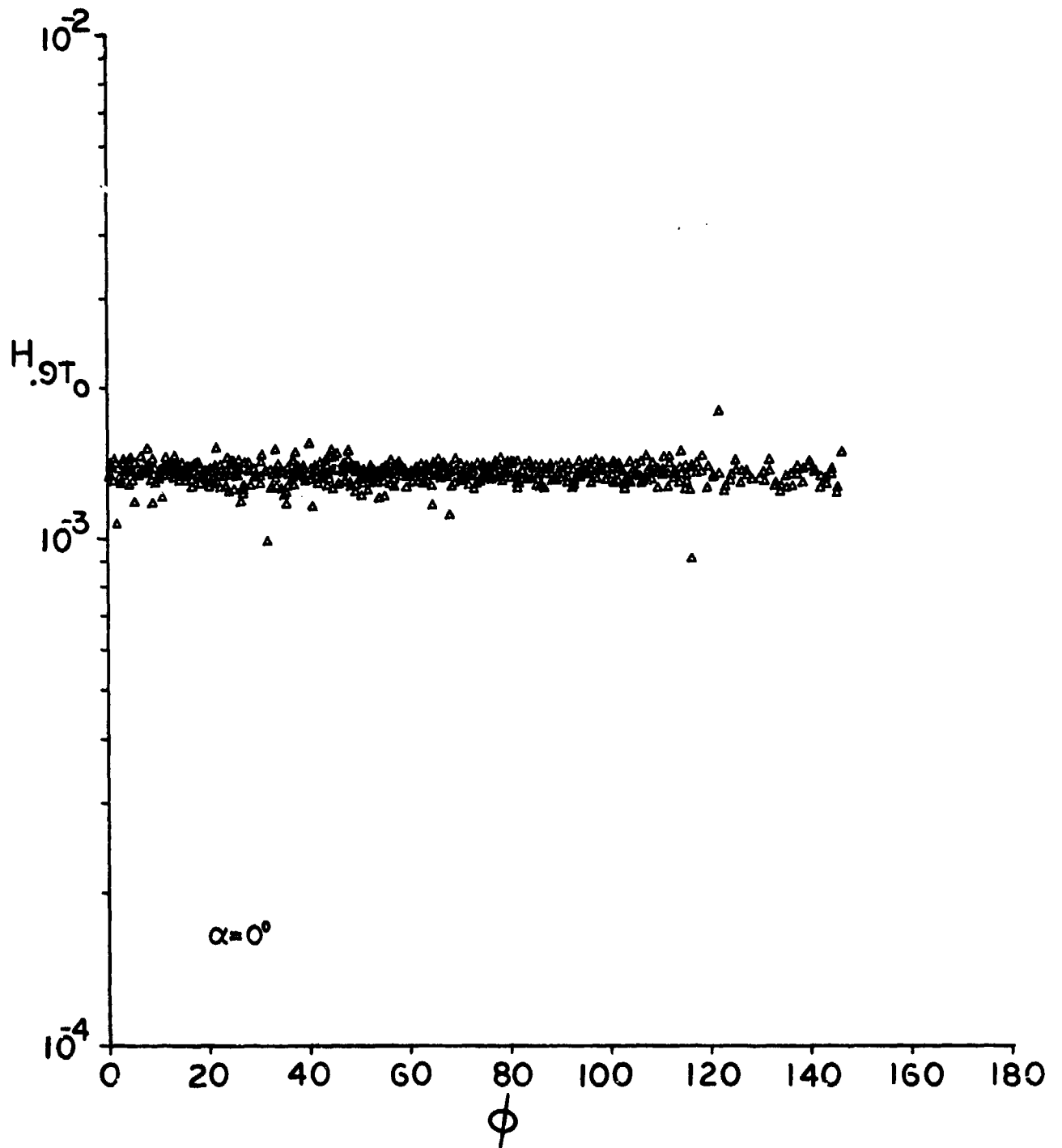


FIGURE 4.11 TRIPPED UNDISTURBED HEATING,  $\alpha = 0^\circ$

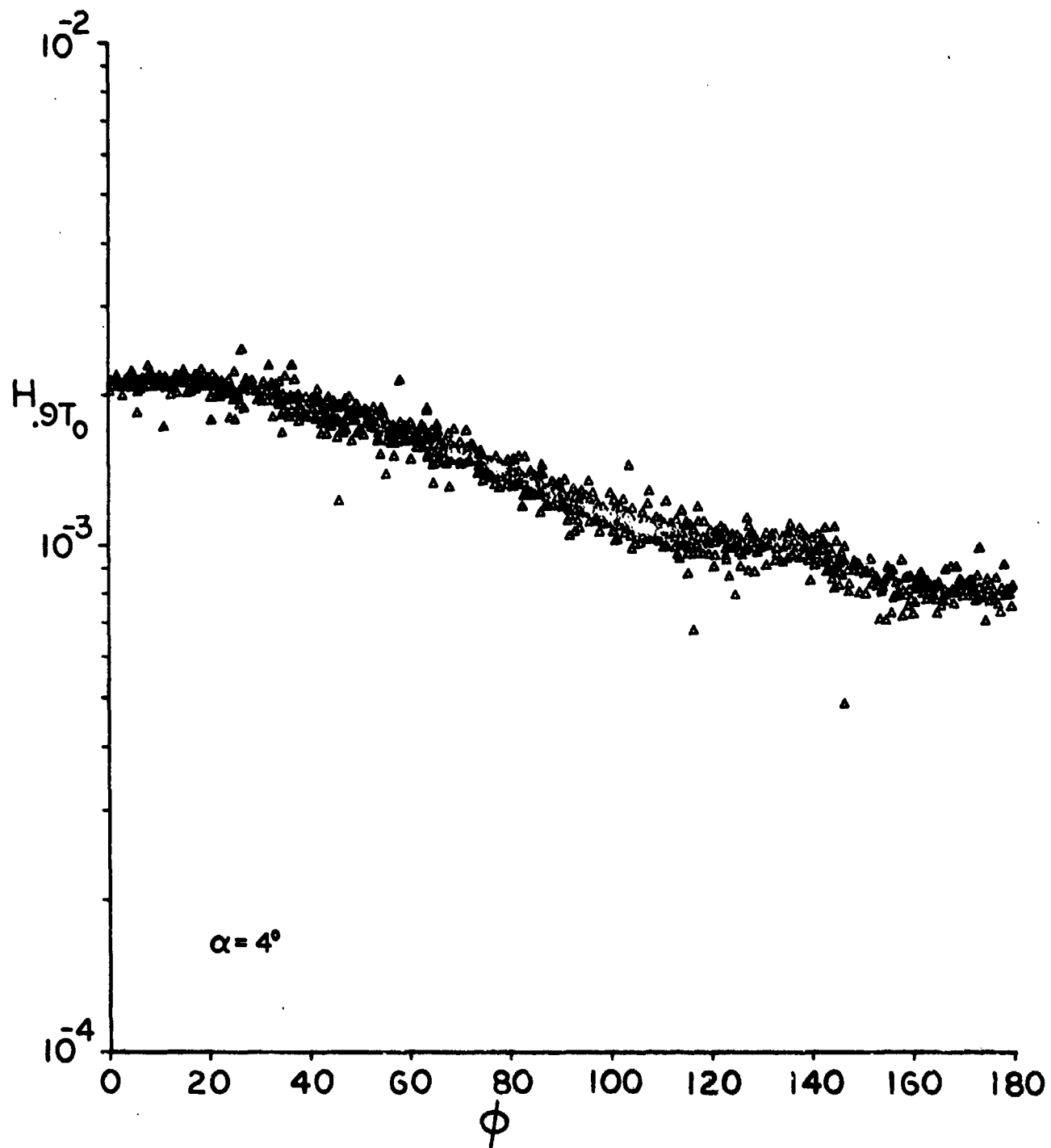


FIGURE 4.12 TRIPPED UNDISTURBED HEATING,  $\alpha = 4^\circ$



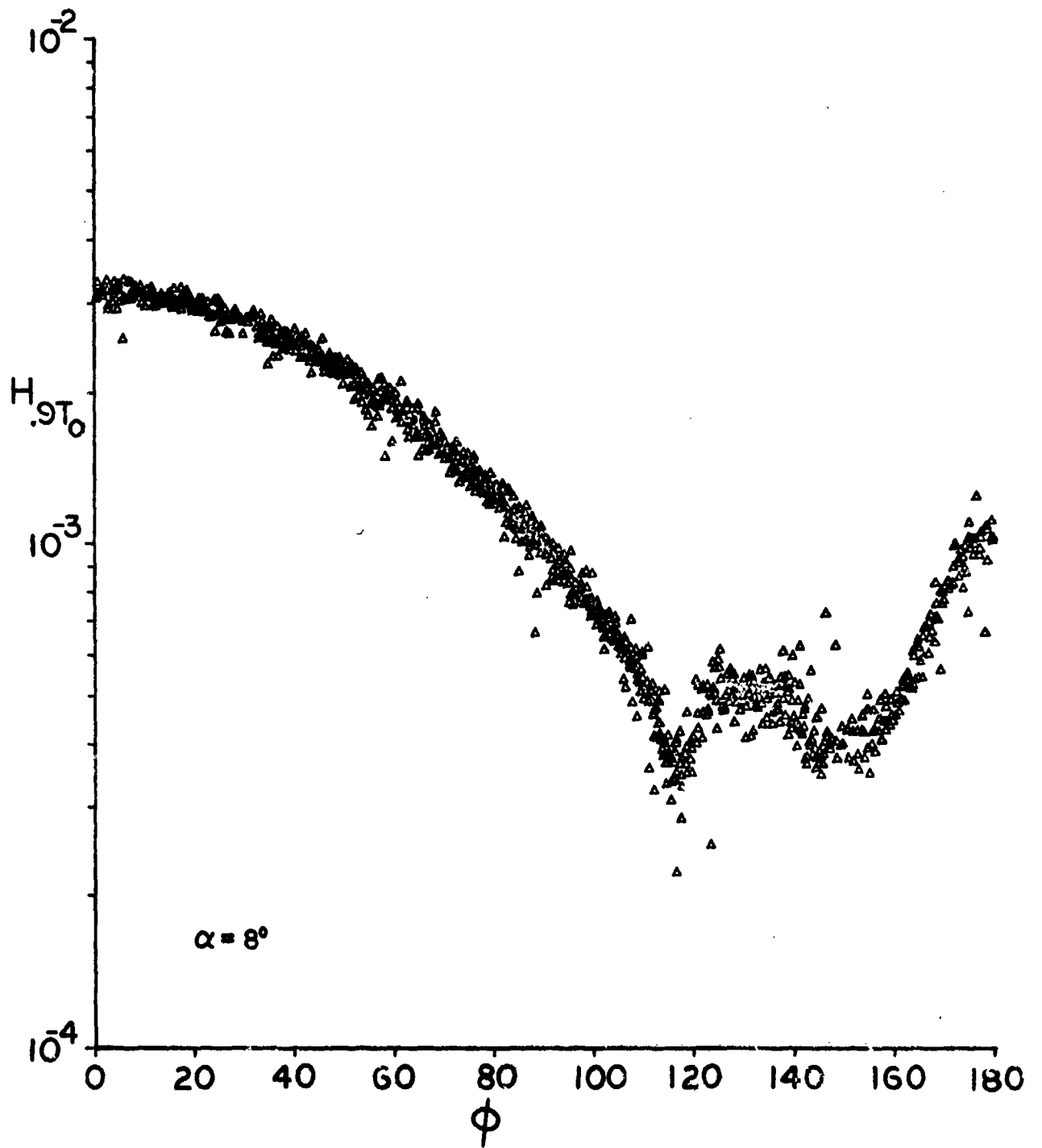


FIGURE 4.13 TRIPPED UNDISTURBED HEATING,  $\alpha = 8^\circ$

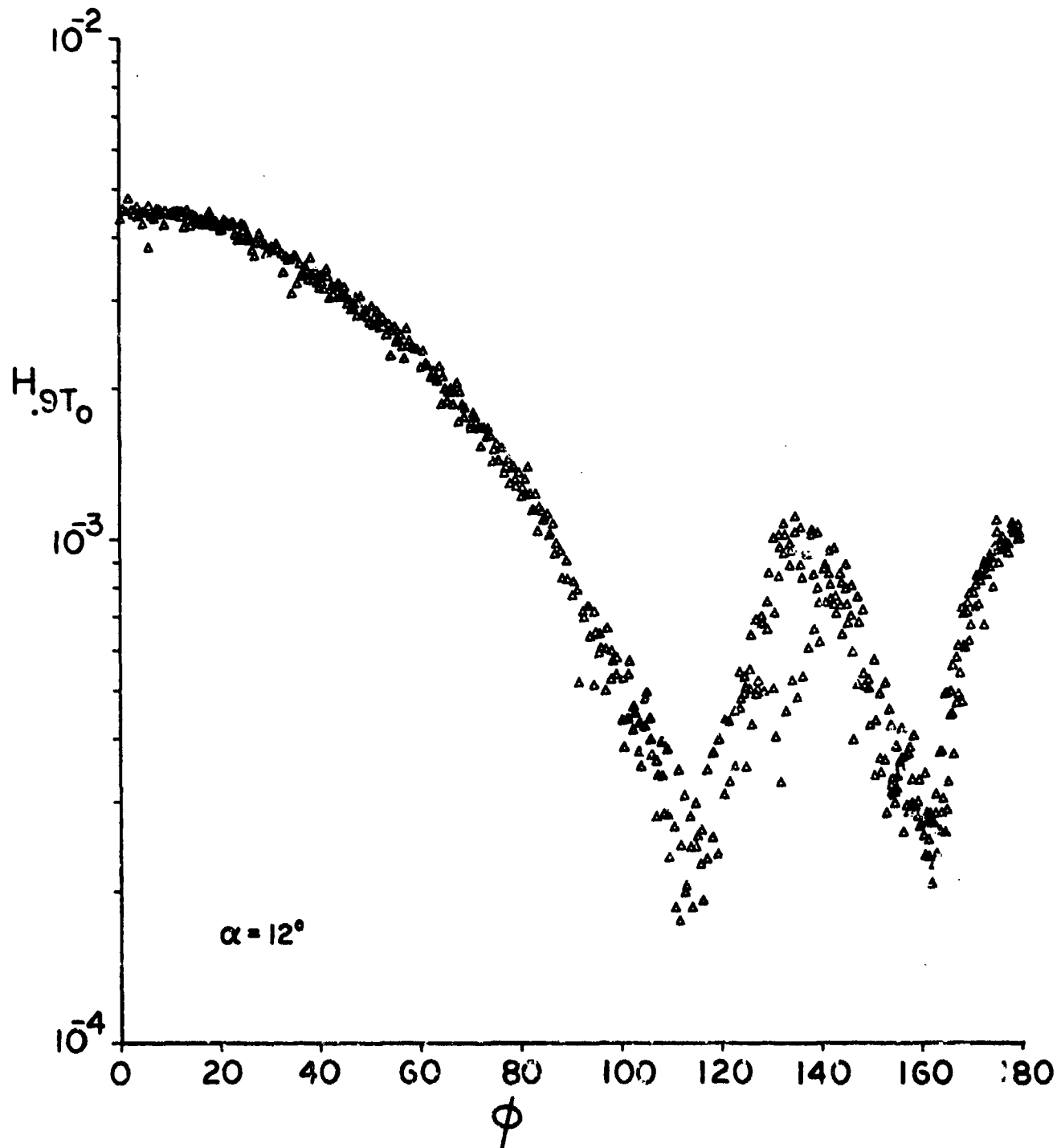


FIGURE 4.14 TRIPPED UNDISTURBED HEATING,  $\alpha = 12^\circ$

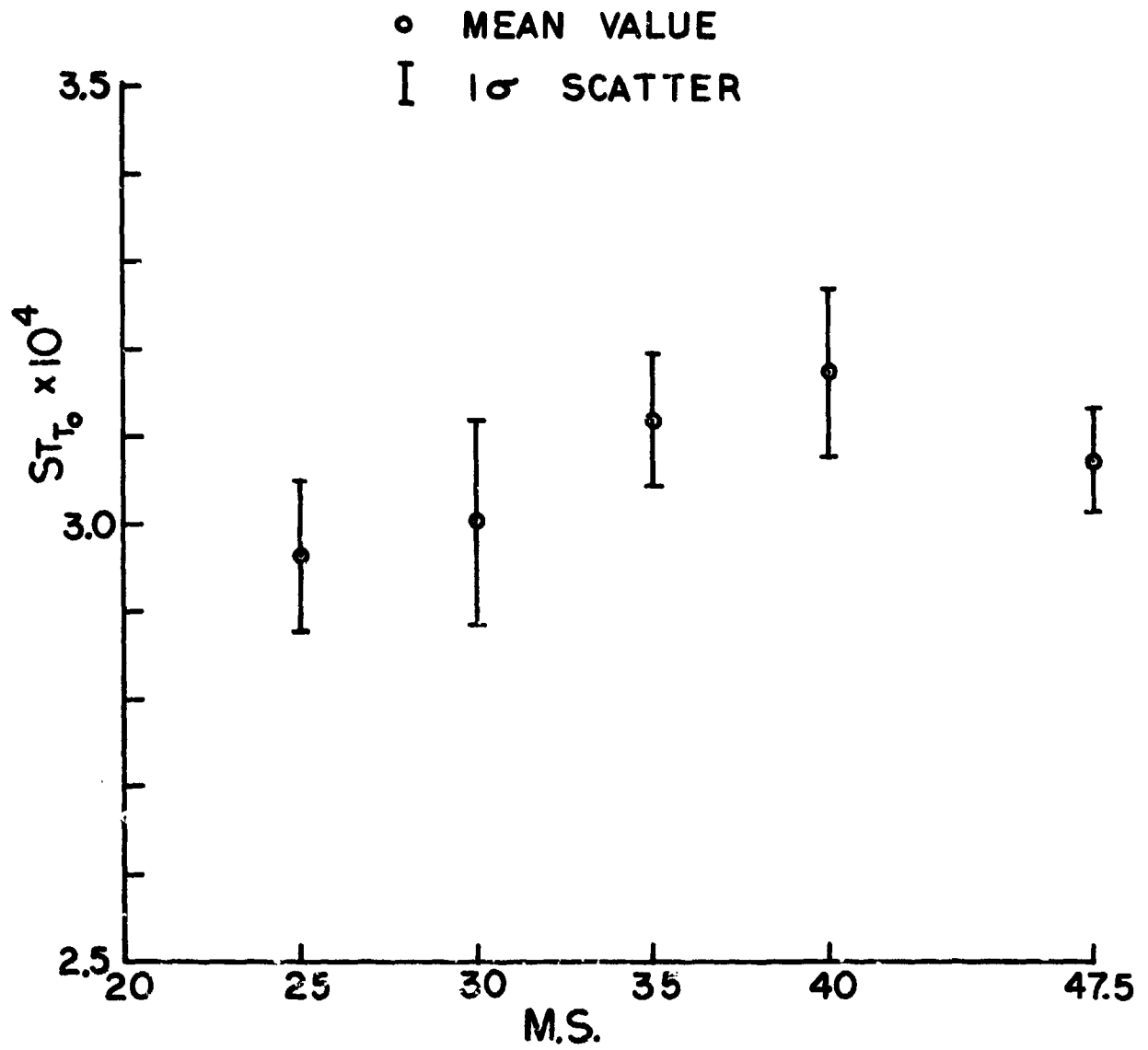


FIGURE 4.15 TRIPPED LONGITUDINAL HEATING DISTRIBUTION FOR  $\alpha=0^\circ$

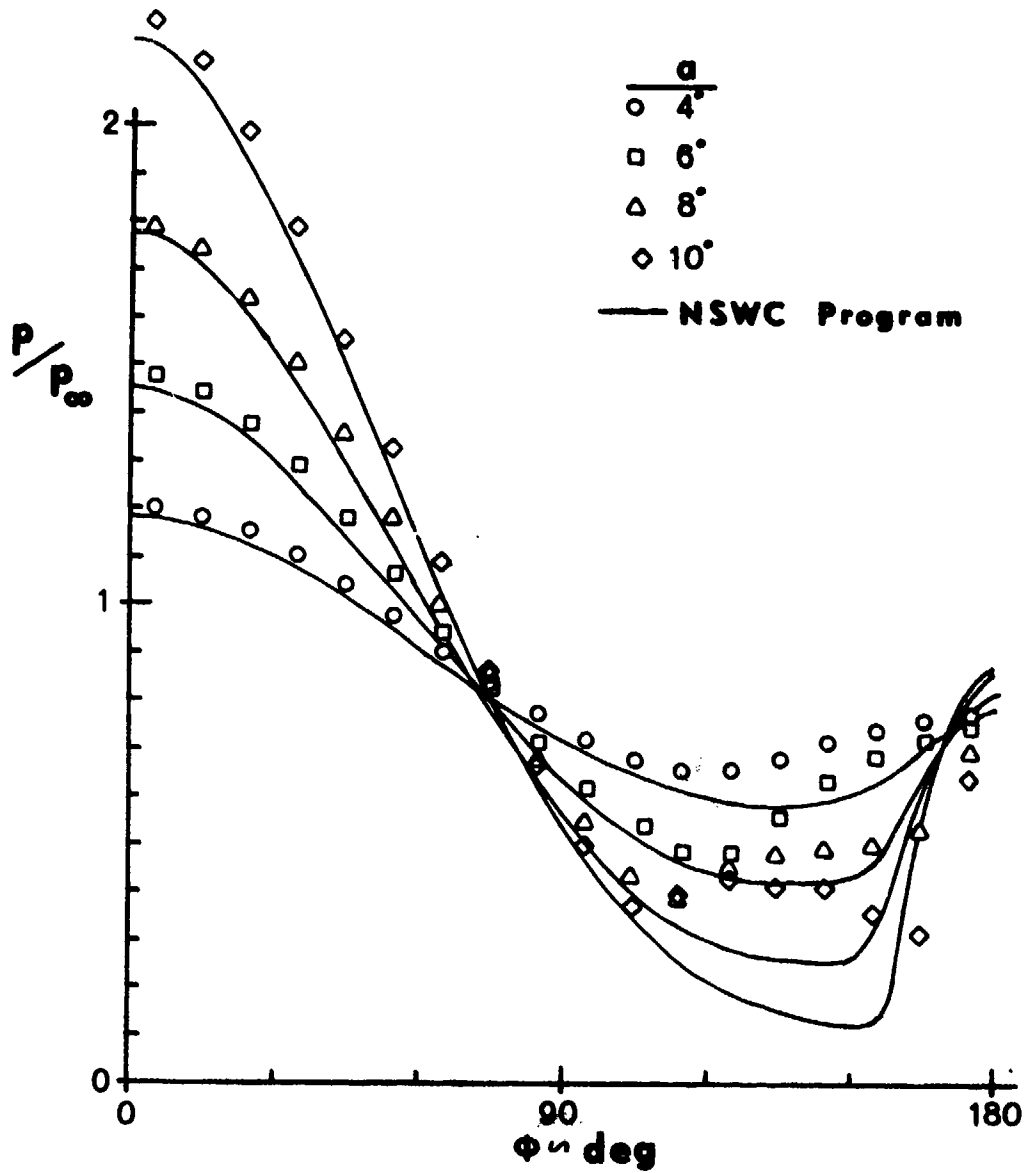


FIGURE 4.16 SURFACE PRESSURE DATA

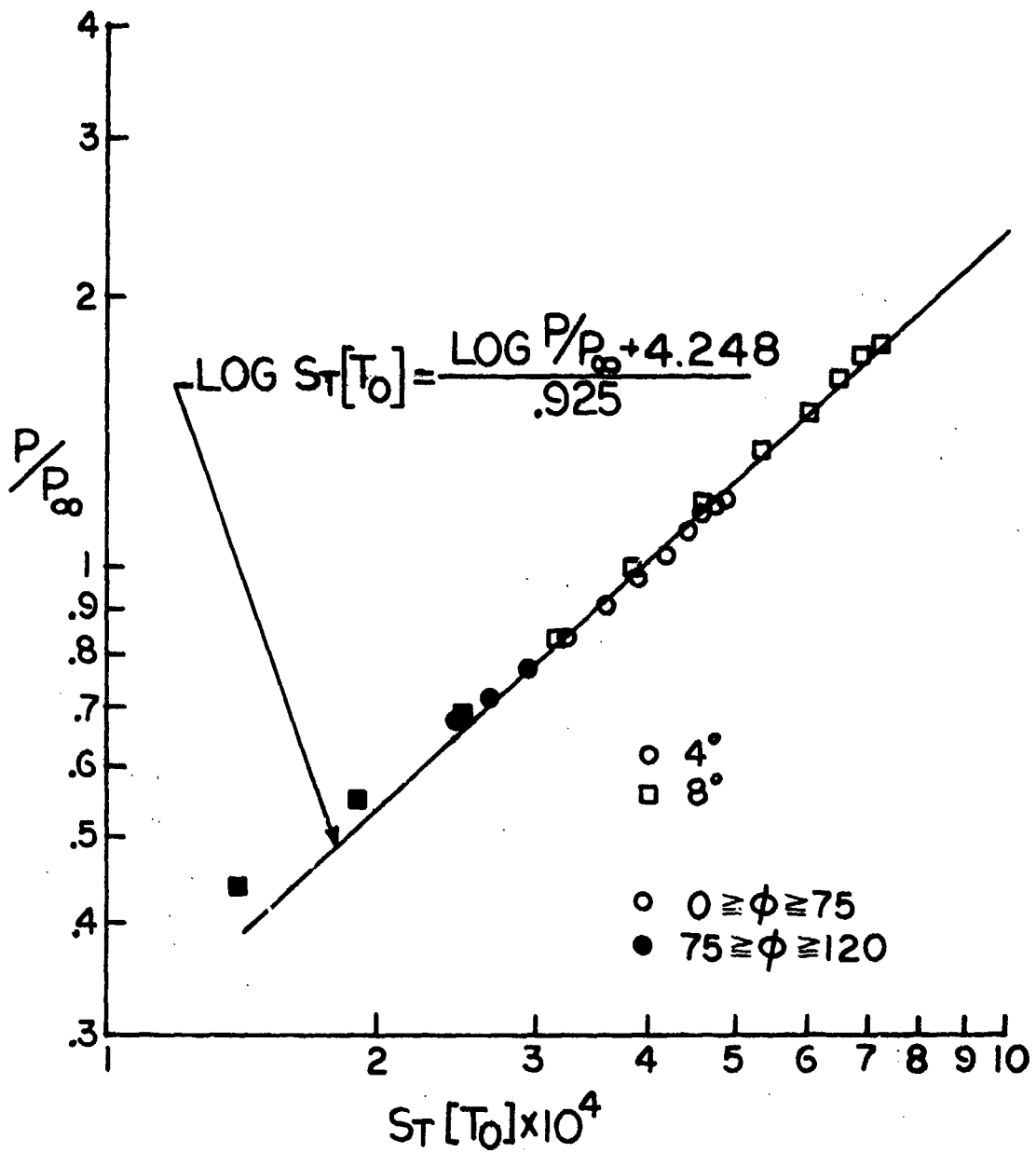


FIGURE 4.17 UNDISTURBED PRESSURE-HEATING CORRELATION

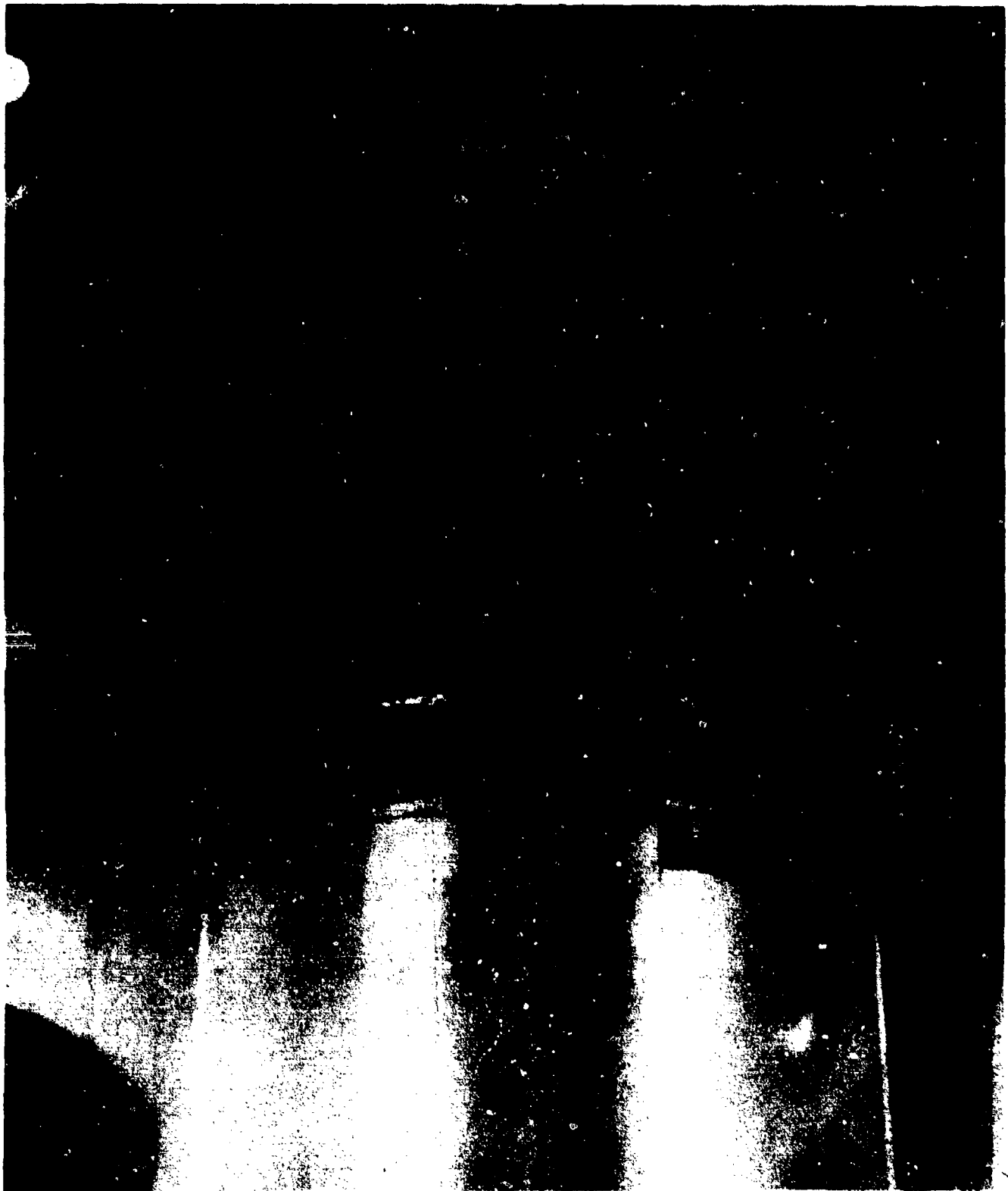


FIGURE 4.18 LEEWARD CENTERLINE OIL FLOW,  $\alpha = 0$

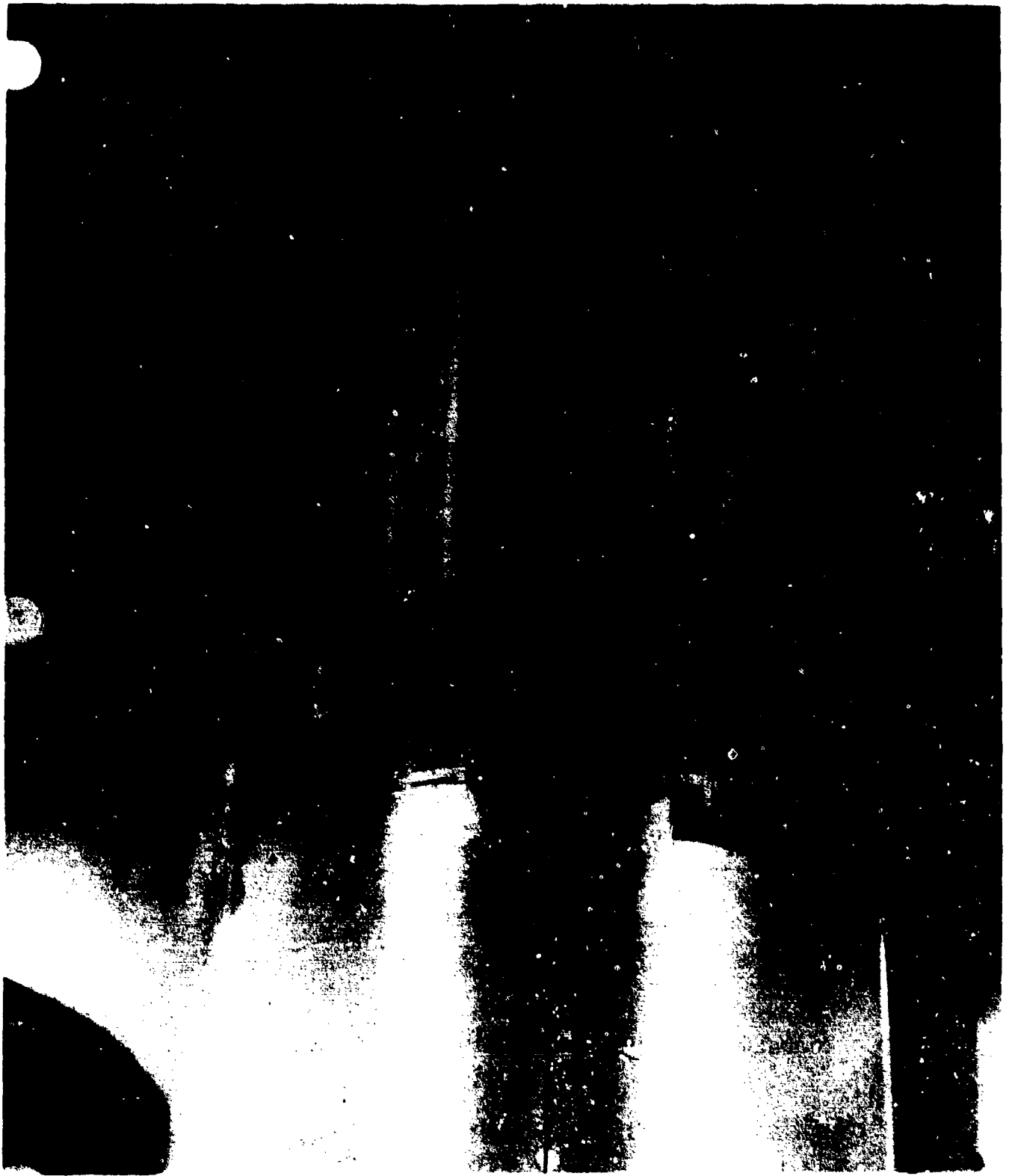


FIGURE 4.19 LEEWARD CENTERLINE OIL FLOW,  $\alpha=10^\circ$

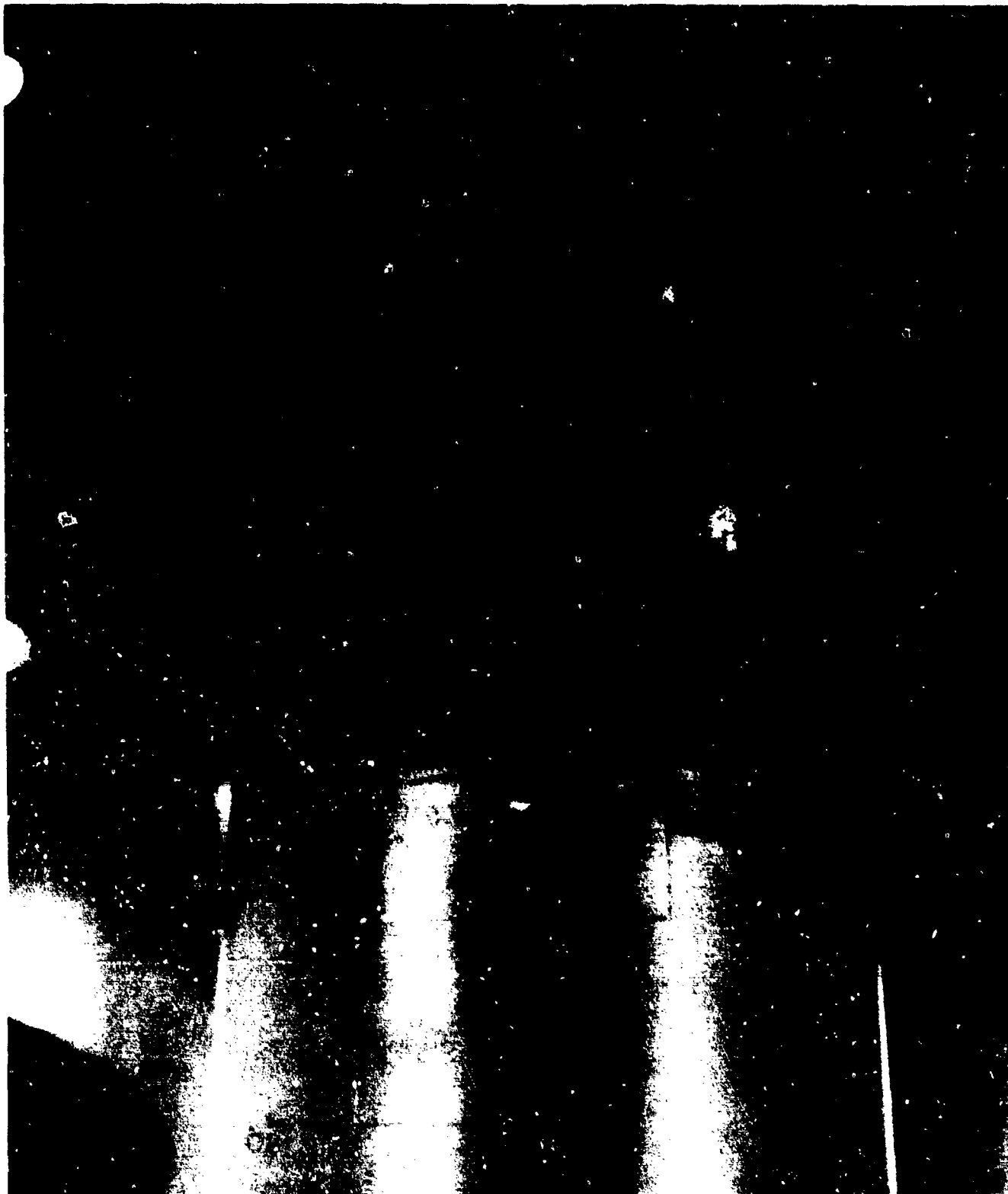


FIGURE 4.20 LEEWARD CENTERLINE OIL FLOW,  $\alpha=12^\circ$   $\frac{r}{\delta}$



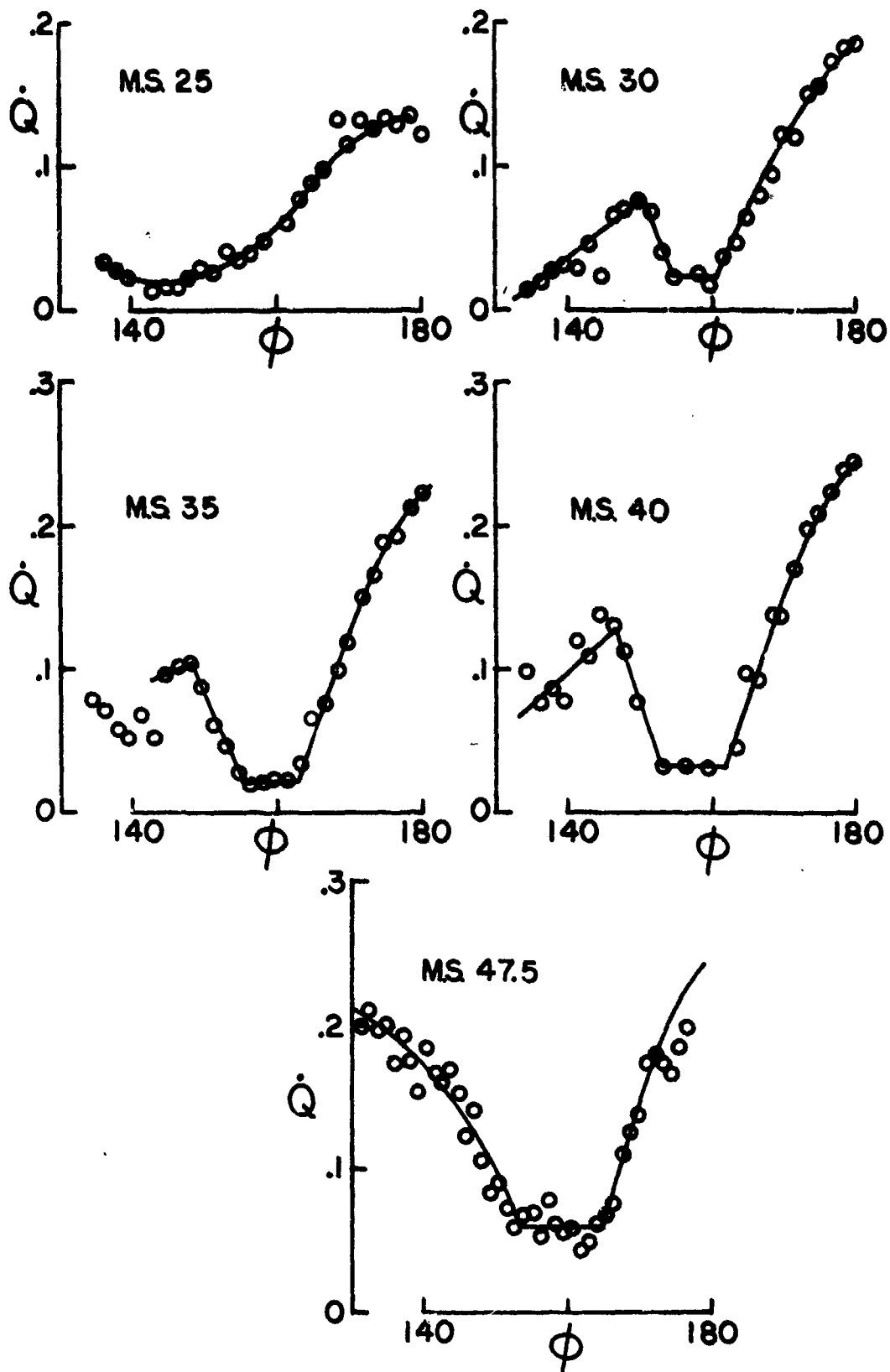


FIGURE 4.21 LEEWARD SEPARATION INDUCED HEATING MINIMUM,  $\alpha=12^\circ$

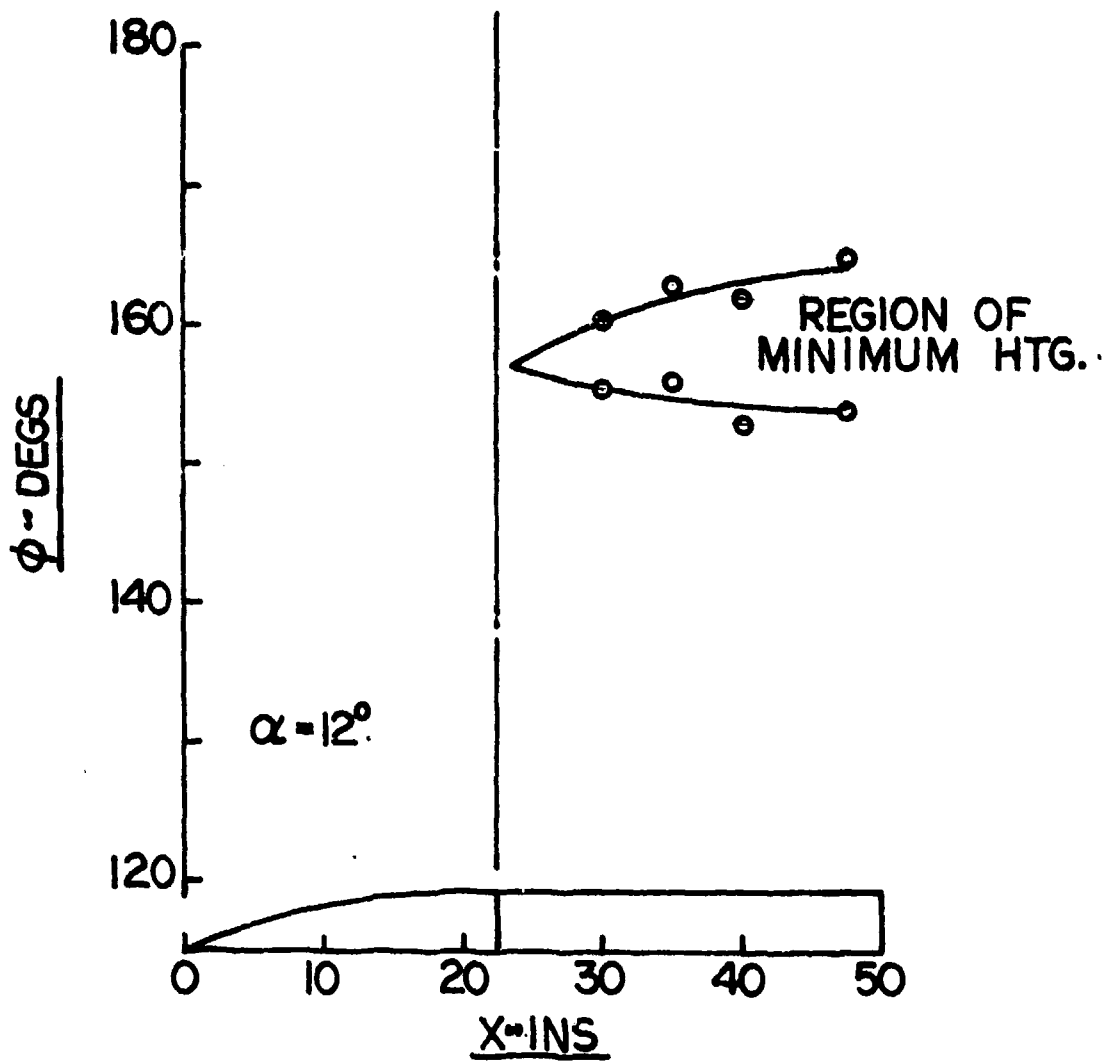


FIGURE 4.22 EXTENT OF MINIMUM HEATING REGION,  $\alpha = 12^\circ$

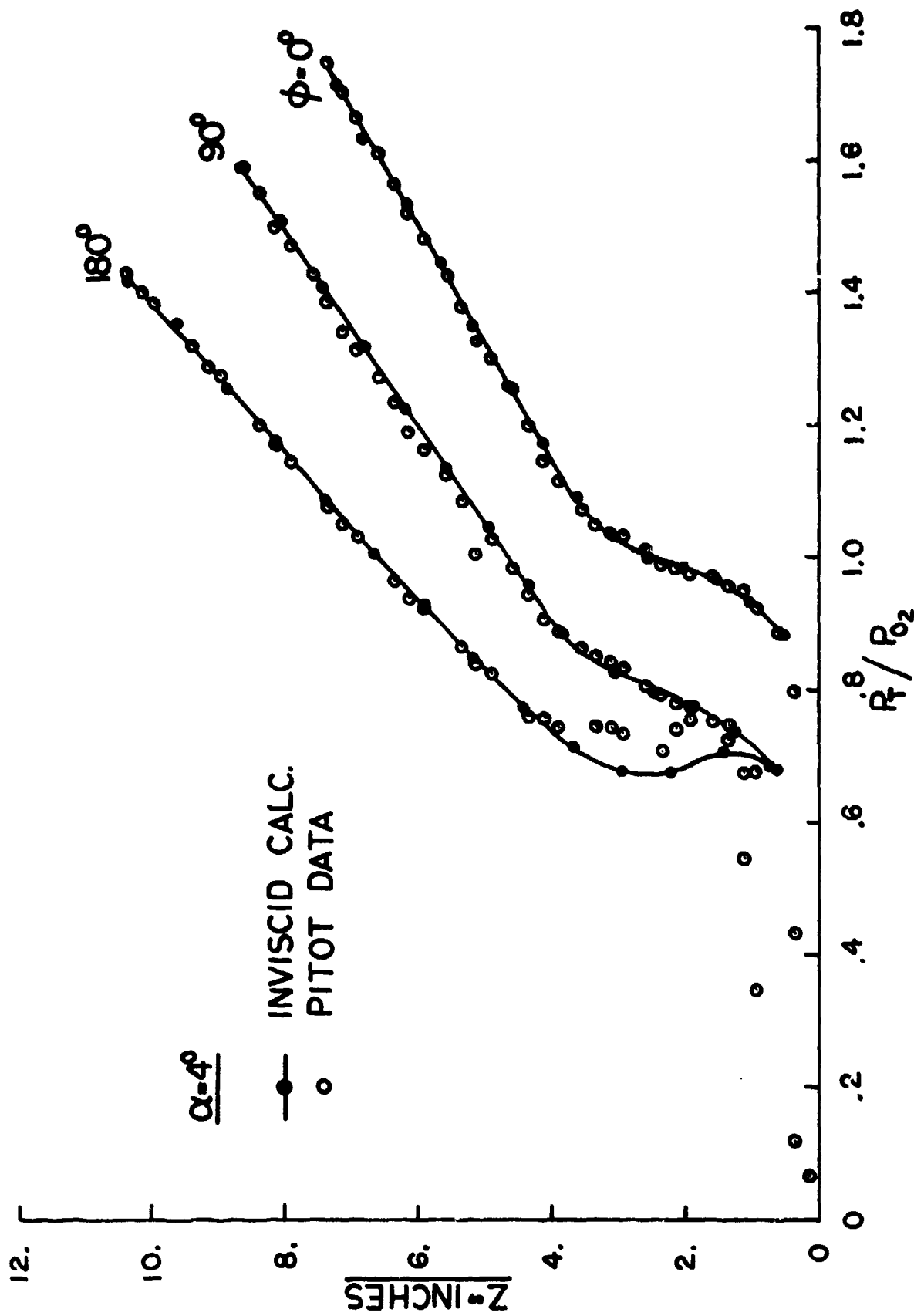


FIGURE 4.23 SHOCK LAYER PITOT PRESSURE PROFILES,  $\alpha=4^\circ$

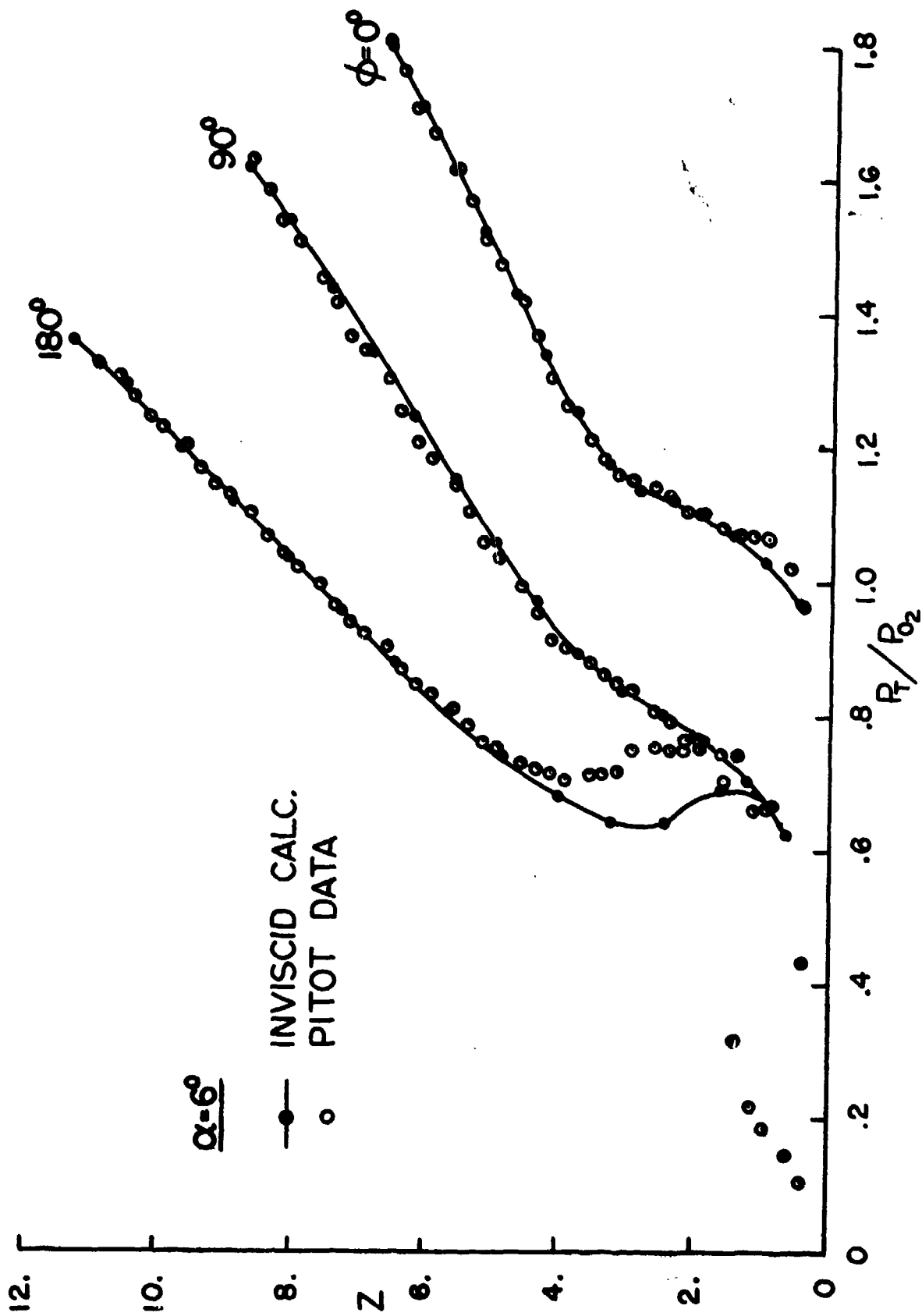


FIGURE 4.24 SHOCK LAYER PITOT PRESSURE PROFILES,  $\alpha=6^\circ$

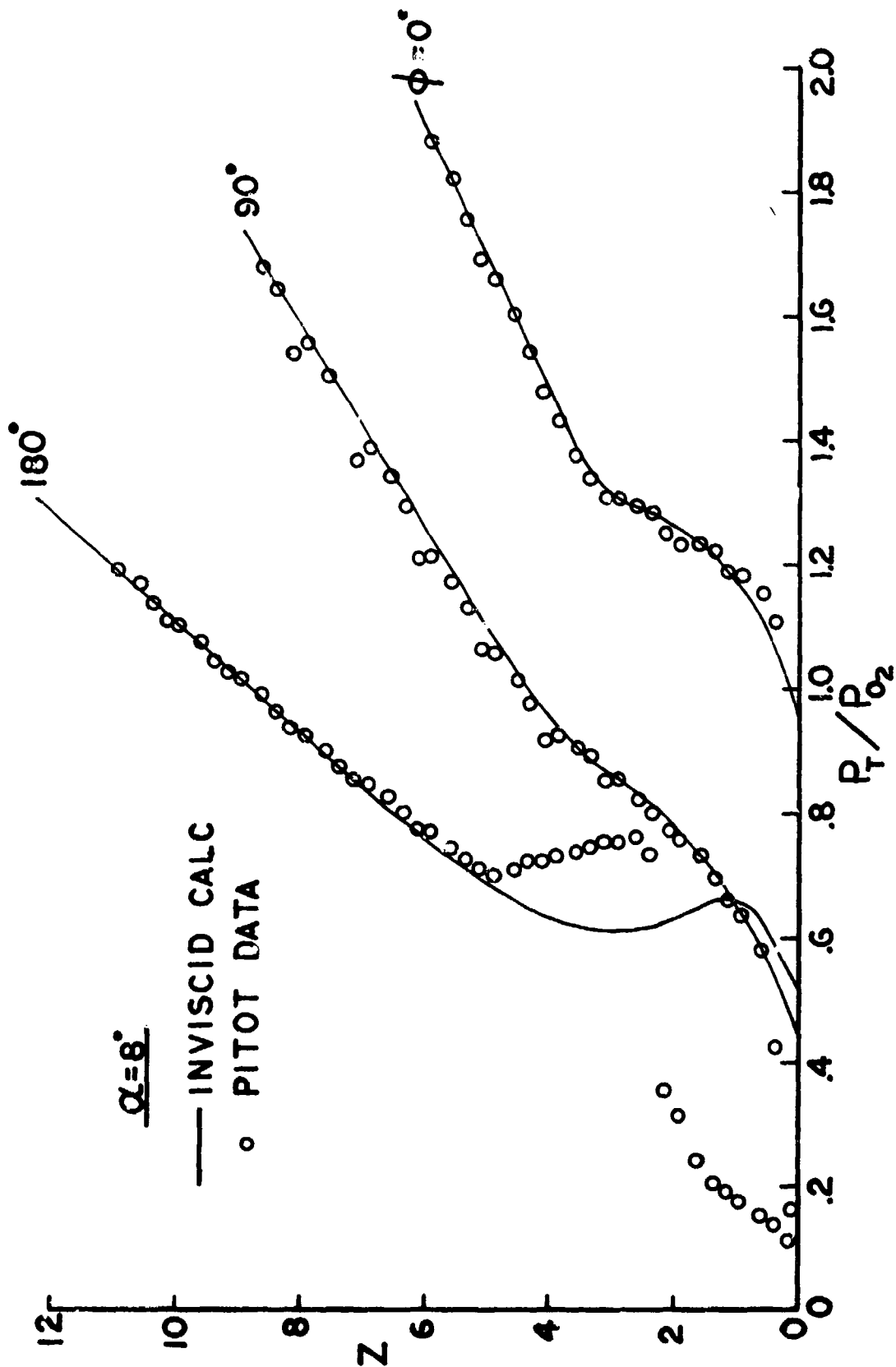


FIGURE 4.25 SHOCK LAYER PITOT PRESSURE PROFILES,  $\alpha=8^\circ$

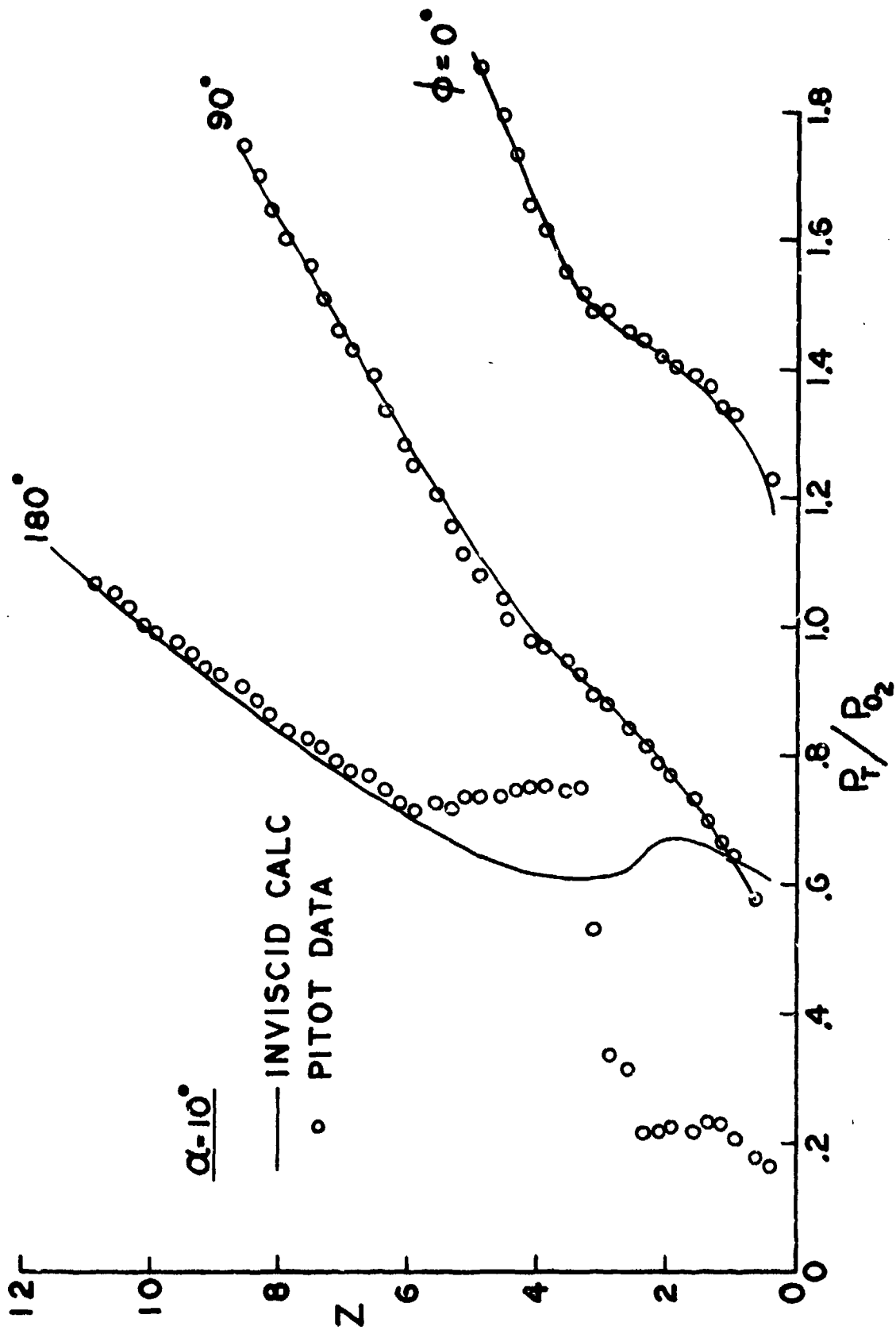


FIGURE 4.26 SHOCK LAYER PITOT PRESSURE PROFILES,  $\alpha=10^\circ$

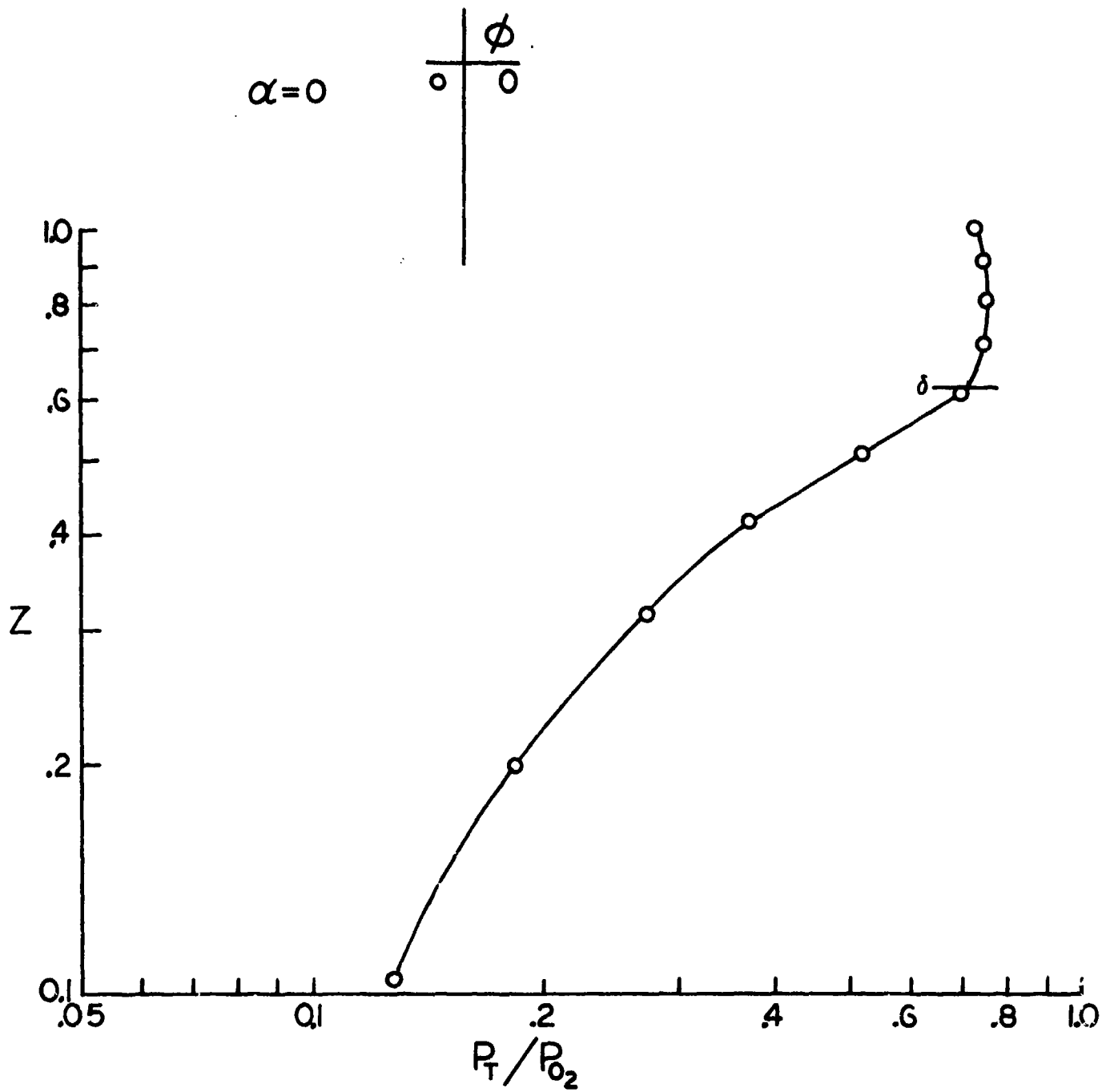


FIGURE 4.27 BOUNDARY LAYER PITOT PROFILES,  $\alpha=0^\circ$

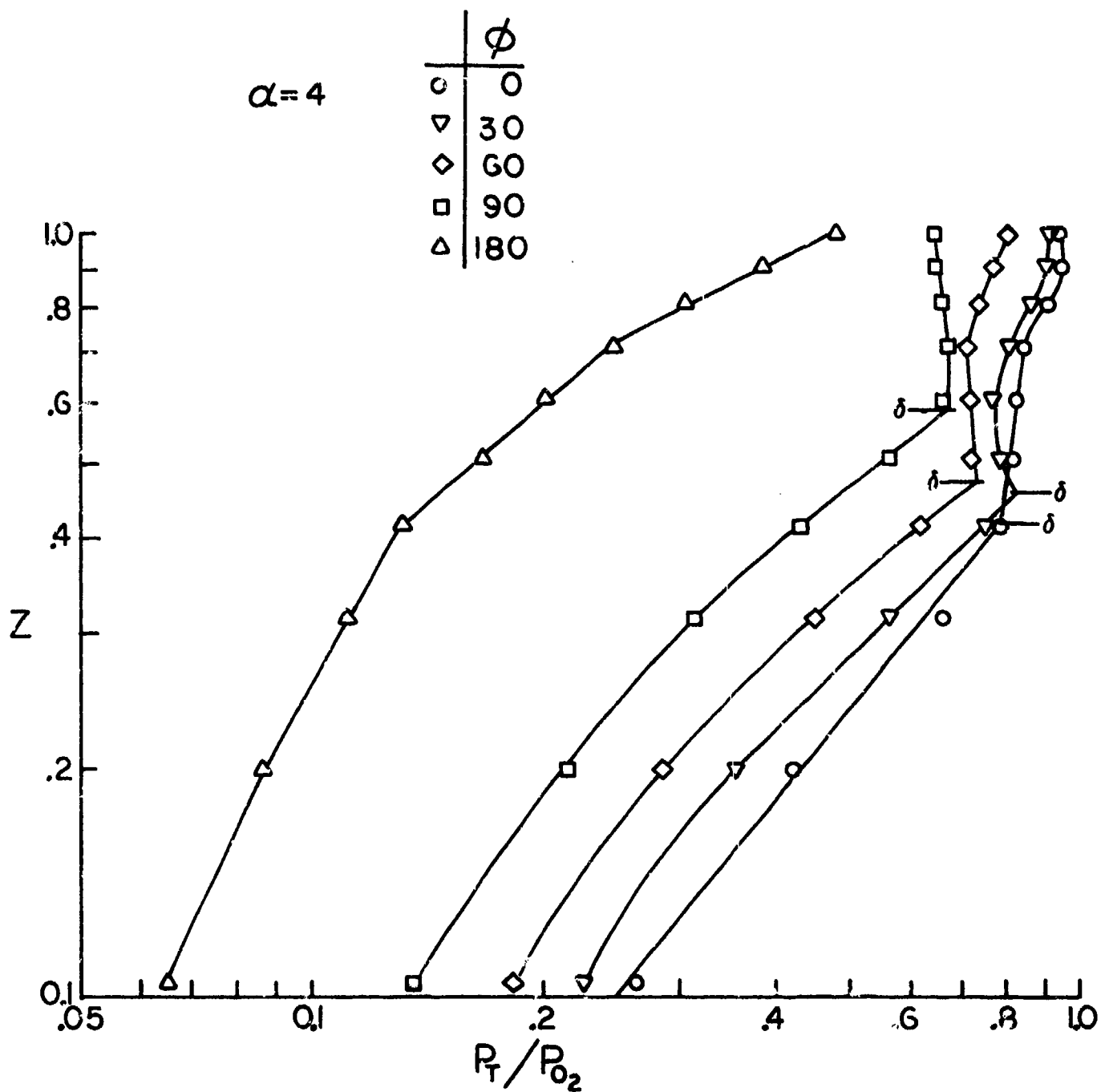


FIGURE 4.28 BOUNDARY LAYER PITOT PROFILES,  $\alpha = 4^\circ$



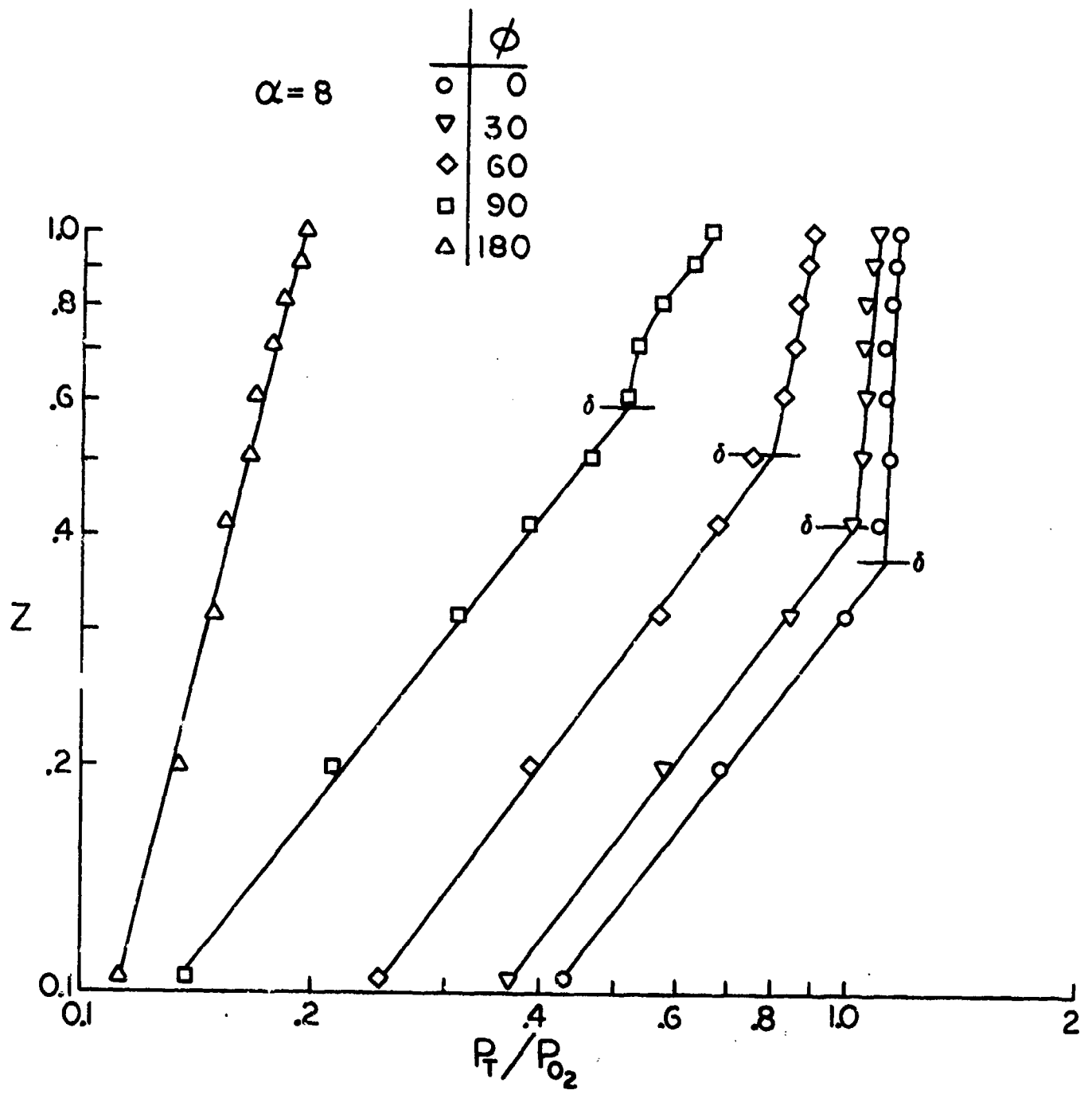


FIGURE 4.29 BOUNDARY LAYER PITOT PROFILES,  $\alpha = 8^\circ$

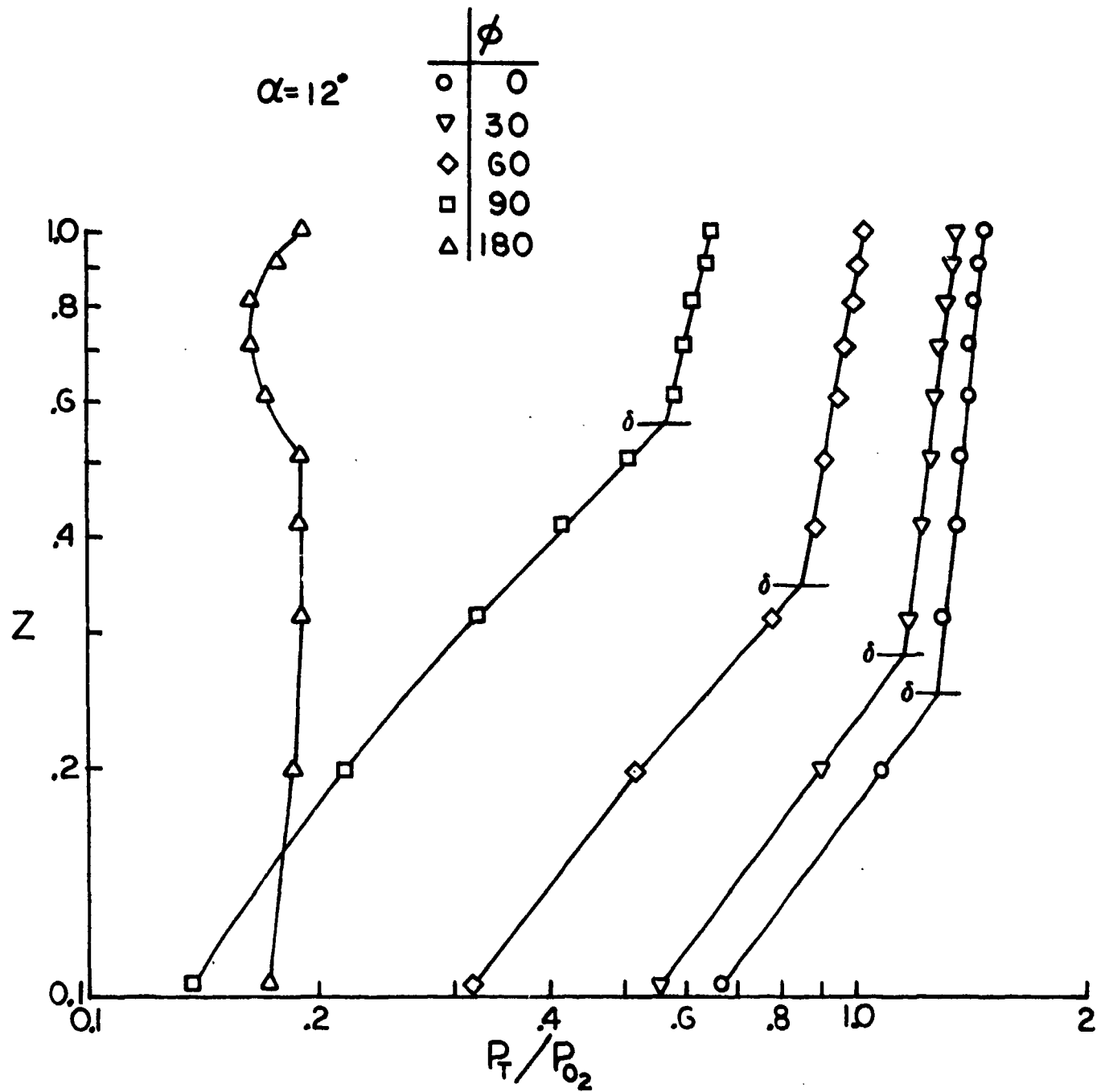


FIGURE 4.30 BOUNDARY LAYER PITOT PROFILES,  $\alpha = 12^\circ$

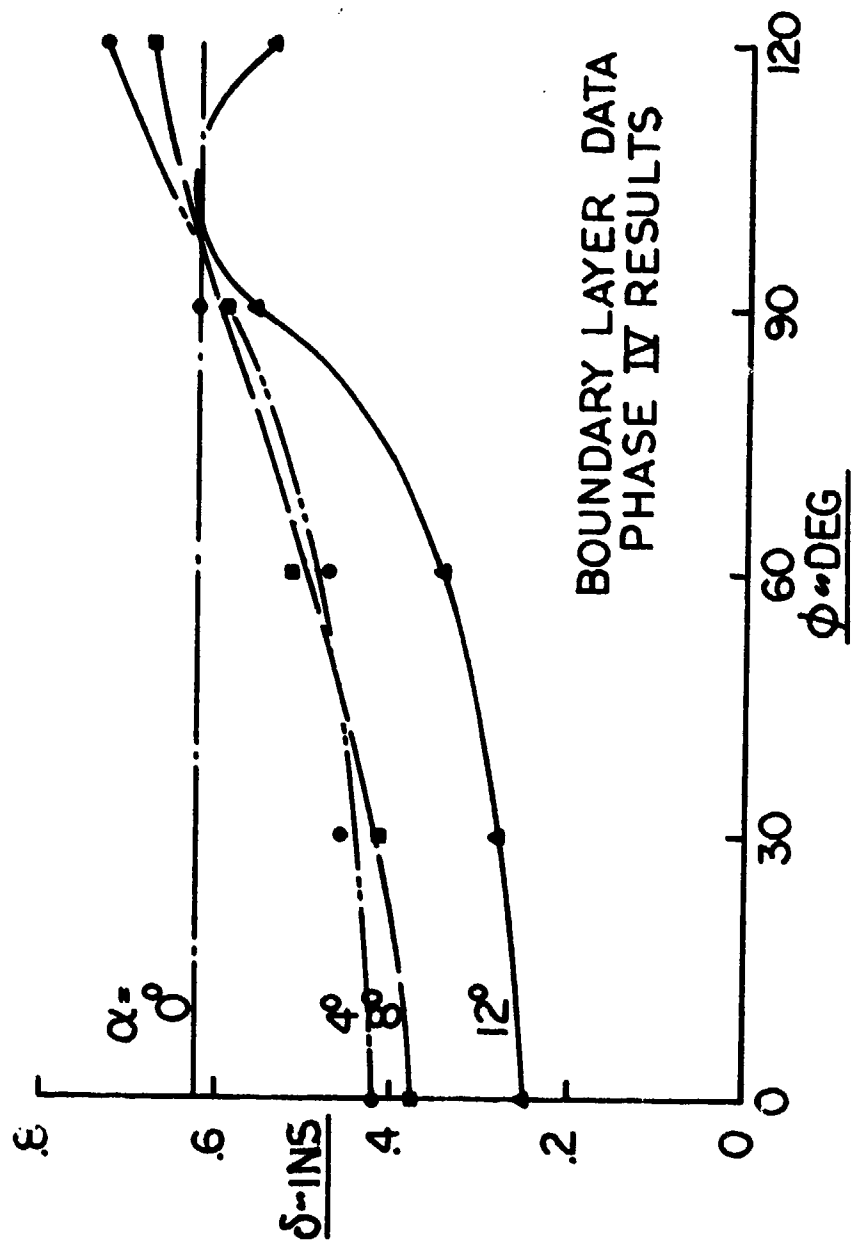


FIGURE 4.31 BOUNDARY LAYER THICKNESS

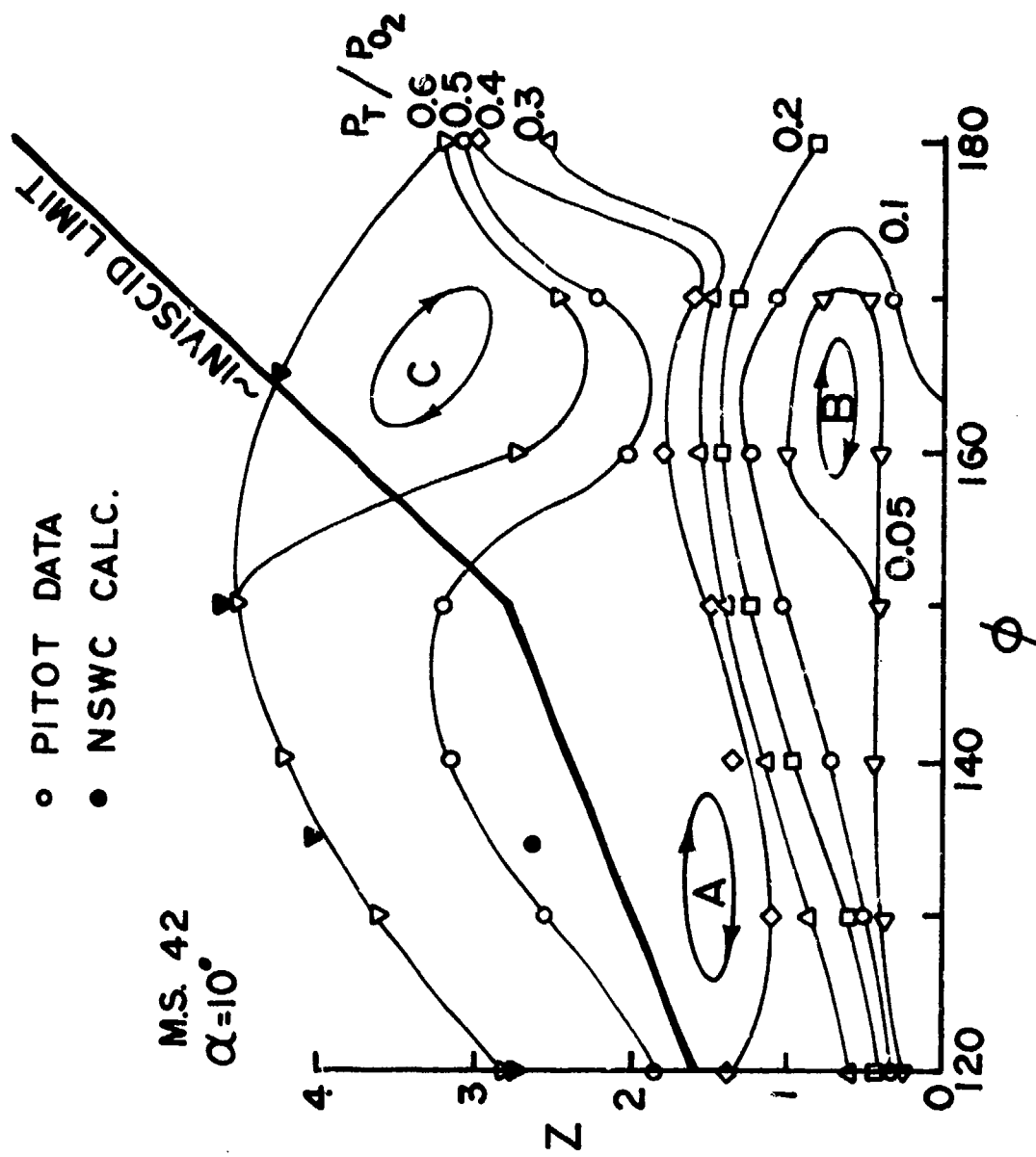


FIGURE 4.32 CONSTANT PITOT PRESSURE CONTOURS,  $\alpha=10^\circ$

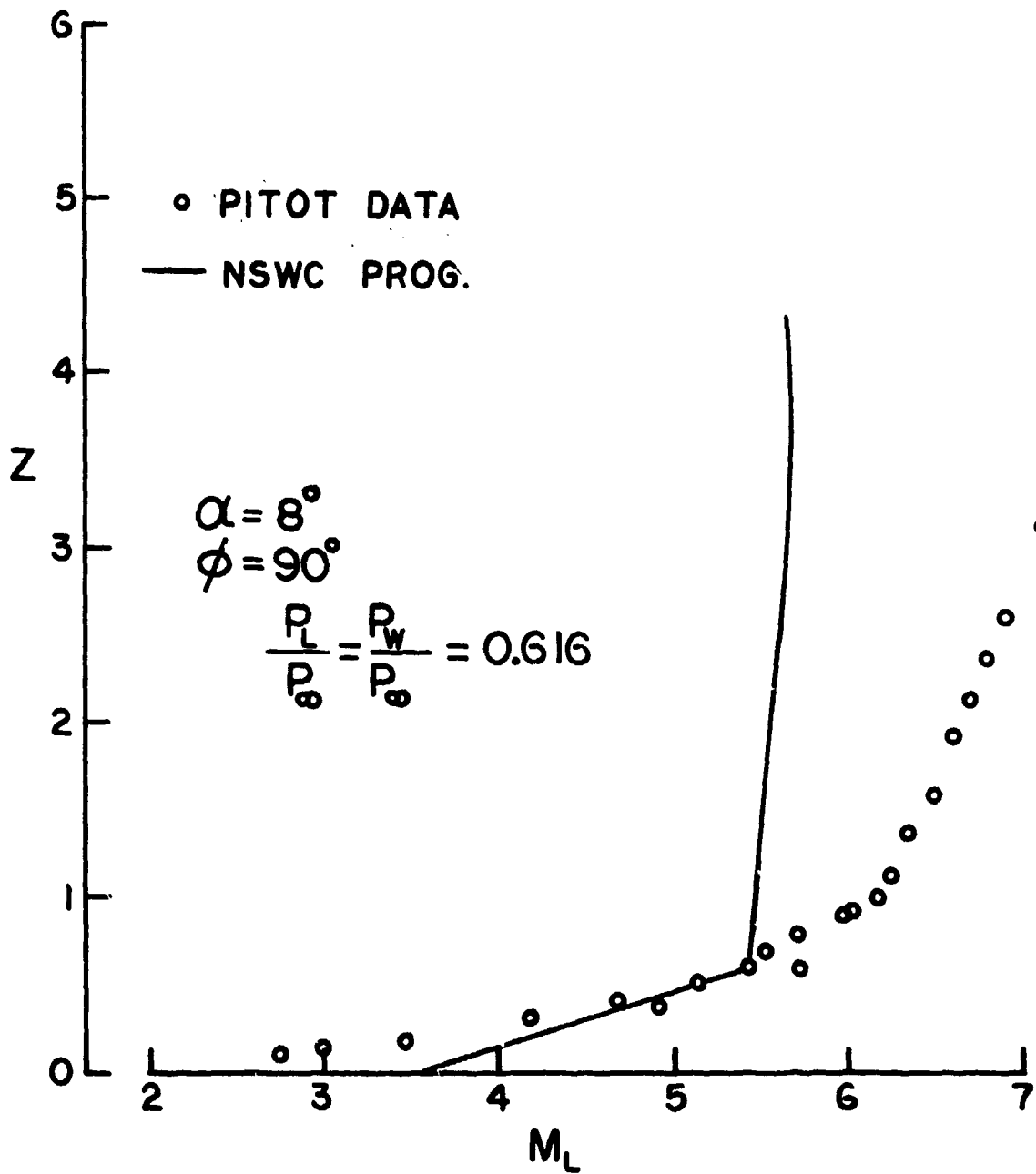


FIGURE 4.33 COMPARISON OF NSWC AND EXPERIMENTAL MACH NUMBERS

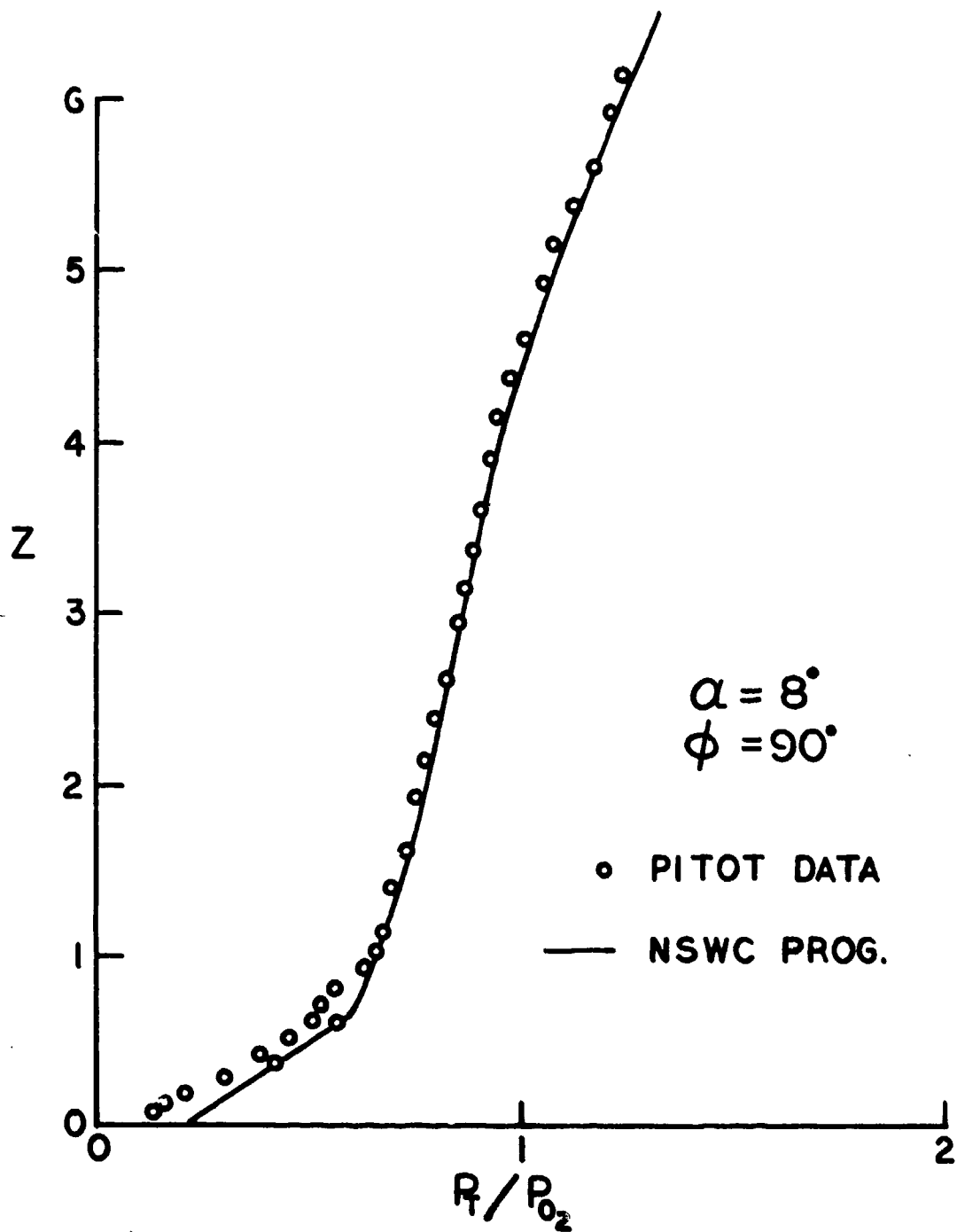


FIGURE 4.34 COMPARISON OF NSWC TO EXPERIMENTAL PITOT PRESSURES

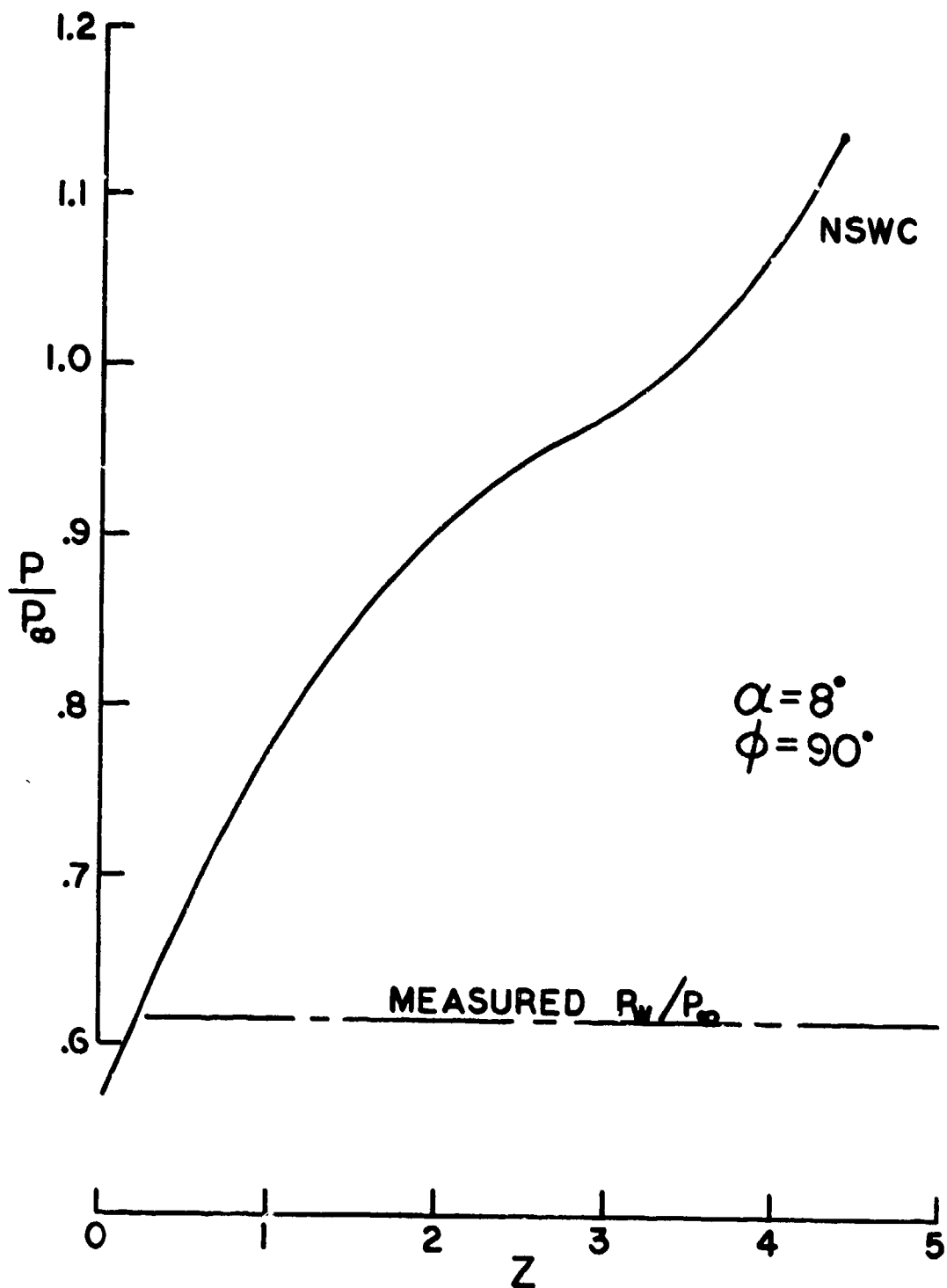


FIGURE 4.35 NSWC STATIC PRESSURE PROFILE

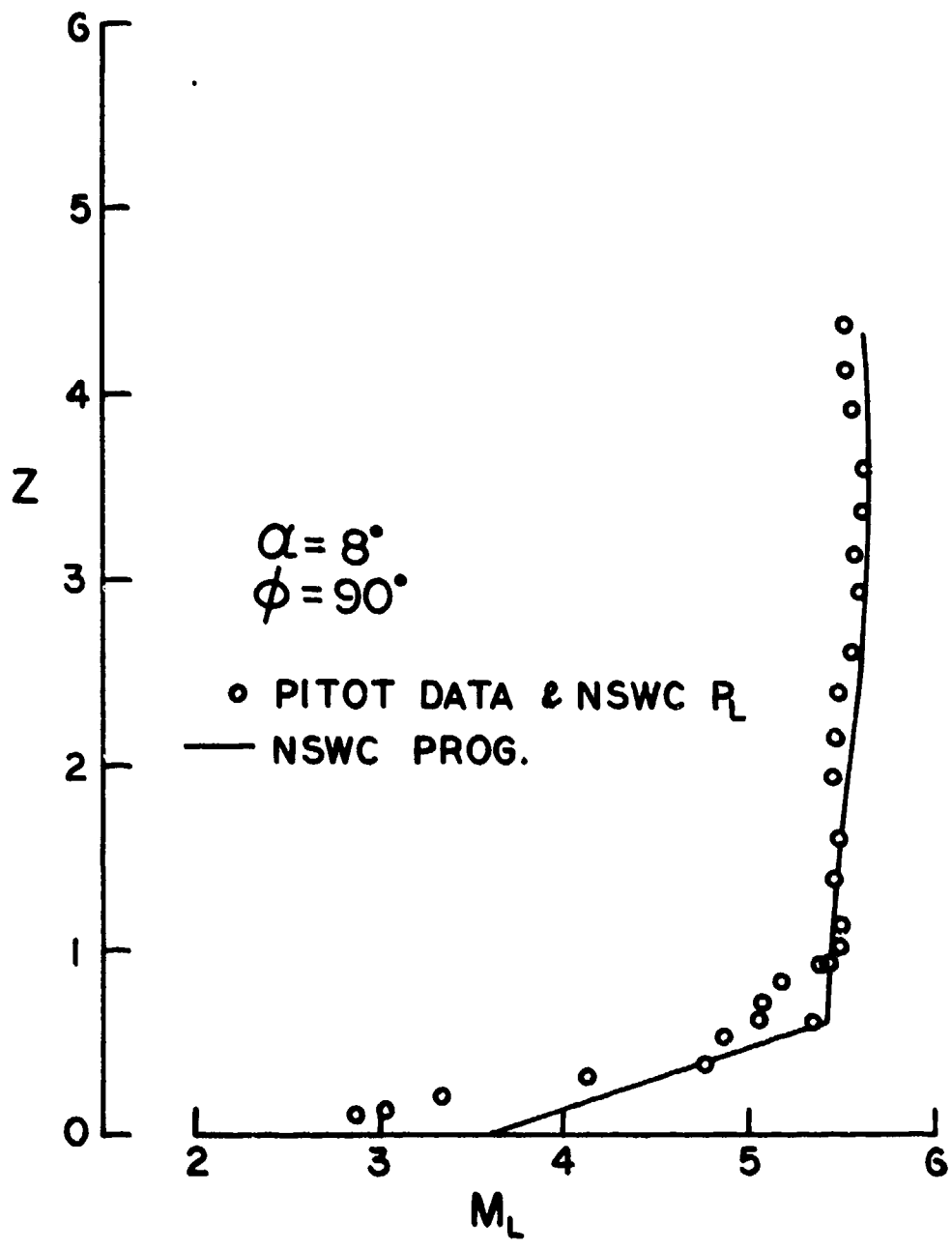


FIGURE 4.36 EXPERIMENTAL MACH NRS. USING NSWC  $R_L$



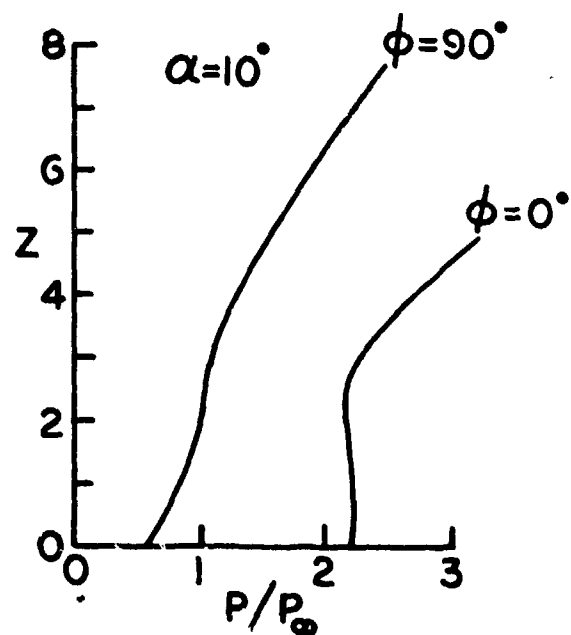
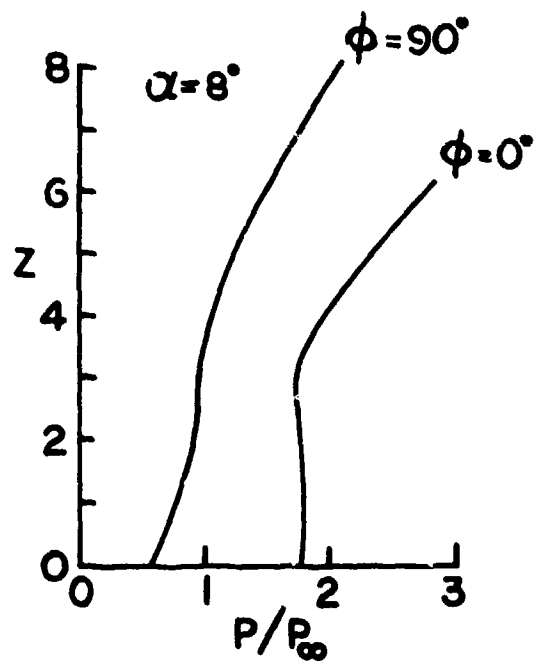
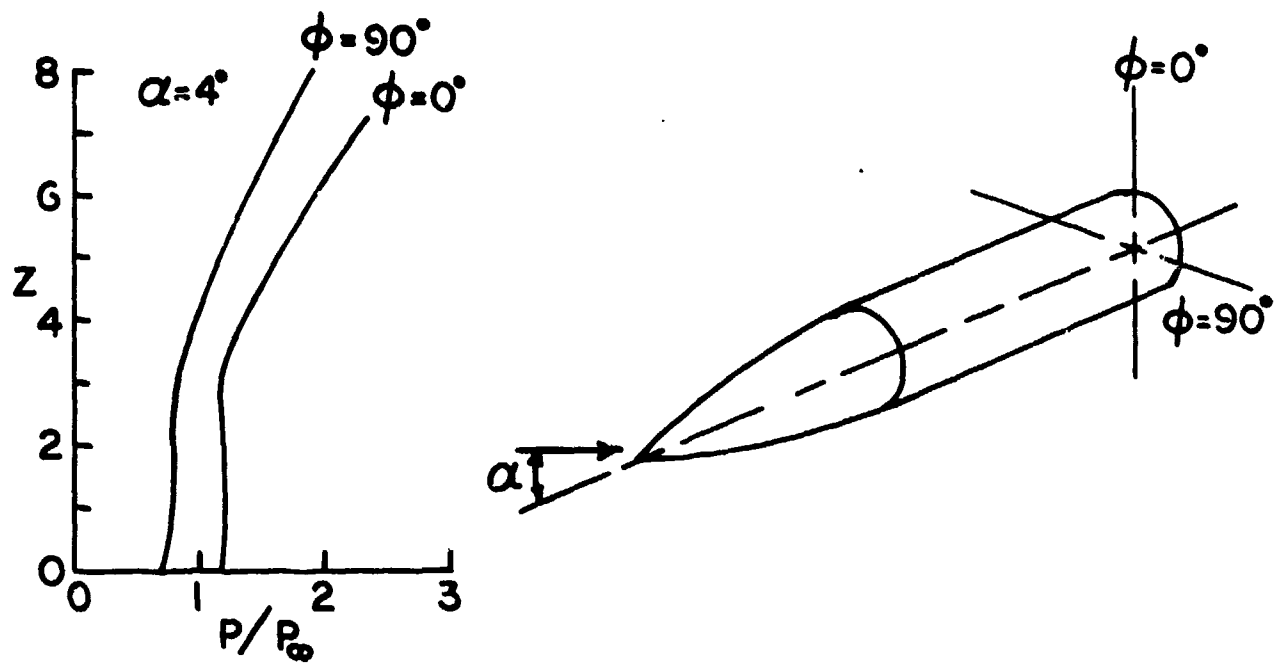


FIGURE 4.37 NSWC STATIC PRESSURE PROFILES

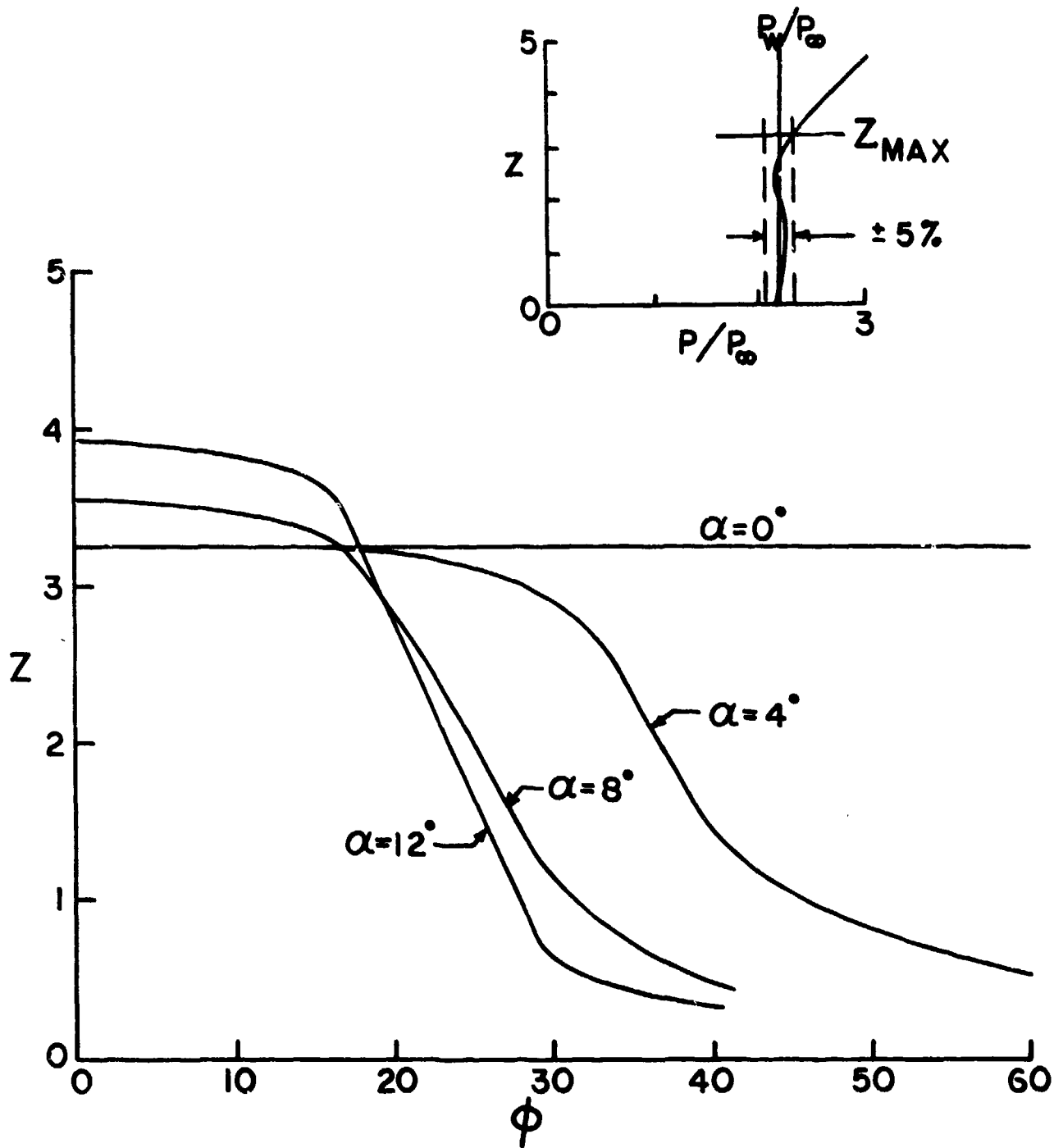


FIGURE 4.38 MAXIMUM Z FOR  $P_L = P_W \pm 5\%$  (NSWC)

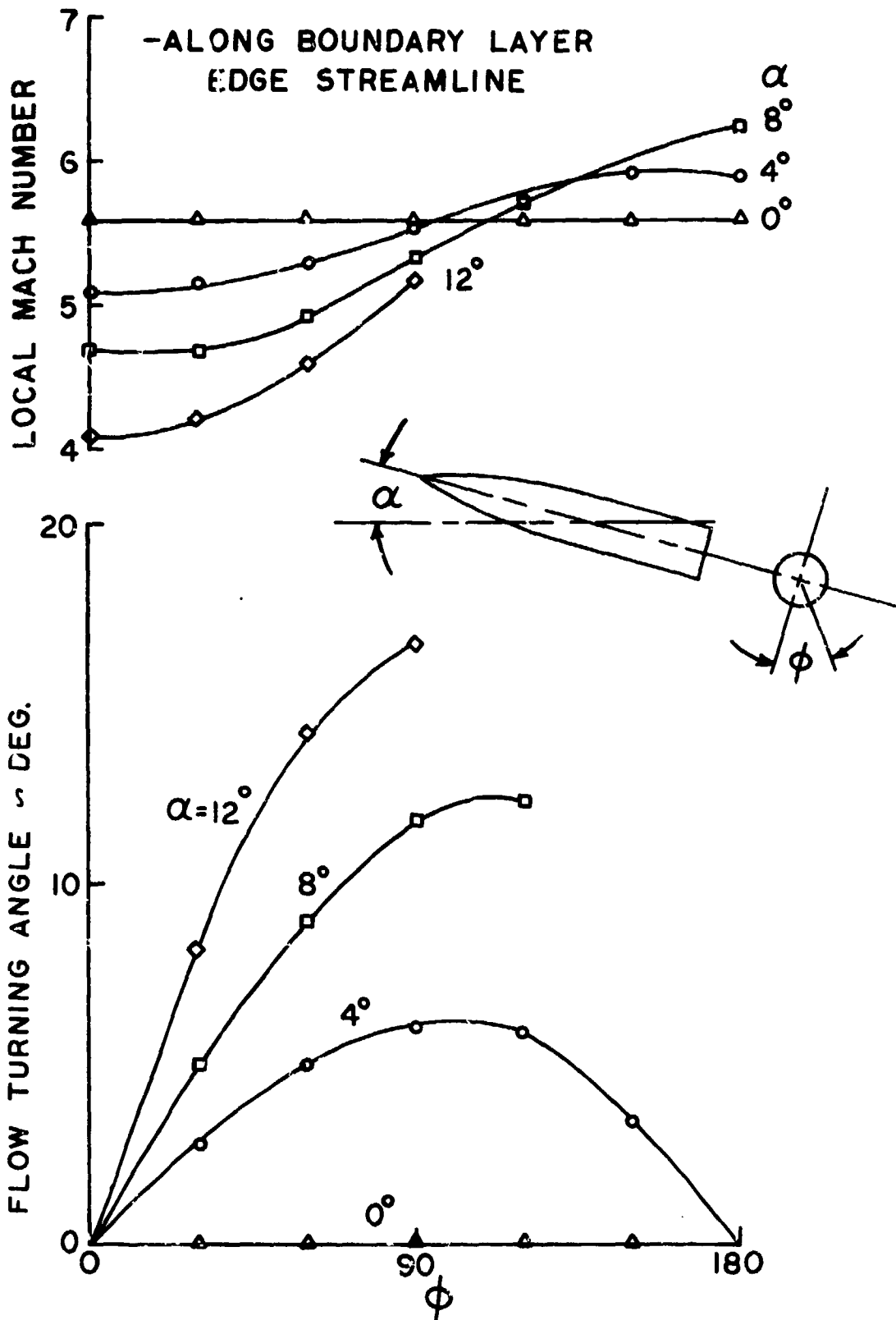


FIGURE 4.39 MACH NUMBER AND FLOW ANGULARITY AT THE BOUNDARY LAYER EDGE

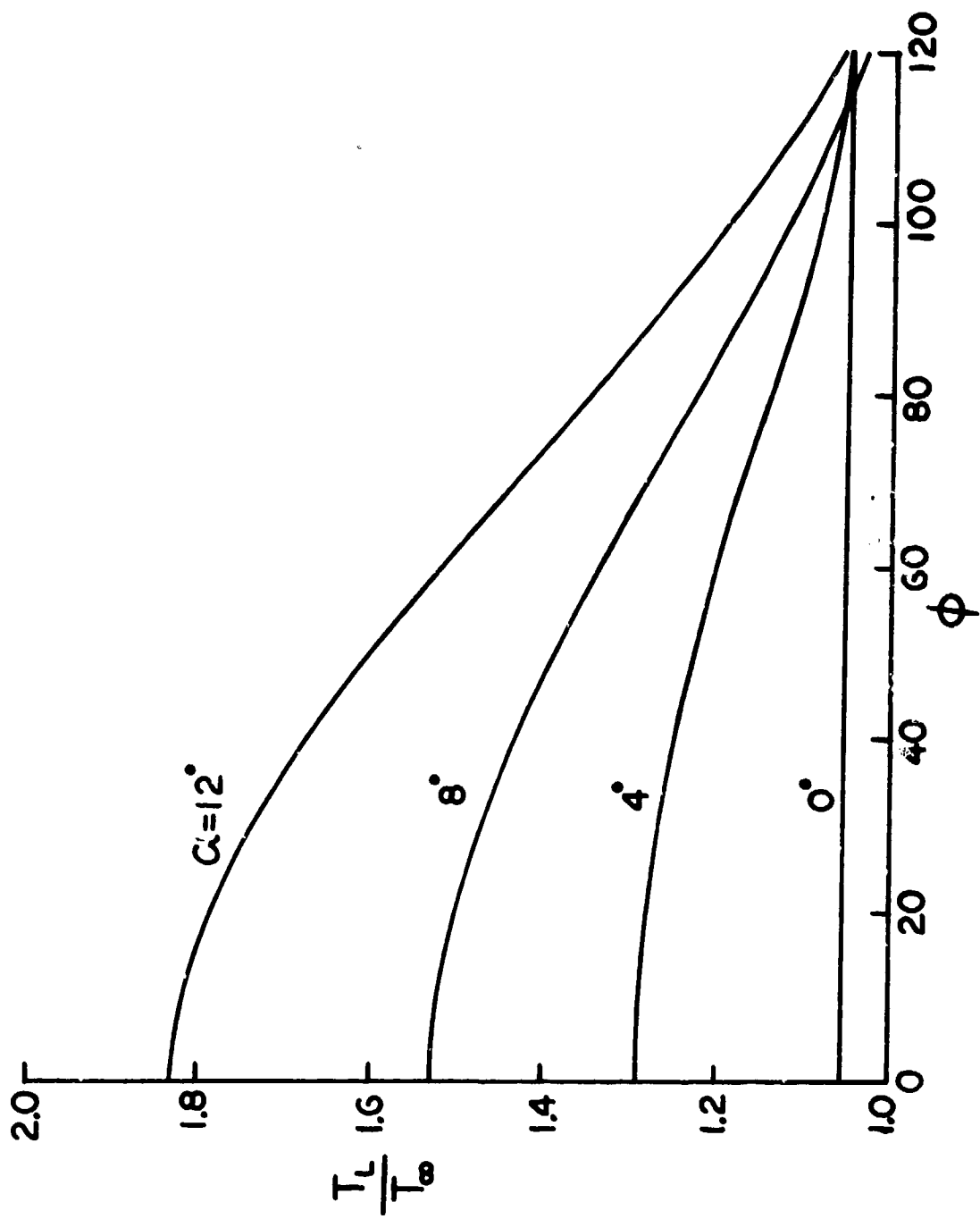


FIGURE 4.40 LOCAL STATIC TEMPERATURE RATIO (NSWC PROG.)

## 5.0 SEALED FIN INTERACTIONS

The aerodynamic heating produced in the interaction region of fins sealed to the missile body will be discussed in this section. Examples of the interaction heat transfer distributions on the missile body are shown in Figure 5.1. The most significant feature is the large peak which occurs close to the fin. In Subsection 5.1 through 5.3 the peak heating rates produced by unswept fins having wedge half angles of  $6^\circ$ ,  $7.5^\circ$ ,  $9^\circ$  and  $10^\circ$  will first be discussed for the case of the missile at zero angle of attack. The complications of variable local Mach number and cross flow will then be added by pitching the missile to angle of attack and rolling the fin off the windward centerline. In Subsection 5.4 the location of peak heating in the interaction region is correlated and compared to existing fin-flat plate data.

In Subsection 5.5 the effects of fin leading edge sweep and bluntness on peak heating in the interaction region are discussed. The final subsection deals with the aerodynamic heating on the fin surface for swept and unswept fins. The heating rates are compared to laminar and turbulent flat plate theory and good agreement is noted.

### 5.1 Peak Heating at Zero Angle of Attack

Using the undisturbed data of Section 4.0 as the reference values, the interference heating ratios (peak to undisturbed) were calculated for the most elementary case of the ogive-cylinder at zero angle of attack. Figure 5.2 presents these data and for comparison, data for a fin on a flat plate<sup>(3)</sup>. In spite of reasonable agreement of Mach number and Reynolds number between experiments substantial differences in interference effects are noted. Also shown in this figure is a peak heating correlation by Hayes<sup>(4)</sup> for fin-flat plate interactions. This correlation is a function

of  $M_L \sin \theta$  and  $\Delta x/\delta$  and is shown to predict the flat plate data very well.

Subsequent flow field probing on the ogive-cylinder indicated that the local Mach number at the fin station was 5.6 compared with 5.85 for the fin-flat plate data. It also showed that the boundary layer thickness on the ogive-cylinder was 0.63 inches yielding an  $\Delta x/\delta$  ratio of 8.7 compared to 20 for the fin-flat plate data. The peak heating correlation was recomputed based on these data for the ogive-cylinder, however the effects were found to be insignificant in improving the agreement with the ogive-cylinder heating data. A final area of difference which will now be discussed is that the ogive-cylinder data are tripped and the fin-flat plate data are not.

A tripped fin-flat plate interaction test was conducted in 1964 and the results presented in reference 5. The peak heating data from this test are shown in Figure 5.3 as a function of distance from the fin leading edge,  $\Delta x$ , and for various fin deflection angles. From an evaluation of pitot data on the clean flat plate it was determined that at the fin leading edge the boundary layer was 0.51 inches thick so that a value of  $\Delta x/\delta = 8.7$  was achieved at  $\Delta x = 4.4$  inches.

In Figure 5.4 the tripped flat plate data is cross plotted at a value of  $\Delta x/\delta = 8.7$  together with the ogive-cylinder data. Agreement between the data sets is apparent, but of more importance is the agreement with the oblique shock pressure ratio to the 0.8 power. This pressure correlation was derived from two dimensional interaction data<sup>(5)</sup>. This indicates that for three dimensional interactions occurring downstream of a tripping device the peak heating agrees with that of two dimensional

interactions at equal shock strengths. The vorticity associated with three dimensional peak heating may not be present. This is in contradiction to the results of Hayes for untripped boundary layers on fin-flat plate models. The significance of this is clear when it is pointed out that all systems data taken to date have been taken on models employing trip strips, and that typically the  $\Delta x/\delta$  is 10 or less.

Evaluating the bulk of the tripped fin-flat plate data it appears that the data approach the values predicted by Hayes only after  $\Delta x/\delta$  values greater than 25 are attained as shown in Figure 5.5.

## 5.2 Peak Heating at Angle of Attack, Zero Roll

We will now consider the more general case of an interaction caused by a fin located on the windward centerline as the ogive-cylinder is pitched to angle of attack. As the angle of attack increases the local Mach number at the fin leading edge decreases. The pitot pressure data and the NSWC program, both described in Section 4, were employed to evaluate the boundary layer thickness and the local Mach number at the boundary layer edge. These parameters were presented in Figures 4.31 and 4.39 respectively.

The selection of the boundary layer edge as the characteristic point for such interactions is consistent with the prevailing concept that three dimensional flows separate easily and that, once separated, a new boundary layer is formed of the inviscid flow. The original boundary layer does not pass over the separated region. This has been confirmed empirically through evaluation of oil flow data and it is consistent with the comments of Eichelbrenner<sup>(6)</sup> concerning three dimensional boundary layers.

Figure 5.6 indicates the fin interaction data for missile angles of attack up to  $12^{\circ}$ . Also shown is the oblique shock pressure ratio to the 0.8 power. While some data scatter exists, the scatter is within  $\pm 10\%$  of the pressure correlation. Since the variation in  $\Delta x/\delta$  with angle of attack is not considered in this correlation some data scatter is expected.

### 5.3 Peak Heating at Angle of Attack, Arbitrary Roll

In the most general case the ogive-cylinder is free to pitch to angle of attack and, at the same time, the fin is rolled to arbitrary angles off the windward centerline. Within this report fin interaction data will be limited to fin roll angles of  $120^{\circ}$  or less by the requirement that attached flow on the cylinder be maintained at the fin location. Intuitively, as the fin roll angle increases, for a given angle of attack, the flow angle with respect to the model centerline and the local Mach number also increase. Correlation of the peak heating data depends upon understanding these variations in a quantitative manner. The pitot data and NSWC program were again used to define these parameters at the boundary layer edge. Local Mach numbers and flow turning angles are shown in Figure 4.39 as a function of model peripheral angle and angle of attack.

Using these "data" a correlation of the peak heating data for arbitrary orientation was derived and is shown in Figure 5.7. The fin shock wave angle,  $\theta$ , is that caused by the sum of the fin wedge half angle and the flow turning angle at the boundary layer edge. Again the oblique shock pressure ratio to the 0.8 power is also shown. Excellent agreement,  $\pm 10\%$  of the pressure correlation, is noted for



these data. All of the data in Figure 5.7 were taken on the cylinder between the fin centerline and the cylinder's windward centerline. A similar correlation is possible for data taken between the fin centerline and the cylinder's leeward centerline where smaller but positive effective fin deflection angles occur. Figure 5.8 indicates such data using the symbolism of Figure 5.7. Data generally agree with the pressure correlation to  $\pm 10\%$ ; however, they are biased to be slightly higher than the pressure correlation at very low effective wedge angles. This may be due to viscous effects which increase the effective wedge angle of the fin.

#### 5.4 Location of Peak Aerodynamic Heating

The peak aerodynamic heating location on the ogive-cylinder was evaluated against parameter suggested by Token<sup>(7)</sup> as applicable to the fin-flat plate case. This correlation is noted in Figure 5.9 for both positive and negative angles of attack and for the fin located on the windward centerline as defined at positive angles of attack. Token's relationship is

$$\psi - \delta_f = K(\theta - \delta_f) \quad (\text{Eq. 5.3.1})$$

where  $K=0.24$  according to Token<sup>(7)</sup>

$\delta_f$  = effective fin deflection angle

$\psi$  = angle to peak heating location

$\theta$  = shock wave angle

The data indicate that  $K=0.24$  forms a lower bound to the ogive-cylinder data while  $K=0.375$  forms an upper bound. Data scatter is due partly to the sensitivity of the data to the angular difference,  $\psi - \delta_f$ . A one degree change

in this difference amounts to a peripheral dimension of 0.074 inches which is less than the gage spacing.

When the fin is rolled off the windward centerline the peak moves closer to the fin. The data trend is however too small to be accurately evaluated from the available data. For practical applications it is the same as for the fin located on the windward centerline.

A comparison of the ogive-cylinder data and fin-flat plate data<sup>(4)</sup> is shown in Figure 5.10 and indicates that a reasonable correlation is obtained using Token's value of  $K=0.24$ .

#### 5.5 Effects of Fin Sweep and Bluntness on Peak Heating

The preponderance of data taken and presented in this report is for unswept fins. It was earlier observed that fin sweep is only a minor influence on the peak heating for fin-flat plate geometries<sup>(5)</sup>. Such modifications to the peak heating were adequately accounted for by the expression

$$\frac{H_{\text{swept}}}{H_{\text{unswept}}} = \cos^{0.24} \Lambda \quad (\text{Eq. 5.5.1})$$

where  $\Lambda$  = leading edge sweep angle

Sufficient data were taken during the present test program to verify this conclusion. Data were taken for fins with a ten degree wedge half angle and having sweep angles of  $0^\circ$ ,  $45^\circ$  and  $60^\circ$ . Dimensions of the fins were given in Table 2.1.

Figure 5.11 indicates the peak heating data for each fin and for several model roll positions. All the data were taken at zero angle of attack. A least squares curve fit through the data average values indicates the correlation expression

$$\frac{H_{\text{swept}}}{H_{\text{unswept}}} = \cos^{0.281} \Lambda \quad (\text{Eq. 5.5.2})$$

This relationship is quite close to Eq. 5.5.1 and emphasizes the fact that sweep effects offer a minimum perturbation to the basic phenomena observed in unswept sharp fin data.

There were no data taken during this test program on blunted fins. A limited amount of data on fin blunting have been taken during the lower Mach number tests of Token<sup>(7)</sup> and earlier during fin-flat plate tests at Mach 6<sup>(5)</sup>. In both of these test programs there were measurable effects of L.E. bluntness on the induced heating. In Token's data it was observed that relatively large heating increases occur due to bluntness at low values of  $\Delta x/\delta$  and that most of the heating increase could not be accounted for by the corresponding pressure rise due to bluntness. This is shown in Figure 5.12 by the shaded area. The usual pressure correlation has been used to transform Token's sharp fin heating correlation into a blunt fin correlation by multiplying it by the blunt to sharp peak pressure ratios to the 0.8 power. This blunt fin correlation still falls well below the blunt fin data. Cross plotting all of Token's blunt fin data in Figure 5.13 indicates that heating increases due to bluntness are more pronounced near the fin leading edge ( $\Delta x/\delta \rightarrow 0$ ) and at the lower fin deflection angles. Similar, but less detailed, results are observed in the Mach 6.05 data<sup>(5)</sup> as noted in Figure 5.14. In this figure it is observed that increasing the fin deflection angle from  $7.5^\circ$  to  $15^\circ$  reduces the influence of L.E. bluntness on the induced heating.

The heating is higher in the immediate L.E. region of the fin because bluntness creates vorticity in the L.E. region as shown in Figure 5.15. This vorticity is swept downstream along the fin. This is contrasted to the sharp fin case where a finite distance downstream of the fin leading edge is required to initiate and sustain vortical motion. Downstream of this point the effect of bluntness is nominal.

It is also clear in Figure 5.13 that the effects of bluntness are strongly dependent on fin deflection angle. For a blunt fin at zero deflection the fin bluntness effects dominate the interaction. For the more practical cases, having even a moderate cross flow due to model pitch and roll attitude will increase the effective fin deflection angle and reduce the effects of bluntness to nominal values. The degree of cross flow attainable was shown in Figure 4.39.

#### 5.6 Heating to Surface of Fins

The effect of the shock wave/boundary layer interaction on aerodynamic heating to the fin surface was investigated by selecting two fins for instrumentation and testing. An  $18^\circ$  wedge unswept fin and a  $20^\circ$  wedge  $60^\circ$  swept fin were instrumented as shown in Figure 5.16 and 5.17. Heat transfer distributions were measured along the span of each fin and were compared to laminar and turbulent theory for flat plate flow. An example of the data for the unswept fin at a  $90^\circ$  roll position is presented in Figure 5.18 and is shown to agree well with the Van Driest II turbulent theory.

The Van Driest II calculations were performed by first obtaining free stream properties as a function of Z from the NSWC program. An

oblique shock calculation was made at each value of  $Z$  using NSWC local flow angularity, fin wedge angle, and the NSWC local Mach number. The flow properties behind the oblique shock were then used in the Van Driest II calculations.

Similar calculations were made for the local flow properties on the  $60^\circ$  swept fin. The Van Driest II turbulent theory and Eckert's laminar theory were calculated and compared to the data as shown in Figure 5.19. Heating rates close to the missile body agree well with turbulent theory. As the initial running length decreases with span the heating rates appear to approach laminar values, although a laminar distribution was never obtained. The measured heating on the fin is at least contained between laminar and turbulent theory with no interaction induced peaks as observed on the missile body.

20° WEDGE, 0° SWEEP FIN, ROLL = 0°

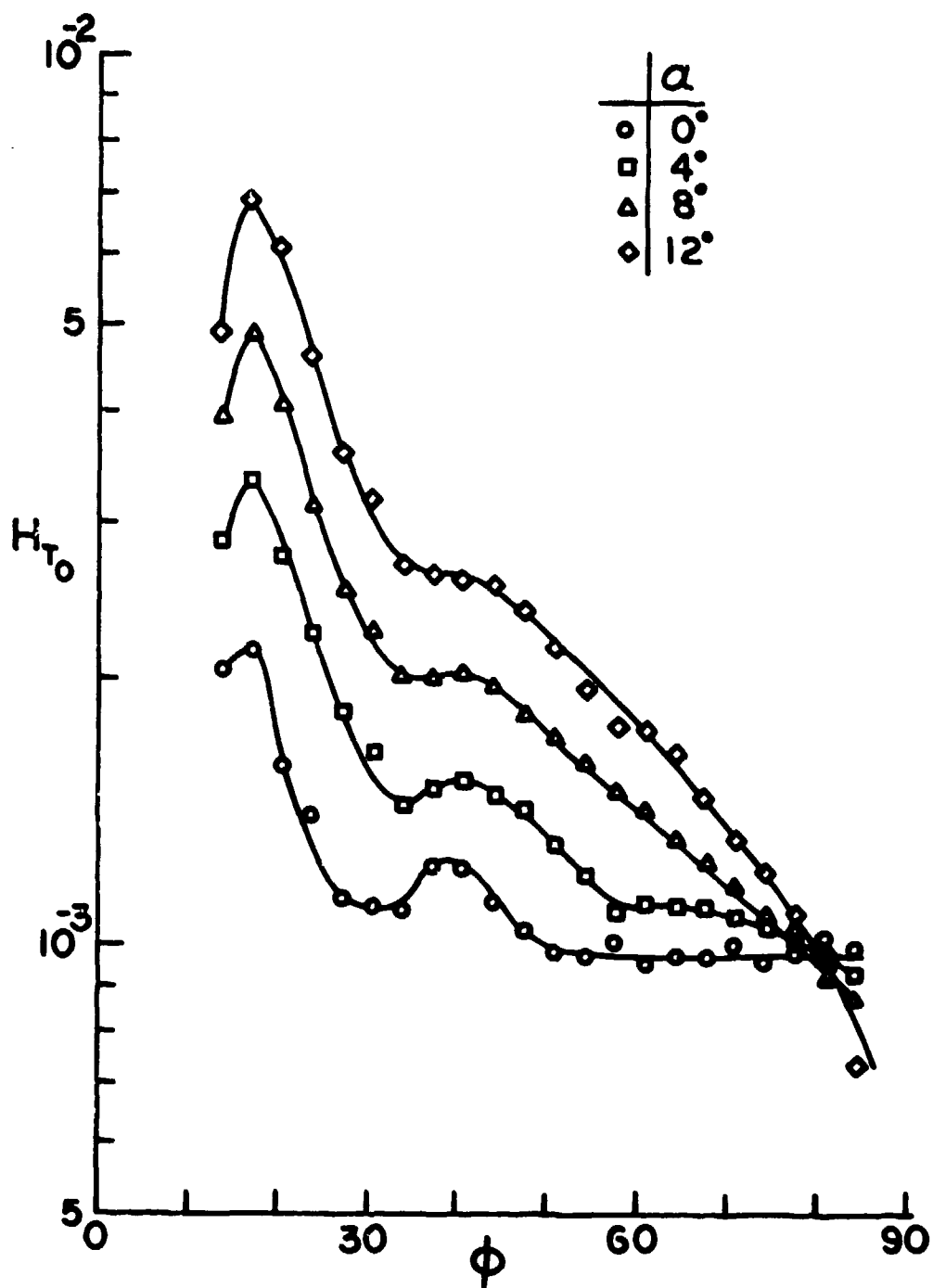


FIGURE 5.1 HEAT TRANSFER DISTRIBUTIONS

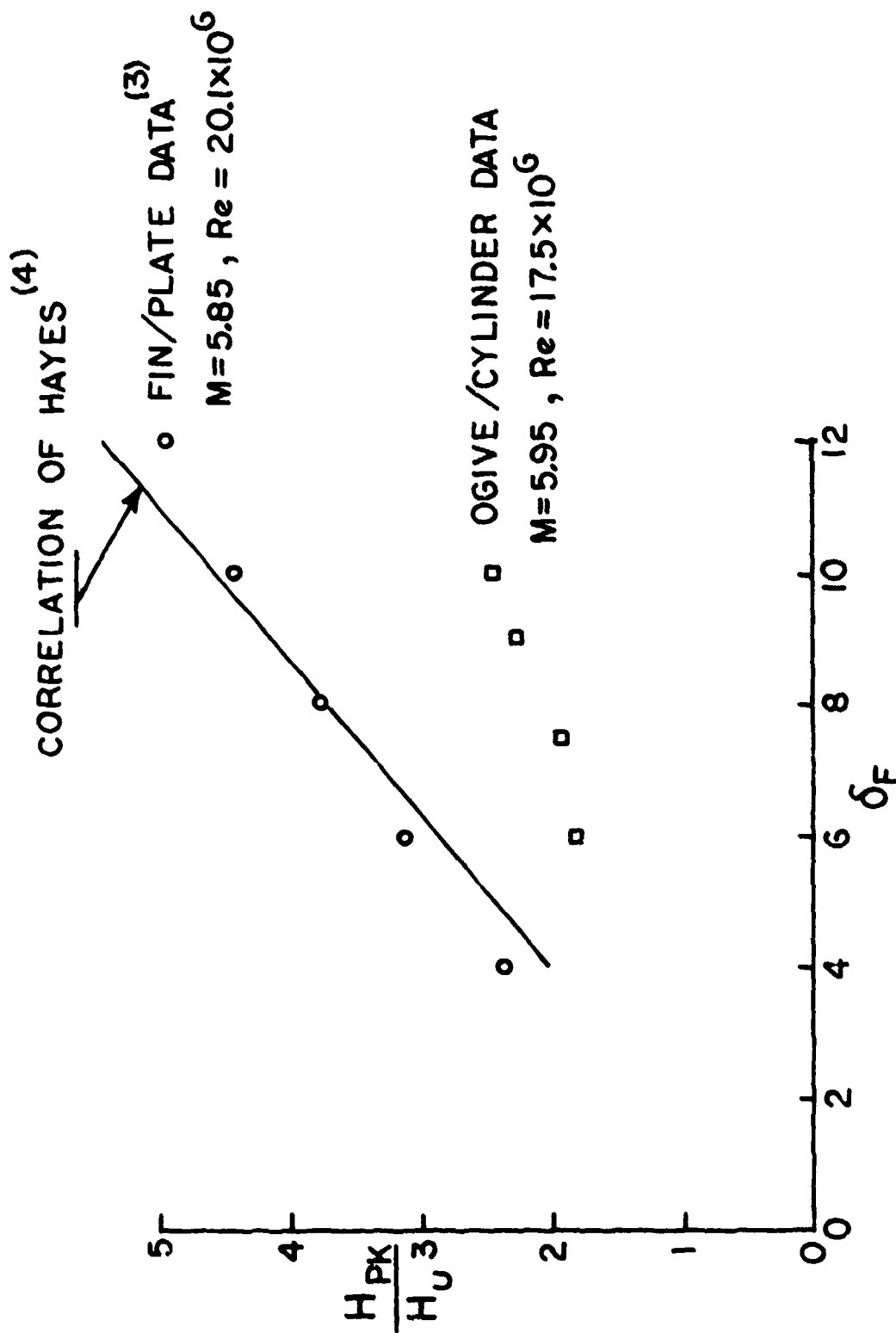


FIGURE 5.2 FIN/PLATE CORRELATION AND OGIVE/CYLINDER DATA

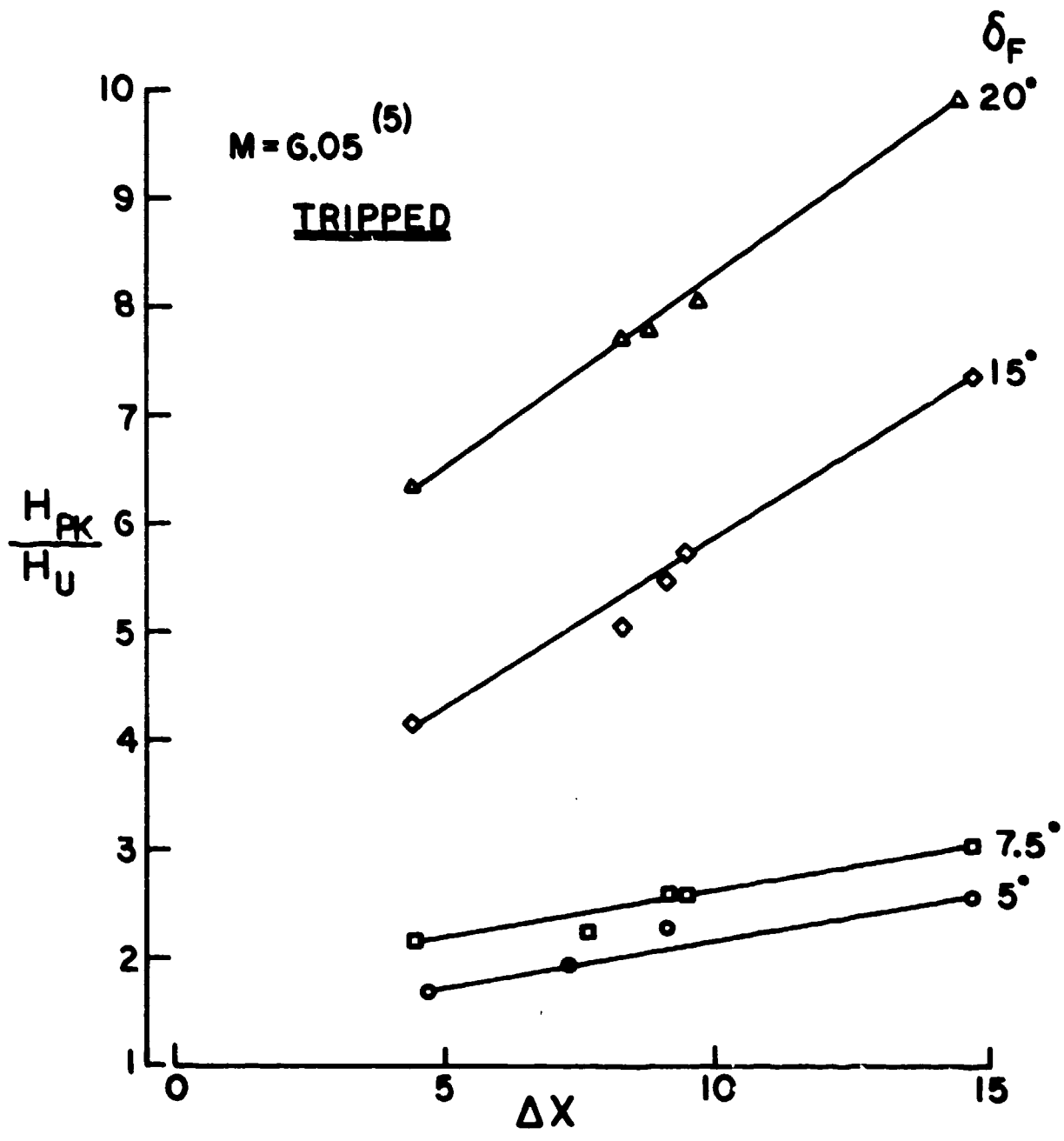


FIGURE 5.3 TRIPPED FIN/PLATE PEAK HEATING



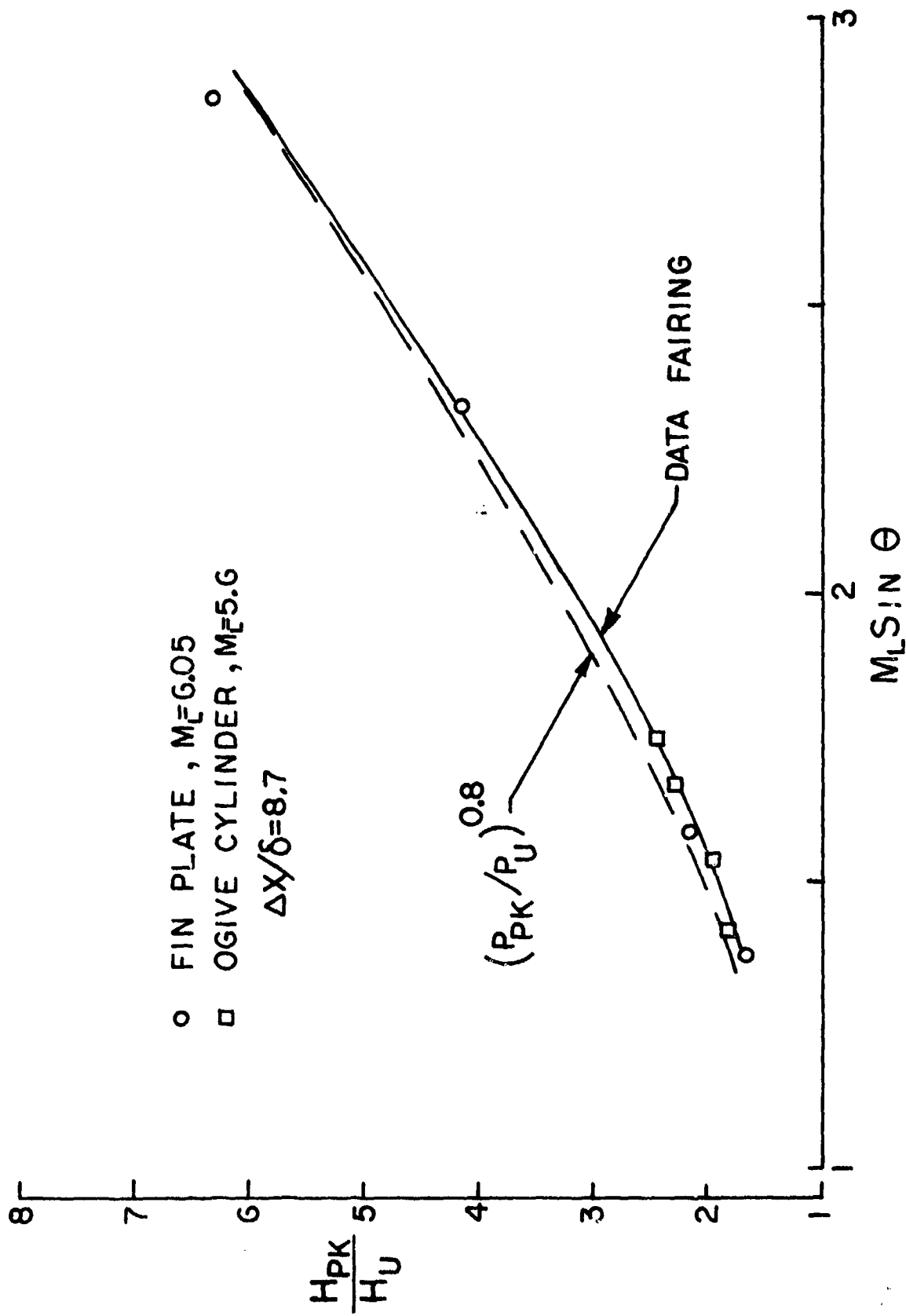


FIGURE 5.4 OGIVE/CYLINDER PEAK HEATING CORRELATION AT  $\alpha = 0^\circ$

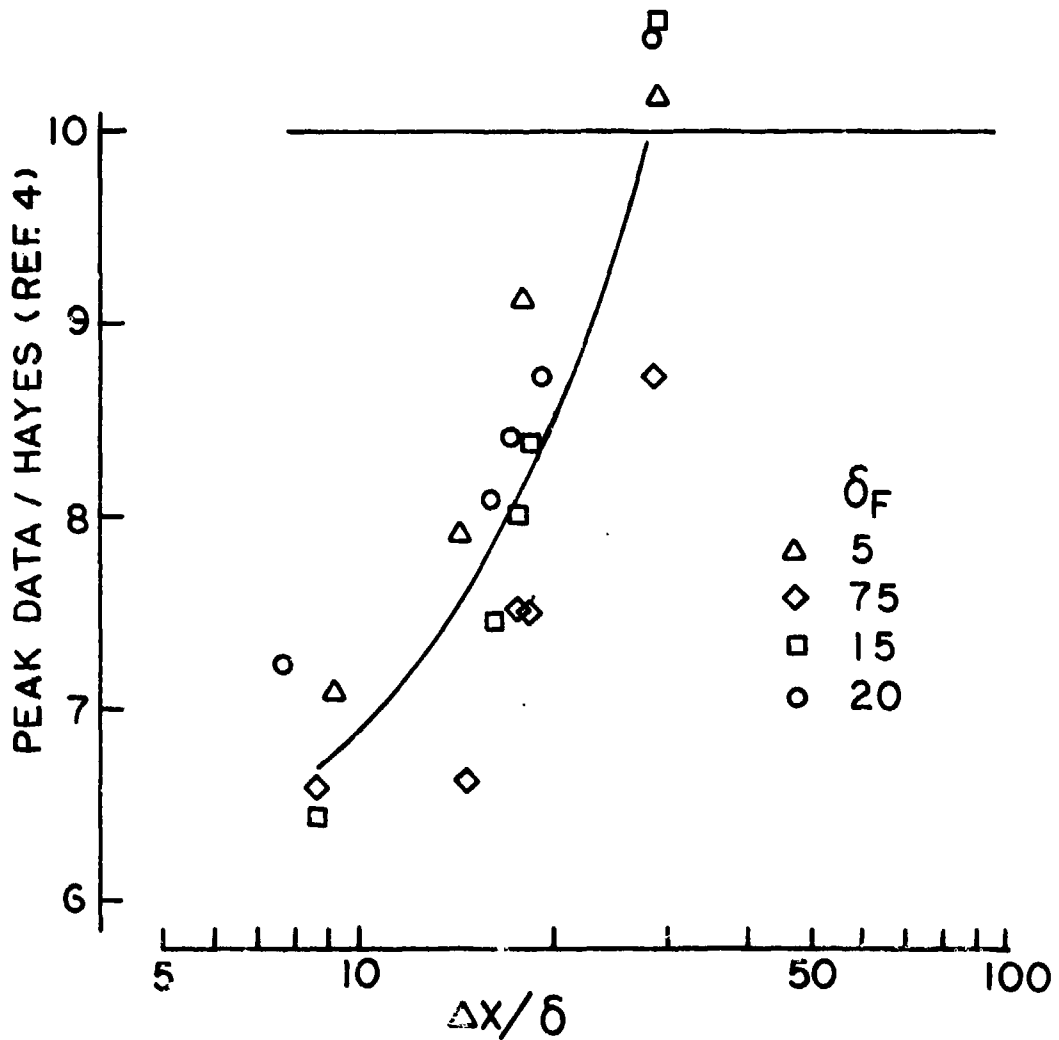
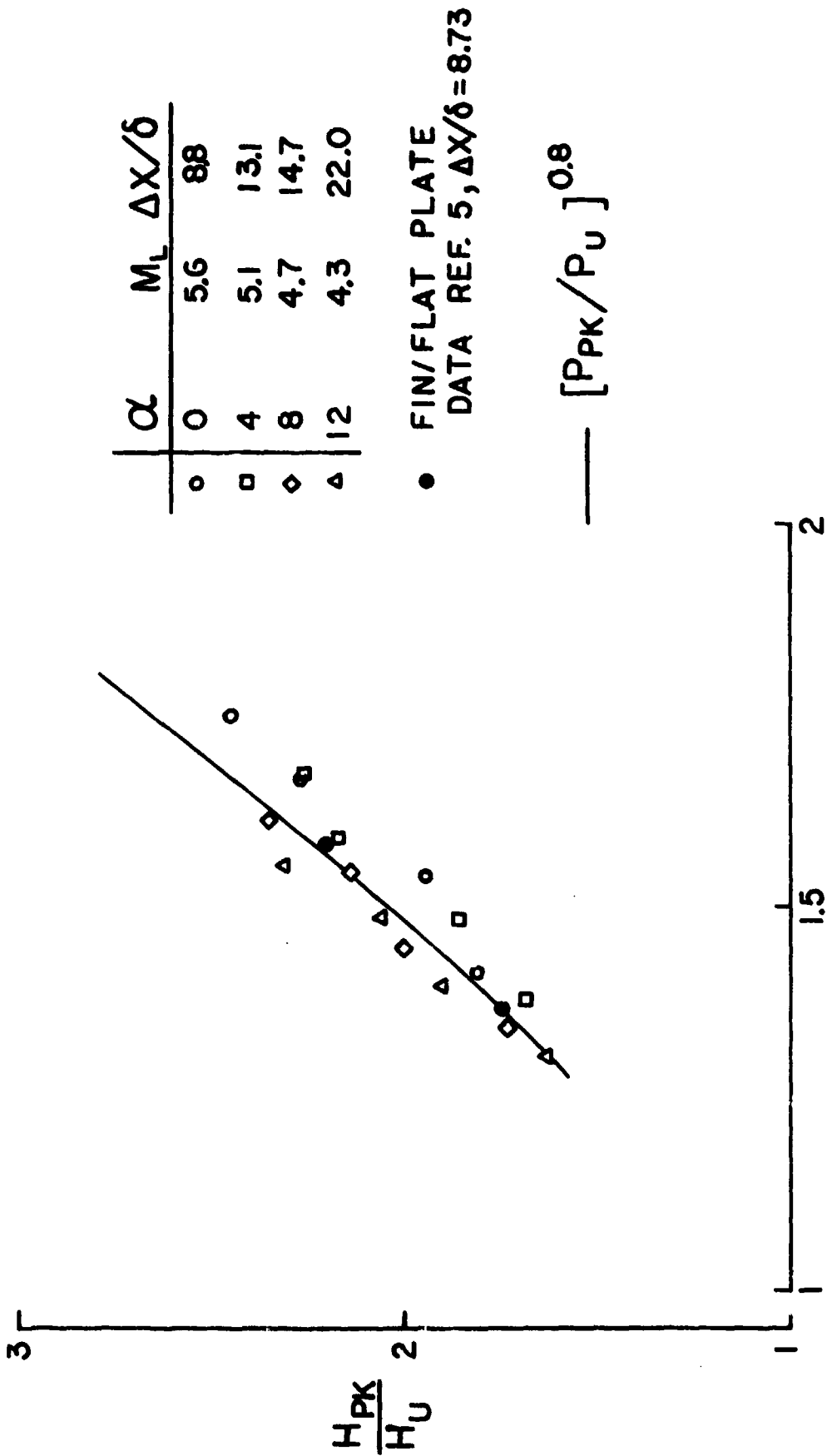


FIGURE 5.5 COMPARISON OF TRIPPED TO UNTRIPPED FIN/PLATE DATA



$M_L \sin \theta$

FIGURE 5.6 OGIVE/CYLINDER PEAK HEATING AT ANGLE OF ATTACK, ROLL=0°

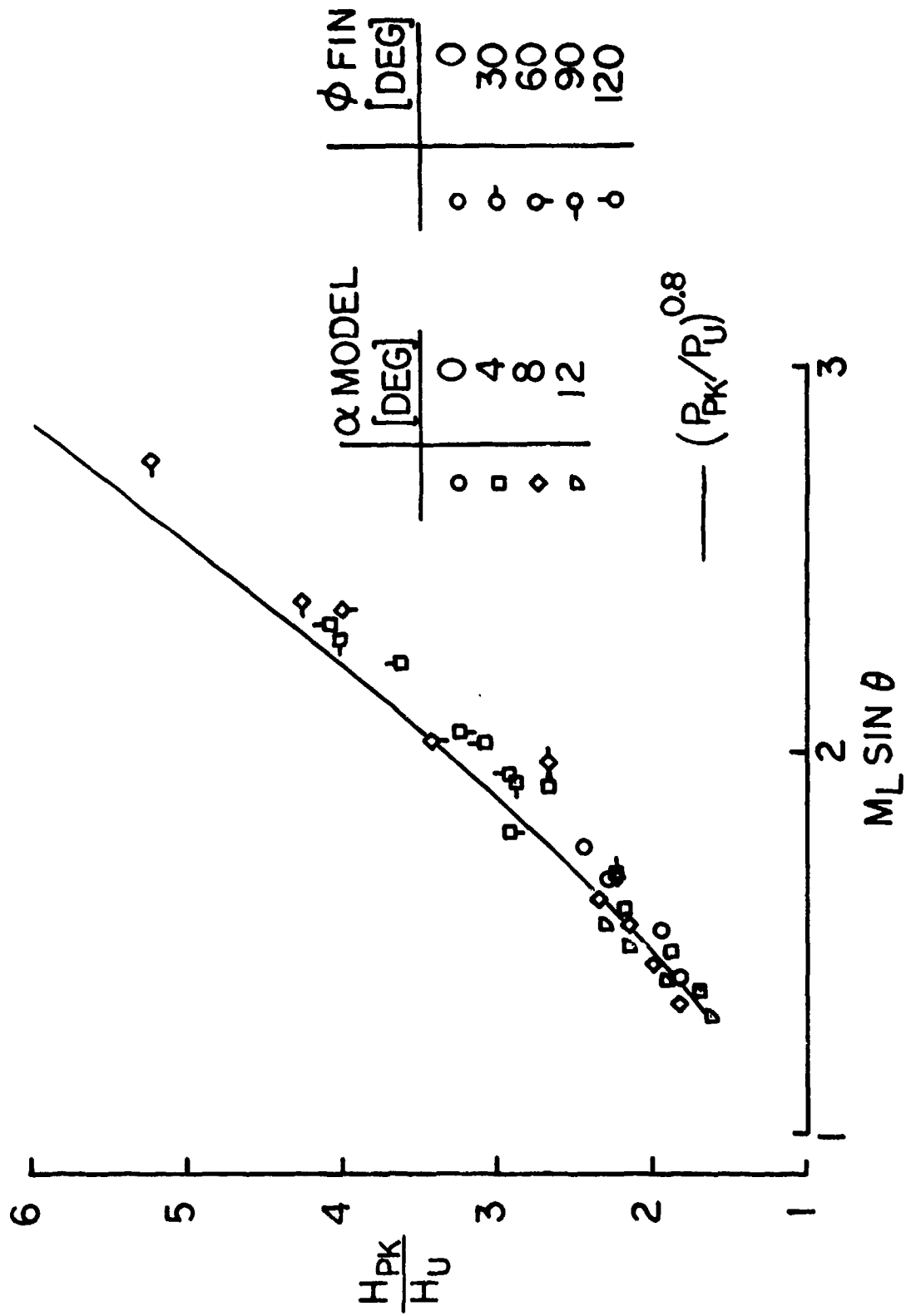


FIGURE 5.7 PEAK HEATING CORRELATION AT ANGLE OF ATTACK & ROLL

SYMBOLS : SEE FIGURE 5.7

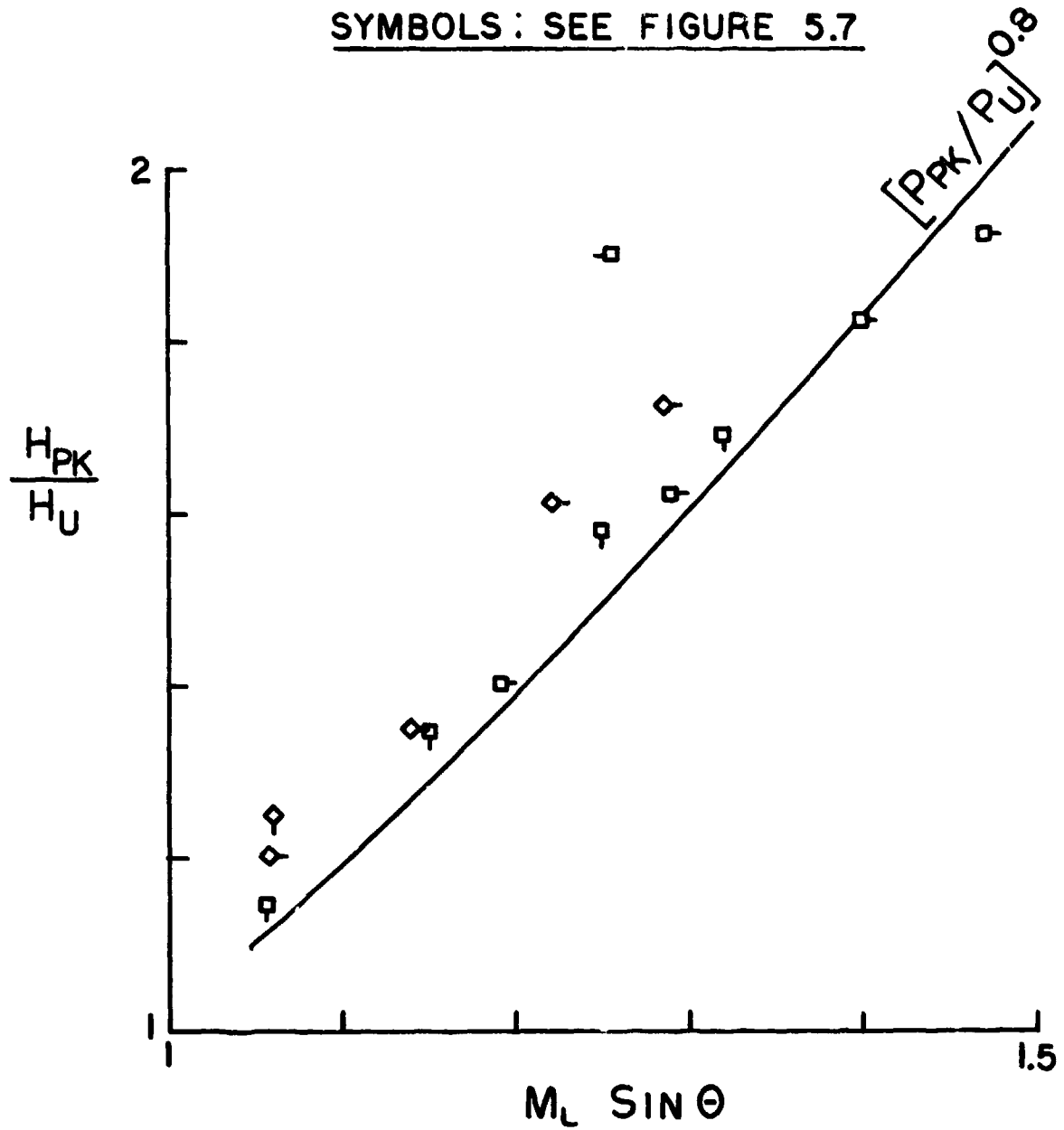


FIGURE 5.8 PEAK HEATING CORRELATION FOR THE LEE SIDE OF THE FIN

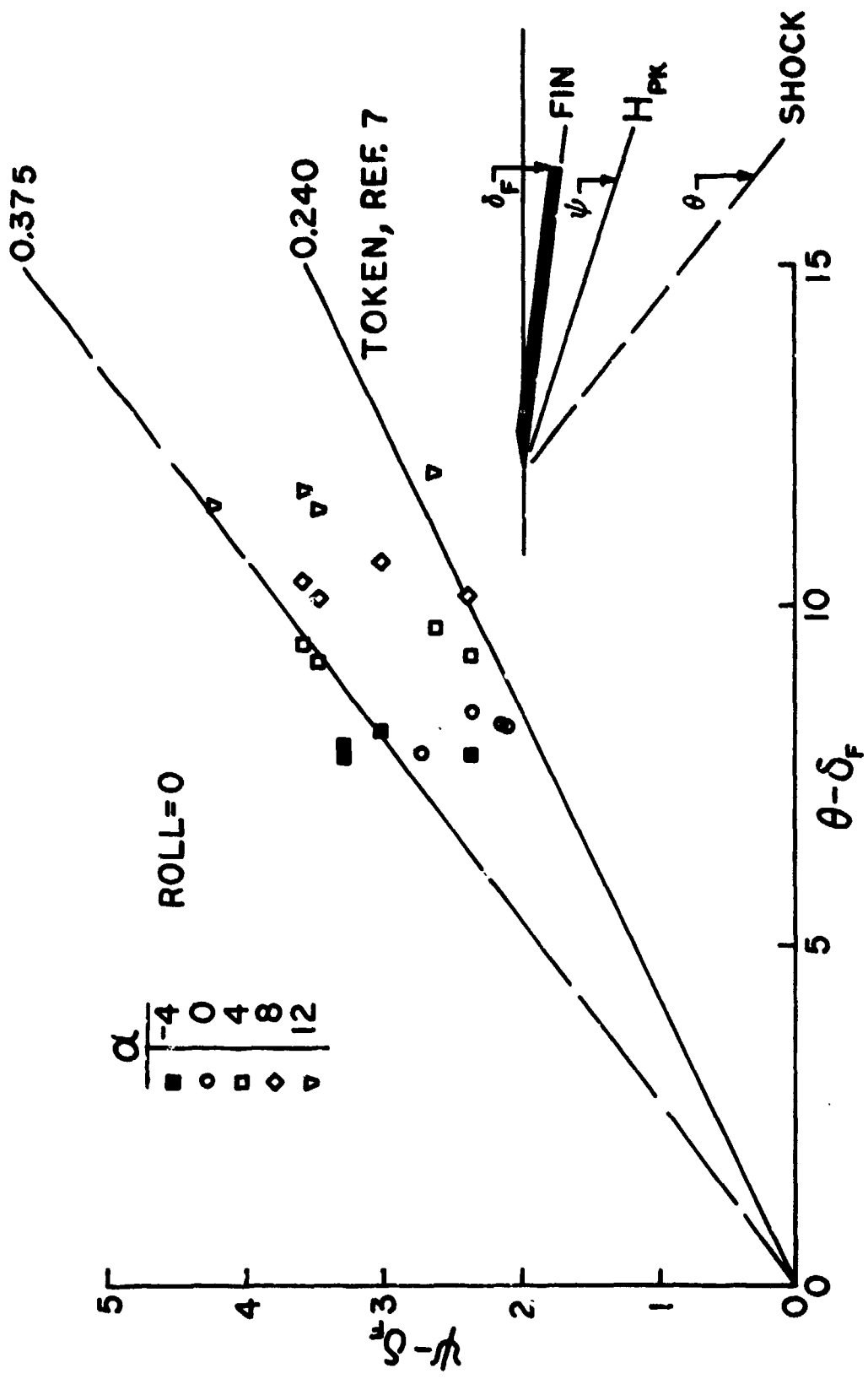


FIGURE 5.9 PEAK HEATING LOCATION AND TOKEN'S PREDICTION

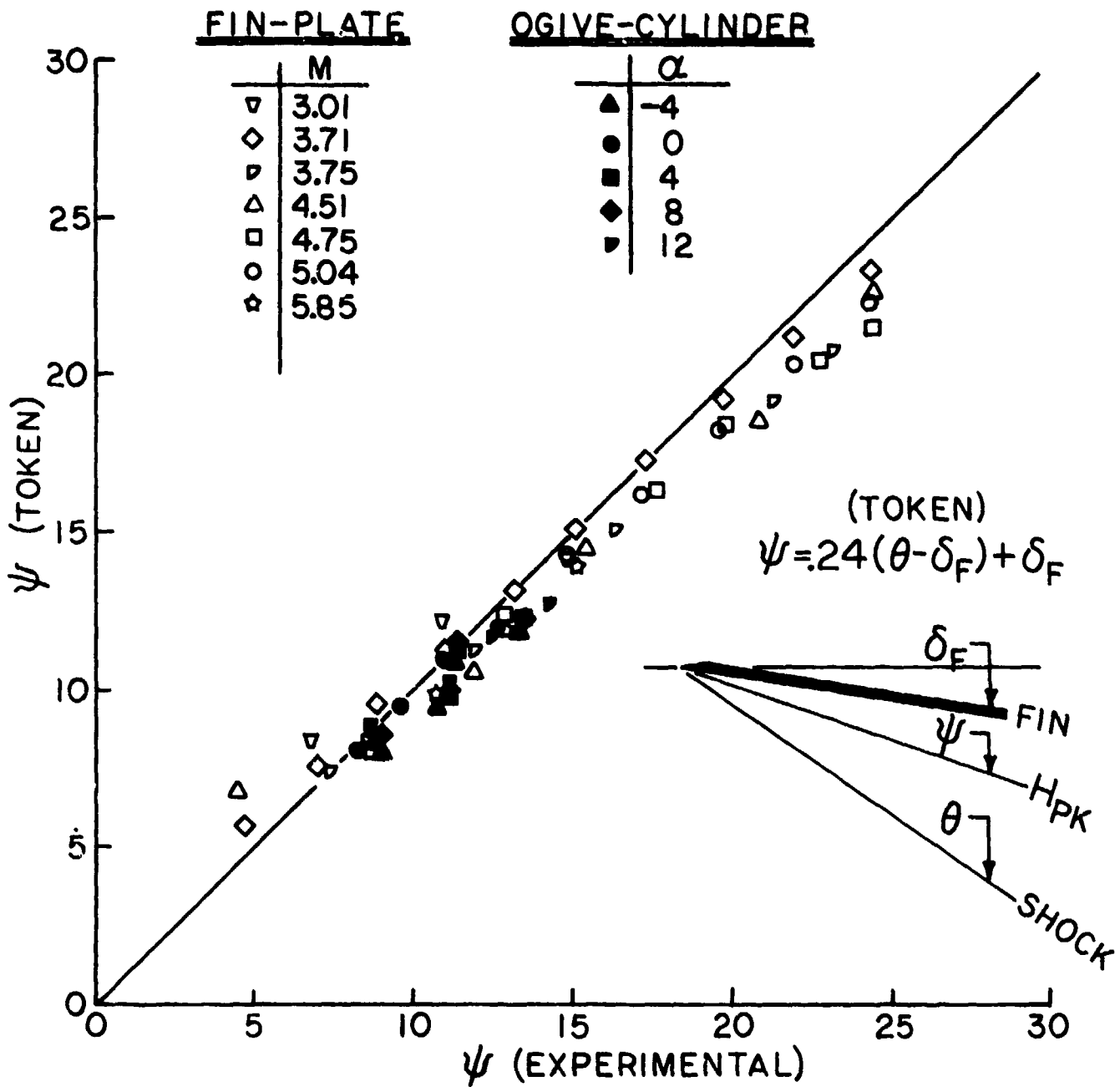


FIGURE 5.10 COMPARISON OF FIN/PLATE AND OGIVE/CYLINDER PEAK HEATING LOCATIONS

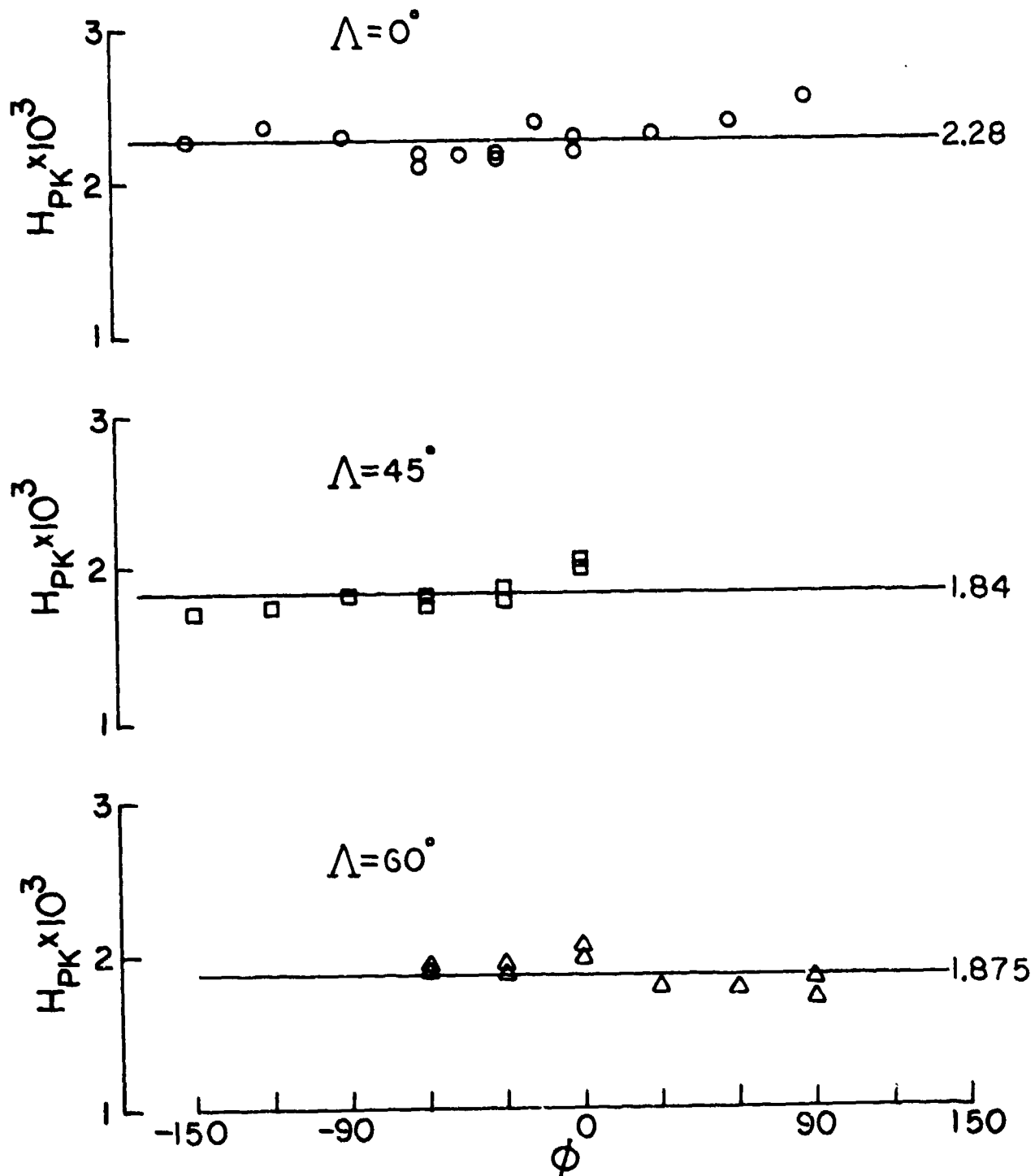


FIGURE 5.11 SWEEPED FIN PEAK HEATING AT ZERO ANGLE OF ATTACK



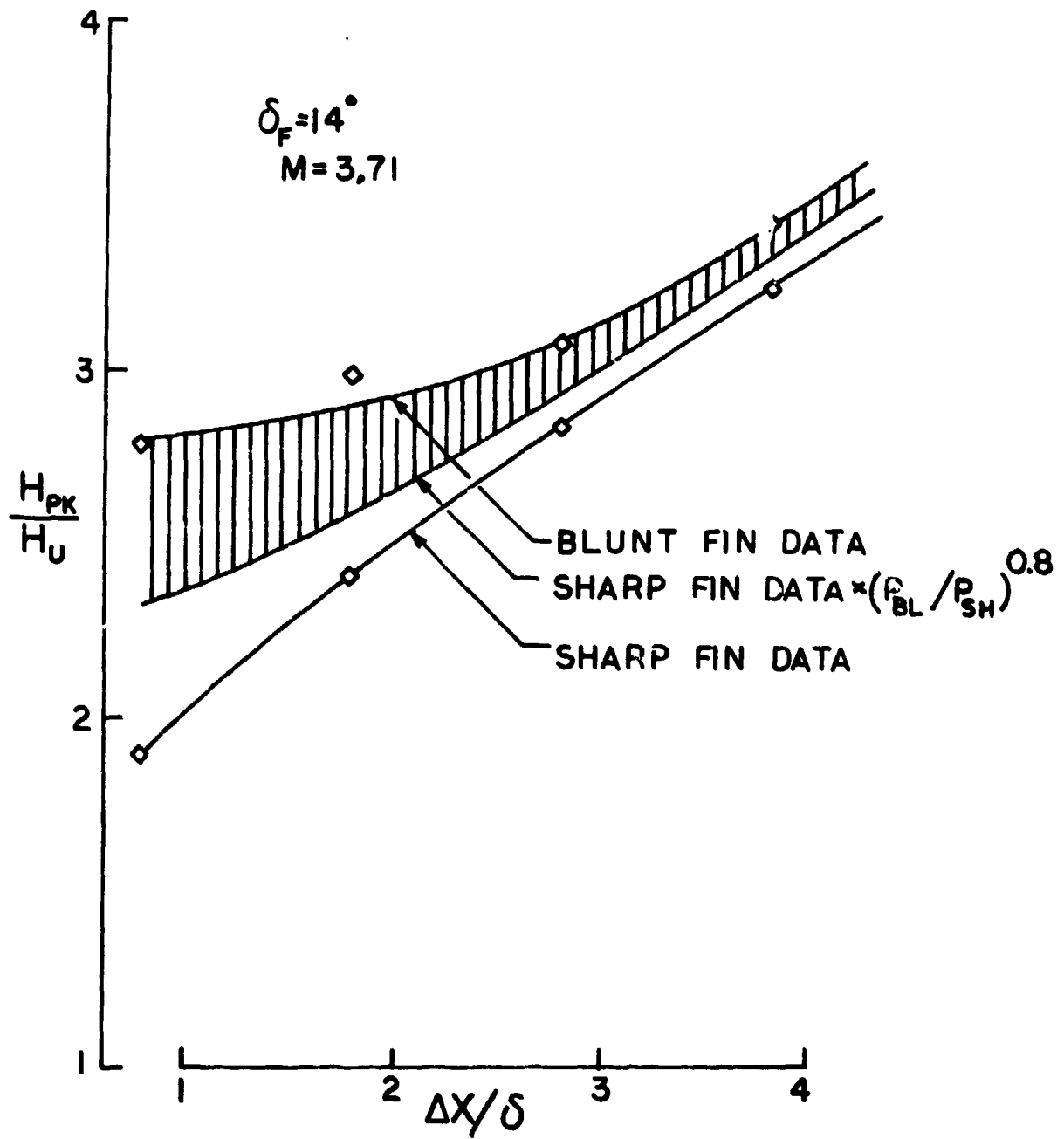


FIGURE 5.12 BLUNT AND SHARP FIN PEAK HEATING COMPARISON

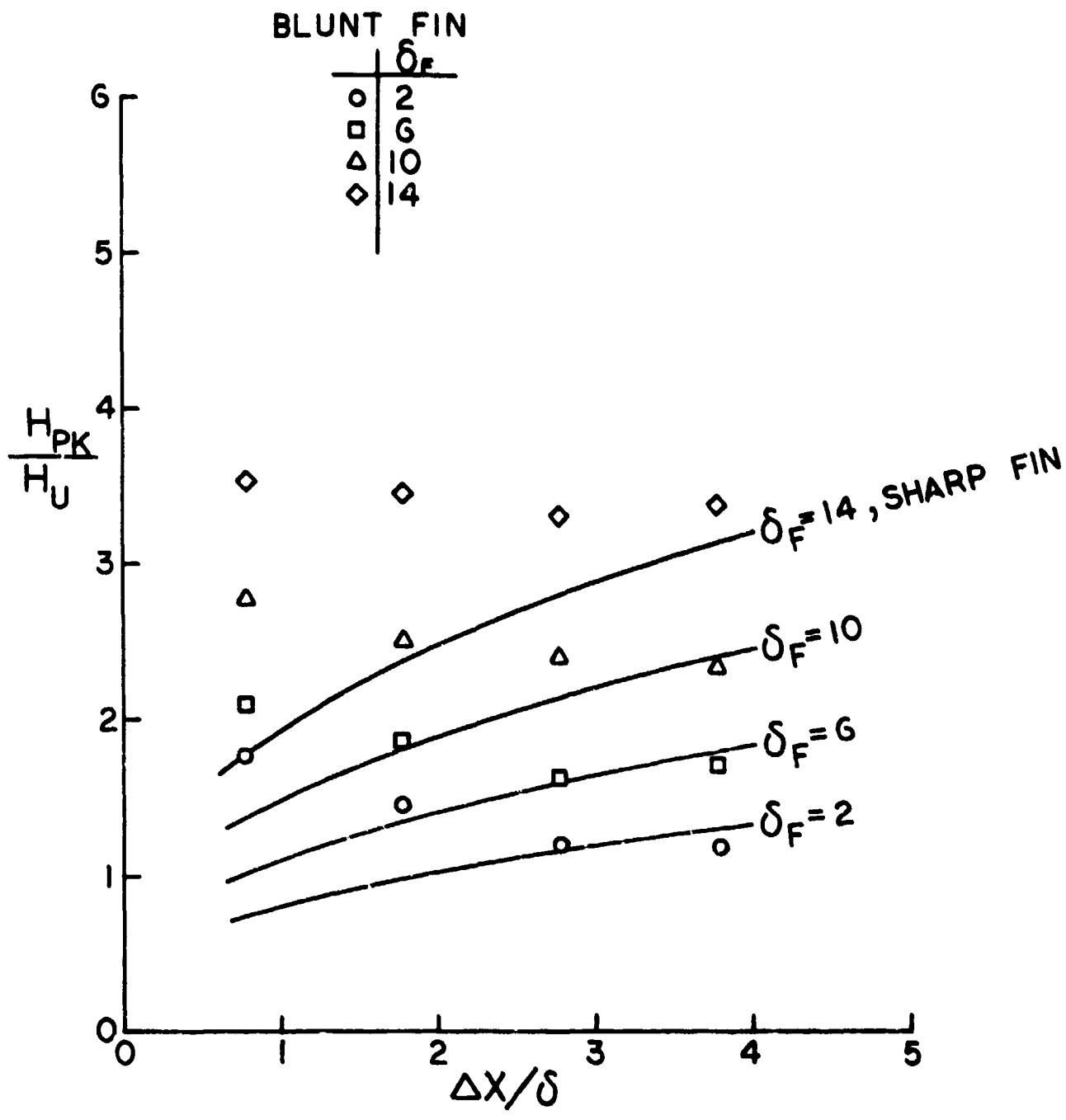


FIGURE 5.13 EFFECTS OF FIN LEADING EDGE BLUNTNESS ON PEAK HEATING AT MACH 3.71

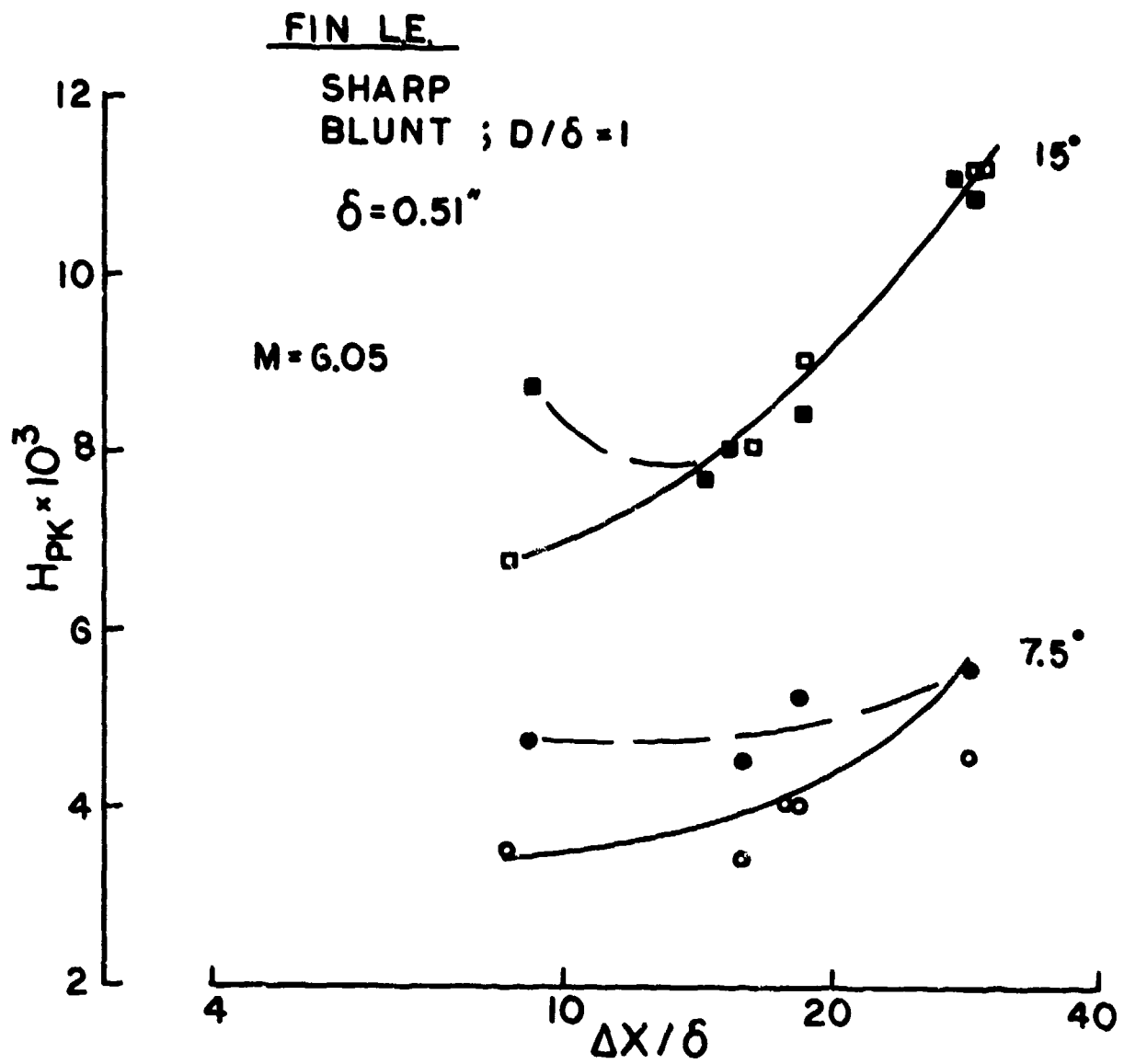
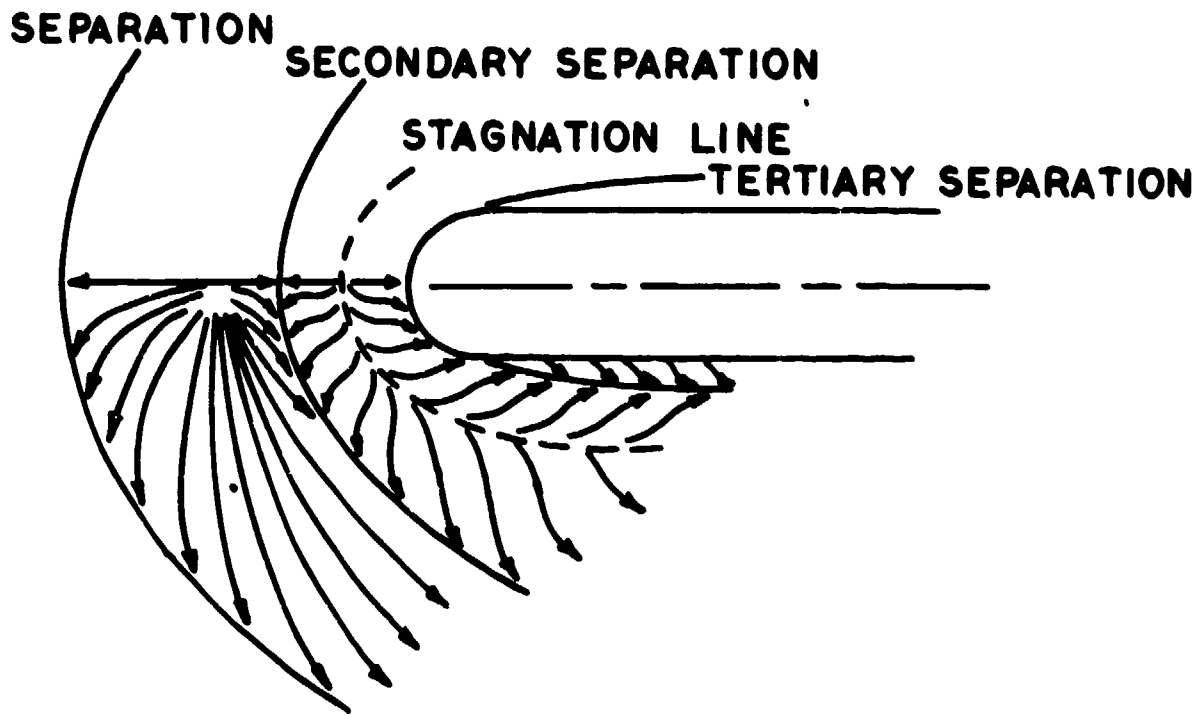


FIGURE 5.14 FIN BLUNTNESS EFFECTS AT MACH 6



REF. AGARD CP 71-71

**FIGURE 5.15 VORTICAL FLOW FIELD AT A BLUNT FIN LEADING EDGE**

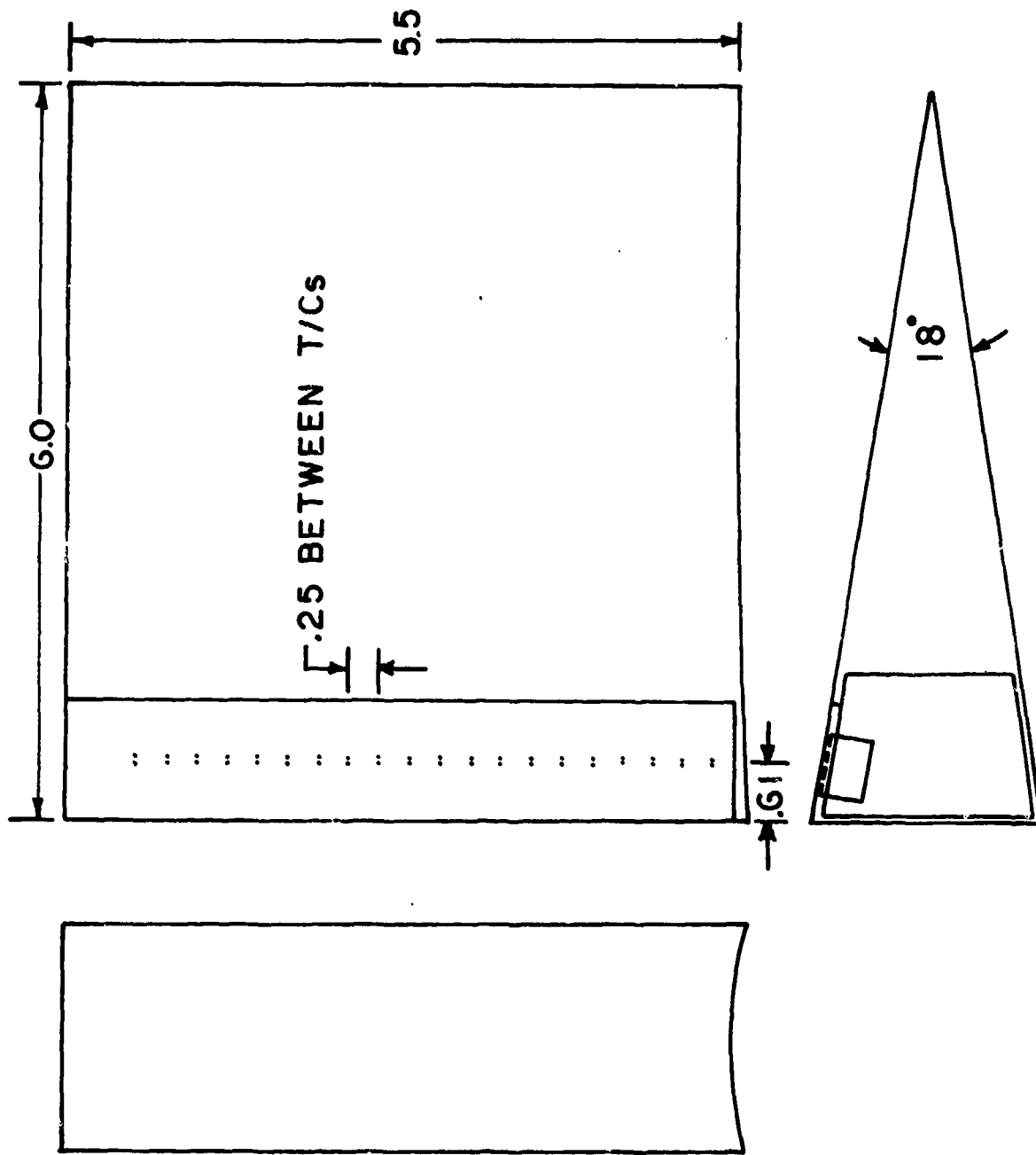


FIGURE 5.16 INSTRUMENTED FIN, ZERO SWEEP

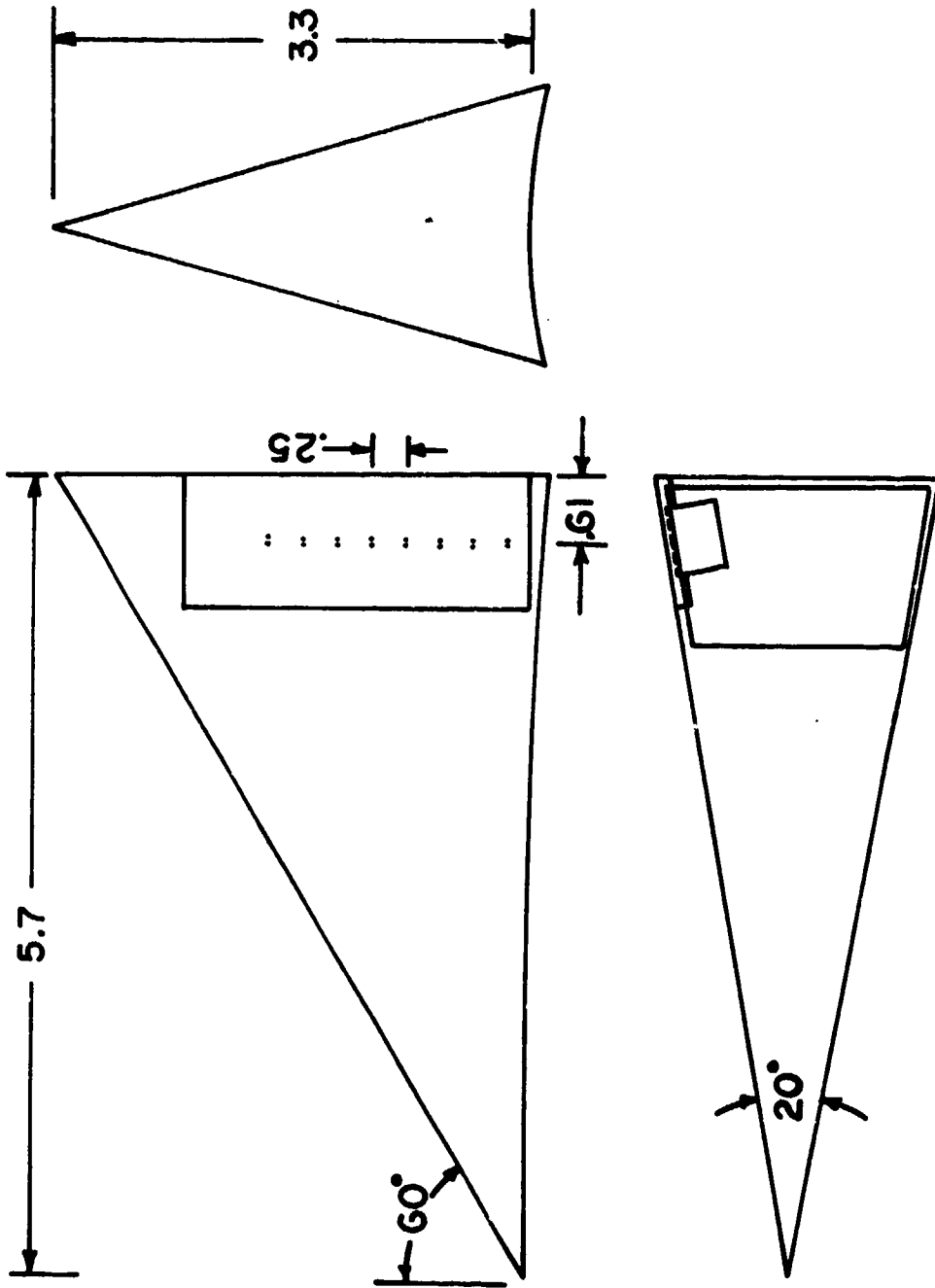


FIGURE 5.17 INSTRUMENTED FIN , 60° SWEEP

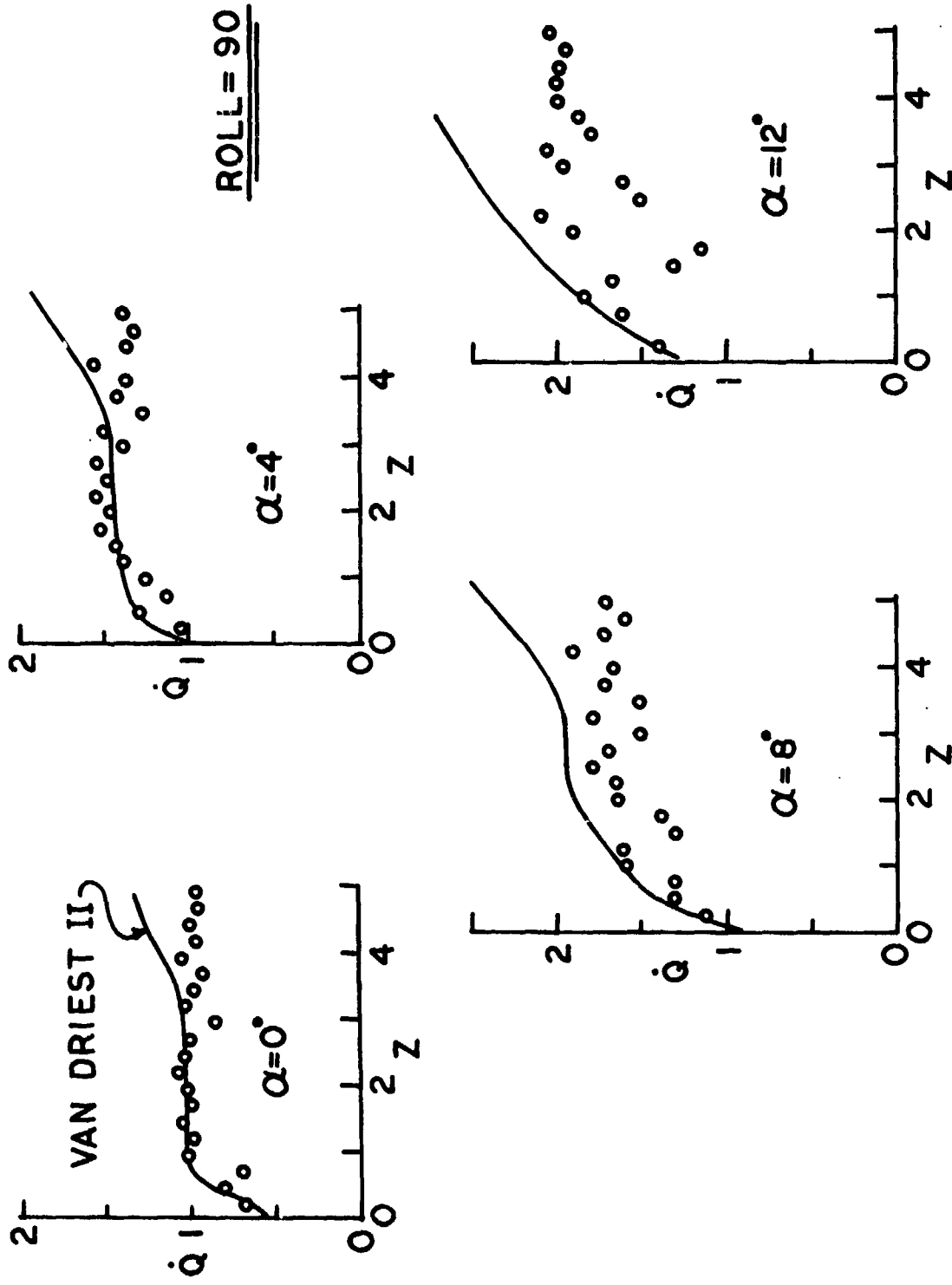


FIGURE 5.18 FIN SURFACE HEATING,  $0^\circ$  SWEEP FIN

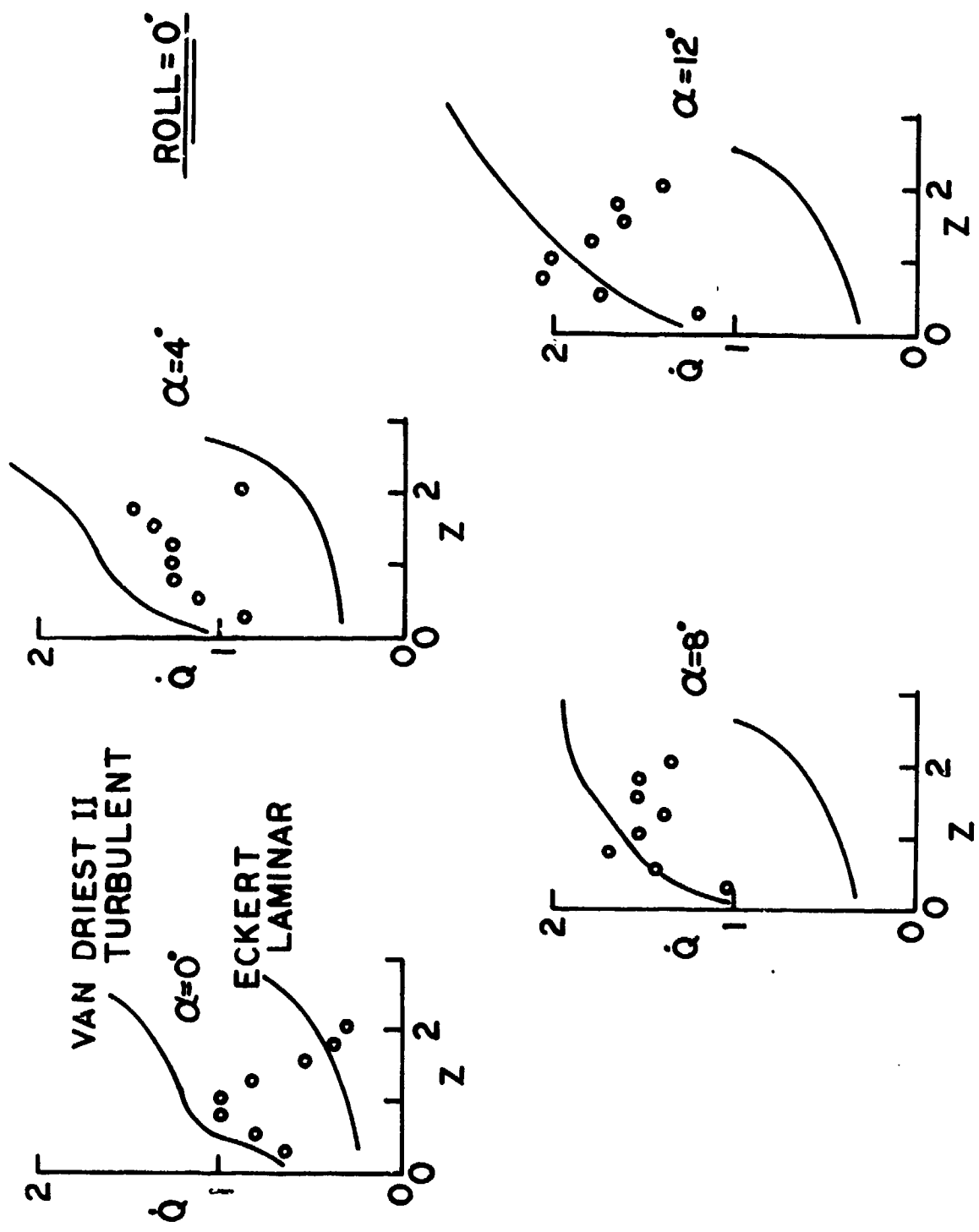


FIGURE 5.19 FIN SURFACE HEATING , 60° SWEEP FIN



## 6.0 FIN/TORQUE TUBE INTERACTION

A  $15^\circ$  wedge  $60^\circ$  swept fin was mounted on a 0.625 inch diameter torque tube to study the effect of fin/body gaps on the peak interaction heating observed in the sealed fin tests. The general configuration of the fin/torque tube model is shown in Figure 6.1. A new thin skin thermocouple insert containing 85 thermocouples was installed upstream of the torque tube to measure the interaction heating under the fin. Details of this new insert are shown in Figure 6.2. The length of the torque tube was varied to provide fin/body gaps from 0.0 to 0.5 inches in 0.1 inch increments. At each gap height the model was pitched  $0^\circ$ ,  $4^\circ$ ,  $8^\circ$  and  $12^\circ$  and rolled so that the fin was  $0^\circ$ ,  $30^\circ$ ,  $60^\circ$  and  $90^\circ$  off the windward centerline. Heat transfer distributions were measured downstream of the torque tube in a circumferential direction (as was done for the sealed fins) and upstream of the torque tube in the axial direction. Oil flow photographs were also taken at selected attitudes and a few examples will be shown to define the major characteristics of the surface flow.

In Figures 6.3 through 6.5 the model is at  $8^\circ$  angle of attack and the fin is on the windward centerline. Figure 6.3 shows the surface flow for a gap of 0.1 inches. The boundary layer thickness at this attitude is about 0.4 inches and the significant feature is the very weak effect of the fin even at this small gap height. In Figure 6.4 at a gap height of 0.3 inches the surface disturbance is from the torque tube only. Two oil accumulation lines are observed, one marking the primary separation and a secondary line marking the leading edge of the vortex around the torque tube. This was defined as a Type I separation

pattern. Figure 6.5 shows the surface flow field at a gap height of 0.5 inches. The separation pattern has changed under the fin so that the primary separation line is no longer continuous but intersects the secondary separation line at the fin perimeter. This was defined as a Type II separation. The two types of separation are sketched in Figure 6.6 for clarity and their effect on the peak heating upstream of the torque tube will be noted later.

In Figure 6.7 the fin is rolled  $60^\circ$  off the windward centerline and the gap height is 0.1 inches. As the fin is rolled off centerline the effective angle of attack increases due to model angle of attack and an increase in local flow angularity. As shown in Figure 6.7 the interaction becomes a complex combination of effects from the fin and the torque tube making analysis very difficult.

#### 6.1 Heat Transfer Downstream of the Torque Tube

The heat transfer distributions downstream of the torque tube were found to be very similar to those of the sealed fins. A comparison of the gapped and sealed distributions is shown in Figure 6.8 for  $12^\circ$  pitch and  $30^\circ$  roll. A slight increase in peak heating with gap is noted but the location of the peak and the shape of the distribution remains essentially unchanged.

The ratio of peak to undisturbed heat transfer coefficients is shown in Figure 6.9 as a function of angle of attack and gap height for each of the four roll angles. The effect of gap height can be seen by comparing data points with the zero gap (sealed fin) data. Maximum heating occurs at a gap of about 0.1 inches and is, at the most, 50%

over sealed levels. Also note for later comparison to upstream peak heating levels that the range in peak heating here is 1.5 to 5.0 times the undisturbed level.

## 6.2 Heat Transfer Upstream of the Torque Tube

Selected heat transfer distributions taken on the fin centerline upstream of the torque tube are shown in Figure 6.10. The interaction was found to extend about two diameters upstream of the torque tube with the peak heating location being no more than 0.3 diameters upstream. For small gaps the Type I separation pattern is produced and the peak heating level increases with gap height. At some gap height, which varies with model attitude, a switch to the Type II separation occurs. The conditions under which this occurs could not be correlated but for the case in Figure 6.10 it occurs at a gap of 0.4 inches. The result is a decrease in peak heating. Once the Type II separation is established the peak heating level again increases with increasing gap height.

The upstream peak heating ratio is presented in Figure 6.11 as a function of gap height and angle of attack for each roll attitude. The filled symbols are for Type I separation conditions and the open symbols are for Type II separation. The reduction in heating for the latter is apparent. A significant point here is the overall range in heating levels, 4 to 17 times undisturbed levels, compared to 1.5 to 5 times undisturbed for the downstream interaction.

In Figure 6.12 the peak heating levels are compared to Nestler's<sup>(8)</sup> correlation for peak heating upstream of unswept cylinders. The data are generally bounded by Nestler's correlation except at large pitch and

roll attitudes. The local Mach number and Reynolds number for the Nestler calculations were obtained from the NSWC program.

Although no correlation of the upstream peak heating was found it was concluded that the upstream heating problem is about five times that of the downstream case and is therefore the design point for thermal protection of gapped control surfaces.

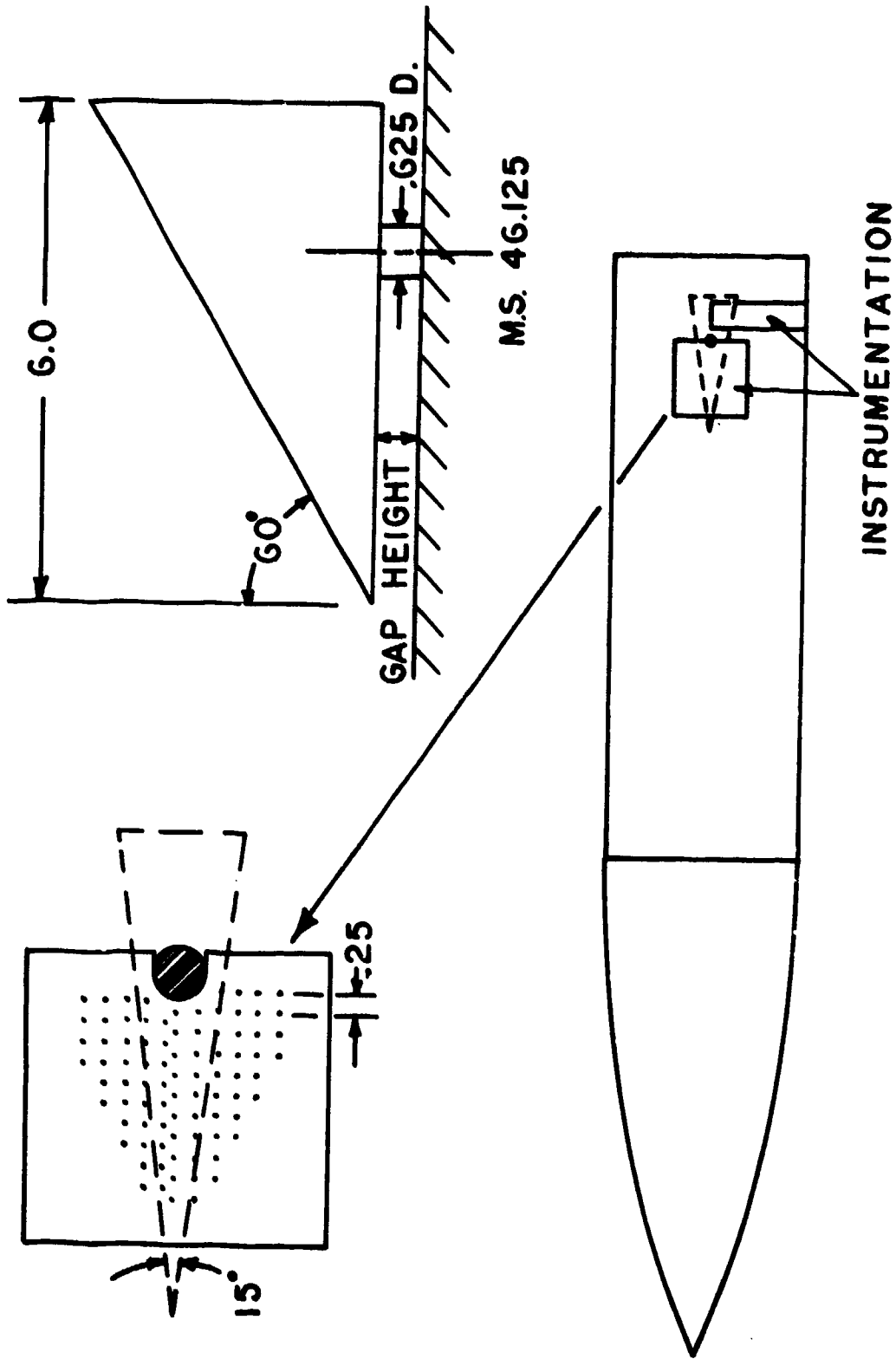


FIGURE G.I FIN-TORQUE TUBE MODEL

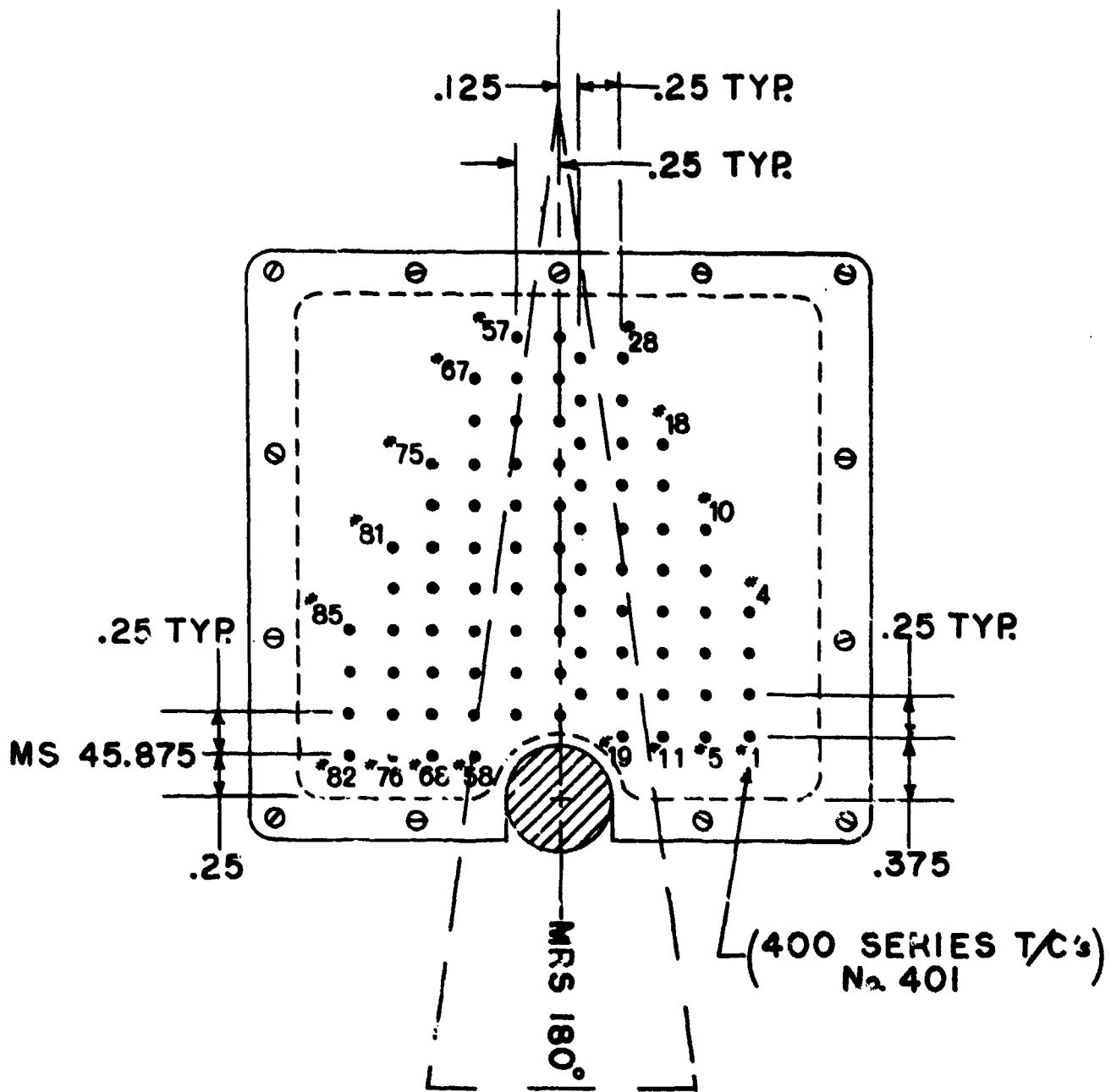


FIGURE 6.2 THERMOCOUPLE LOCATIONS FOR TORQUE TUBE FIN INSERT



FIGURE 6.3 FIN-TORQUE TUBE |;  $\alpha=8^\circ$ ,  $\phi=0^\circ$ , GAP=0.1

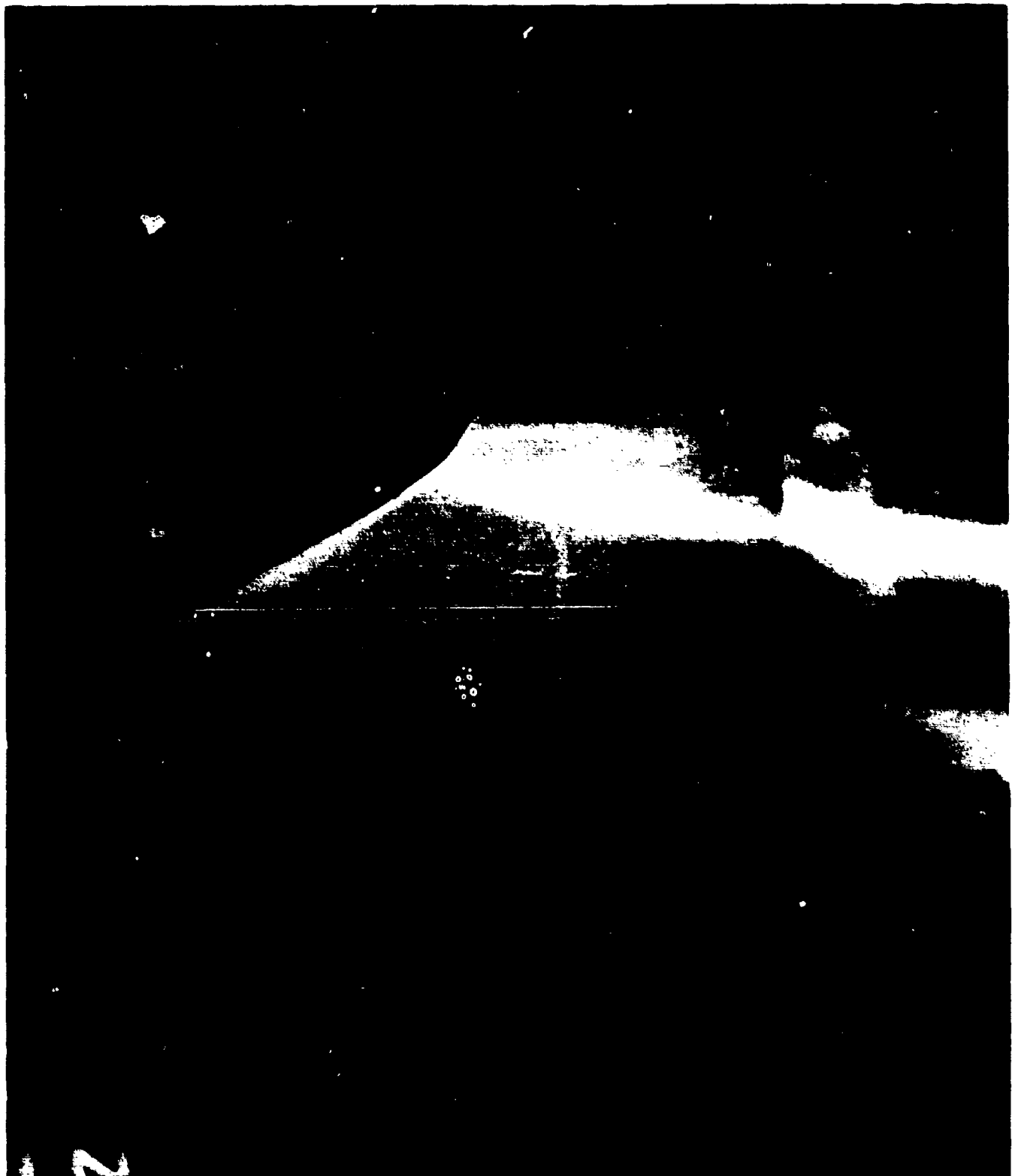


FIGURE 6.4 FIN-TORQUE TUBE ;  $\alpha=8^\circ$ ,  $\phi=0^\circ$ , GAP=0.3

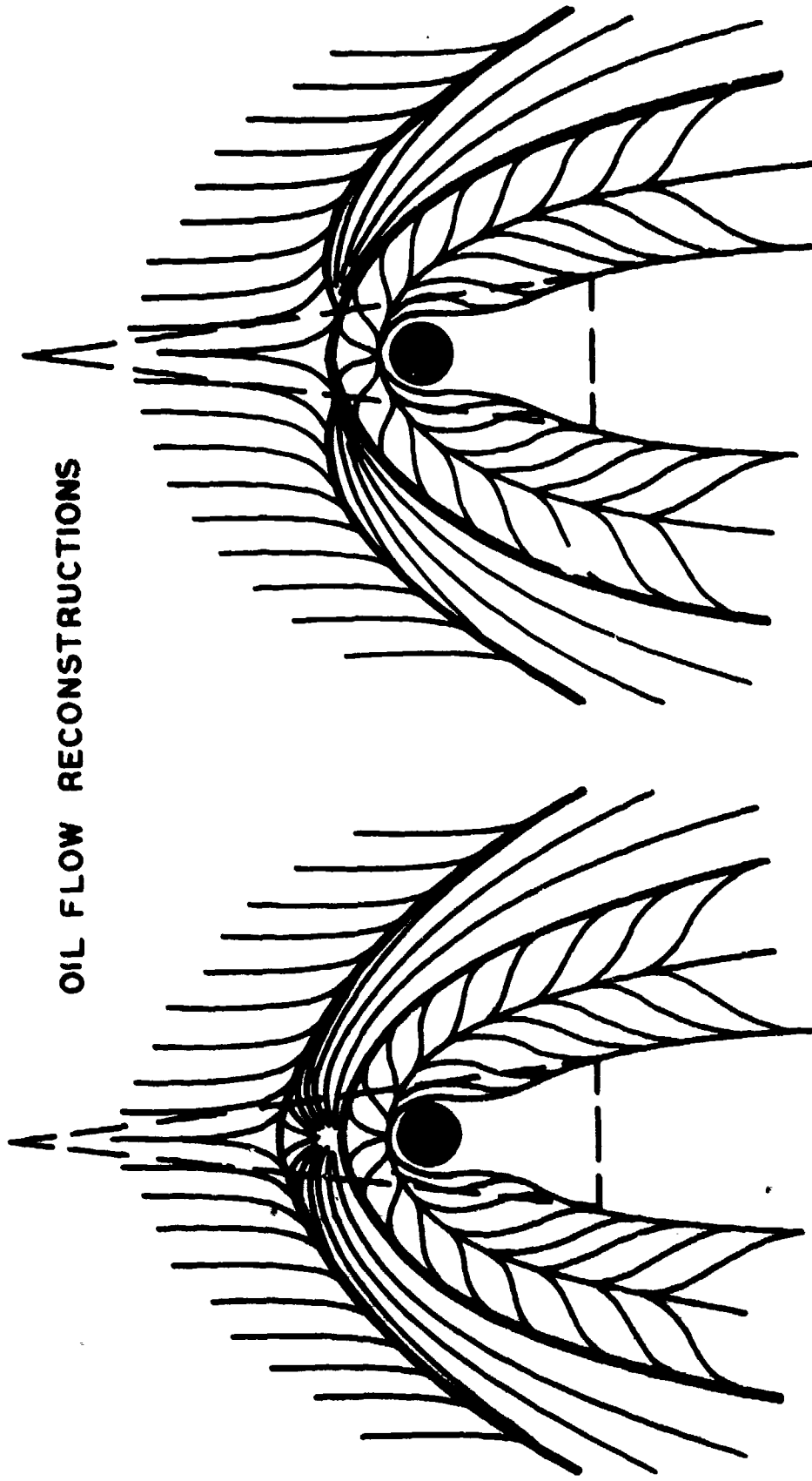




FIGURE 6.5 FIN-TORQUE TUBE ;  $\alpha=8^\circ$ ,  $\phi=0^\circ$ , GAP=0.5

**TYPE I SEPARATION**

**TYPE II SEPARATION**



**FIGURE 6.6 SEPARATION UPSTREAM OF TORQUE TUBE**

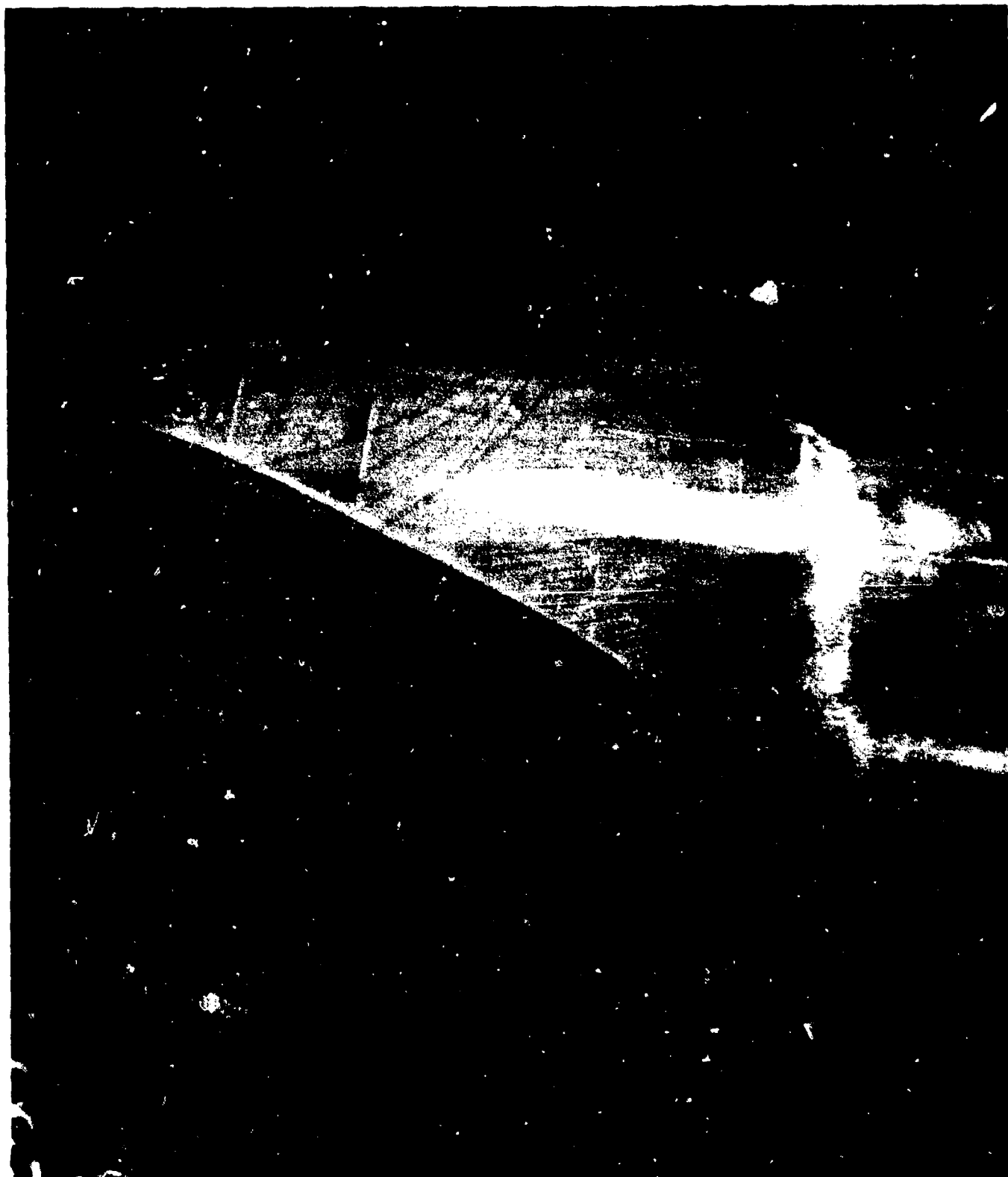


FIGURE 6.7 FIN-TORQUE TUBE ;  $\alpha=8^\circ$ ,  $\phi=60^\circ$ , GAP=0.1

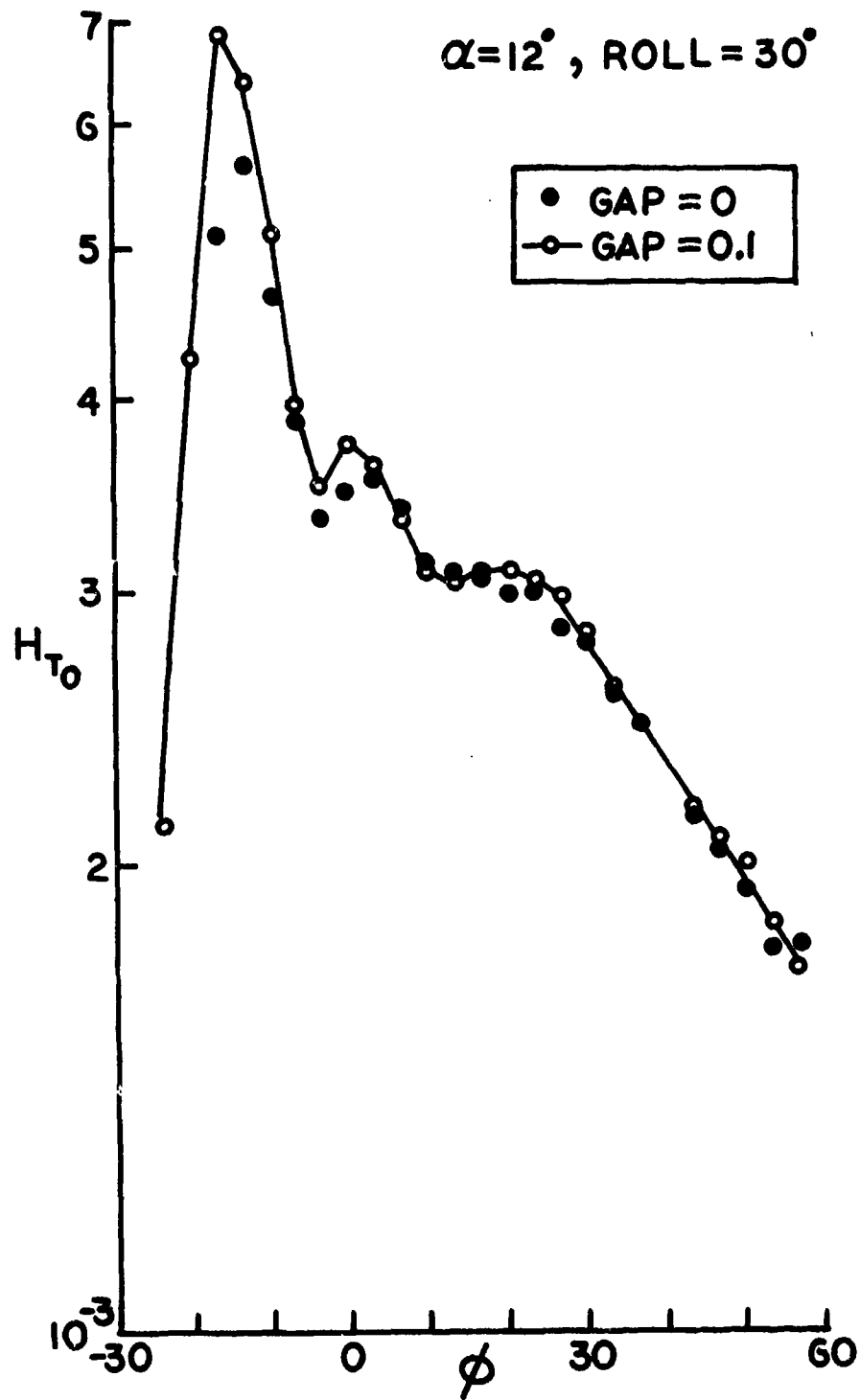


FIGURE 6.8 DOWNSTREAM HEAT TRANSFER DISTRIBUTIONS

$\alpha$	0	4	8	12
	○	□	△	◇

●— SEALED FIN CORRELATION

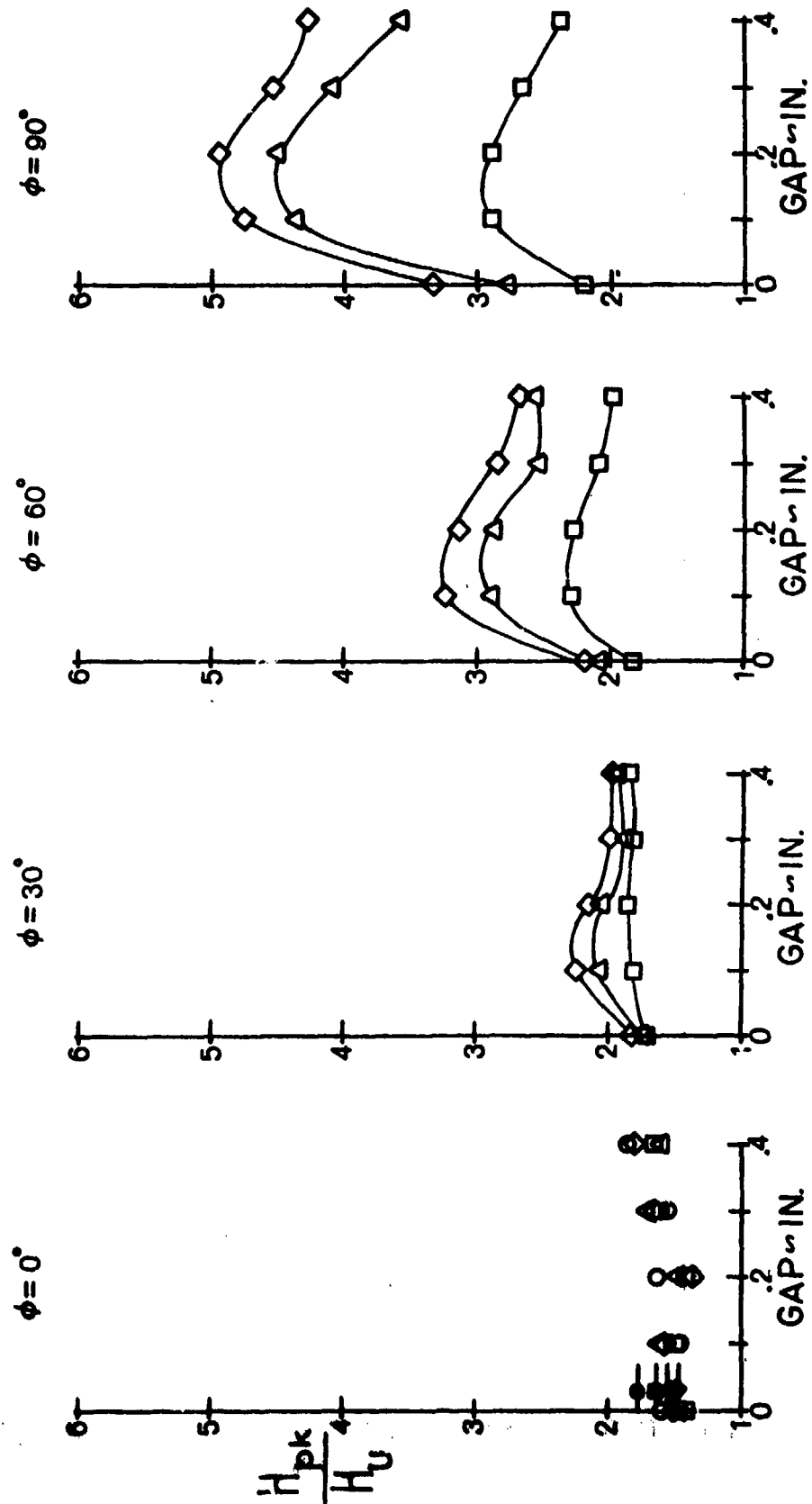
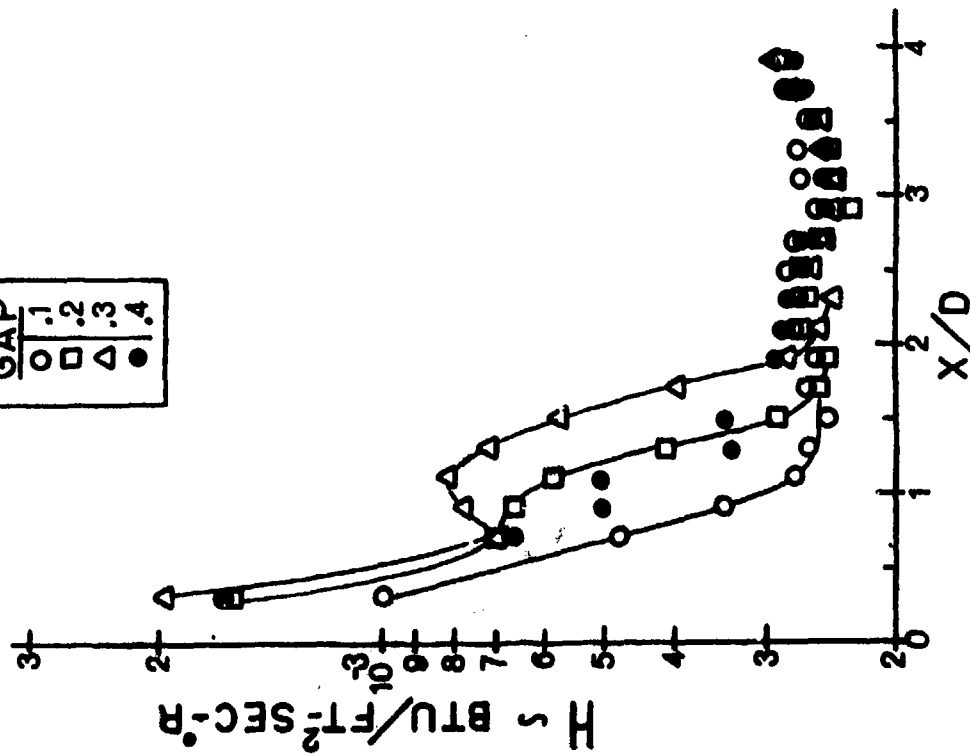


FIGURE 6.9 PEAK HEATING DOWNSTREAM OF TORQUE TUBE

$\alpha = 8^\circ, \phi = 0^\circ$

GAP	1	2	3	4
	○	□	△	●



$GAP = .3, \phi = 0^\circ$

$\alpha$	0	4	8	12
	○	□	△	◇

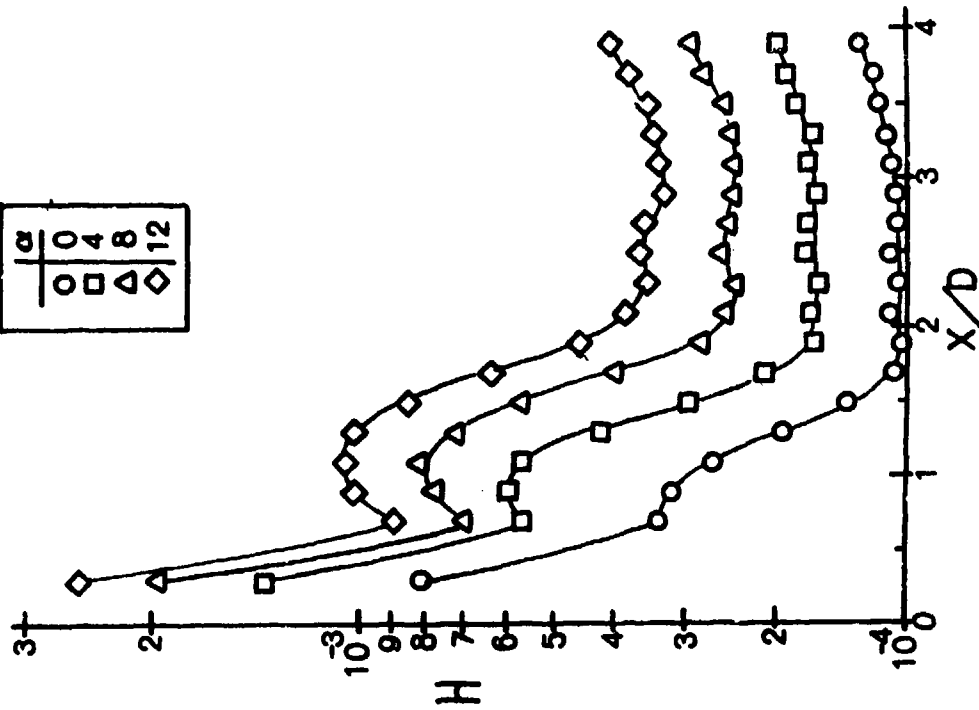


FIGURE 6.10 UPSTREAM HEAT TRANSFER DISTRIBUTIONS

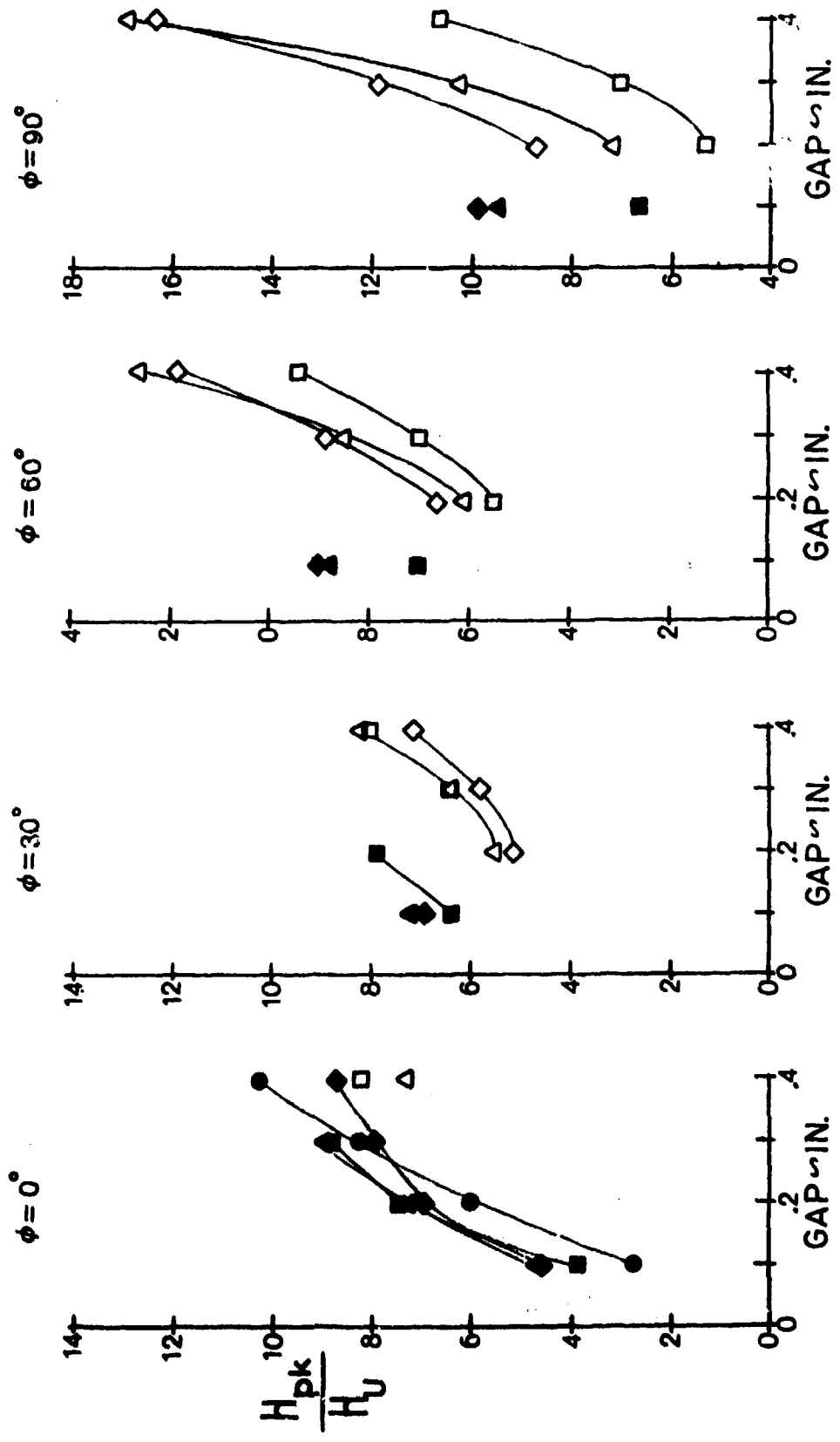
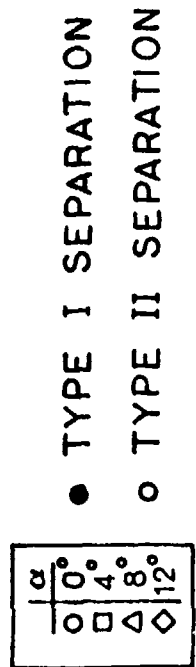


FIGURE 6.11 PEAK HEATING UPSTREAM OF TORQUE TUBE

$$\frac{H_{Nestler}}{H_U} = \frac{22 M_L}{Re_x^{.15}}$$

$\alpha$
0°
4°
8°
12°

- TYPE I SEPARATION
- TYPE II SEPARATION

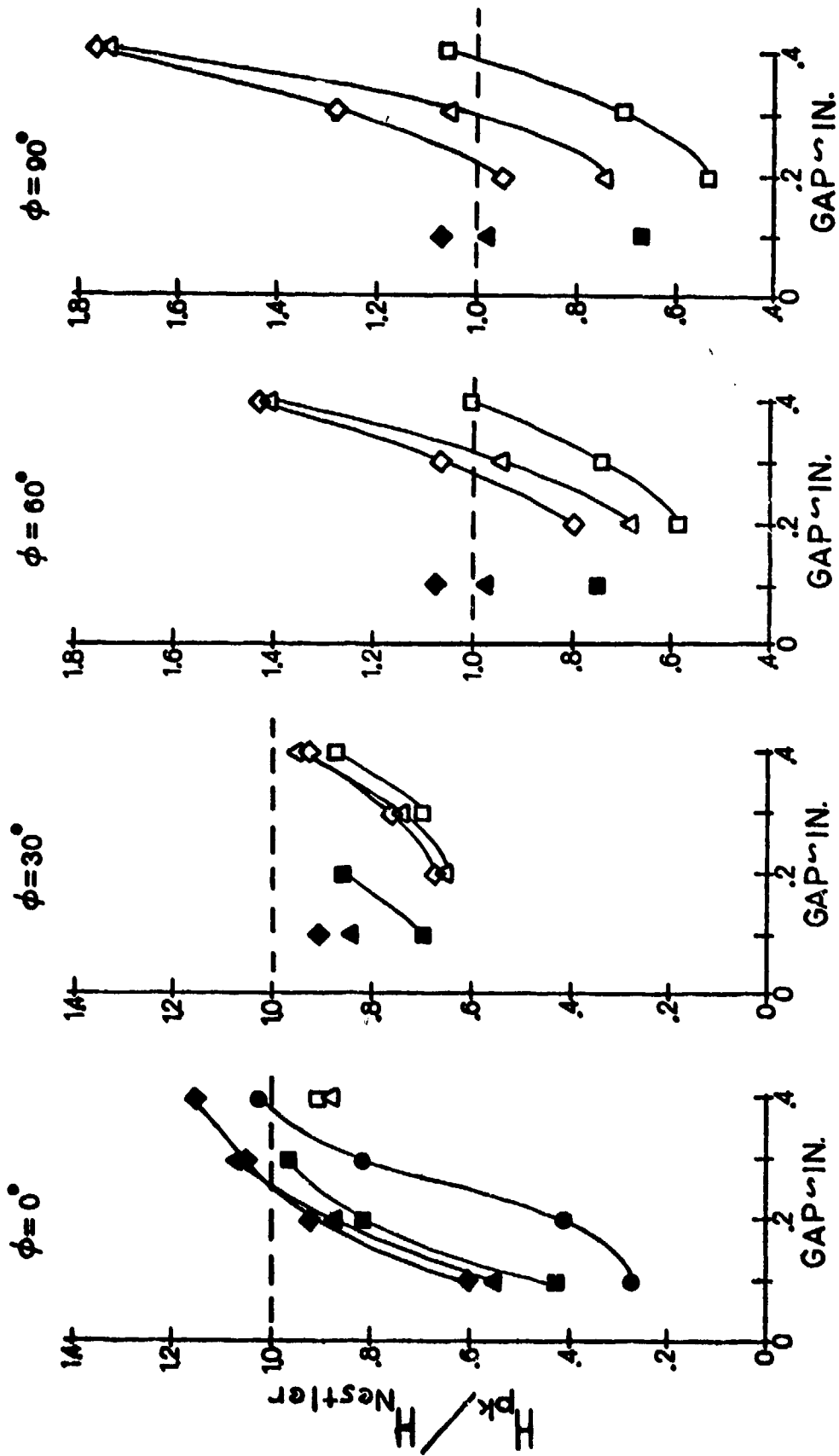


FIGURE 6.12 COMPARISON OF UPSTREAM PEAK HEATING TO NESTLER'S CORRELATION FOR UNSWEPT CYLINDERS



## 7.0 INTERACTION RECOVERY TEMPERATURES

In the last phase of testing the recovery temperatures were inferred in the interaction region of a sealed unswept  $20^\circ$  wedge fin. From previous experience it was found that for run times long enough to establish equilibrium wall temperatures damage to the thin skin inserts would also occur. A method was therefore devised whereby the recovery temperatures could be extrapolated from heat transfer data.

The method consisted of making several runs at each pitch-roll attitude. Each run was made at a different wall temperature with the model being heated or cooled to a uniform temperature before the run. For each thermocouple the heat transfer rate measured during each run was plotted as a function of the wall to stagnation temperature ratio as shown in Figure 7.1. In theory, these data should follow a linear function assuming no conduction or radiation effects are present. A linear least squares curve fit of the data was formed and extrapolated to  $Q = 0$ . At this point the temperature ratio should be  $T_r/T_o$ .

The recovery temperature ratios and local static temperatures given in Figure 4.40 were then used to compute recovery factors through the interaction region at each pitch-roll attitude. These recovery factor profiles are presented in Appendix B. Recovery factor profiles are also presented for the undisturbed flow on the windward surface of the ogive-cylinder. These were generated by cross plotting the recovery factors obtained at each of the model roll positions and which were more than 45 degrees from the fin surface. It was shown through oil flow and heat transfer data that the interaction region does not extend more than 45 degrees from the fin. The undisturbed recovery factor profile for zero

angle of attack contains only 22 points because only one roll position ( $\phi=0^\circ$ ) was tested. The undisturbed profiles exhibit two peculiar aspects which remain unexplained. The first is the sharp roll off of the recovery factor for  $\phi=90^\circ$  and  $\alpha=4^\circ$ ,  $8^\circ$  and  $12^\circ$  and the second is the elevated value at zero angle of attack. Except for these cases the undisturbed recovery factors agree well with the theoretical value of 0.88.

The recovery temperature ratios for the undisturbed region at zero angle of attack are shown in Figure 7.2. The average value is 0.940 which gives a recovery factor of 0.931. A second method of deriving the average recovery temperature ratio was tested on these data. This method uses the fact that the heat transfer coefficient should be independent of wall temperature when based on the correct recovery temperature. Ten runs were made at zero angle of attack, each at a different wall temperature. For each run the average value of  $Q$  and  $T_w$  was taken for the 22 thermocouples in the undisturbed region. These are shown in Table 7.1. A recovery temperature was assumed and the heat transfer coefficient was calculated for each run. The average value of the heat transfer coefficients of the 10 runs was taken and the one sigma scatter computed. This was repeated for several assumed recovery temperatures and the results plotted as shown in Figure 7.3. The actual recovery temperature is then given by the point where minimum scatter (i.e. wall temperature dependence) occurs. This method gives a recovery temperature ratio of 0.945 which agrees well with the results shown in Figure 7.2. The point of minimum scatter in Figure 7.3 also provides a measure of the basic noise in the data which is 2.88% of the average value for this case. In Figure 7.4 the data of Table 7.1 has been

plotted so that the variation in the heat transfer coefficient with the assumed recovery temperature can be seen. As shown, a large error in the heat transfer coefficient can result from an error in the recovery temperature.

TABLE 7.1  $T_R$  EXTRAPOLATION (METHOD II)

Run	$\dot{Q}$	$T_w$	$H_{.88T_0}$	$H_{.9T_0}$	$H_{.92T_0}$	$H_{.945T_0}$	$H_{.96T_0}$	$H_{.98T_0}$	$H_{T_0}$	
1	.301	525	1.350	1.254	1.171	1.082	1.034	.9773	.9262	
14	.336	514	1.436	1.339	1.254	1.162	1.113	1.053	1.000	
18	.305	539	1.459	1.350	1.255	1.154	1.101	1.037	.9807	
31	.261	579	1.544	1.403	1.286	1.164	1.101	1.028	.9631	
42	.226	608	1.614	1.439	1.299	1.157	1.087	1.004	.9339	
47	.226	608	1.614	1.439	1.299	1.157	1.087	1.004	.9339	
60	.175	646	1.716	1.471	1.287	1.113	1.029	.9358	.8578	
61	.180	643	1.714	1.475	1.295	1.123	1.040	.9474	.8696	
74	.217	622	1.722	1.517	1.356	1.197	1.119	1.028	.9518	
75	.245	594	1.591	1.433	1.303	1.171	1.104	1.025	.9570	
			$H_{AVE} \times 10^3$	1.576	1.412	1.280	1.148	1.081	1.004	.9374
			$\pm \sigma$ (%)	8.15	5.53	3.73	2.88	3.12	3.89	4.79

An example of the interaction recovery factor profiles of Appendix B is shown in Figure 7.5. The characteristic features to be noted are the trough located just outboard of the peak heating location and a sharp peak at the location of separation. The recovery factors at these locations are shown in Figure 7.6 as a function of model roll angle. Such large variation in the recovery factor has significant effect on the heat transfer coefficients as is shown in Figure 7.7. Here a comparison is shown between heat transfer coefficients based on  $T_0$  ( $R=1$ ) and those based on the recovery factors of Figure 7.5.

A final significant feature noted in Figure 7.5 is that the recovery

factor at the peak heating location is very close to that of the undisturbed flow. This is shown in Figure 7.8 to be true for most of the data. The exceptions are the cases where  $\phi=90^\circ$  and where  $\alpha=0^\circ$ . The undisturbed recovery factor at these model attitudes varies significantly from theory, as mentioned earlier, and is the cause of divergence in Figure 7.8. Since the recovery factors at the peak and undisturbed locations are the same the ratio of peak to undisturbed heat transfer coefficient is nearly independent of the recovery factor. The correlation for peak heating derived in Section 5.3 is therefore still valid as shown in Figure 7.9

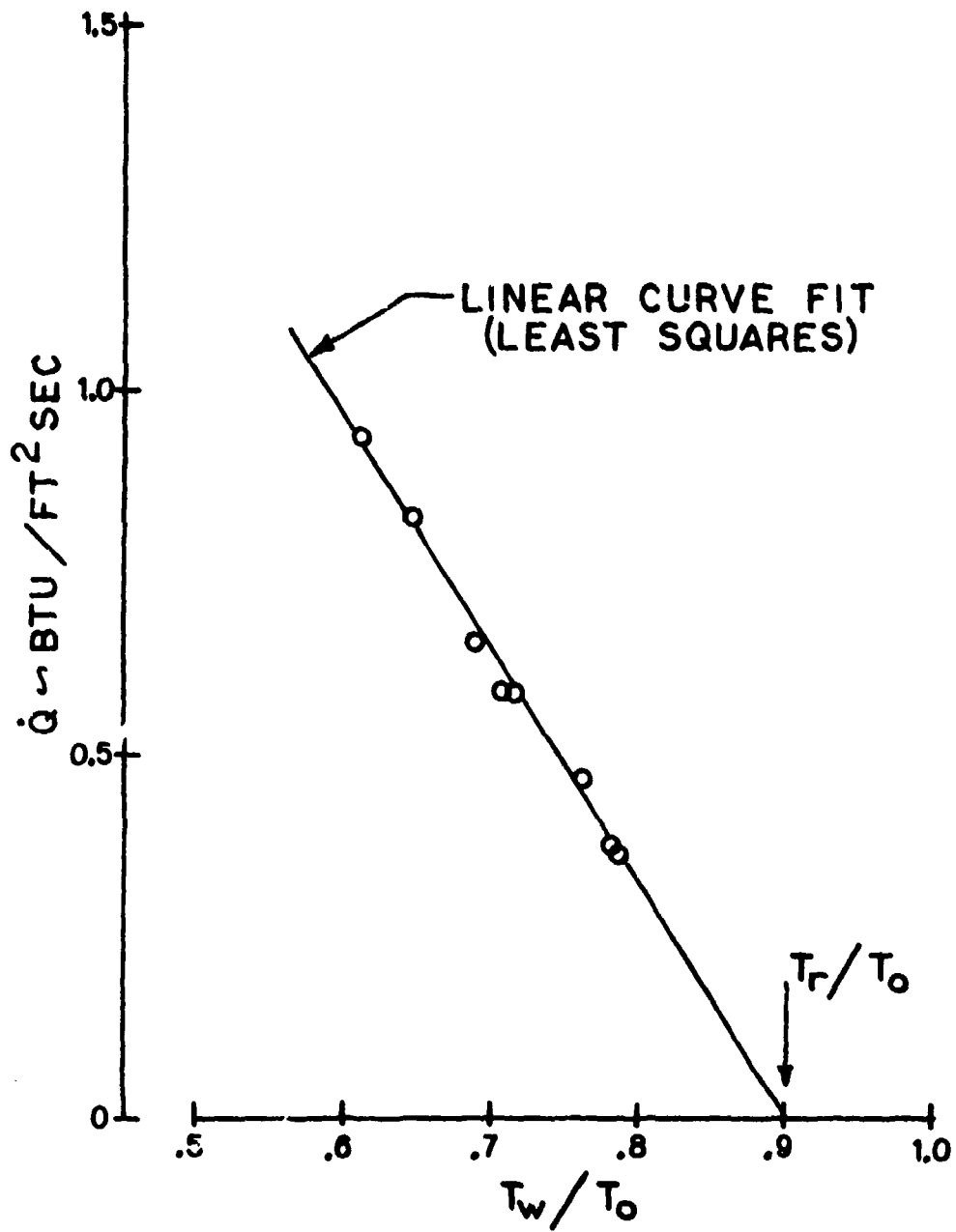


FIGURE 7.1 RECOVERY TEMP EXTRAPOLATION

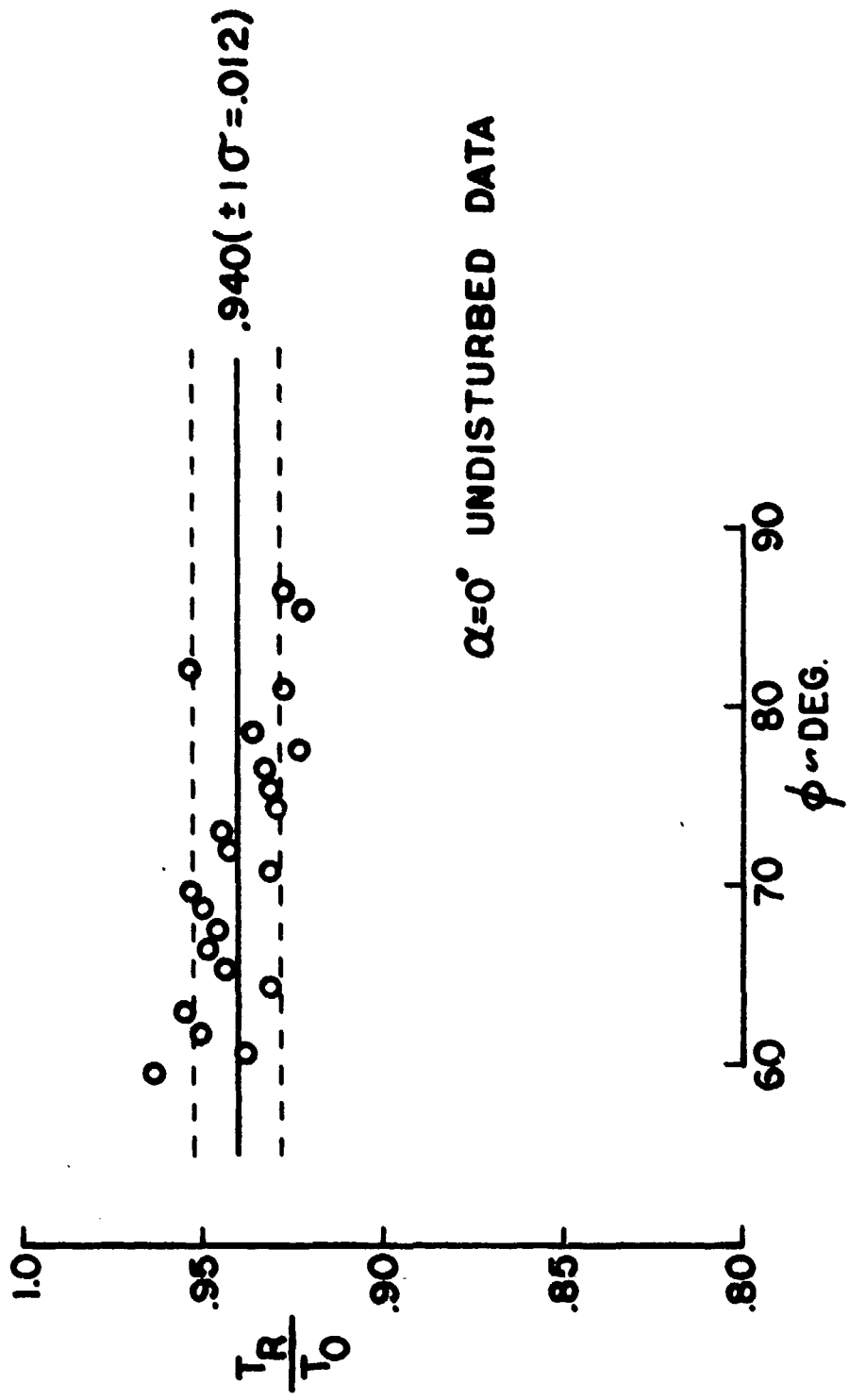


FIGURE 7.2 SCATTER BAND FOR RECOVERY TEMPERATURE RATIO

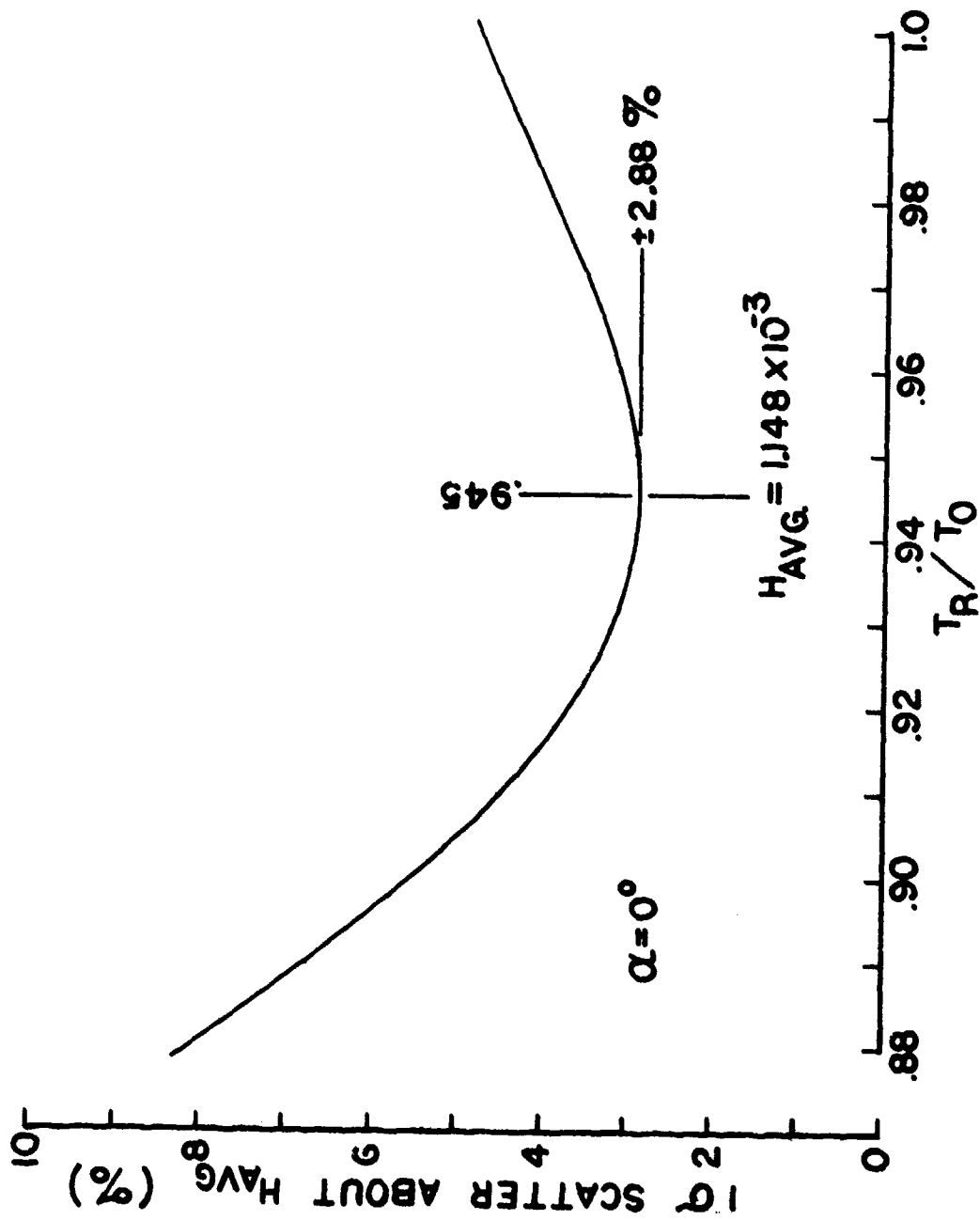


FIGURE 7.3  $T_r/T_0$  EXTRAPOLATION FROM MINIMUM SCATTER OF  $H_{T_r}$  WITH  $T_w$

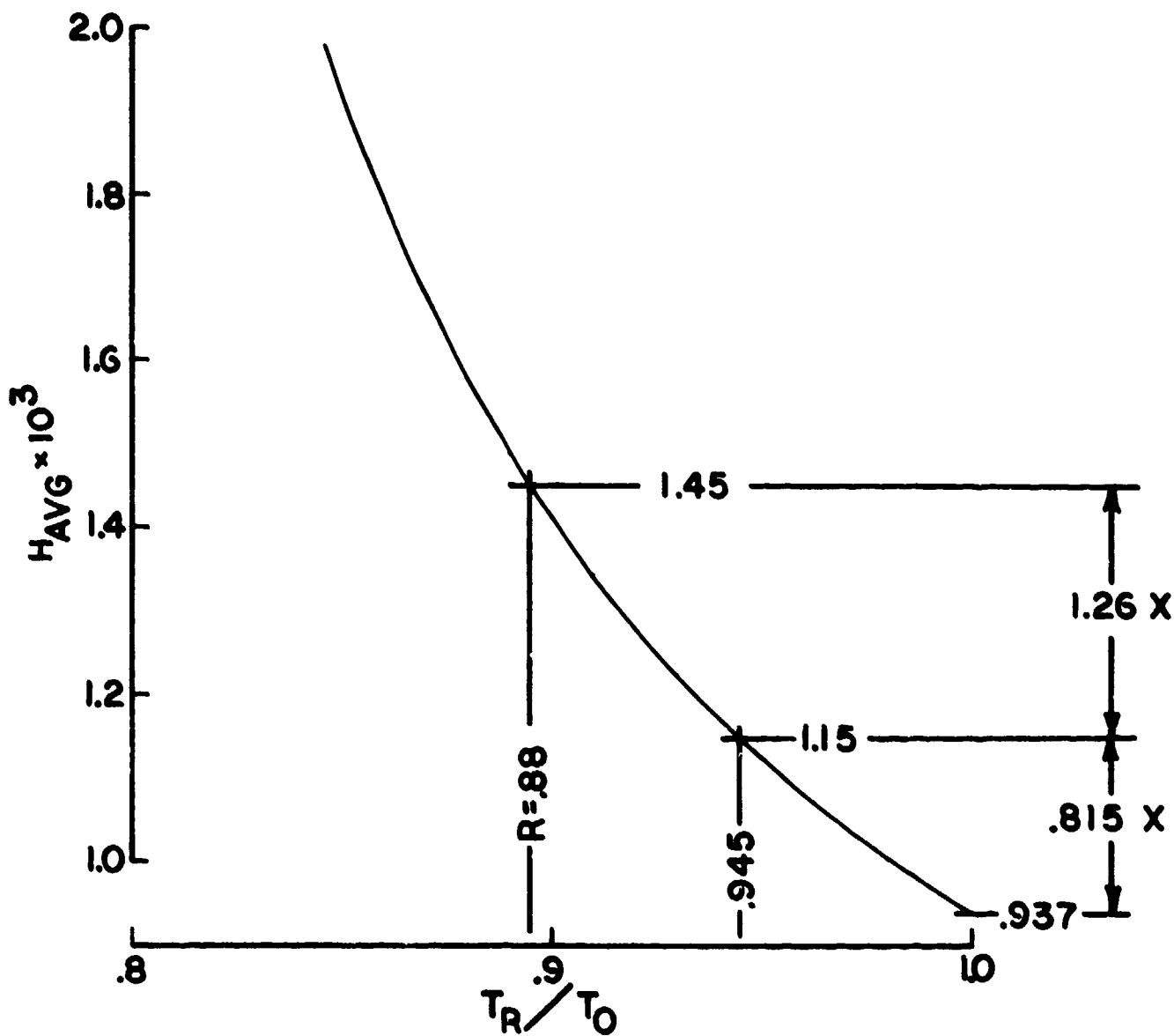


FIGURE 7.4 EFFECT ON H OF ERROR IN THE CHOICE OF THE RECOVERY FACTOR



$\alpha = 4^\circ$ ,  $ROLL = 60^\circ$

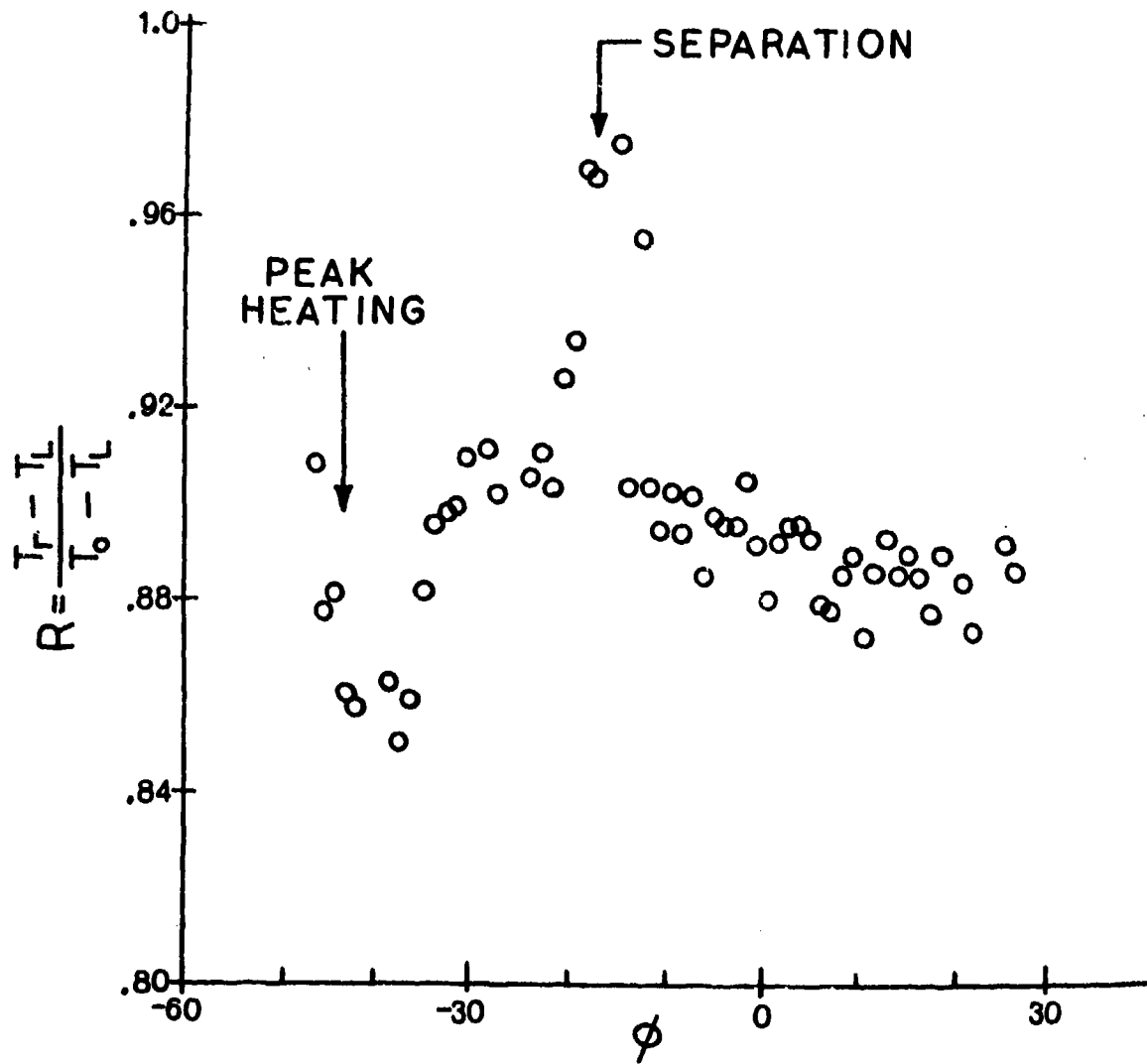


FIGURE 7.5 RECOVERY FACTORS

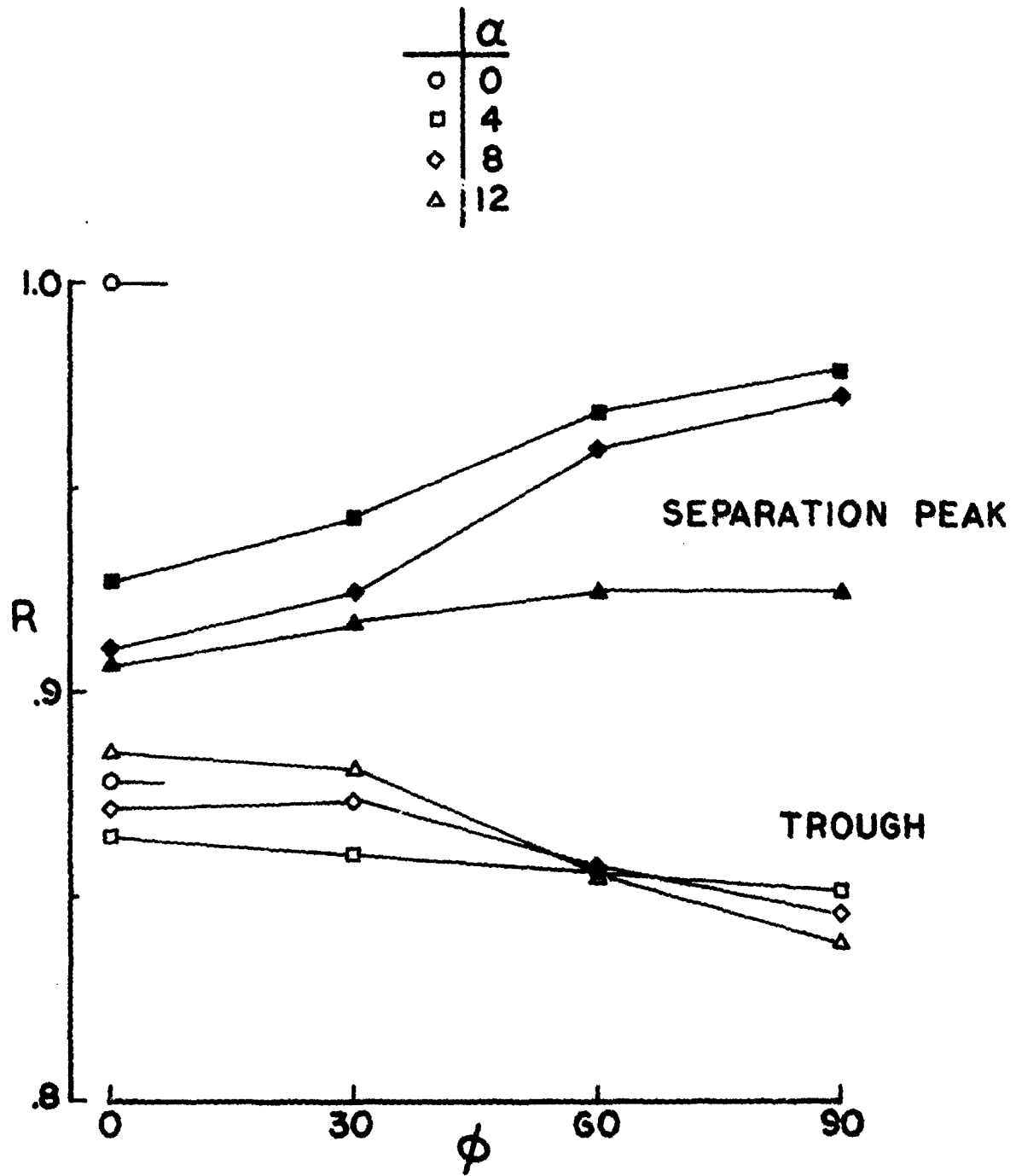


FIGURE 7.6 RECOVERY FACTORS AT THE TROUGH AND SEPARATION PEAK

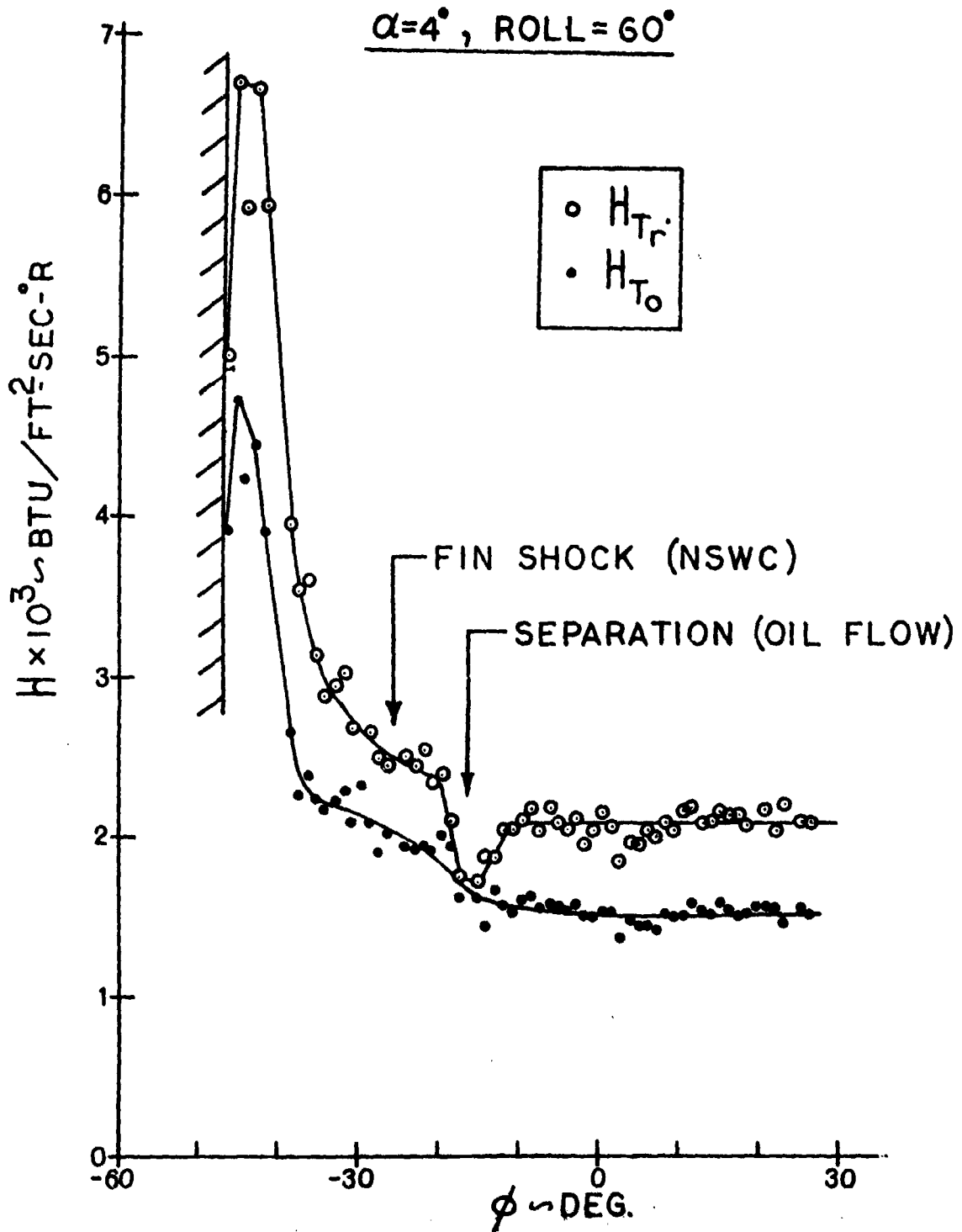


FIGURE 7.7 HEAT TRANSFER COEFFICIENT CORRECTIONS FOR RECOVERY TEMP

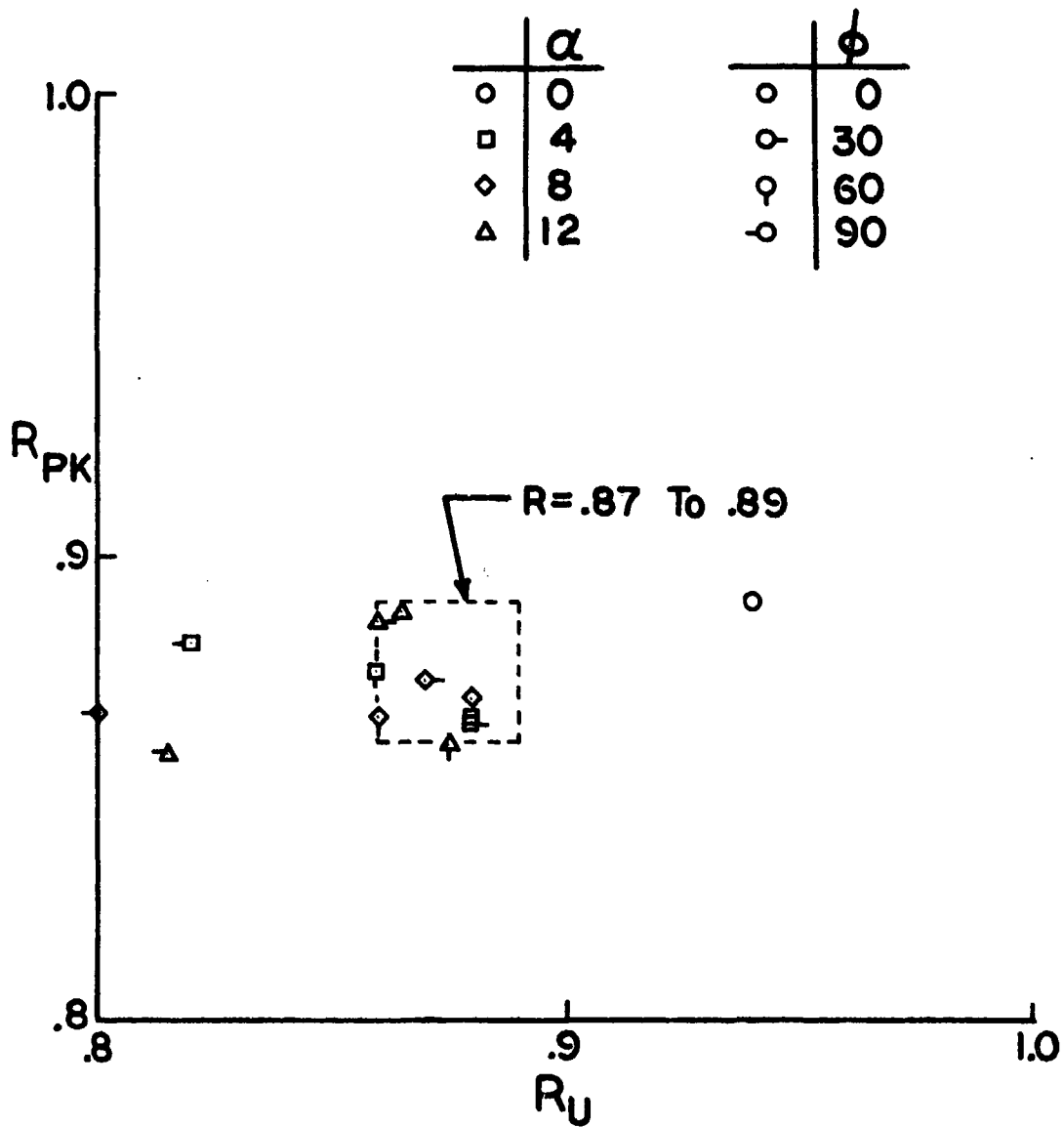


FIGURE 7.8 RECOVERY FACTORS AT PEAK HEATING LOCATION AND UNDISTURBED REGION

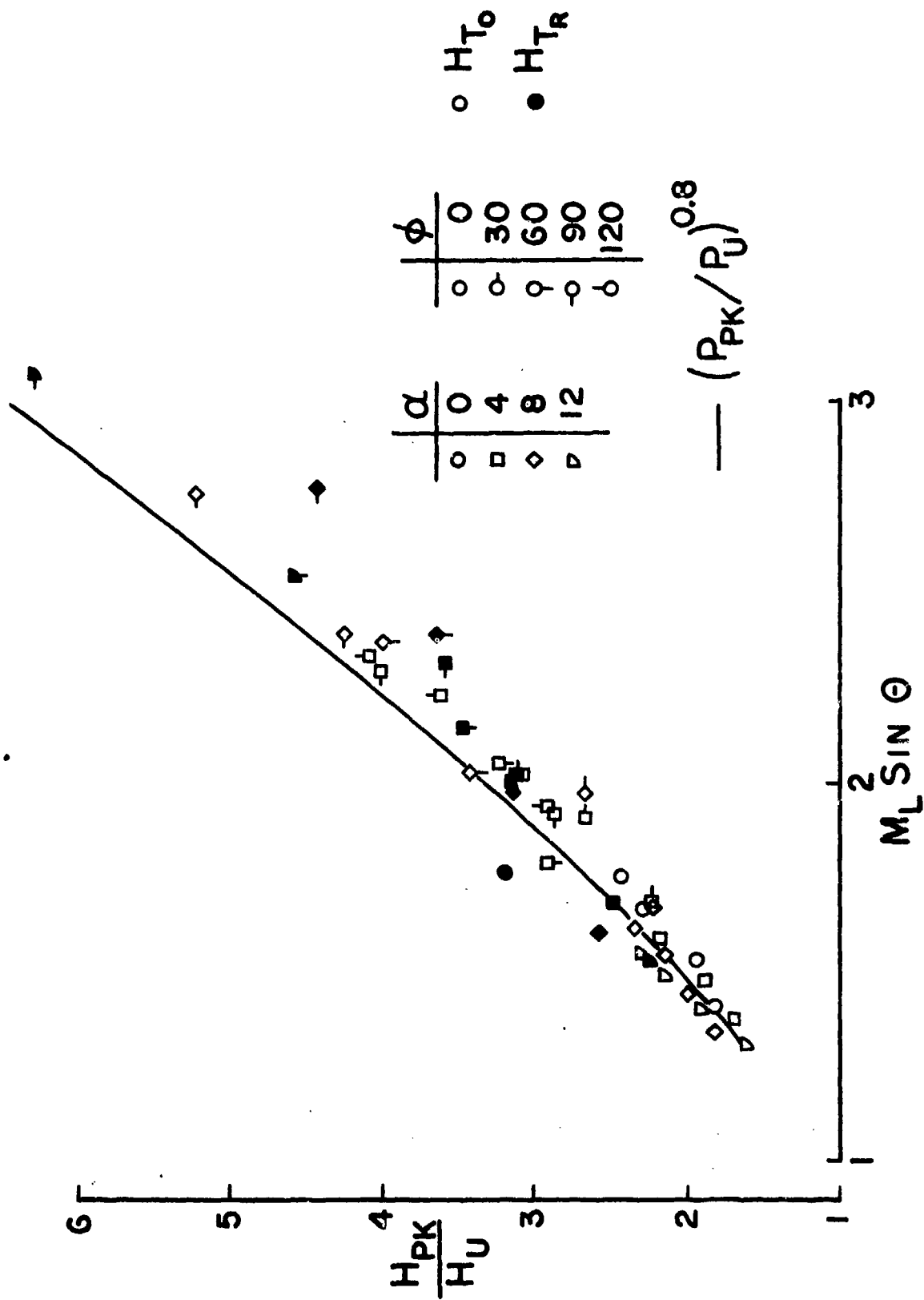


FIGURE 7.9 RECOVERY TEMPERATURE EFFECT ON PEAK HEATING  
CORRELATION FOR SEALED FINS

## 8.0 CONCLUSIONS

An extensive analytical and experimental test program was conducted investigating three-dimensional shock wave turbulent boundary layer interactions produced by fins on an ogive-cylinder. Flow field data were taken on the ogive-cylinder with the fins removed and the data were compared to predictions of an inviscid flow field computer program. Excellent agreement between the data and the inviscid solution was demonstrated. Heat transfer data were then taken in the interaction region of several fin configurations attached to the ogive-cylinder and the peak heating rates were correlated in terms of the inviscid flow properties.

All data were taken in the AEDC/VKF Tunnel B at Mach 6 and a unit Reynolds number of  $4.9 \times 10^6$  per foot. Analysis of the undisturbed flow field data and the peak interaction heating data produced the following significant conclusions.

1) For the ogive-cylinder configuration at angles of attack up to at least  $12^\circ$ , and within the attached flow region of the cylinder, the local flow field properties are well predicted by the inviscid flow field program of Reference 2.

2) The peak interaction heating rate for fins sealed to the cylinder may be predicted at any model attitude (at least within the test limits) by the following simple relation.

$$\frac{H_{pk}}{H_u} = \left( \frac{P_2}{P_1} \right)^{0.8}$$

The pressure ratio,  $P_2/P_1$ , is the oblique shock value for a particular model attitude and considers variations in the local Mach number and flow angularity as defined by the inviscid program. The local flow properties are evaluated at the edge of the boundary layer at the fin leading edge.

3) The location of the peak interaction heating on the ogive-cylinder was found to agree with Token's<sup>(5)</sup> relation derived from fin-flat plate data.

$$\psi = 0.24(\theta - \delta_F) + \delta_F$$

Where  $\psi$  = Angle to peak heating location  
 $\theta$  = Shock wave angle  
 $\delta_F$  = Fin deflection angle

4) Aerodynamic heating on the fin surface does not exhibit the interaction induced peaks observed on the cylinder. The heating levels are well predicted by flat plate laminar and turbulent theory if local free stream properties are defined by the inviscid program.

5) Effects of fin leading edge sweep on the peak heating levels can be accounted for by the following relation from Reference 5.

$$\frac{H_{\text{swept}}}{H_{\text{unswept}}} = \cos^{0.24} \Lambda$$

where  $\Lambda$  is the sweep angle

6) For a swept fin mounted on a torque tube allowing variations in the fin-cylinder gap height, the gap has little effect on the interaction heat transfer distributions. The peak heating was increased by a maximum of 50% over the sealed fin levels and was 1.5 to 5.0 times the undisturbed level.

Peak heating under the fin and upstream of the torque tube represents the most severe case of interaction heating observed during this effort. The peak heating levels could not be correlated but were generally bounded by Nestler's<sup>(8)</sup> correlation for peak heating upstream of unswept cylinders.

Peak heating rates 4 to 17 times the undisturbed levels were observed. Additional study of this interaction is suggested since the peak heating in this region would be the design point for the thermal protection of gapped control surfaces.

7) Recovery factors were evaluated in the interaction region of a fin sealed to the cylinder. The recovery factor at the peak heating location was found to be the same as that of the undisturbed flow and has a value of 0.88. The recovery factor profiles through the interaction region reveal a trough just outboard of the peak heating location having a nominal value of 0.85. A sharp increase in the recovery factor to a nominal value of 0.95 was noted at the location of 3-D separation (as determined from oil flow photographs).



### REFERENCES

1. Test Facilities Handbook (Tenth Edition), "Von Karman Gas Dynamics Facility, Vol 4", Arnold Engineering Development Center, May 1974.
2. Solomon, J.M., Ciment, M., Ferguson, R.E., Bell, J.B., Wardlaw, A.B., "A Program for Computing Steady Inviscid Three Dimensional Supersonic Flow on Reentry Vehicles", NSWC/WOL/TR 77-28, Feb. 1977.
3. Christophel, R.G. and Rockwell, W.A., "Tabulated Mach 6 3-D Shock Wave Turbulent Boundary Layer Interaction Heat Transfer Data", AFFDL-TM-74-212-FXG, Nov. 1974.
4. Hayes, J.R., "Prediction Techniques for the Characteristics of Fin Generated Three Dimensional Shock Wave Turbulent Boundary Layer Interactions", AFFDL-TR-77-10, May 1977.
5. Neumann, R.D. and Burke, G.L., "The Influence of Shock Wave Boundary Layer Effects on the Design of Hypersonic Aircraft", AFFDL-TR-68-152, March 1969.
6. Eichelbrenner, E.A., "Three Dimensional Boundary Layers", Annual Review of Fluid Mechanics, Vol 5, 1973, pp 339-360.
7. Token, K.H., "Heat Transfer Due to Shock Wave Turbulent Boundary Layer Interactions on High Speed Weapon Systems", AFFDL-TR-74-77, April 1974.
8. Nestler, D.E., "Results of Heat Transfer Tests of a Blunt Cone with Protuberances at Mach 10", 3rd International Heat Transfer Conference, Vol II, 1966.
9. Hayes, J.R.; Neumann, R.D., "Tabulated Mach-6 Turbulent Heat Transfer Data for the 1/4 Scale Missile Model", AFFDL-TM-78-32-FXG, Feb. 1978.

## APPENDIX A

### EFFECTS OF THE TRIP STRIP ON THE MEASURED AERODYNAMIC HEATING

In spite of the large scale of the modular missile model and the resultant Reynolds number at the point of interaction of over  $10 \times 10^6$ , the boundary layer on the model was not always fully turbulent. In order to achieve fully turbulent data on the model in the region of interaction, a strip of grit was applied to the model nose. Shadowgraph data of the nose region prior to and after the application of the grit indicates that the strip, itself, creates a localized disturbance and changes the thickness of the perceived boundary layer. These characteristics are noted in figures A-1 and A-2 which were taken at angles of attack of zero and 12 degrees. These differences appear to diminish as the flow proceeds downstream of the disturbance however, there is no assurance from these data that the flow in the tripped state has the same characteristics as it would without tripping.

In order to examine this question further, a quarter scale model of the modular missile model shown in figure A-3 was constructed and tested in the AFFDL Mach 6 tunnel<sup>(9)</sup>. This facility generates Reynolds numbers which are substantially higher than those in Tunnel "B" - even when the reduced scale of the model is considered. The untripped quarter scale model was tested in this facility at zero angle of attack and the results are shown in figure A-4. This figure indicates data taken in the AFFDL and AEDC facilities with both tripped and untripped boundary layers. These data are plotted as a function of the freestream Reynolds number to the gage,  $Re_{\theta_x}$ , and correlated with the Eckert turbulent theory using a surface pressure level,

$P_L/P_\infty$  of 0.86 as derived from measurements in Tunnel "B" and confirmed through numerical calculations.

The AEDC data were all taken at one unit Reynolds number but at various stations on the body while the AFFDL data were taken at one station on the body while varying the unit Reynolds number of the facility. Both sets of untripped data agree well with one another and trend toward the theory line. In addition, the tripped data also trend toward the theory line and agree with the untripped data in the limit of large Reynolds numbers (large distances from the trip strip).

It is concluded from this exercise that the tripped data are fully turbulent and representative of fully turbulent data at the start of the interaction process.

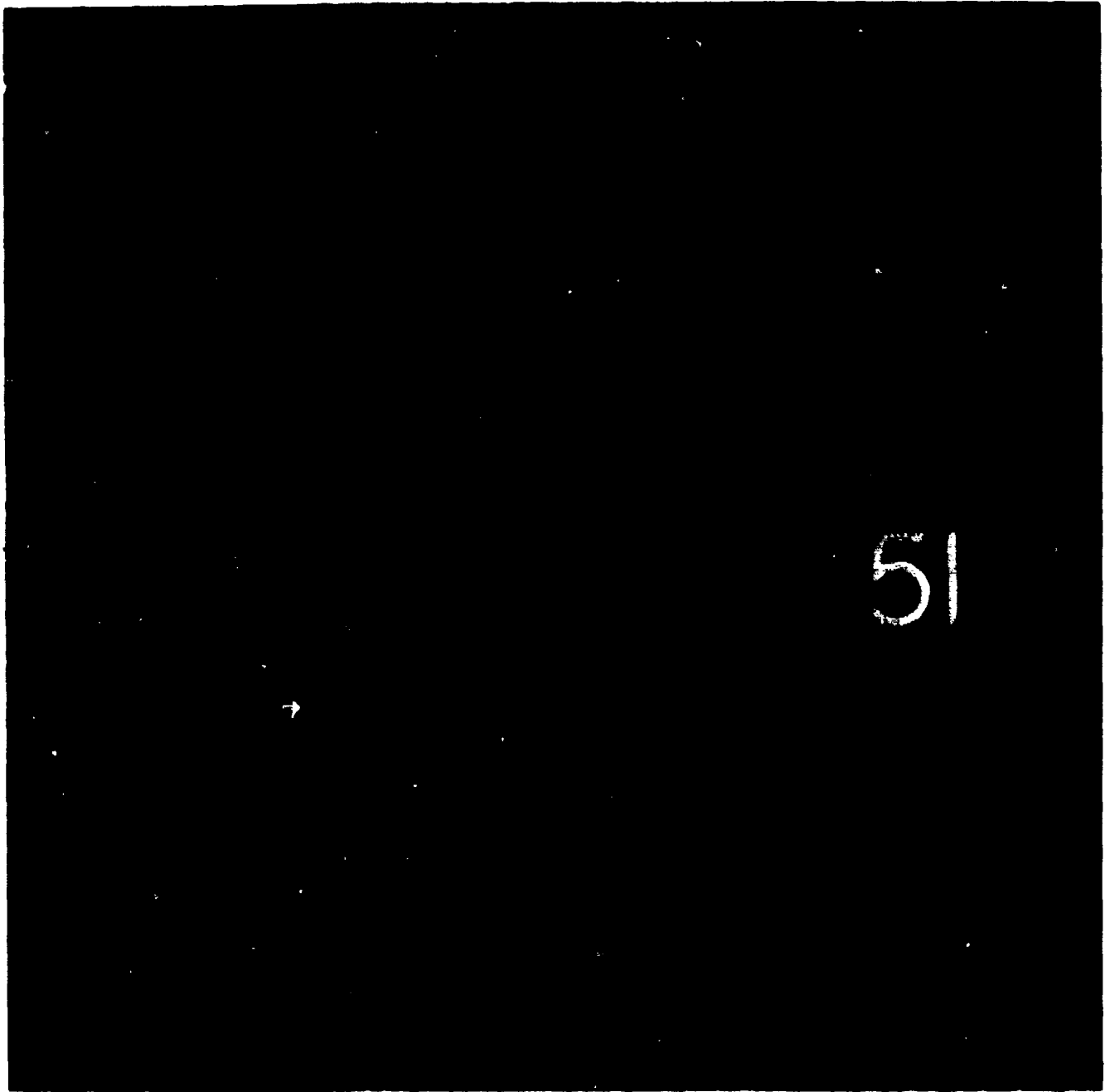


FIGURE A-1a  $\alpha=0^\circ$ , UNTRIPPED

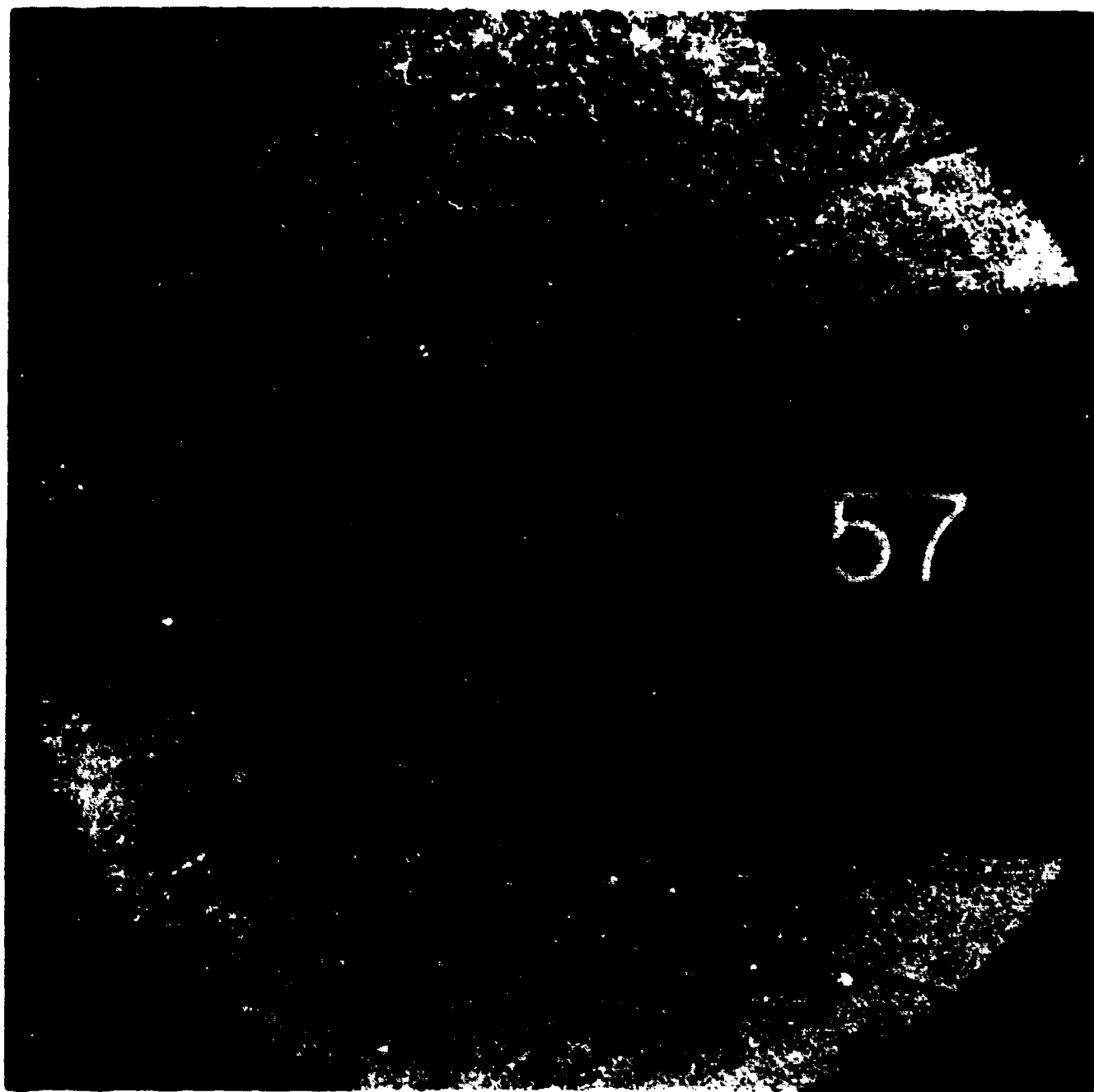


FIGURE A-1b  $\alpha=0^\circ$ , TRIPPED

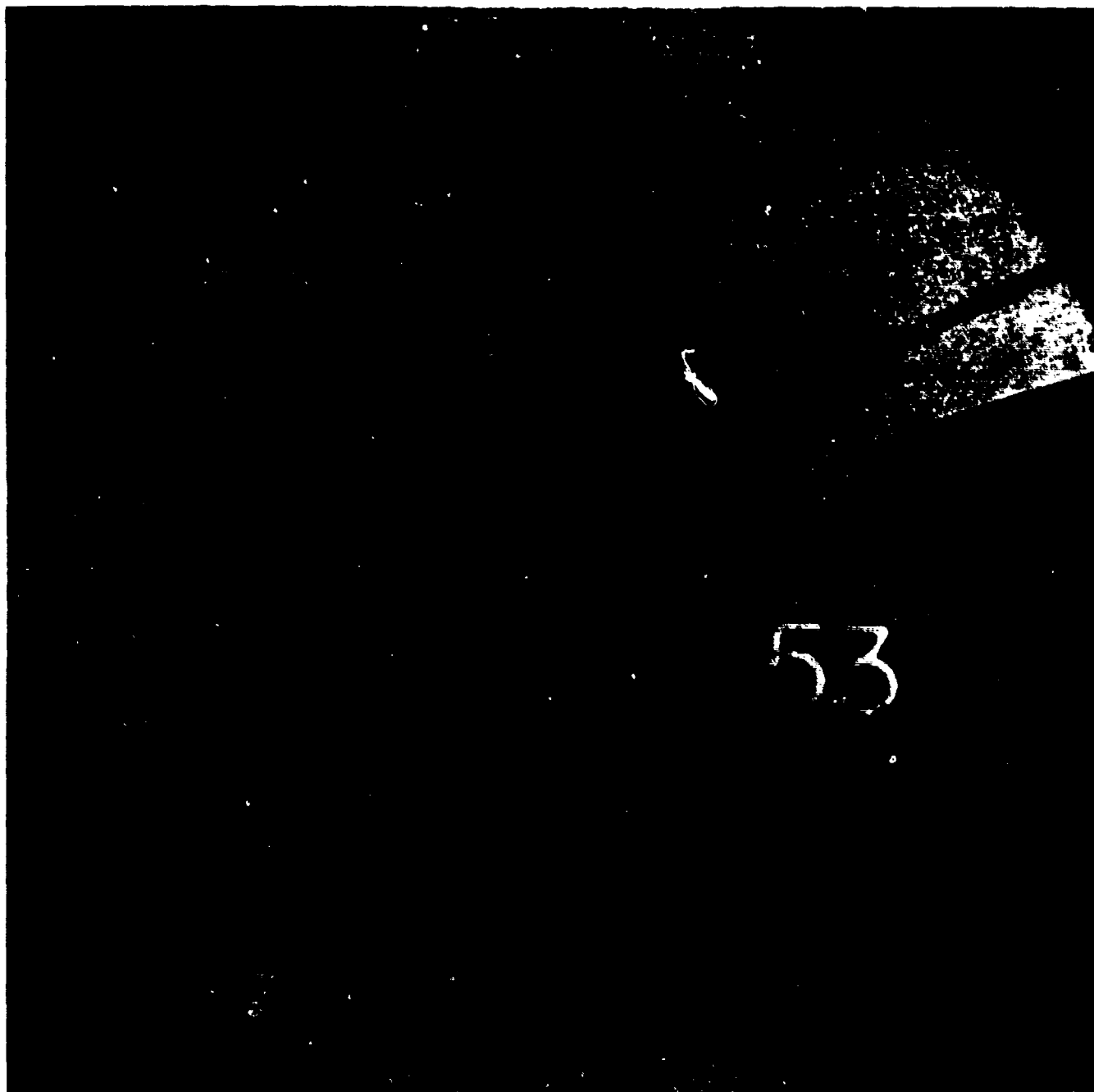


FIGURE A-2a  $\alpha=12^\circ$ , UNTRIPPED

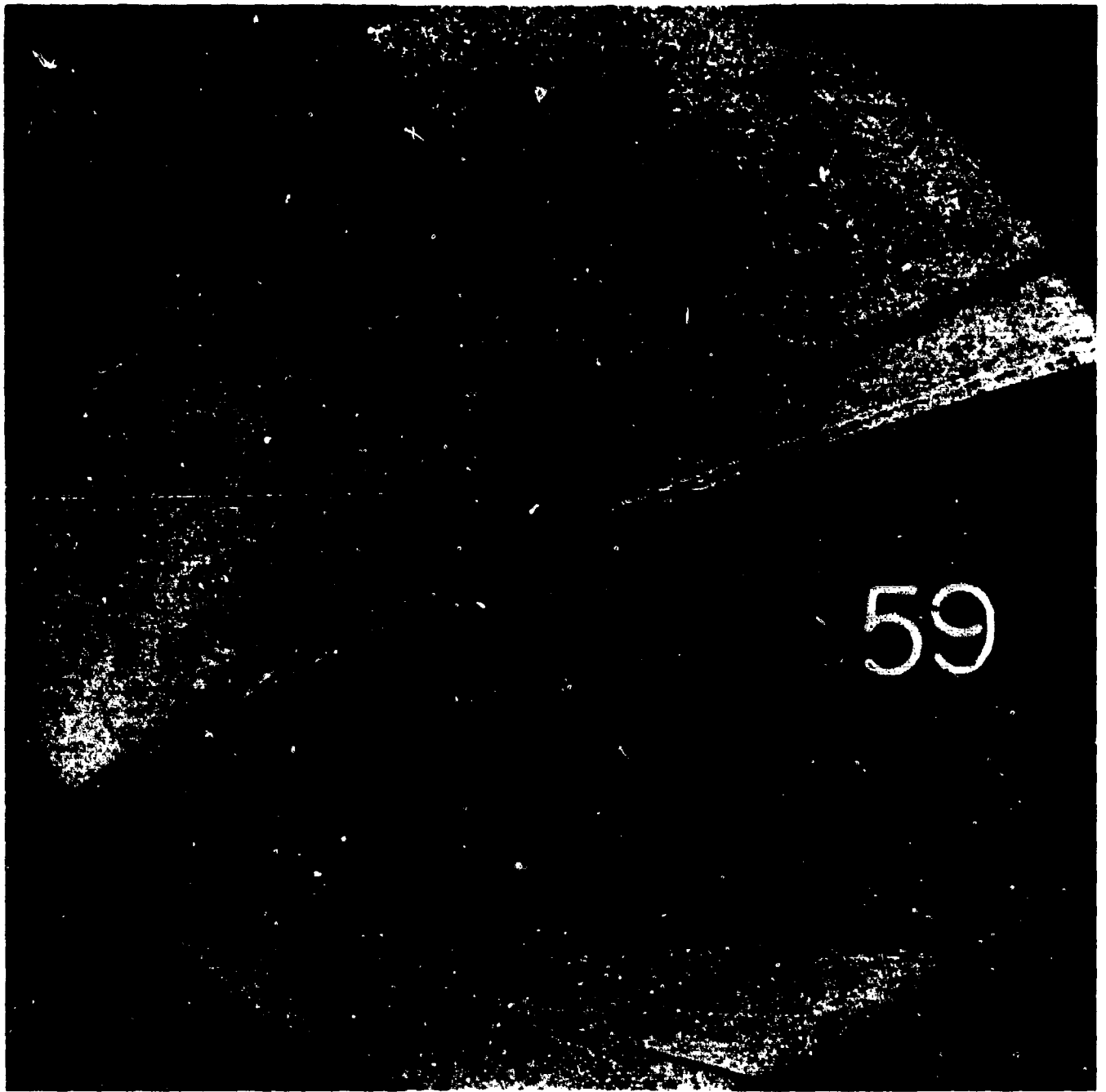


FIGURE A-2b  $\alpha=12^\circ$ , TRIPPED

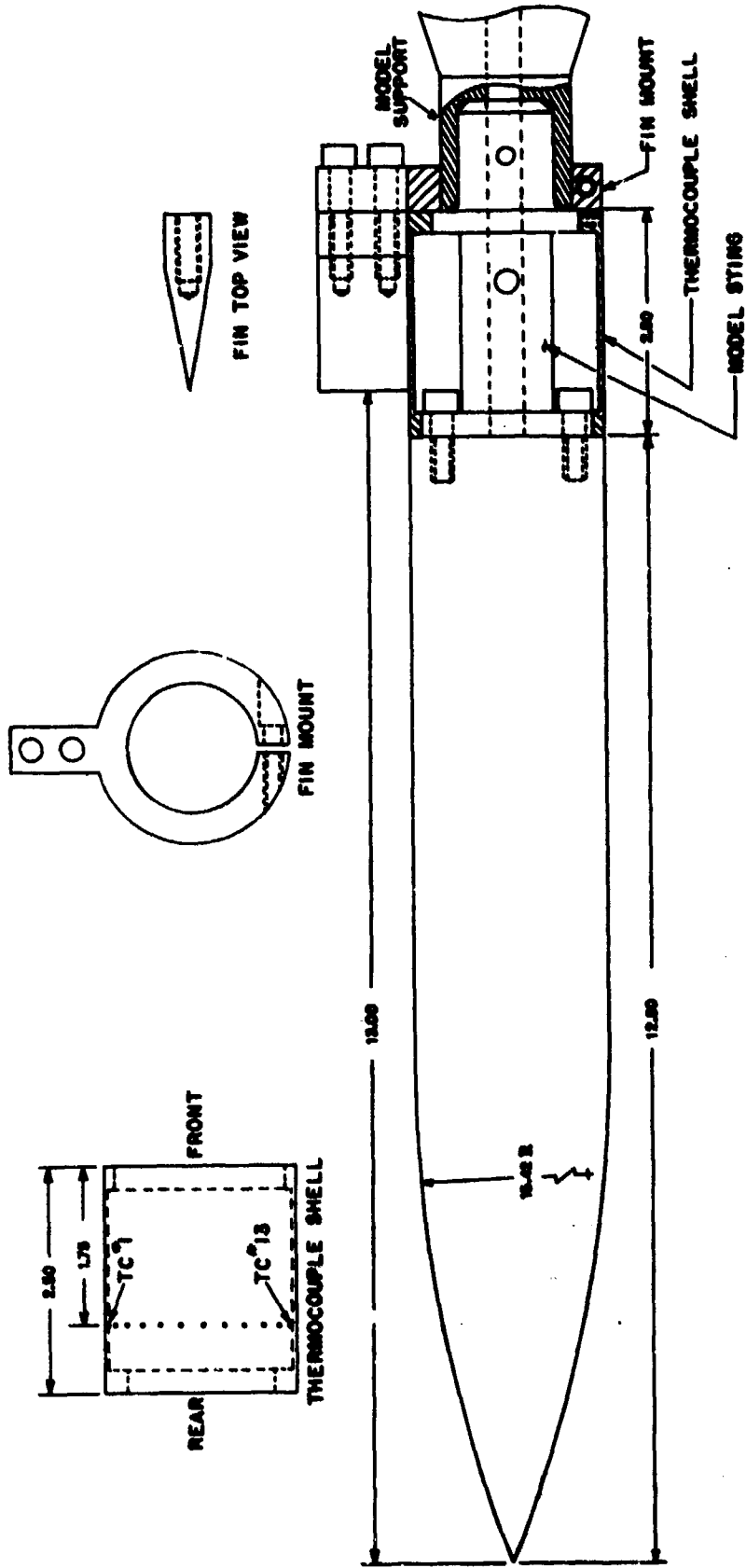


FIGURE A-3 1/4 SCALE MISSILE MODEL



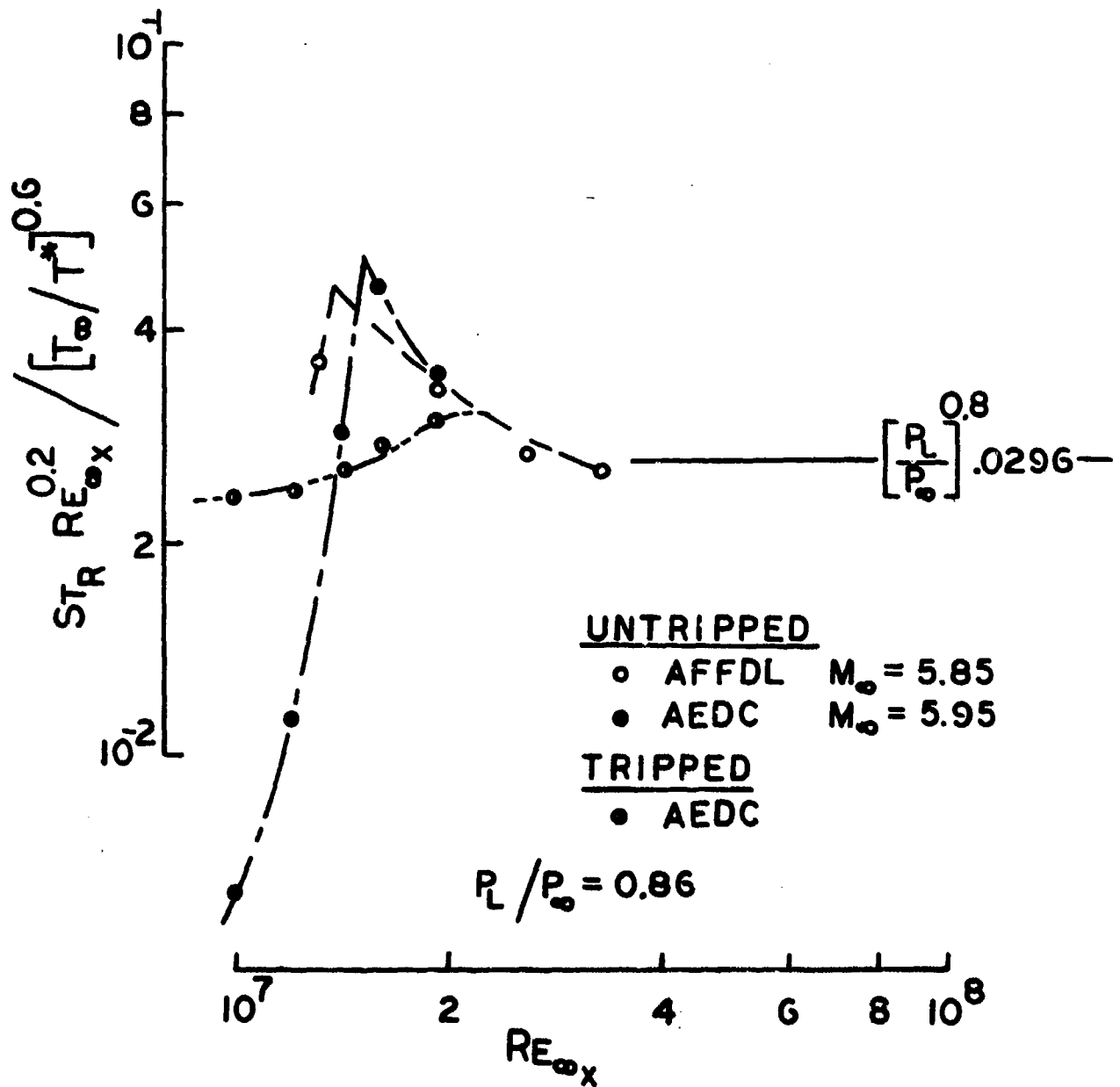


FIGURE A-4 UNDISTURBED DATA CORRELATION

## APPENDIX B

### INTERACTION RECOVERY FACTOR PROFILES

Recovery temperature ratios,  $T_R/T_O$ , were derived from thin skin heat transfer data in the interaction region of a  $20^\circ$  wedge fin according to the method described in Section 7.0. Test data were taken for angles of attack of  $0^\circ$ ,  $4^\circ$ ,  $8^\circ$  and  $12^\circ$  and with the fin rolled  $0^\circ$ ,  $30^\circ$ ,  $60^\circ$  and  $90^\circ$  off the windward centerline of the ogive-cylinder. Recovery factors were then calculated as

$$R = \frac{T_R - T_L}{T_O - T_L}$$

where  $T_L$  is the local static temperature as defined in figure 4.40.

The recovery factor profiles through the interaction region are shown for each model attitude in figures B-1 through B-13.

Oil flow photographs and the heat transfer profiles demonstrated that the interaction region does not extend beyond  $45^\circ$  from the fin centerline station. At each angle of attack the recovery factors measured at locations greater than  $45^\circ$  from the fin were plotted for all roll positions. This generated recovery factor profiles of the undisturbed flow field on the cylinder as shown in figures B-14 through B-17.

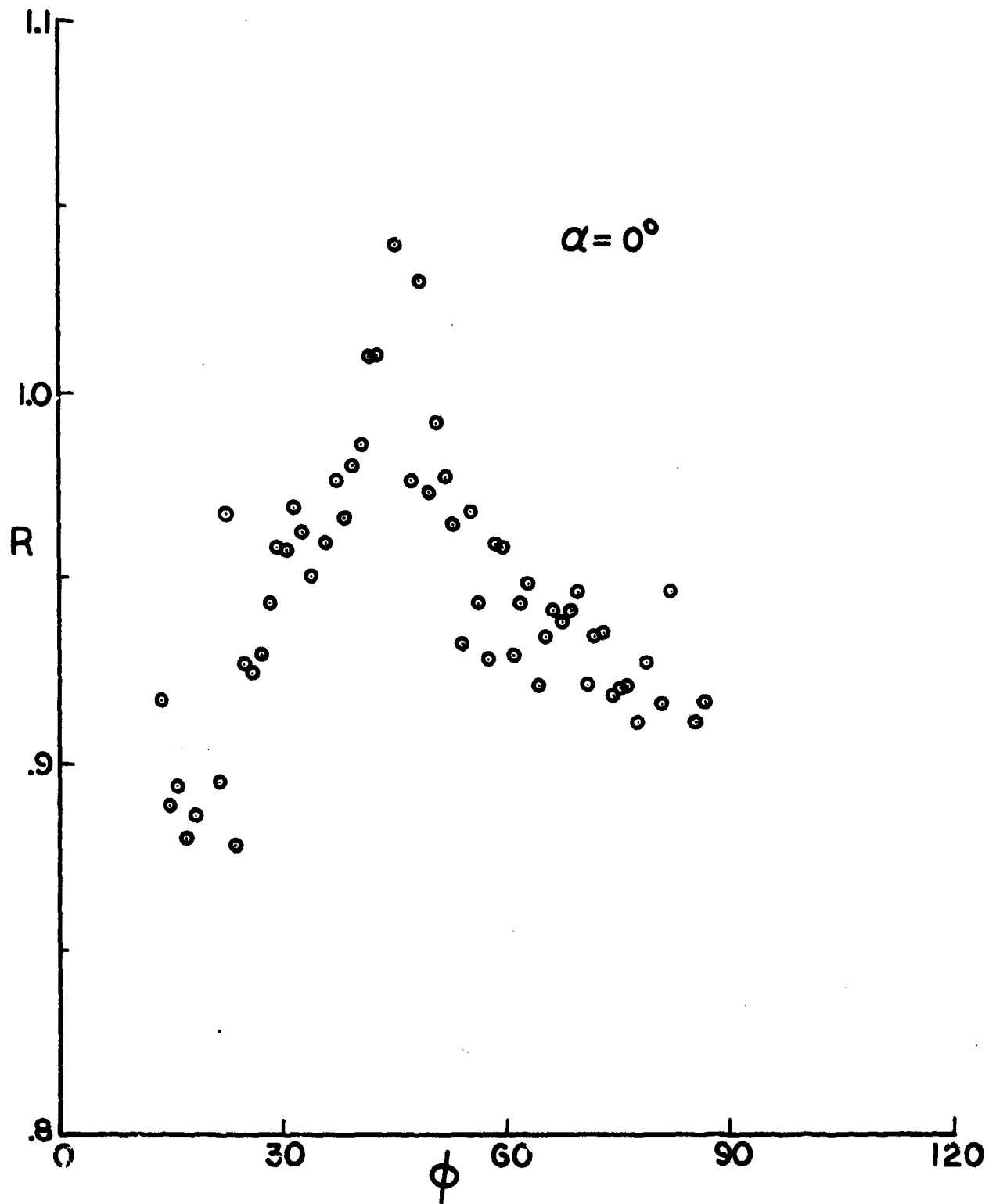


FIGURE B-1 RECOVERY FACTORS ;  $\alpha=0^\circ$ , ROLL =  $0^\circ$

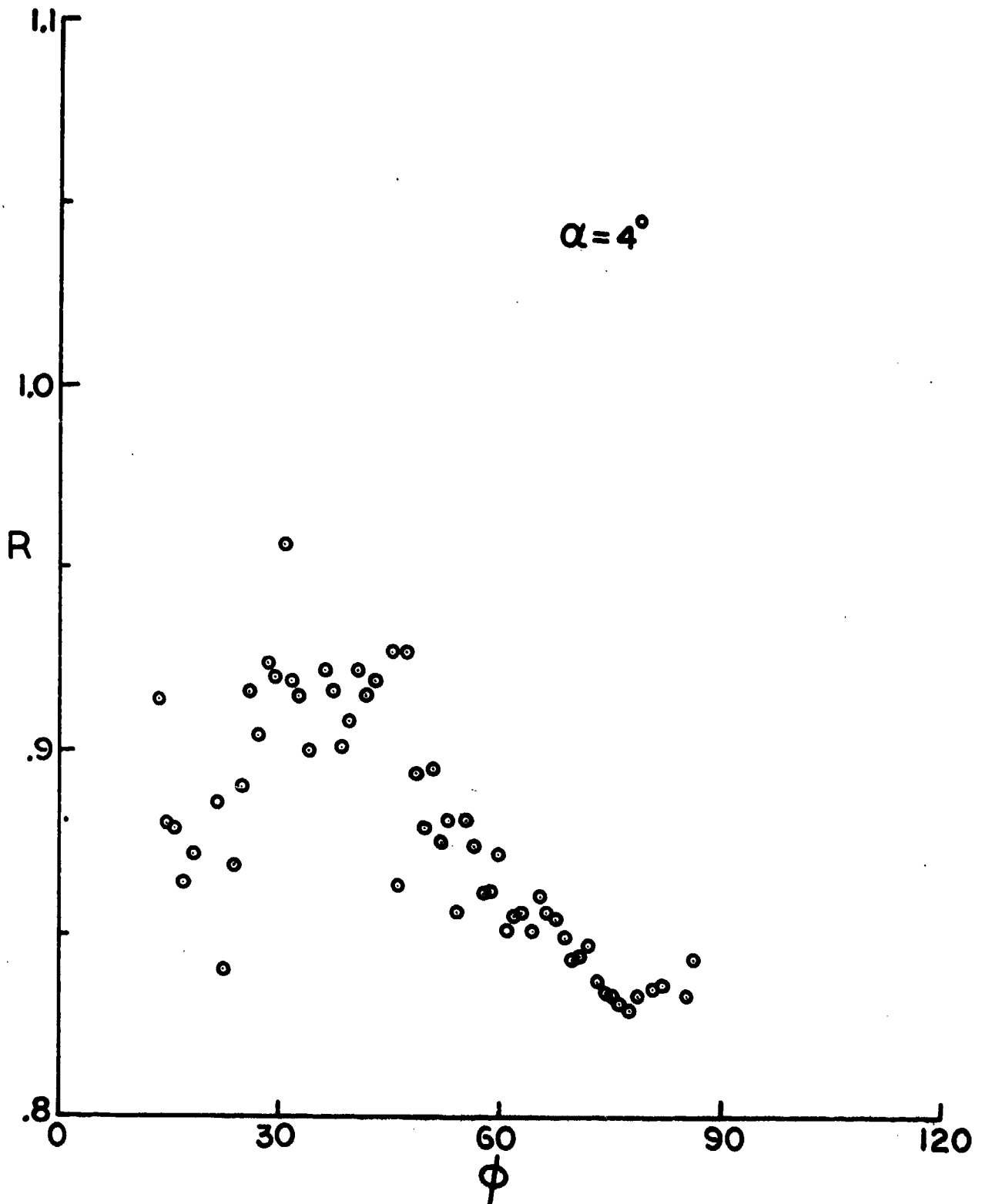


FIGURE B-2 RECOVERY FACTORS ;  $\alpha=4^\circ$ , ROLL=0°

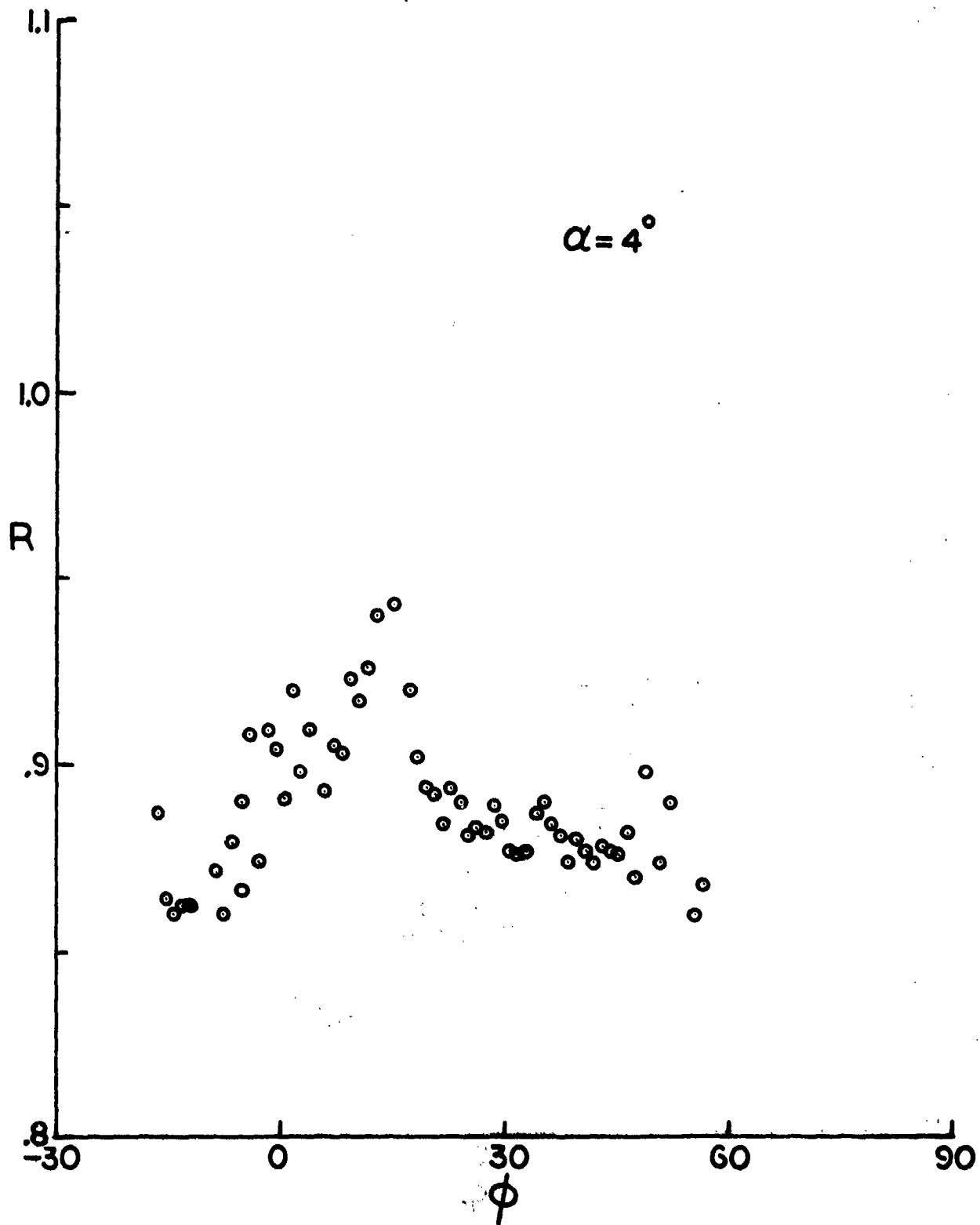


FIGURE B-3 RECOVERY FACTORS ;  $\alpha=4^\circ$  ; ROLL= $30^\circ$

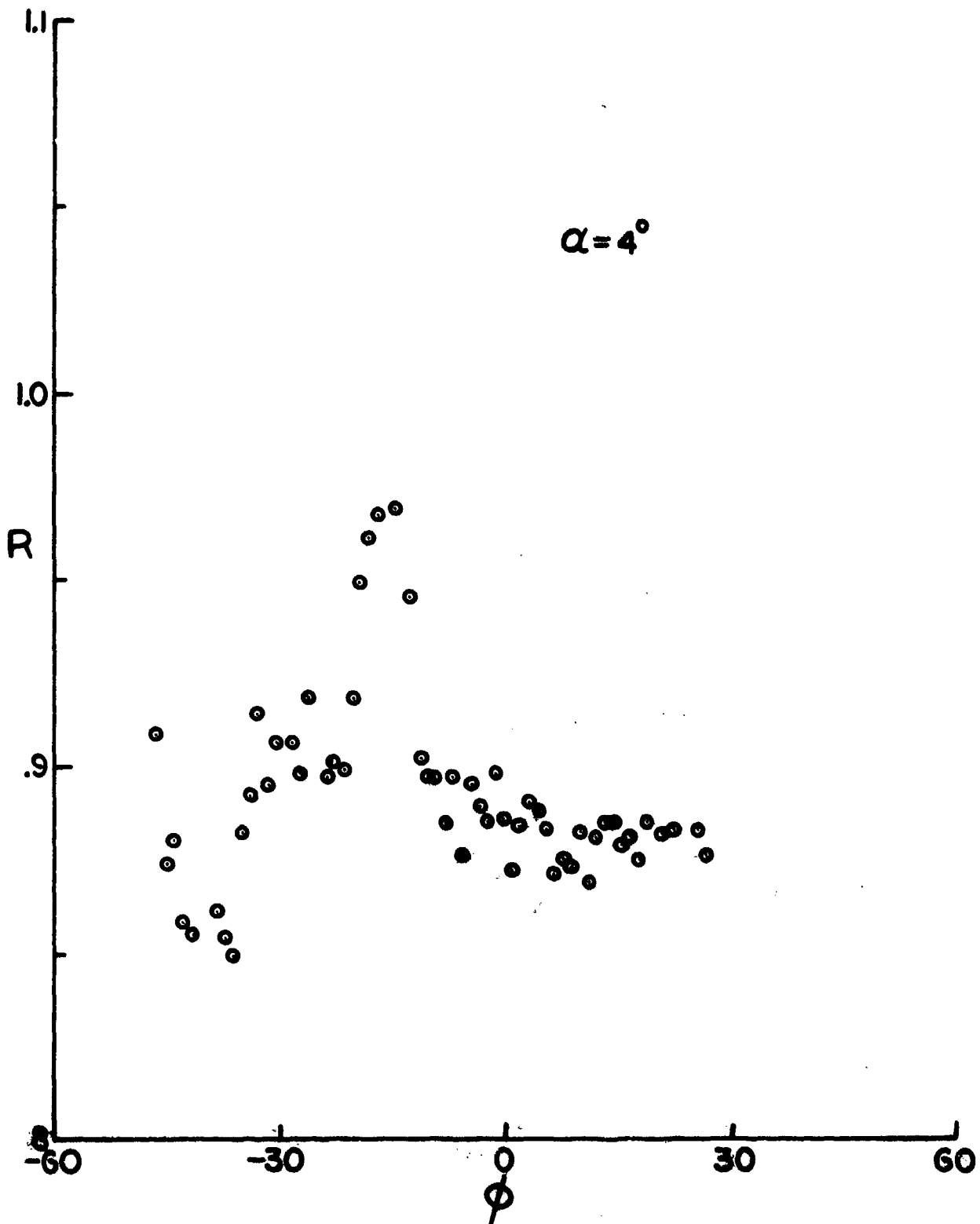


FIGURE B-4 RECOVERY FACTORS ;  $\alpha = 4^\circ$  , ROLL =  $60^\circ$

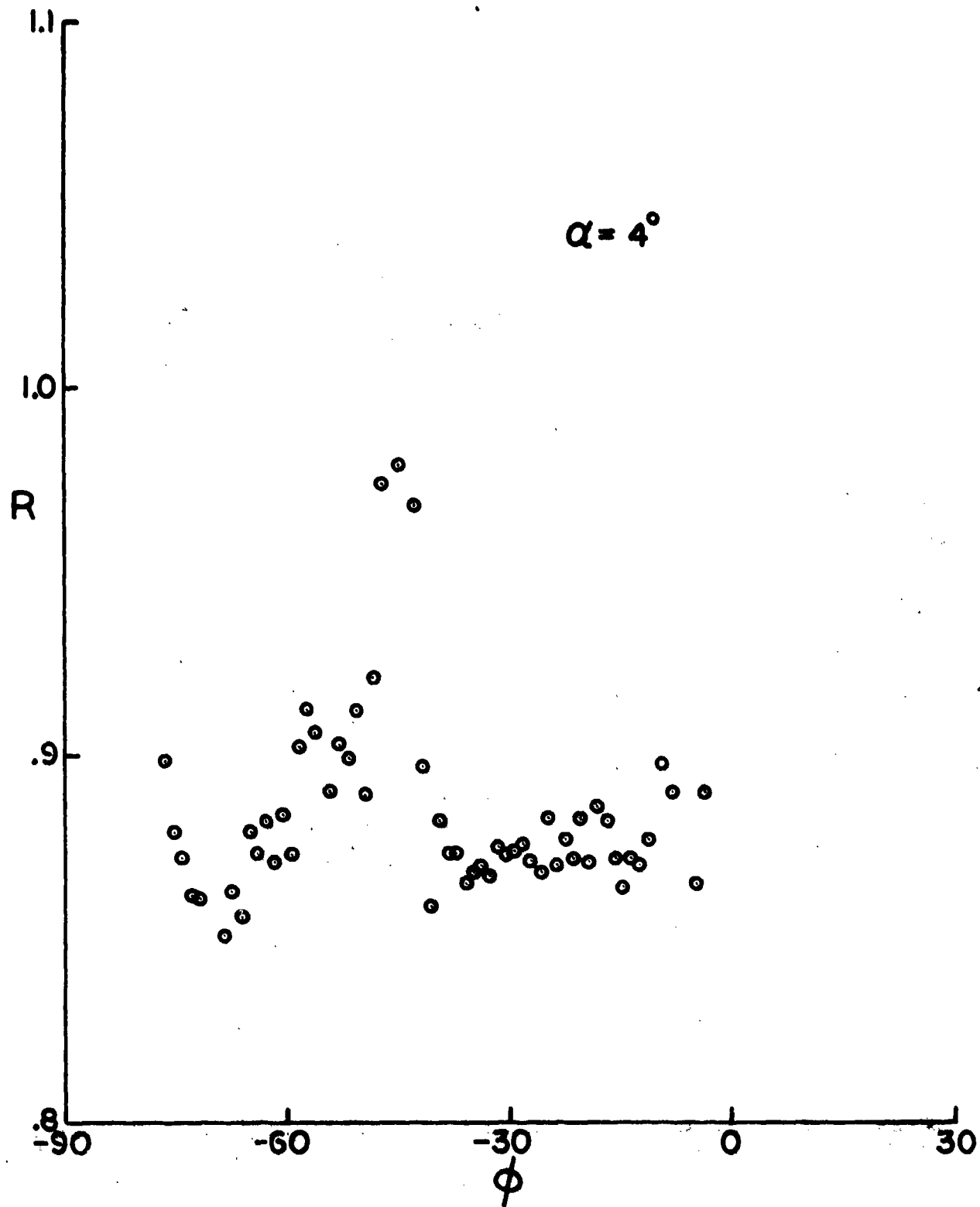


FIGURE B-5 RECOVERY FACTORS ;  $\alpha=4^\circ$ , ROLL =  $90^\circ$

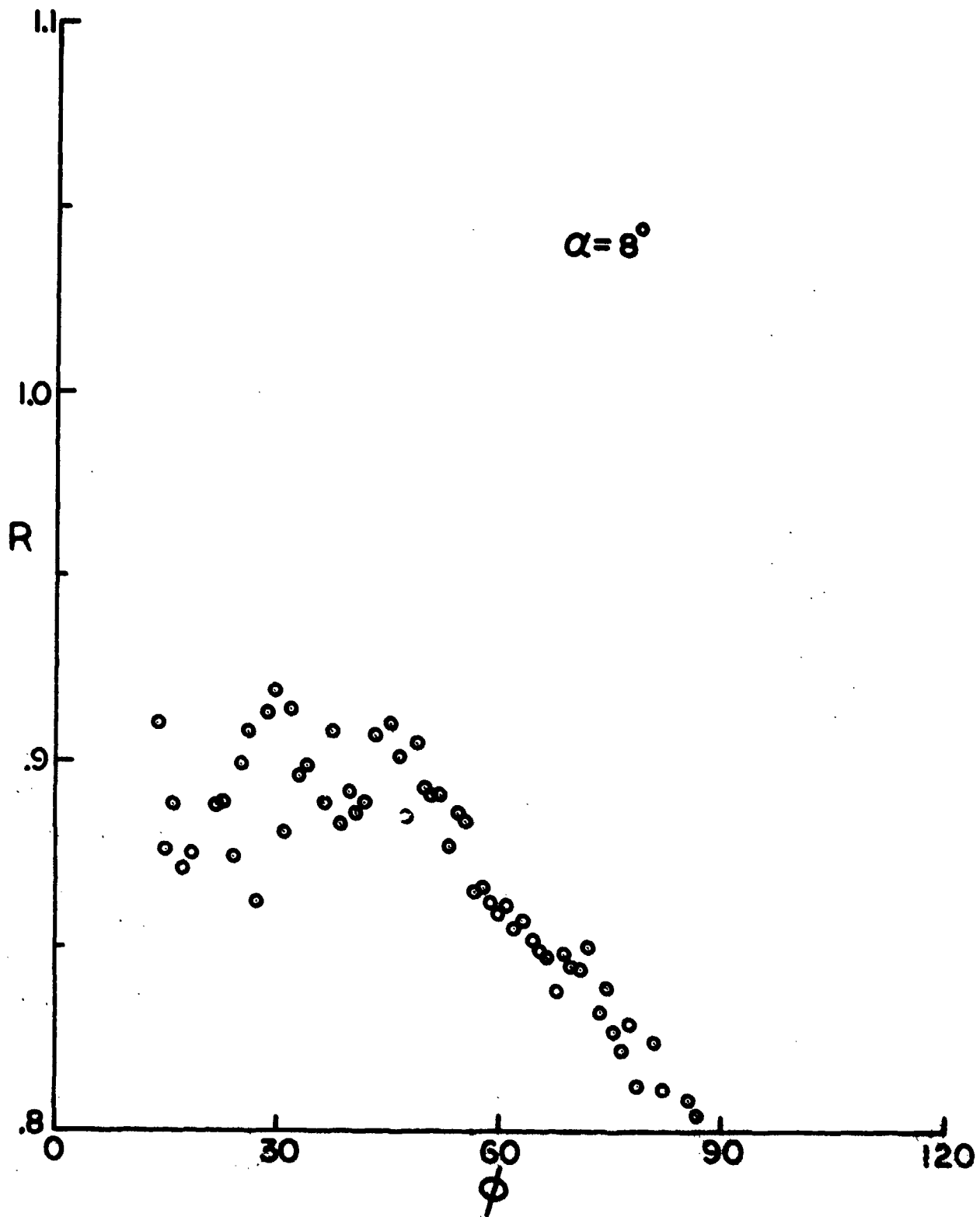


FIGURE B-6 RECOVERY FACTORS;  $\alpha = 8^\circ$ , ROLL =  $0^\circ$



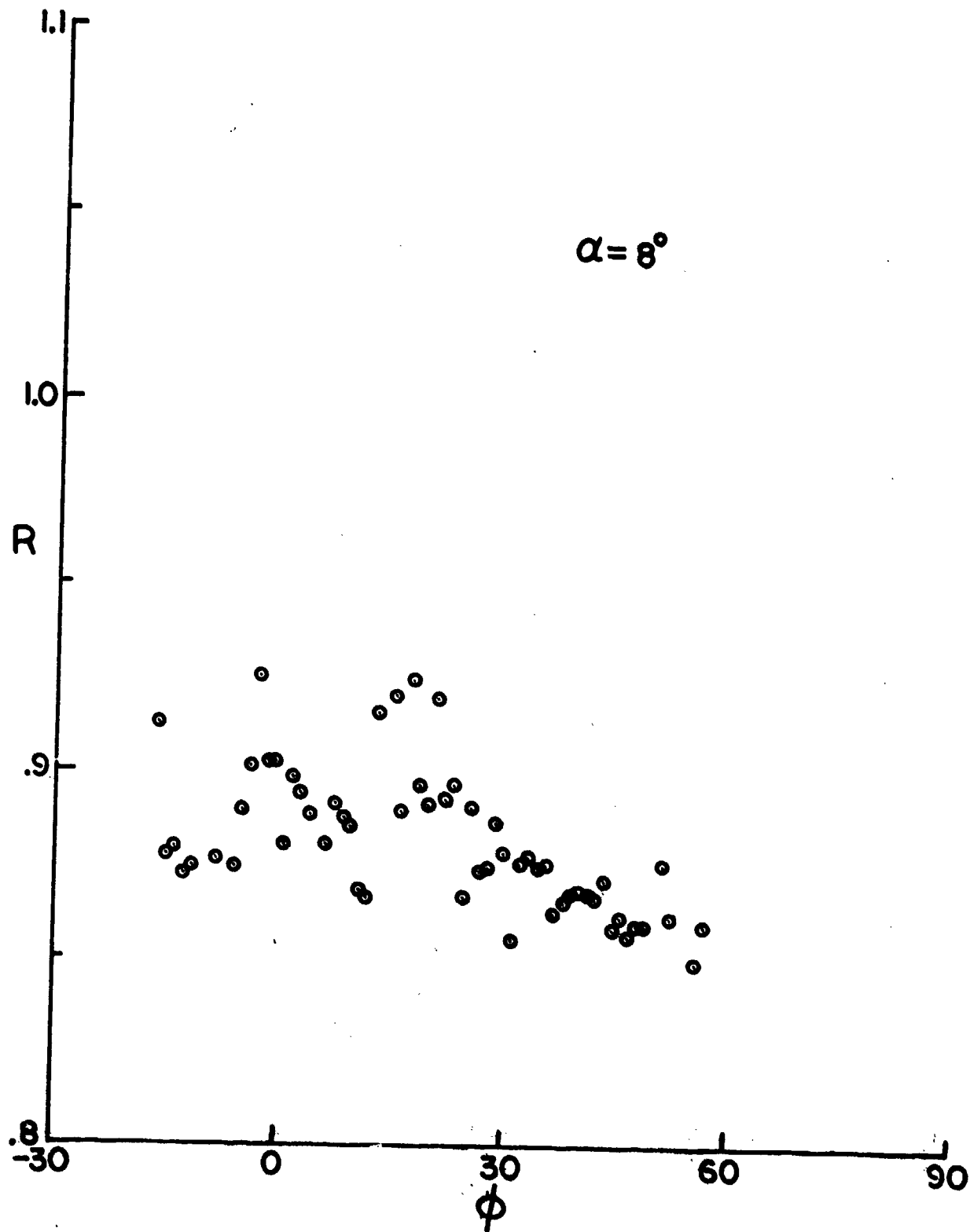


FIGURE B-7 RECOVERY FACTORS ;  $\alpha=8^\circ$ , ROLL=30°

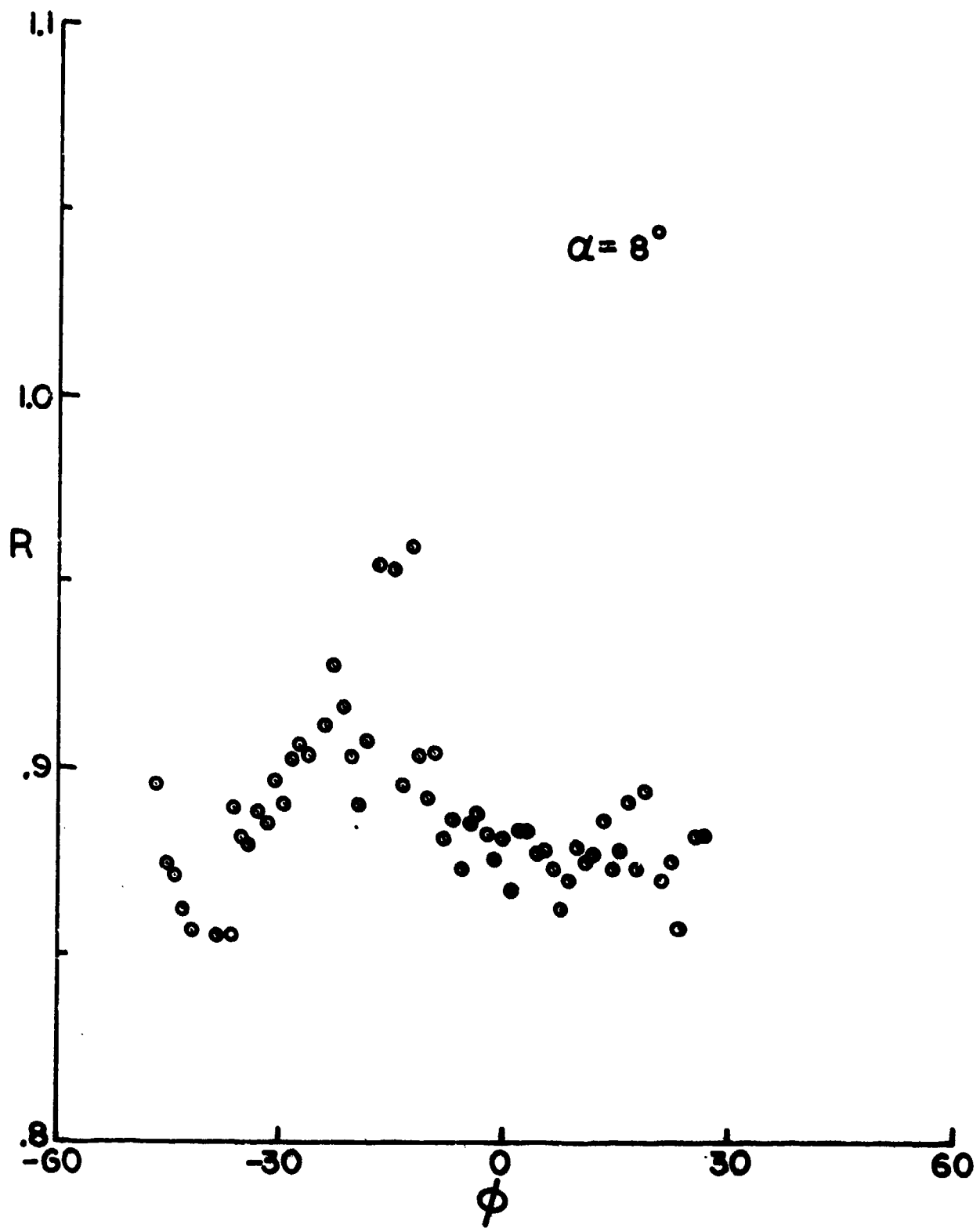


FIGURE B-8 RECOVERY FACTORS ;  $\alpha=8^\circ$ , ROLL=60°

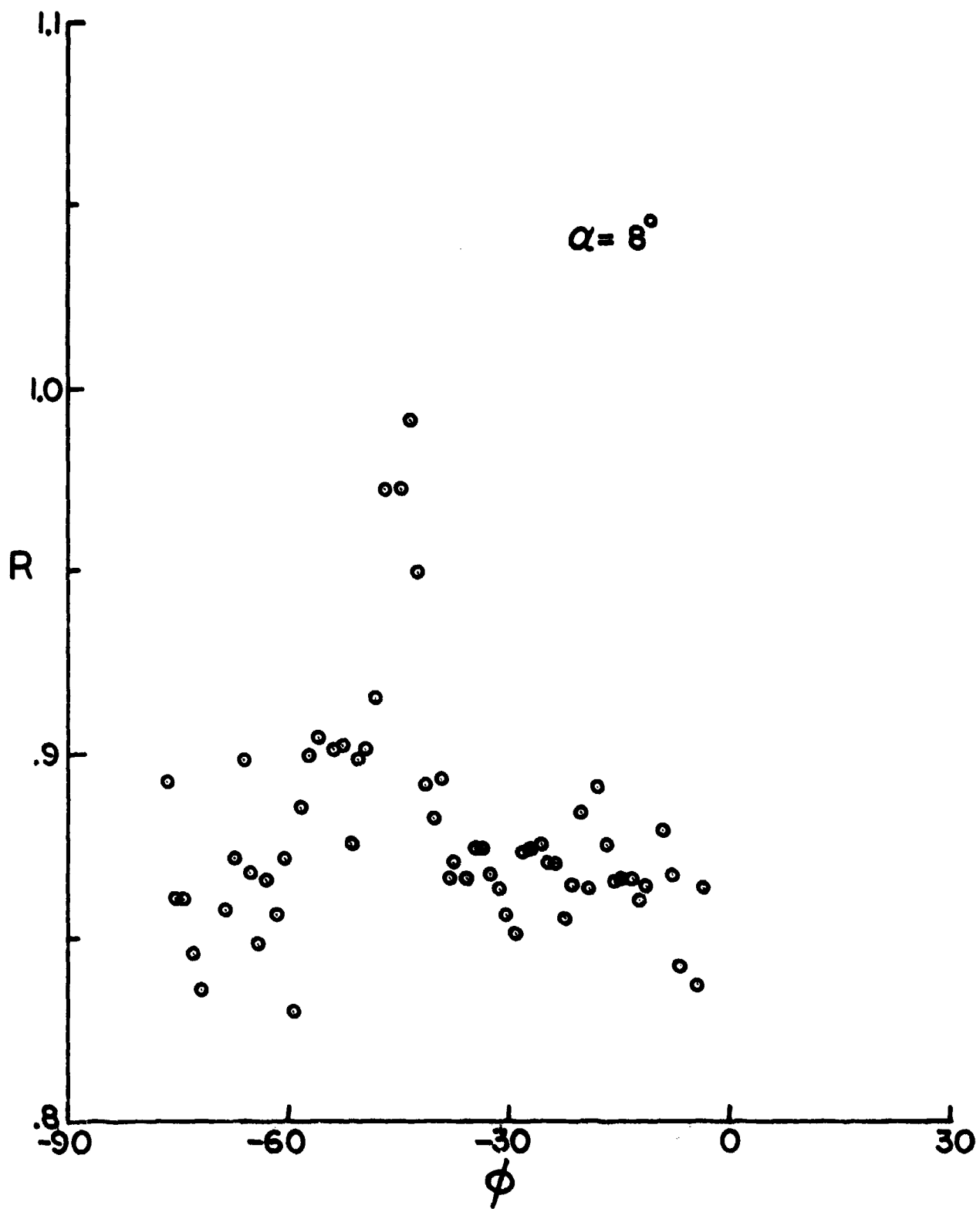


FIGURE B-9 RECOVERY FACTORS ;  $\alpha = 8^\circ$ , ROLL =  $90^\circ$

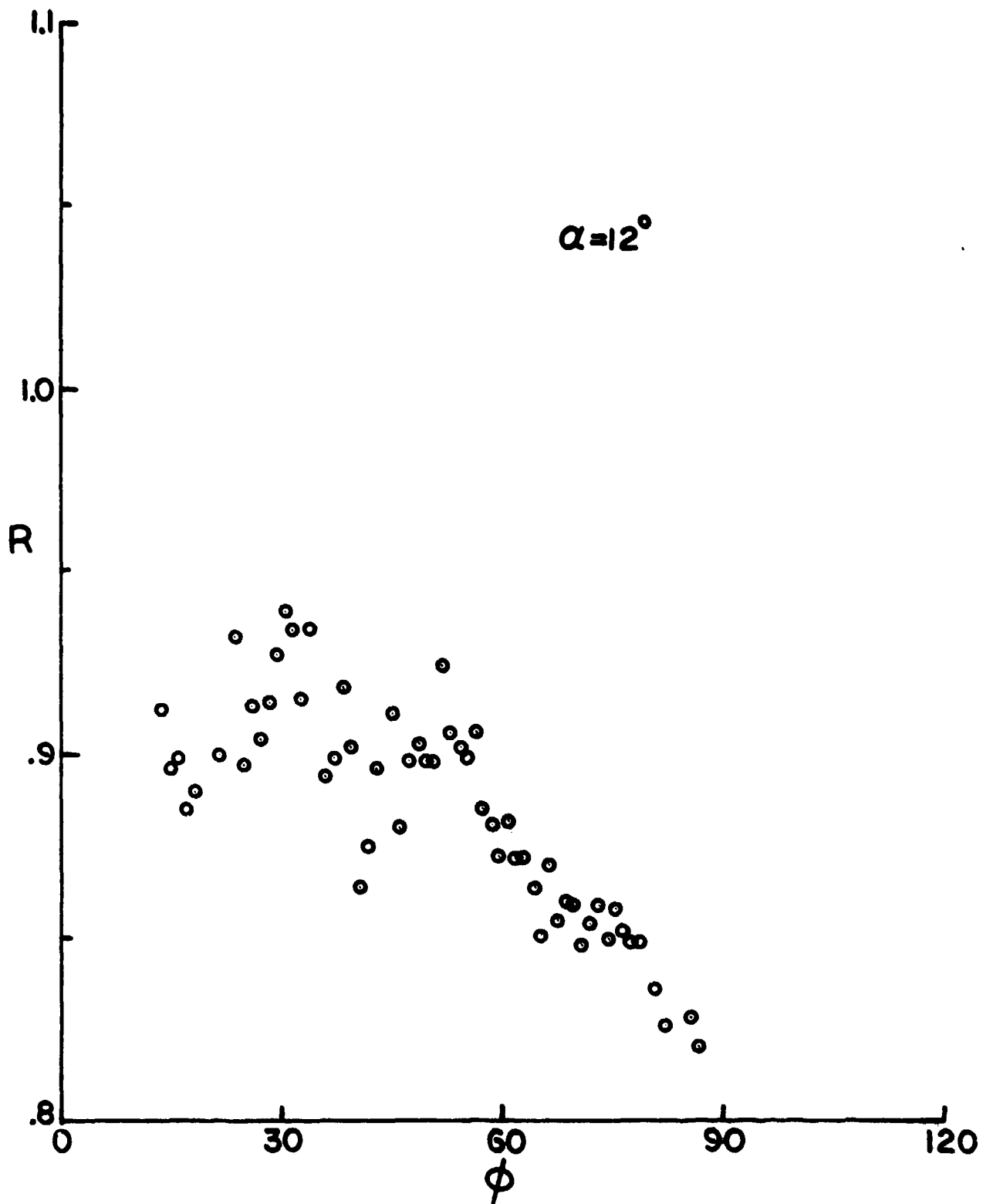


FIGURE B-10 RECOVERY FACTORS ;  $\alpha = 12^\circ$ , ROLL =  $0^\circ$

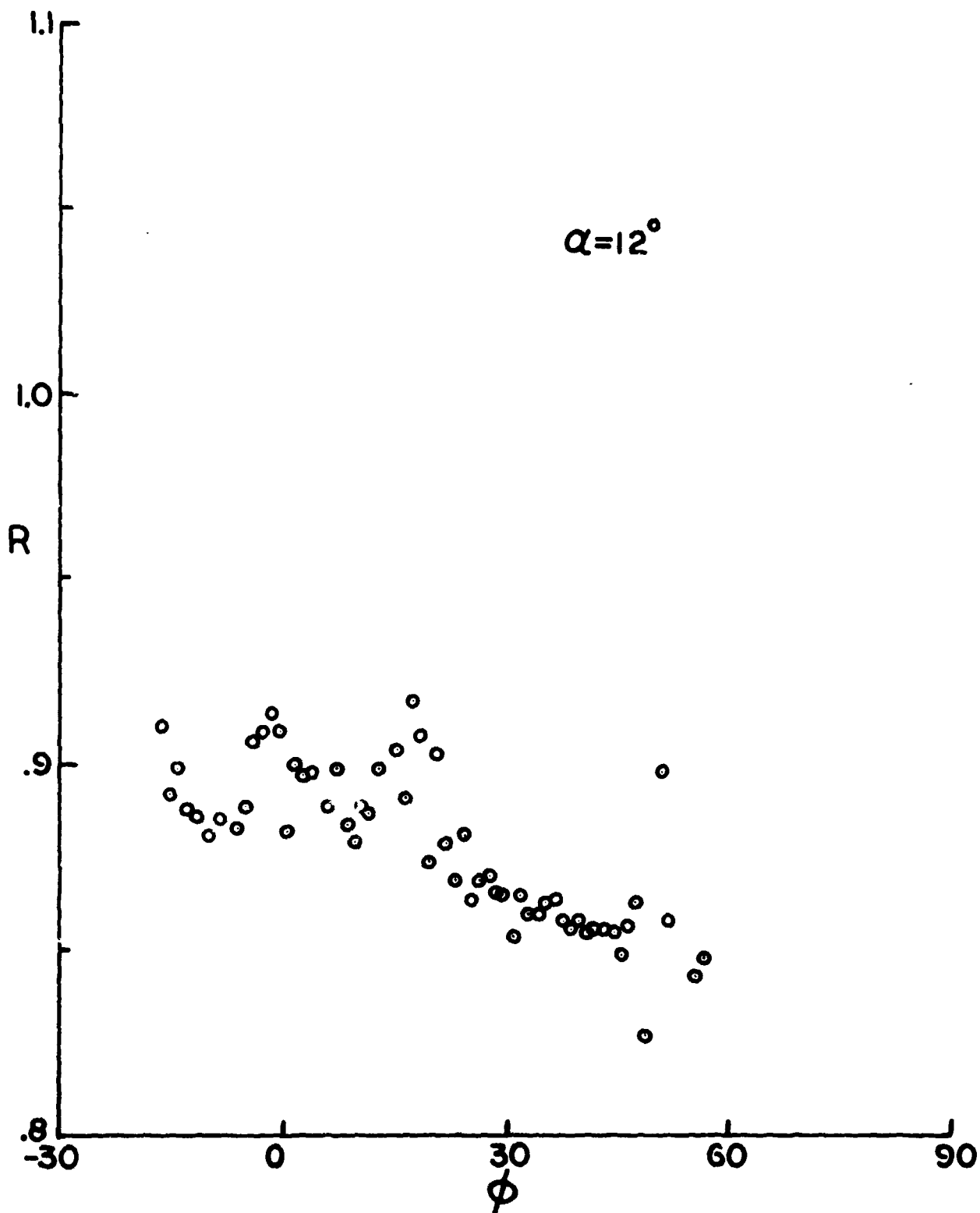


FIGURE B-II RECOVERY FACTORS ;  $\alpha = 12^\circ$ , ROLL =  $30^\circ$

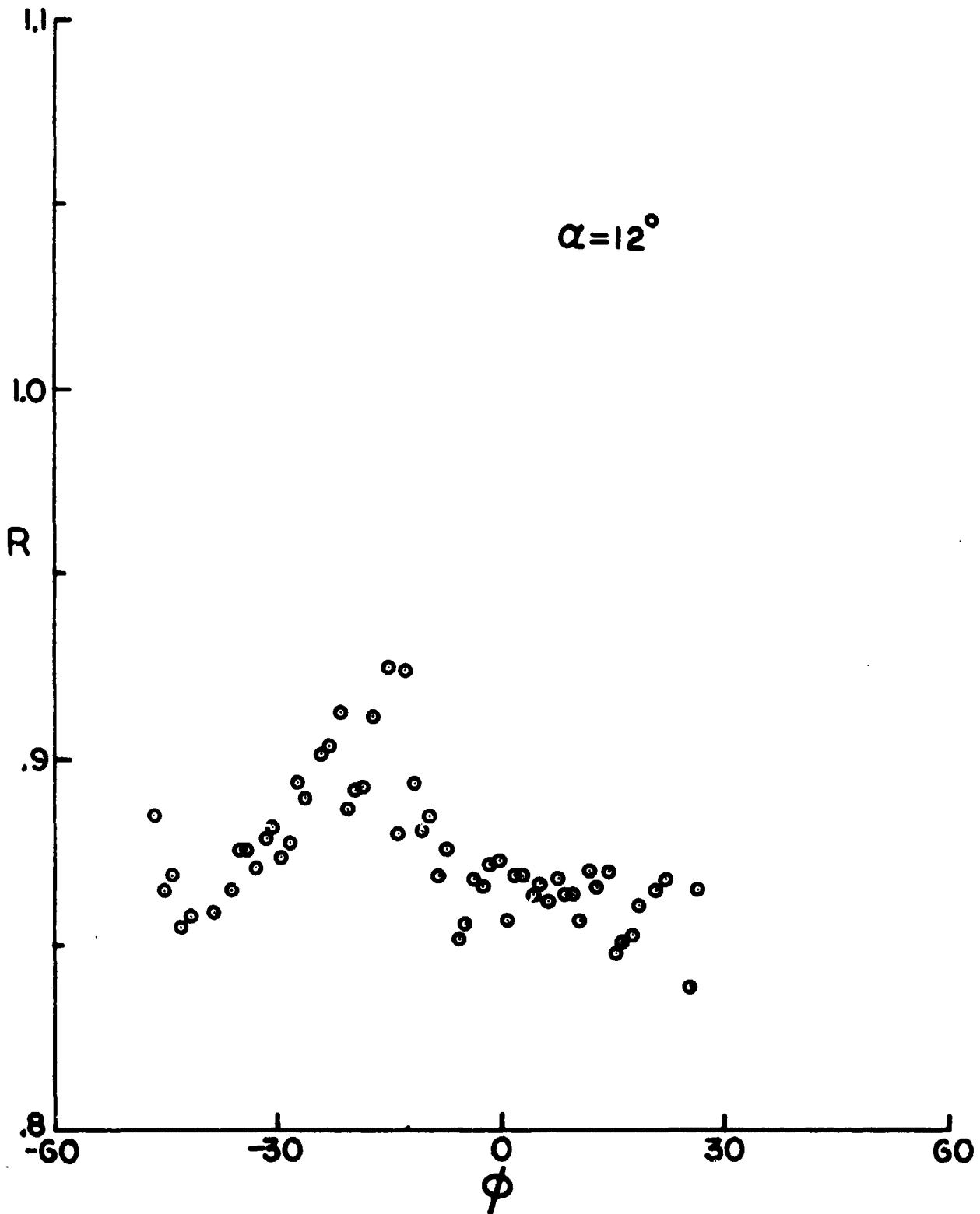


FIGURE B-12 RECOVERY FACTORS ;  $\alpha = 12^\circ$ , ROLL =  $60^\circ$

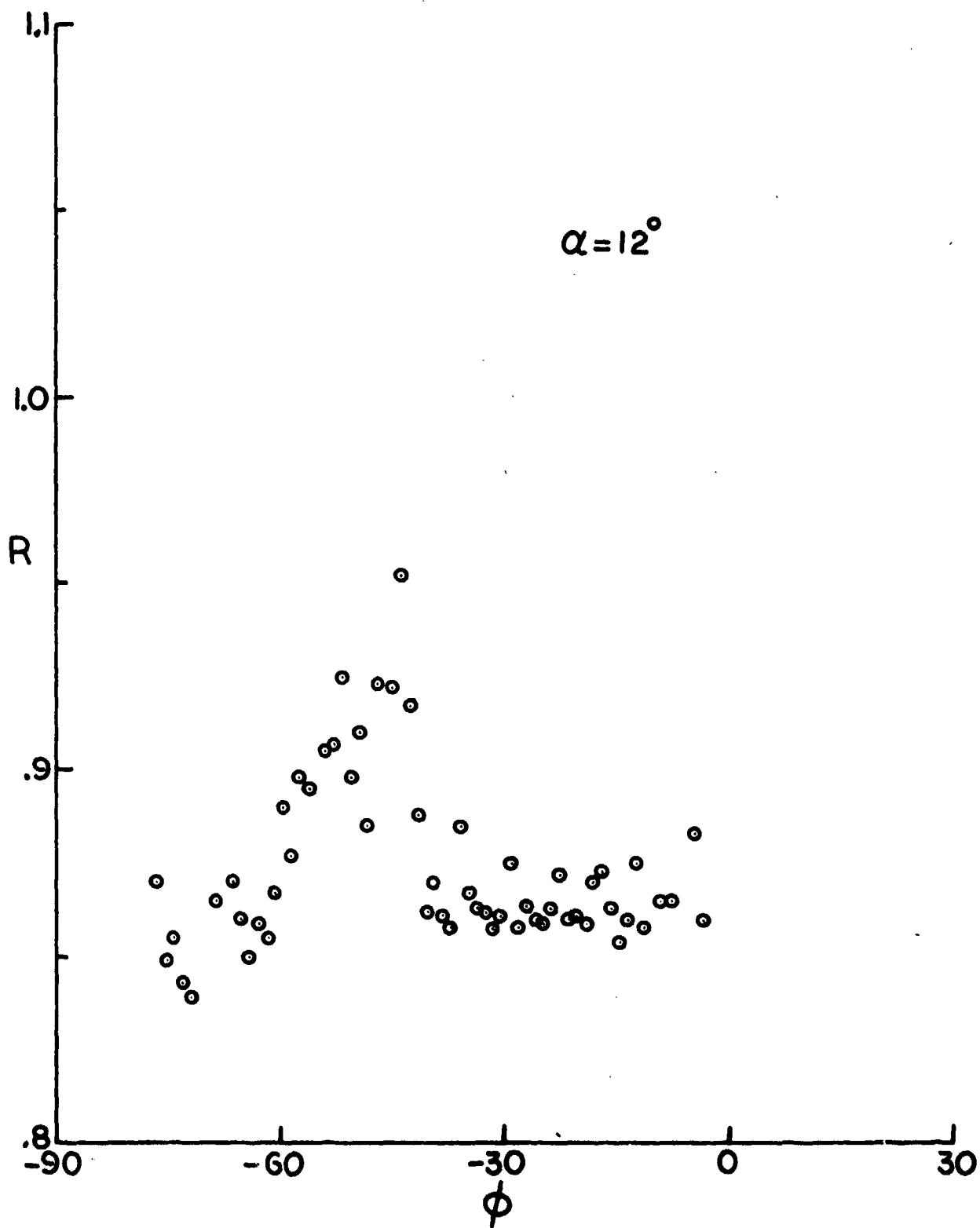


FIGURE B-13 RECOVERY FACTORS ;  $\alpha = 12^\circ$  ,  $ROLL = 90^\circ$

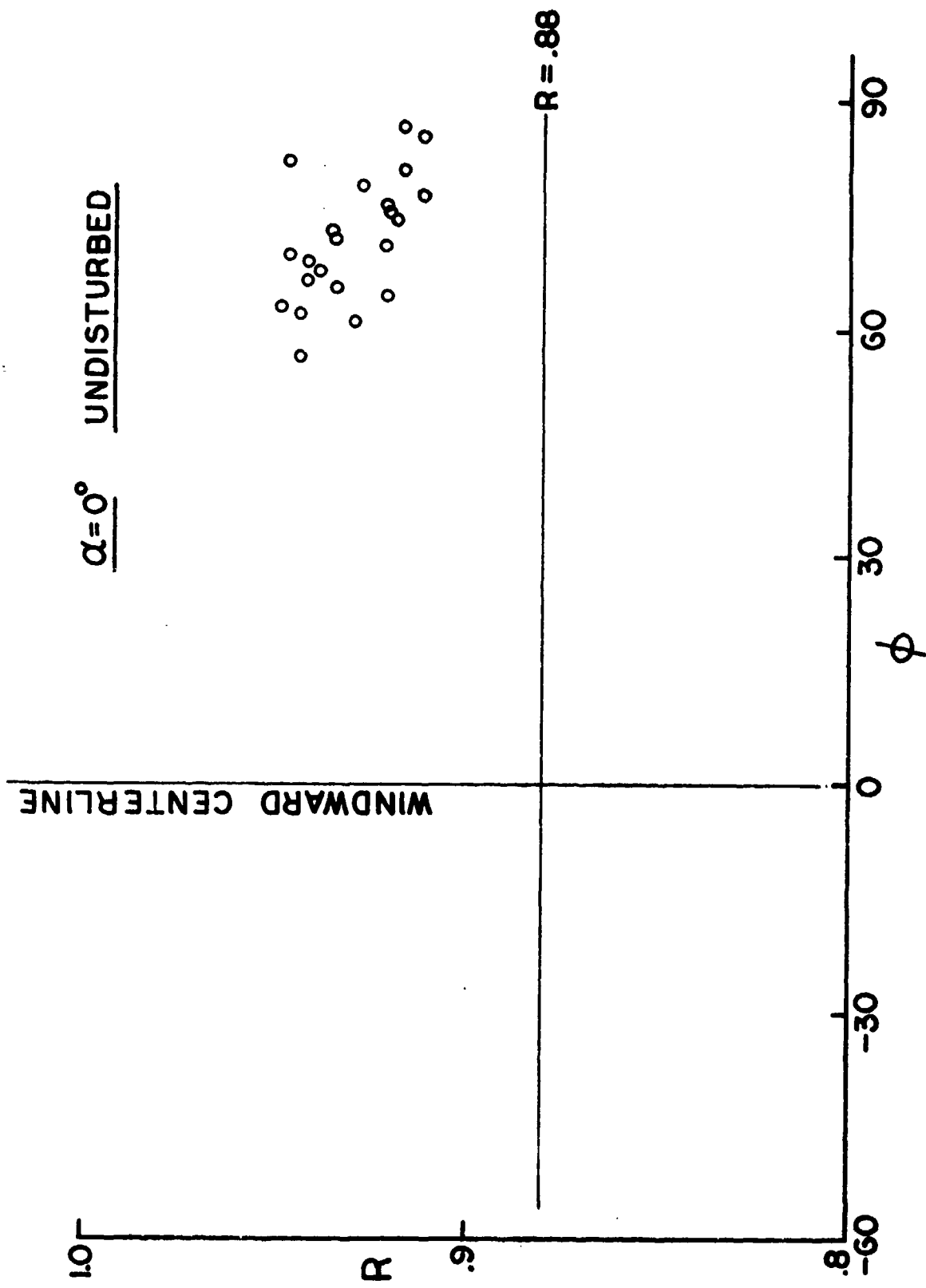


FIGURE B-14 RECOVERY FACTORS , UNDISTURBED FLOW ,  $\alpha = 0^\circ$



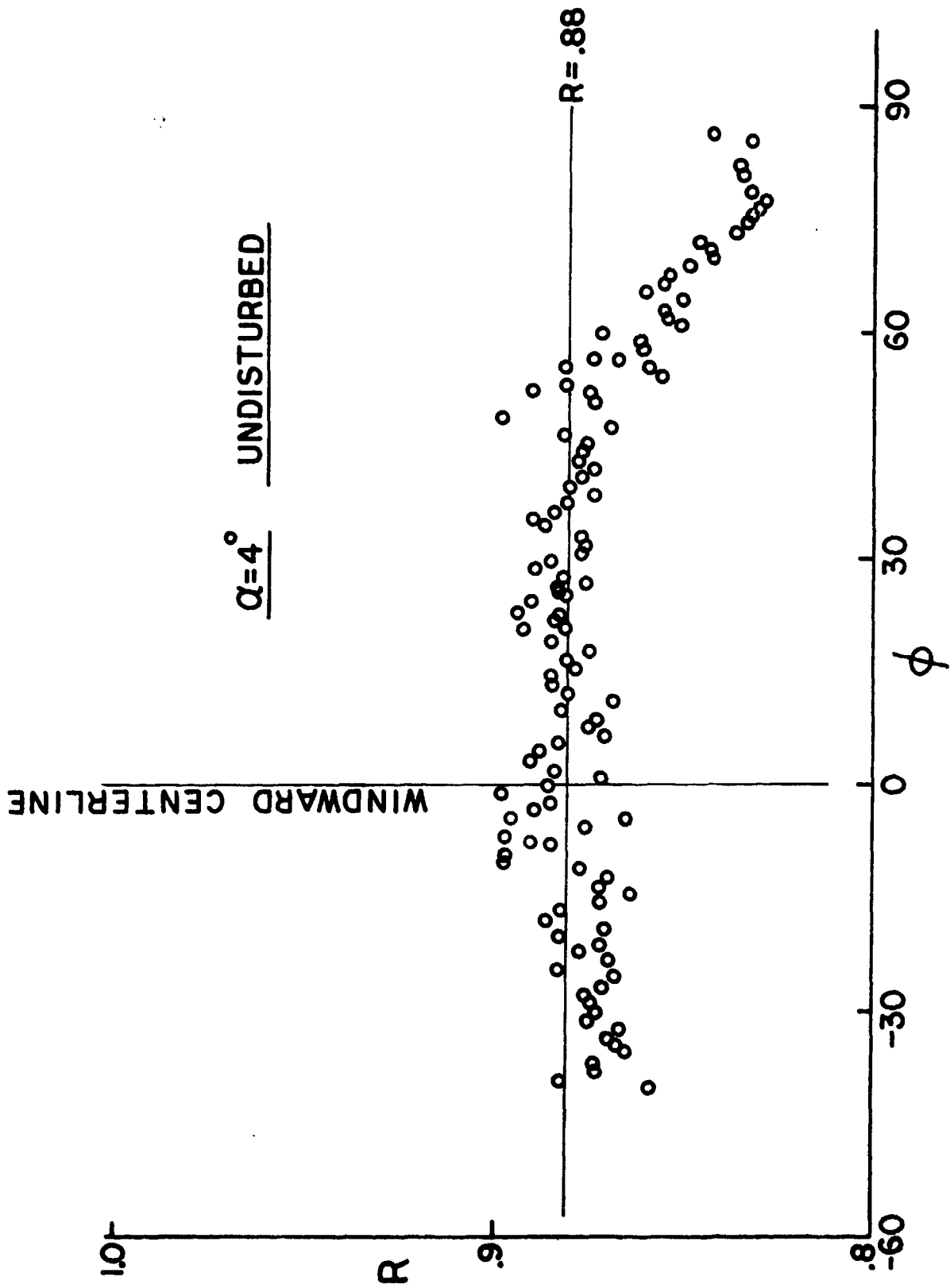


FIGURE B-15 RECOVERY FACTORS, UNDISTURBED FLOW,  $\alpha = 4^\circ$

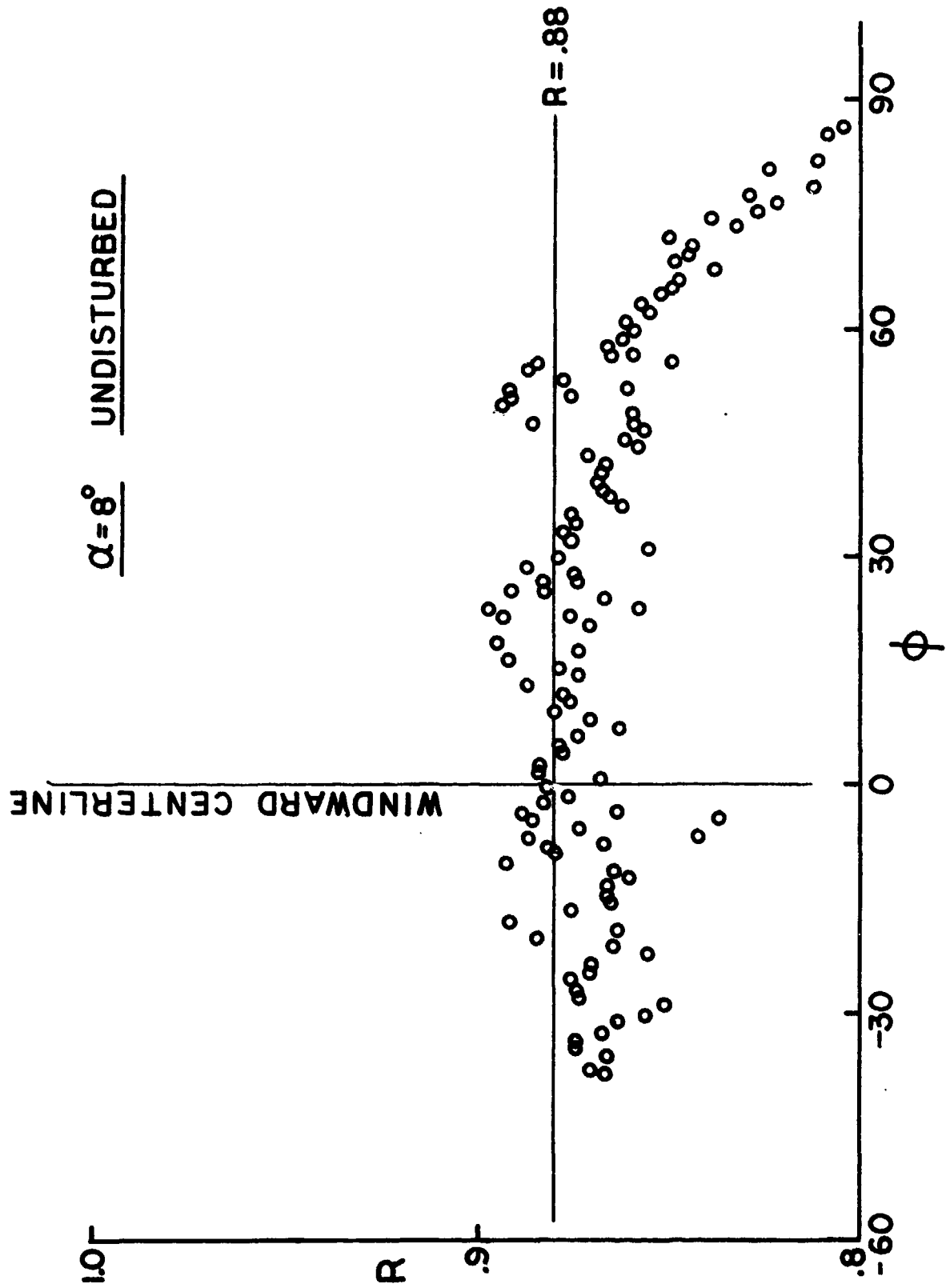


FIGURE B-16 RECOVERY FACTORS, UNDISTURBED FLOW,  $\alpha = 8^\circ$

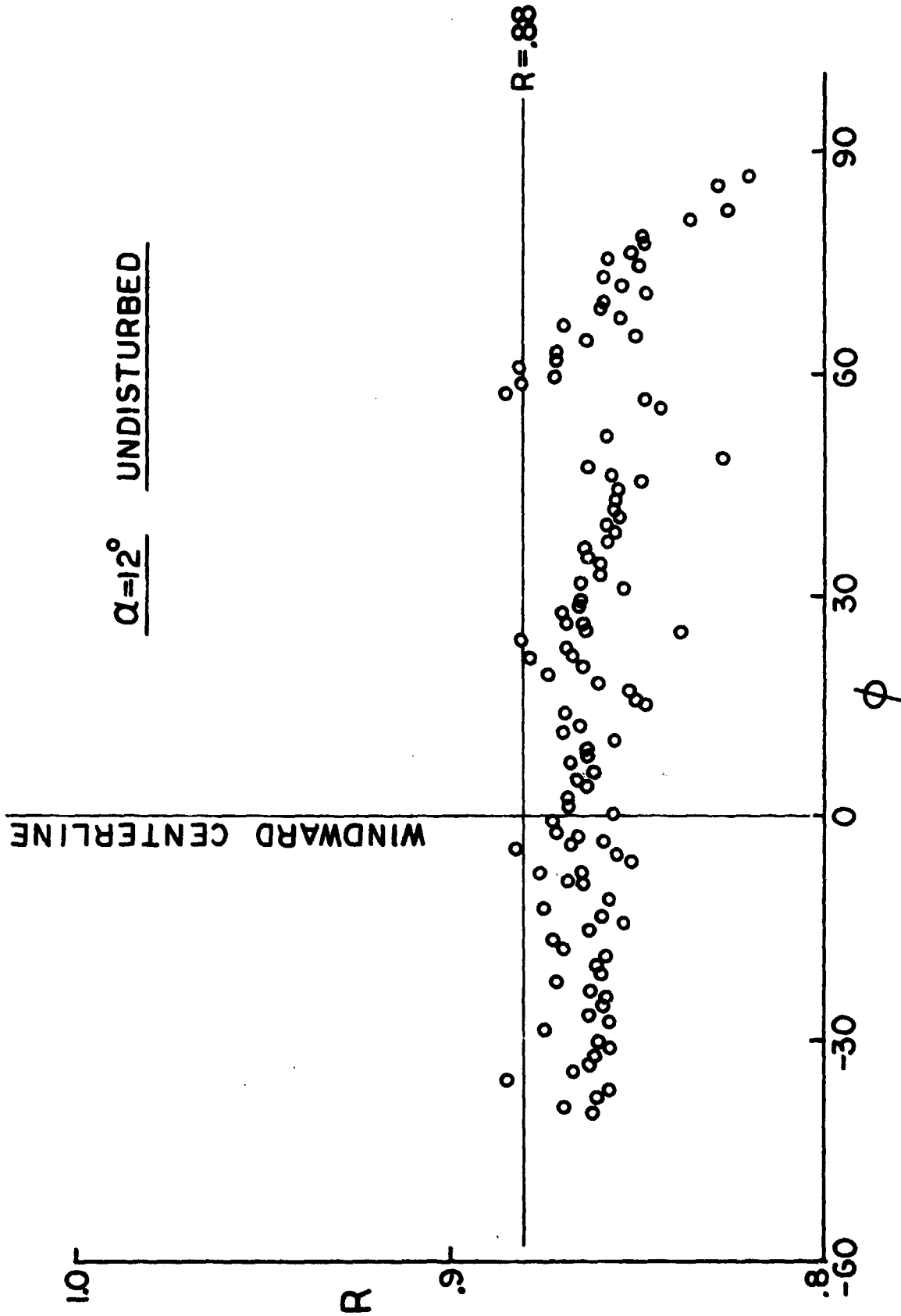


FIGURE B-17 RECOVERY FACTORS, UNDISTURBED FLOW,  $\alpha = 12^\circ$